

A 3% Measurement of the Beam Normal Single Spin Asymmetry in Forward Angle  
Elastic Electron-Proton Scattering using the  $Q_{\text{weak}}$  Setup

A dissertation presented to  
the faculty of  
the College of Arts and Sciences of Ohio University

In partial fulfilment  
of the requirements for the degree  
Doctor of Philosophy

D. Buddhini P. Waidyawansa  
August 2013

©2013 D. Buddhini P. Waidyawansa. All Rights Reserved.

This dissertation titled  
A 3% Measurement of the Beam Normal Single Spin Asymmetry in Forward Angle  
Elastic Electron-Proton Scattering using the  $Q_{\text{weak}}$  Setup

by  
D. BUDDHINI P. WAIDYAWANSA

has been approved for  
the Physics and Astronomy Department  
and the College of Arts and Sciences by

Julie Roche  
Associate Professor of Physics and Astronomy

Robert Frank  
Dean, College of Arts and Sciences

## Abstract

WAIDYAWANSA, D. BUDDHINI P., Ph.D., August 2013, Physics and Astronomy  
A 3% Measurement of the Beam Normal Single Spin Asymmetry in Forward Angle  
 Elastic Electron-Proton Scattering Using the  $Q_{weak}$  Setup

Director of Dissertation: Julie Roche

The beam normal single spin asymmetry generated in the scattering of transversely polarized electrons from unpolarized nucleons is an observable of the imaginary part of the two-photon exchange process. Moreover, it is a potential source of false asymmetry in parity violating electron scattering experiments. The  $Q_{weak}$  experiment uses parity violating electron scattering to make a direct measurement of the weak charge of the proton. The targeted 4% measurement of the weak charge of the proton probes for parity violating new physics beyond the Standard Model. The beam normal single spin asymmetry at  $Q_{weak}$  kinematics is at least three orders of magnitude larger than 5 ppb precision of the parity violating asymmetry. To better understand this parity conserving background, the  $Q_{weak}$  Collaboration has performed elastic scattering measurements with fully transversely polarized electron beam on the proton and aluminum. This dissertation presents the analysis of the 3% measurement (1.3% statistical and 2.6% systematic) of beam normal single spin asymmetry in electron-proton scattering at a  $Q^2$  of  $0.025 \text{ (GeV/c)}^2$ . It is the most precise existing measurement of beam normal single spin asymmetry available at the time. A measurement of this precision helps to improve the theoretical models on beam normal single spin asymmetry and thereby our understanding of the doubly virtual Compton scattering process.

This work was funded by the National Science Foundation under grant No. 065342 and No. 0969788. The data discussed in this dissertation were taken at Jefferson Lab, a facility operated currently by Jefferson Science Associates, LLC under U.S. DOE Contract No. DE-AC05-06OR23177.

*I dedicate this dissertation as a token of my gratitude to my mother and father for all their hard work and sacrifices which paved the path bringing me where I am today.*

## Acknowledgements

As a graduate student, one always hopes to find a good research project and good advisers who can guide them and help them along their way to reaching their goal of either becoming scientists or engineers, etc. To this end, I have been lucky to have the opportunity to work with two good advisers on an interesting research project. Therefore, I would like to start by thanking my advisers, Julie Roche and Paul King, for not only for giving me the opportunity to be involved with the  $Q_{\text{weak}}$  experiment, but also for teaching me how to become a proper physicist. I appreciate your guidance, patience and the time spent on solving analysis issues, correcting presentations, reports and especially, the thesis writing process which was long and tiring. Moving beyond my dissertation research, you have taught me how to improve my presentation skills and networking skills so I can present myself to the outside world as a physicist who is capable of undertaking responsibilities. Together, you both have helped me to take the first steps in my research career. This is just the start. I look forward to collaborating with you in many interesting projects in the future and I hope I will continue to get all those good career advices from you. Next I would like to thank my non-official adviser and mentor at Jefferson Lab, Dave Mack. Thanks Dave for amongst other things, taking me under your wing when I first moved from Ohio to Jefferson Lab. I appreciate the time you took to look over my work and the helpful discussions on how to improve it and for helping me with my thesis writing, even though it was not a part of your job description.

The  $Q_{\text{weak}}$  experiment is the combined effort of many collaborators, institutions and funding agencies. I take this opportunity to acknowledge the efforts of the  $Q_{\text{weak}}$  Collaboration, the Jefferson Lab physics and accelerator divisions in putting together this next generation of parity violating experiment. A special thanks is due to Wouter Deconinck and Jeong Han Lee who lead the software development and DAQ maintenance alongside Paul King. You guys made the work easier for us graduate students. I would also like to convey my gratitude to Dave Gaskell, Joe Grames and Riad Suleiman for the helpful discussions on the implementation of the transverse polarization monitoring and feedback and providing me with the opportunity to test it during the experiment. Thanks Juliette Mammei for taking over the execution of the first transverse measurement in my absence and for your help and advice on the beam normal single spin asymmetry analysis. No collaboration is complete without its graduate students. I would like to thank Katherine Myers, John Leacock, Amrendra Narayan, Scott McEwan, John Leacock, Juan Carlos, Adesh Subedhi, Manolis

Kargiantoulakis and Nurussaman for all their help. I enjoyed working with you and I hope I'll get to work with you in the future too.

Moving from Sri Lanka, half way across the world and across cultures, to USA was a life changing experience. I would like to thank my batch mates, the staff and faculty of the Ohio University department of physics for making that transition easier for me. I only spent about one and half year at Ohio University before moving to Jefferson Lab in Virginia for my research. I do miss being in the university premises and I always appreciate the welcome I get during my occasional visits. Next I would like to thank my Sri Lankan family here, my friends in Athens, Hampton Roads and Washington D.C. Having you guys here and spending time with you organizing cultural events, trips and get-togethers helped me to forget all the things I was missing out back home. Special thanks goes to Anusha and Lanka for letting me crash at their place during the last few days when I was doing a mad dash to meet the dissertation deadline. I would also like to thank Rushmi, my best friend, for her moral support in pulling me through whenever I was feeling down. The distance between Australia and USA has never stopped you from coming to my aid when I needed a friend.

Finally, I would like to thank my family, my mother, my father and my brother. I know it has been hard for you to not to have me by your side all these years. But I know you endure it because you know it is the best thing for me. I can never thank or repay you enough for the sacrifices you had to made along the way to get me where I am today. Last but not least, I would like to thank Rakitha. You are the best thing that has ever happened to me and I have Ohio University and  $Q_{\text{weak}}$  to thank for that. I could not have asked for a better life partner who understands my strengths and weaknesses better than anyone else in the world. I look forward to many more years of adventures in my personal and research life together with you.

# Table of Contents

Abstract . . . . .	3
Acknowledgements . . . . .	5
List of Tables . . . . .	12
List of Figures . . . . .	15
1 Introduction . . . . .	20
2 Physics Motivation and the Formalisms . . . . .	23
2.1 The $Q_{\text{weak}}$ Experiment . . . . .	23
2.1.1 The Standard Model of the Electroweak Interaction . . . . .	23
2.1.2 The Parity Violating Electron-Proton Asymmetry . . . . .	26
2.1.3 The Weak Charge of the Proton . . . . .	29
2.1.4 Motivation for a 4% Measurement of $Q_w^p$ . . . . .	31
2.1.5 Theoretical Interpretability . . . . .	35
2.2 The Beam Normal Single Spin Asymmetry Measurement . . . . .	37
2.2.1 Electron Scattering in the Born Approximation . . . . .	38
2.2.2 Scattering Beyond the Born Approximation . . . . .	39
2.2.3 The Two-Photon Exchange Contribution . . . . .	40
2.2.4 Experimental Inputs of the Two-Photon Exchange . . . . .	44
2.2.5 Imaginary Part of the Two-Photon Exchange . . . . .	47
2.2.6 Beam Normal Single Spin Asymmetry in Electron-Nucleon Scattering . . . . .	49
2.2.7 As a False Asymmetry in PVES . . . . .	53
3 $Q_{\text{weak}}$ Setup Design and Implementation . . . . .	55
3.1 Design Parameters . . . . .	56
3.2 Polarized Electron Beam at Jefferson Lab . . . . .	57
3.2.1 Polarized Electron Source . . . . .	59
3.2.2 Helicity Generation and Fast Helicity Reversal . . . . .	62
3.2.3 Spin Manipulation with the Double Wien . . . . .	63

		8
3.3	Beam Polarimetry . . . . .	65
3.3.1	Basel-Hall C Møller Polarimeter . . . . .	65
3.3.2	Hall C Compton Polarimeter . . . . .	66
3.4	Electron Beam Monitoring . . . . .	67
3.4.1	Beam Position . . . . .	67
3.4.2	Beam Current . . . . .	77
3.4.3	Beam Energy . . . . .	79
3.5	The Primary Target . . . . .	81
3.6	The Toroidal Magnet and the Collimator System . . . . .	82
3.7	The Čerenkov Detector Array . . . . .	84
3.8	Tracking Detector System . . . . .	86
4	Data Acquisition and Analysis Software . . . . .	87
4.1	The Data Acquisition System . . . . .	87
4.1.1	CEBAF Online Data Acquisition . . . . .	87
4.1.2	Integrating-Mode DAQ . . . . .	88
4.1.3	Tracking-Mode DAQ . . . . .	92
4.2	QwAnalysis Software . . . . .	92
4.2.1	Parity Analysis Engine . . . . .	93
5	False Asymmetries and Random Noise . . . . .	101
5.1	Helicity Correlated Beam Asymmetries . . . . .	101
5.1.1	Sources of HCBA . . . . .	102
5.1.2	Minimizing HCBA in the Commissioning Period and Run I . . . . .	106
5.2	False Asymmetry Due to Helicity Control Signals . . . . .	114
5.2.1	The Delayed Helicity Signal . . . . .	115
5.2.2	Helicity Signal Leakage Measurements . . . . .	116
5.2.3	MPS and QRT Signal Leakage Measurements . . . . .	120
5.2.4	Quartet Polarity Dependence of the Helicity, MPS, QRT Leakage . . . . .	122
5.3	Random Noise . . . . .	125
5.3.1	Electronic Noise Measurements Under Realistic Conditions . . . . .	126
5.3.2	Electronic Noise in the Detector Electronic Chains . . . . .	130
5.3.3	Noise in LED driven PMTs . . . . .	132
6	Beam Normal Single Spin Asymmetry Analysis . . . . .	134
6.1	Experimental Setup and the Full Data Set . . . . .	134



	9
6.2	General Analysis Considerations . . . . . 135
6.3	Azimuthal Dependence of the Raw Asymmetry . . . . . 137
6.4	Beam Asymmetry Correction Using Linear Regression . . . . . 138
6.4.1	Helicity Correlated Beam Asymmetries Measured at the Target 139
6.4.2	Detector Sensitivities to HCBA . . . . . 141
6.4.3	Beam Asymmetry Correction . . . . . 143
6.5	Azimuthal Modulating Physics Asymmetry . . . . . 145
6.5.1	Detector Acceptance Correction . . . . . 148
6.5.2	Regression Scheme Dependence . . . . . 149
6.5.3	Non-linearity of the System . . . . . 153
6.6	The Extraction of the Beam Normal Single Spin Asymmetry . . . . . 155
6.6.1	Beam Polarization . . . . . 155
6.6.2	Backgrounds . . . . . 157
6.6.3	Electromagnetic Radiative Corrections . . . . . 163
6.7	Beam Normal Single Spin Asymmetry from the Proton . . . . . 167
7	Beam Normal Single Spin Asymmetry Leakage . . . . . 169
7.1	BNSSA Leakage Due to Symmetry Breaking in the Detector Array . 169
7.1.1	Leakage via Transverse Measurements . . . . . 170
7.1.2	Leakage via Simulations . . . . . 171
7.2	Residual Transverse Polarization in the Electron Beam . . . . . 174
7.2.1	Transverse Polarization Monitoring . . . . . 175
7.3	BNSSA Leakage on Parity Violating Asymmetry . . . . . 179
7.3.1	Systematic Uncertainty for the 19% $Q_w^p$ Measurement . . . . . 179
7.3.2	Systematic Uncertainty for the Final $Q_w^p$ Measurement . . . . . 180
8	Results and Conclusions . . . . . 183
8.1	Contributions Towards the Measurement of the Weak Charge of the Proton . . . . . 183
8.1.1	Data Acquisition and Analysis Related Work . . . . . 183
8.1.2	Helicity Correlated False Asymmetries . . . . . 184
8.1.3	Transverse Polarization Monitoring and BNSSA Leakage . . . . . 185
8.2	The Determination of the Weak Charge of the Proton . . . . . 185
8.3	The 3% Measurement of the Beam Normal Single Spin Asymmetry . . 187
	Bibliography . . . . . 193

	10
Appendix A: Beam Position Monitoring Misc . . . . .	209
A.1 List of BPMs Used by $Q_{\text{weak}}$ and Their Configurations . . . . .	209
A.2 Error on Position Estimates Due to an Error on $\alpha$ Gains of the BPMs . . . . .	212
A.3 BPM Resolutions . . . . .	213
A.4 Stability of the BPM Pedestals . . . . .	213
A.5 Linear Least Square Fit Algorithm used to Project Beam Position and Angle at the $Q_{\text{weak}}$ Target . . . . .	214
A.6 Error Associated With Beam Projection on the $Q_{\text{weak}}$ Target . . . . .	215
A.7 Extracting the Differential Non-linearity Factor of the BPMs . . . . .	216
A.8 Locations of the BPMs in the Injector and Hall C Beamlines . . . . .	218
Appendix B: Čerenkov Detector Post-Experiment Survey . . . . .	230
Appendix C: PMT Weight Estimates for the Transverse Running . . . . .	234
C.1 Stability of Improper Weights . . . . .	234
C.2 Weights Used in Pass5 Transverse Analysis . . . . .	235
Appendix D: Data Acquisition and Analysis Software Misc . . . . .	240
D.1 List of Integrating DAQ signals . . . . .	240
D.2 Integrating-Mode Data Rate and Data Size . . . . .	242
D.3 VME QWEAK 8 Channel 18 bit ADC module . . . . .	243
D.4 Helicity Pattern Generator . . . . .	244
D.5 Sign of the Physics Asymmetry . . . . .	246
Appendix E: Helicity Magnets First Performance Check at 960 Hz . . . . .	247
E.1 Helicity Magnet Locations . . . . .	247
E.2 Test Procedure . . . . .	247
E.3 Induced Position Differences . . . . .	248
Appendix F: Noise Studies Misc . . . . .	253
F.1 The List of Hall C Patch Panel Channels Used for $Q_{\text{weak}}$ Signals and Their Channel Noise Content . . . . .	253
F.2 Full Results from the Čerenkov Detector Electronics Chain Noise Mea- surements . . . . .	255
Appendix G: Transverse Data Analysis Misc . . . . .	258
G.1 IHWP Reversal and Slug Numbers . . . . .	258

	11
G.2 Beam Parameters . . . . .	259
G.3 Detector Sensitivity to Beam Parameters . . . . .	262
G.4 Beam Asymmetry Correction . . . . .	262
G.5 Aluminum Background Analysis . . . . .	265
G.6 Inelastic Background Analysis . . . . .	266
G.7 $Q^2$ Dependence of the Measured Asymmetry . . . . .	269
G.8 Regression Scheme Dependence Study . . . . .	269
G.9 Error Analysis . . . . .	271
Appendix H: BNSSA Leakage Analysis Misc . . . . .	274
H.1 Correlations Between Azimuthal Dependence of the Regressed Asymmetries and Helicity Correlated Beam Asymmetries . . . . .	274
H.2 Residual Transverse Polarization in the Wiens . . . . .	278
Appendix I: Theory Calculations . . . . .	283

## List of Tables

### Table

2.1	Standard Model neutral-current couplings of the fermions. . . . .	28
2.2	Electroweak radiative corrections applied on the weak charge of the proton	37
2.3	Some available model calculations of single spin asymmetries. . . . .	48
3.1	Proposed error budget of the $Q_{\text{weak}}$ experiment . . . . .	55
3.2	Design parameters of the $Q_{\text{weak}}$ experiment. . . . .	56
3.3	The Wien filter and solenoid angle settings used by the experiment. . . .	65
3.4	BPM combinations used to project beam position at the target. . . . .	75
4.1	Read-out modules used in the integrating-mode DAQ. . . . .	90
4.2	Event cuts used in the parity analysis engine. . . . .	97
4.3	Formation of asymmetries, differences and yields. . . . .	99
4.4	Formation of an asymmetry from a single main detector. . . . .	100
4.5	Formation of the asymmetry from the Čerenkov detector array. . . . .	100
5.1	Specifications on the helicity correlated beam asymmetries for $Q_{\text{weak}}$ . . .	101
5.2	Pockels cell base voltages for minimum $\alpha$ phase. . . . .	107
5.3	HCBA measured at the injector after polarized source setup. . . . .	111
5.4	HCBA cancellation with slow helicity reversal. . . . .	112
5.5	Helicity leakage observed in an hour long measurement. . . . .	119
5.6	Helicity leakage observed in a 10 hour long measurement. . . . .	120
5.7	MPS/QRT leakage. . . . .	122
5.8	Sub-block dependence of the leakage from the MPS, heicity and QRT. . .	124
5.9	Improved noise levels in electronics when using new cables and connectors.	130
5.10	Results from the VQWK ADC channel noise measurement. . . . .	130
5.11	Noise measured in the Čerenkov detector electronics chains. . . . .	132
5.12	Noise in LED driven PMTs . . . . .	133
6.1	Beam currents used on different targets during transverse running period.	135
6.2	Amount of transverse data available for analysis after quality cuts. . . .	136
6.3	Average helicity correlated beam asymmetries. . . . .	141
6.4	The physics asymmetry from the LH2-cell target. . . . .	145
6.5	Regression schemes used to study the the regression scheme dependence.	149

	13
6.6	Regression scheme dependence of the physics asymmetry. . . . . 151
6.7	Differences between the physics asymmetry extracted from five-parameter regression and other regression schemes. . . . . 152
6.8	Beam polarization in Transverse_Run I and Transverse_RunII. . . . . 157
6.9	Physics asymmetry from the DS4Al target. . . . . 158
6.10	Aluminum target window background correction. . . . . 160
6.11	Inelastic asymmetry from the LH2-cell target. . . . . 160
6.12	Inelastic background correction. . . . . 162
6.13	Simulated $Q^2$ at the scattering vertex with radiative corrections . . . . . 164
6.14	Energy loss correction factors for the different radiative effects . . . . . 164
6.15	Summary of the systematic corrections. . . . . 168
6.16	Summary of the errors. . . . . 168
7.1	BNSSA leakage extracted from the LH2-cell transverse data set. . . . . 170
7.2	Azimuthal angles of the Čerenkov detectors from survey . . . . . 172
7.3	Relative azimuthal shifts between the detectors in opposite octants. . . . . 172
7.4	Residual transverse polarization in different Wien periods. . . . . 181
8.1	World data on the beam normal single spin asymmetry measurements. . . . . 188
8.2	Theoretical predictions for BNSSA at $Q_{\text{weak}}$ kinematics . . . . . 189
8.3	Remainder of the BNSSA measurements and their relative precisions. . . . . 192
A.1	List of BPMs in the injector beamline used by $Q_{\text{weak}}$ . . . . . 210
A.2	List of BPMs in the Hall C beamline used by $Q_{\text{weak}}$ . . . . . 211
A.3	Dependence of the resolution of BPM 3H07B on beam current. . . . . 213
A.4	BPM calibration runs taken during $Q_{\text{weak}}$ . . . . . 214
C.1	Run ranges using the new detector weights in transverse data. . . . . 235
C.2	New PMT weights used for the transverse running period. . . . . 237
D.1	List of signals digitized via the integrating-mode DAQ. . . . . 240
D.2	Integrating-mode readout module output rates. . . . . 242
D.3	Features of the VQWK ADCs. . . . . 243
E.1	List of runs taken during helicity magnet tests. . . . . 248
F.1	Noise levels on the Hall C patch panel channels used by $Q_{\text{weak}}$ . . . . . 253
F.2	Noise measurements with beam in the hall. . . . . 255

	14
F.3	Noise measurements when there is no beam in the hall. . . . . 256
F.4	Noise measurements with switched power supplies. . . . . 256
F.5	Effect of background noises on detector signal chains. . . . . 257
F.6	Noise measurements with preamplifier switched. . . . . 257
G.1	Durations of the IHWP reversals in the transverse data set. . . . . 258
G.2	Slug numbers assigned for the transverse data set. . . . . 258
G.3	Detector sensitivities to the beam parameters. . . . . 262
G.4	Average HCBA measured in slug 200005. . . . . 262
G.5	Average detector sensitivities measured in slug 200005. . . . . 263
G.6	Beam asymmetry corrections applied on raw asymmetries in slug 200005. 264
G.7	Inelastic asymmetry from the aluminum target. . . . . 268
G.8	Relative changes in the asymmetry due to changes in light weighted $Q^2$ . . 270
G.9	Regression corrections applied on the vertical LH2-cell asymmetries. . . . 270
G.10	Regression corrections applied on the horizontal LH2-cell asymmetries. . . 271
I.1	Theory calculation from A.Afanasev . . . . . 283
I.2	Theory calculation from M.Gorchtein . . . . . 284
I.3	Theory calculation from B.Pasquini . . . . . 286

## List of Figures

### Figure

2.1	Fundamental particles in the Standard Model framework. . . . .	23
2.2	Early experimental evidence for the electro-weak mixing. . . . .	24
2.3	The tree-level Feynman diagrams of the electron-proton scattering. . . . .	27
2.4	Running of the weak-mixing angle in the $\overline{MS}$ scheme. . . . .	30
2.5	Experimental constraints on the quark couplings $C_{1u}$ and $C_{1d}$ . . . . .	33
2.6	Sensitivity of new PV physics to the relative precision of $Q_w^p$ . . . . .	34
2.7	Sensitivity of $Q_w^p$ and $Q_w^e$ to new PV physics . . . . .	35
2.8	Extracting $Q_w^p$ using global PVES asymmetries. . . . .	36
2.9	First-order and some of the second-order Feynman diagrams in electron-proton scattering. . . . .	38
2.10	Radiative corrections on electron-proton scattering with and without the soft-photon treatment of the two-photon exchange. . . . .	41
2.11	Resolving the Rosenbluth discrepancy using the two-photon exchange correction. . . . .	42
2.12	$P_L/P_L^0$ vs $\varepsilon$ from measurements. . . . .	43
2.13	Measurements of the $\frac{\sigma^{e^+p}}{\sigma^{e^-p}}$ ratio. . . . .	45
2.14	The Compton scattering treatment of the two-photon exchange process. . . . .	47
2.15	Kinematics of a beam normal single spin asymmetry measurement. . . . .	49
2.16	Comparison of SAMPLE measurement of BNSSA to the estimates from models using only the nucleon intermediate state. . . . .	50
2.17	Comparing measurements of BNSSA to model calculations. . . . .	51
2.18	Comparing measurements of BNSSA to model calculations which use multiple pion excitations in the inelastic intermediate state. . . . .	52
3.1	The CAD diagram of the side-view of the $Q_{\text{weak}}$ apparatus. . . . .	57
3.2	Layout of CEBAF accelerator. . . . .	58
3.3	Schematic of the polarized electron source. . . . .	59
3.4	Cross section of the CEBAF 200 kV inverted electron gun. . . . .	60
3.5	Quantum efficiency (QE) curve and the map of the photocathode. . . . .	60
3.6	Schematic of the laser table. . . . .	61
3.7	Timing diagrams of the true and delayed helicity signals. . . . .	63

	16
3.8 Schematic of the double Wien spin manipulating system. . . . .	64
3.9 Layout of the Hall C Møller polarimeter. . . . .	66
3.10 Layout of the Compton polarimeter. . . . .	66
3.11 Schematic of the beamline used by $Q_{\text{weak}}$ for electron beam monitoring. .	67
3.12 Electronics chain of the transport style SEE BPM. . . . .	68
3.13 Constructed X and Y beam positions. . . . .	70
3.14 Schematic of the arrangement used to determine the BPM resolution . .	71
3.15 Dependence of the BPM resolution on the beam current. . . . .	73
3.16 Calibration plot of BPM3H07C XP wire. . . . .	74
3.17 Beam position difference propagation up to the target. . . . .	76
3.18 Improvements in the differential non-linearity of the BPMs . . . . .	77
3.19 Locations and the electronics chains of BCMs used by $Q_{\text{weak}}$ . . . . .	78
3.20 Charge asymmetry and BCM double difference distributions. . . . .	79
3.21 Liquid Hydrogen target cell design. . . . .	81
3.22 Target noise at $182\mu\text{A}$ as a function of raster size. . . . .	82
3.23 A GEANT simulation of the QTOR steering elastic and inelastic electrons.	83
3.24 CAD drawing showing the location of the collimator system. . . . .	84
3.25 CAD drawing of the Čerenkov detector array and a GEANT simulation of the electron profile on the detectors. . . . .	85
3.26 Light yield variation along the pre-radiated Čerenkov detector 4. . . . .	85
4.1 Basic architecture of the CEBAF Online Data Acquisition (CODA). . . .	88
4.2 Integrating mode DAQ layout. . . . .	89
4.3 Triggering and readout timing diagram of the integrating-mode DAQ . .	91
4.4 Class inheritance diagram of the QwAnalysis software. . . . .	94
4.5 Simplified flow chart of the QwAnalysis parity analysis engine . . . . .	95
5.1 Charge asymmetry generated by the analysing power of the Pockels cell and the analysing power of the photocathode. . . . .	104
5.2 Helicity correlated position differences generated from a linear $\Delta$ phase gradient across the laser spot. . . . .	105
5.3 Pockels cell ringing. . . . .	106
5.4 Pockels Cell translation scans. . . . .	108
5.5 Rotatable Half Wave Plate Scans. . . . .	109
5.6 RHPW optimization. . . . .	110
5.7 Charge feedback applied over 80 s time intervals. . . . .	113



	17
5.8	Position feedback mechanism. . . . . 114
5.9	Representation of the helicity leakage on the detector signals. . . . . 115
5.10	Setups used for the helicity signal leakage measurements. . . . . 117
5.11	Schematic showing the distribution of helicity (HEL), MPS and QRT signals in the electronics racks. . . . . 121
5.12	Quartet polarity dependence of the helicity, QRT and MPS leakage. . . . 123
5.13	Graphical representation of the sub-block dependence of the leakage from the MPS, helicity and QRT signals. . . . . 124
5.14	Setup used for measuring the electronic noise content in the Čerenkov detector signal chain. . . . . 127
5.15	Frequency spectra of the preamplified current signals and the voltage signal. 128
5.16	Asymmetry distributions of the LED driven PMT and the current source. 133
6.1	Azimuthal dependence of the raw asymmetries. . . . . 137
6.2	Comparing the azimuthal dependence of the vertical and horizontal transverse asymmetries. . . . . 138
6.3	Time variation of helicity correlated charge and energy asymmetries. . . 139
6.4	Helicity correlated beam asymmetry distributions. . . . . 140
6.5	Azimuthal dependence of the detector sensitivities. . . . . 142
6.6	Total beam asymmetry correction from linear regression. . . . . 143
6.7	Asymmetries with and without linear regression. . . . . 144
6.8	Azimuthal dependence of $(IN+OUT)/2$ . . . . . 146
6.9	Azimuthal depending physics asymmetry from the LH2-cell target. . . . 147
6.10	Illustration of the azimuthal ( $\phi$ ) averaging of a Čerenkov detector. . . . 148
6.11	Regression scheme dependence of the beam asymmetry corrections. . . . 150
6.12	Comparing physics asymmetry from five-parameter regression and other regression schemes. . . . . 152
6.13	Correlation between the five-parameter regressed Čerenkov detector asymmetry and the charge asymmetry . . . . . 153
6.14	Average charge sensitivity of the raw Čerenkov detector asymmetries. . . 154
6.15	Beam polarization in Transverse_Run I and Transverse_Run II. . . . . 156
6.16	Azimuthal depending physics asymmetry from the DS4Al target. . . . . 159
6.17	Azimuthal depending inelastic physics asymmetry from the LH2-cell target. 161
6.18	Illustration of external and internal radiation in electron-proton scattering. 163
6.19	Simulated $Q^2$ variation over the Čerenkov detector array. . . . . 165

	18
6.20 Simulated changes in the azimuthal fits due to $Q^2$ variation. . . . .	166
7.1 Illustration of the scenarios for a broken symmetry in the detector array.	171
7.2 Simulated BNSSA leakages due to the broken symmetry in the Čerenkov detector array. . . . .	173
7.3 Residual transverse polarization in the beam during the $Q_{\text{weak}}$ commissioning period. . . . .	176
7.4 Residual transverse polarization monitoring results for Wien 0. . . . .	177
7.5 The successful use of transverse monitoring . . . . .	178
7.6 Variation of the residual transverse polarization during $Q_{\text{weak}}$ Run I and Run II. . . . .	181
8.1 Extracting $Q_w^p$ from the global fit of the reduced PVES asymmetries in the forward angle limit. . . . .	186
8.2 The constraints on the neutral-weak quark couplings from the 19% $Q_w^p$ measurement. . . . .	187
8.3 Scattering angle dependence of the beam normal single spin asymmetry model calculations. . . . .	189
8.4 Contributions from the ground and excited intermediate states in the two-photon exchange process into the beam normal single spin asymmetry.	190
8.5 The contributions from the different excited states entering in BNSSA calculation under $Q_{\text{weak}}$ kinematics. . . . .	191
A.1 Comparison of BPM pedestals between Run I and Run II. . . . .	214
A.2 Improvements in the correlations between projected and measured beam positions after removing differential non-linearity. . . . .	217
A.3 Improvements in the differential non-linearity of the BPMs over a range of beam currents. . . . .	217
C.1 % Difference between weighted positive and negative PMT yields before updating the weights. . . . .	236
C.2 % Difference between weighted positive and negative PMT yields with updated weights. . . . .	239
E.1 Position differences induced by the vertical helicity magnets 0L01V and 0L03V. . . . .	249
E.2 Position differences induced by the helicity magnets 0L02H and 0L03H. .	250

E.3	Induced position differences inside sub-blocks and the hw_sum for 0L01V at 960 Hz and 120 Hz. . . . .	251
E.4	Oscilloscope capture of the helicity magnet voltage response. . . . .	251
E.5	Induced position differences induced inside the sub-blocks and the hw_sum for 0L02H 960 Hz and 120 Hz. . . . .	252
G.1	Beam parameter distributions during vertical Transverse_Run I. . . . .	259
G.2	Beam parameter distributions during vertical Transverse_Run II. . . . .	260
G.3	Helicity correlated beam position and angle differences at the target. . .	261
G.4	Detector sensitivities in vertical Transverse_Run I. . . . .	263
G.5	Detector sensitivities in vertical Transverse_Run II. . . . .	264
G.6	(IN+OUT)/2 of the regressed DS4Al asymmetries. . . . .	265
G.7	(IN+OUT)/2 of the inelastic LH2-cell asymmetry. . . . .	266
G.8	IHWP cancellation of the inelastic asymmetry from the DS4Al target. . .	267
G.9	Inelastic asymmetry from the aluminum target. . . . .	268
H.1	Correlations between X differences and the residual transverse polarization.	275
H.2	Correlations between Y differences and the residual transverse polarization.	275
H.3	Correlations between X angle differences and the residual transverse polarization. . . . .	276
H.4	Correlations between Y angle differences and the residual transverse polarization. . . . .	276
H.5	Correlations between energy asymmetry and the residual transverse polarization. . . . .	277
H.6	Correlations between charge asymmetry and the residual transverse polarization. . . . .	277

# 1 Introduction

Electron scattering is a time-honoured tool which is used to access information on the structure of the nucleons. Traditionally, the scattering cross-section in electron scattering is obtained under the Born approximation, where the electromagnetic interaction is mediated by a single photon. Higher order processes such as two photon exchange are treated as small radiative corrections [1] in the order of 2% of the scattering cross-section. This was a negligible correction compared to the precision of the cross-section measurements achieved five decades ago [2]. However, to reach precision below the 2% level where the contributions from the radiative corrections are not negligible, one requires a good understanding of the two-photon exchange mechanism and of its contribution to the different observables such as the proton's electric and magnetic form factor ratio. For example, it was suggested [3, 4] that the discrepancy observed at high  $Q^2$  ( $> 2$  (GeV/c)<sup>2</sup>) between the measurements [5] of the electric and magnetic form factors of the proton from the polarization transfer method and the Rosenbluth separation method, can be explained by the proper treatment of the two-photon exchange correction. But the theoretical calculations of the two-photon correction have uncertainties arising from the lack of information on the intermediate states in the doubly virtual Compton scattering process. In this regard, observables of the two-photon exchange process provide valuable information on the intermediate states which can be used to benchmark theoretical calculations. The beam normal single spin asymmetry generated in the scattering of transversely polarized electrons from unpolarized nucleons is an observable of the imaginary part of the two-photon exchange amplitude. It is a parity conserving asymmetry of several parts per million (ppm) which arises from the interference of the two-photon exchange and one-photon exchange amplitude. Though small, this asymmetry can be measured with high precision, with the aid of parity violating electron-scattering experiments (PVES) such as the  $Q_{\text{weak}}$  experiment.

The  $Q_{\text{weak}}$  experiment [6] at Jefferson Lab searches for physics beyond the Standard Model with the first direct measurement of the weak charge of the proton using parity violating electron-proton scattering. The parity violation in electron-proton scattering has played an important role in the establishment of the Standard Model of particle physics [7], the theory that describes particles and their interactions.

From the observation of the first neutral weak currents in 1973 to the discovery of the Higgs boson in late 2012, the past half a century in particle physics has seen the remarkable accuracy of the Standard Model of particle physics in describing almost all of the particles and interactions found in nature. But there are compelling reasons to believe it is not a complete theory. These reasons motivate the search for new physics beyond the framework of the Standard Model. The proposed 4% measurement of the weak charge of the proton by the  $Q_{\text{weak}}$  experiment will provide sensitivity to new parity violating physics at the TeV scale. An experiment of this precision requires good control and understanding of background asymmetries in the apparatus. For this reason, the  $Q_{\text{weak}}$  experiment made many ancillary measurements of physics processes which are expected to provide considerable corrections to the parity violating asymmetry. One such measurement is the parity conserving beam normal single spin asymmetry. The beam normal single spin asymmetry becomes a false asymmetry in a parity violating asymmetry measurement due to residual transverse polarization in the electron beam and the broken symmetry of the detector system. Due to the uncertainty of the theoretical calculations, a dedicated measurement of the beam normal single spin asymmetry was required to reduce the uncertainty on the false asymmetry correction.

This dissertation contains the analysis of the beam normal single spin asymmetry measured from elastic electron-proton scattering using the  $Q_{\text{weak}}$  apparatus at a four-momentum transfer of  $0.025 \text{ (GeV/c)}^2$ . I will also present a summary of my other contributions to the  $Q_{\text{weak}}$  experiment to aid in its path toward the first direct measurement of the weak charge of the proton. The outline of this dissertation will be as follows. In Chapter 2, I will introduce the  $Q_{\text{weak}}$  experiment and the reasons which motivate a precision measurement of the weak charge of the proton. I will then move onto discussing the role played by the beam normal single spin asymmetry as an observable of the two-photon exchange process and as a systematic error in the parity violating electron scattering experiments. The specific design and the performance of the setup will be presented in Chapter 3 emphasizing the work I have done on the beam monitors to optimize the resolution of the beam position, angle and energy measurements. Moreover, as a member of the data acquisition and analysis group, a significant portion of my work went in the setup and maintaining the integrating mode data acquisition system and the analysis software development. These will be summarized in Chapter 4. Controlling and minimizing false asymmetries and random noise in the experimental setup is an important part of a precision parity violating

asymmetry measurement. Related to this, I have performed several studies to determine the random noise in the detector electronics and the false asymmetry from the leakage of the helicity signal. In addition, I was actively involved in the polarized source studies to minimize helicity correlated false asymmetries in the beam, which are known to be one of the largest systematics in the  $Q_{\text{weak}}$  measurement. The details and the results of these false asymmetries and random noise measurements will be presented in Chapter 5. In Chapter 6, I will present the details of the analysis of the beam normal single spin asymmetry from electron-proton scattering. My work on the residual transverse polarization monitoring and the beam normal single spin asymmetry systematic correction for the  $Q_{\text{weak}}$  parity violating asymmetry will be presented in Chapter 7. I will conclude with a summary of results in the dissertation and a discussion of the implications of the 3% beam normal single spin asymmetry result in Chapter 8.

## 2 Physics Motivation and the Formalisms

### 2.1 The $Q_{\text{weak}}$ Experiment

The  $Q_{\text{weak}}$  experiment makes the first direct measurement of the weak charge of the proton in a search for new parity violating physics beyond the Standard Model. The following subsections provide the motivation for the measurement of the weak charge of the proton and a general introduction to the experiment and its goals.

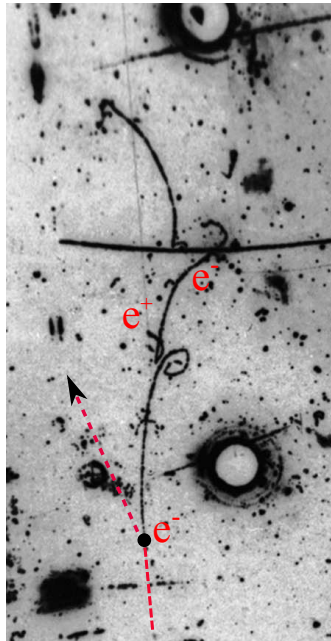
#### 2.1.1 *The Standard Model of the Electroweak Interaction*

The Standard Model is one of the greatest achievements of the fundamental physics. It is an elegant theoretical framework based on the gauge symmetry  $SU(3) \times SU(2) \times U(1)$  which presents fermions as the building blocks of matter whose interactions are mediated via gauge bosons (see Figure 2.1). Since the mid 1970s, numerous experiments have verified the success of the Standard Model as a standard theory of particle physics. Notably, in 1973, the Gargamelle Collaboration at CERN

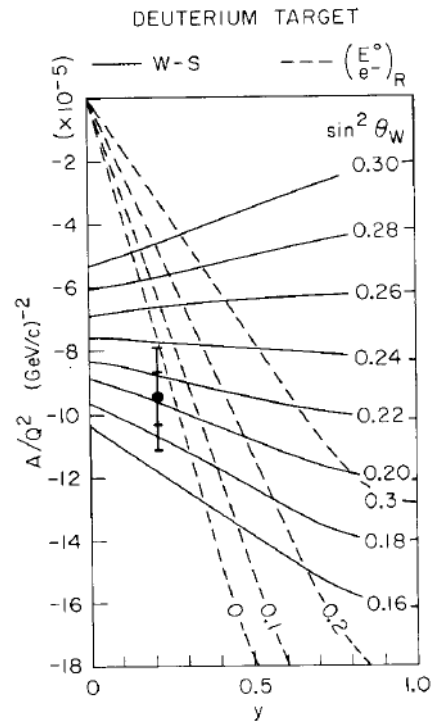
	Fermions			Bosons	
Quarks	$u$ up	$c$ charm	$t$ top	$\gamma$ photon	Force carriers
	$d$ down	$s$ strange	$b$ bottom	$Z$ Z boson	
Leptons	$\nu_e$ electron neutrino	$\nu_\mu$ muon neutrino	$\nu_\tau$ tau neutrino	$W$ W boson	
	$e$ electron	$\mu$ muon	$\tau$ tau	$g$ gluon	
				Higgs boson	

Figure 2.1: Fundamental particles in the Standard Model framework. Figure from Ref. [8].

observed [9–11] the first neutral-current interactions (see Figure 2.2a) confirming the existence of the neutral-weak boson  $Z^0$  which is an essential part of the electroweak unification. In the late 1970s, the Prescott experiment [13] at the Stanford Linear Accelerator (SLAC) measured the first parity violating asymmetry in deep inelastic electron-Deuteron scattering. Even though there were several gauge theories available at the time which predicted parity violation of the weak interaction, only the Standard



(a) First neutral-current observation.



(b) First PV Asymmetry measurement.

Figure 2.2: Early experimental evidence for the electro-weak mixing. (a) Bubble-chamber photo of first neutral-current interaction ( $\bar{\nu}_\mu + e^- \rightarrow \bar{\nu}_\mu + e^-$ ) observed by the Gargamelle experiment in CERN. A neutrino comes from below (no track) and scatters off of an electron which moves upward emitting two photons in the interaction. The two photons are only visible from the production of electron-positron pairs. Figure from Ref. [12]. (b) Results from the Prescott experiment showing the measured four momentum ( $Q^2$ ) weighted asymmetry vs the fractional energy loss of the electron ( $y$ ). The Standard Model predictions (solid lines) of the  $y$ -dependence of the normalized asymmetry,  $A/Q^2$  for different values of the weak mixing angle ( $\sin^2 \theta_w$ ) are in clear agreement with the experimental result. The dashed lines are from a "hybrid" model that assign right-handed electrons to violate parity instead of left-handed electrons. Figure from Ref. [13].



Model was able to correctly estimate the asymmetry at the Prescott kinematics (see Figure 2.2b). This experimental verification of a prediction of the Standard Model boosted the acceptance of the SM over other theories of particle physics at the time. Over the years, the general structure of the Standard Model was confirmed with the observation of the strong force carrier gluon [14] at DESY in 1979 and the measurements of the properties of the weak force carriers  $Z^0$  [15, 16] and  $W^\pm$  [17, 18] in 1983 at CERN. With the recent discovery of the elusive Higgs boson<sup>1</sup> [19, 20] at the Large Hadron Collider, one can say that all the fundamental particles proposed by the Standard Model have been experimentally observed and their existence confirmed. That is a testament to the huge success of a theory that withstood the vigorous experimental tests over the past half-a-century.

In spite of this remarkable and continuing success, there are lingering theoretical and experimental reasons [21] to believe that the Standard Model may not be *the* complete theory of particle physics. Instead it is a very good low energy approximation of a larger theoretical framework. One reason for this belief is the inability [22] of the Standard Model to describe the fourth fundamental force in nature, the gravitational force. Moreover, the Standard Model does not provide an explanation for dark matter and dark energy [23], the matter-antimatter asymmetry in the universe [24], to name a few, for which there are strong experimental evidences. In addition, there are no explanations for the features of the Standard Model such as the mass hierarchy, the different generations of the fermions and the 25 free parameters whose values need to be extracted from experiments rather than being predicted by the theory itself.

These shortcomings of the Standard Model framework have generated a lot of theoretical and experimental enthusiasm over the past decade or so to search for physics beyond the Standard Model. On the theoretical side, some effort is being made to develop grand unified theories which can provide a unified description of all the forces in nature. The others are focused on adding extensions to the Standard Model, such as quantum-gravity, super-symmetry and string theory, to address its shortcomings. On the experimental side, the searches are focused on three frontiers, the high-energy, the cosmic and the intensity. At the high energy frontier, particle colliders [25], such as the Large Hadron Collider (LHC), excite matter into new particles with higher masses in search for the origin of mass and the existence of extra

---

<sup>1</sup>It is yet to be confirmed if the boson discovered at the LHC is indeed the Higgs boson, but the experimental evidence keep pointing to it being the Higgs or a boson that is similar to the Higgs.

dimensions. At the cosmic frontier, ground-based and space-based detectors are used to search for dark matter and dark energy to understand their properties and interactions. In the intensity frontier, low energy high intensity beams are used to perform precision measurements of observables which are either well defined in the Standard Model or are forbidden. Any deviation resulting from these measurements can hint at the presence of new particles and interactions which are beyond the framework of the Standard Model. These measurements at the intensity frontier complement the searches at the high-energy frontier where new particles are expected to be observed directly.

The  $Q_{\text{weak}}$  experiment is an intensity frontier experiment designed to make a precision measurement of the weak charge of the proton, a suppressed quantity in the Standard Model. For this purpose,  $Q_{\text{weak}}$  relies on the parity violation in electron scattering. The parity violation in polarized electron scattering has played an important role in establishing the structure of the electroweak sector of the Standard Model as mentioned earlier. Moving forward, low energy parity violating electron scattering (PVES) is known [26] to be a theoretically clean probe of physics beyond the Standard Model. Parity violation in elastic electron-nucleon scattering allows the contribution from the weak interaction to be extracted experimentally by taking the asymmetry of the experimental cross-section for left-right handed electrons. This asymmetry includes low energy electroweak observables such as the weak charges of the nucleons which are well defined in the Standard Model. Therefore, a measurement of the parity violating asymmetry in elastic electron-nucleon scattering, with sufficient understanding of the hadronic contribution, can be used to make a precision measurement of the weak charges in search of new parity violating physics. The following subsection briefly discuss the derivation of the parity violating electron-proton asymmetry and its relation to the weak charge of the proton.

### ***2.1.2 The Parity Violating Electron-Proton Asymmetry***

Figure 2.3 shows the lowest-order Feynman diagrams corresponding to an electron scattering from a proton involving the exchange of a photon (electromagnetic) or a neutral-weak boson (weak). For low energy ( $|Q^2| \ll M_Z^2$ ) electron-proton scattering, using Quantum Electrodynamics (QED) and applying the Feynman rules of electroweak interaction to these diagrams, one can derive to the first order in  $\alpha$  the

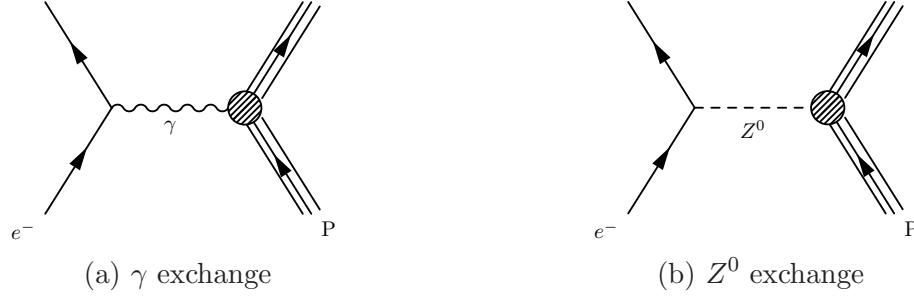


Figure 2.3: The tree-level Feynman diagrams of the electron-proton scattering involving the electromagnetic (a) and weak (b) interaction.

invariant amplitude of the electromagnetic interaction [27]

$$\mathcal{M}^\gamma = \frac{4\pi\alpha}{Q^2} e l^\mu J_\mu^\gamma, \quad (2.1)$$

and the invariant amplitude of the weak interaction

$$\mathcal{M}^Z = \frac{-G_F}{2\sqrt{2}} [g_V^e l^\mu + g_A^e l^{\mu 5}] [J_\mu^Z + J_{\mu 5}^Z]. \quad (2.2)$$

In Equations 2.1 and 2.2,  $\alpha$  is the fine structure constant,  $Q$  is the four-momentum transfer of the photon,  $G_F$  is the Fermi constant,  $e$ ,  $g_V$  and  $g_A$  are the electron's electromagnetic, vector and axial-vector neutral-current couplings respectively. The electron vector and axial-vector currents are given by  $l^\mu \equiv \bar{u}_e \gamma^\mu u_e$  and  $l^{\mu 5} \equiv \bar{u}_e \gamma^\mu \gamma^5 u_e$  respectively with  $u_i$  denoting the electron spinor. The hadronic currents  $J_\mu^\gamma$  and  $J_\mu^Z$  are matrix elements of the form  $J \equiv \langle H | \hat{J} | H \rangle$  where  $|H\rangle$  represents the proton and  $\hat{J}$  is the quark current operator. Under the assumption that the proton structure is dominated by the lighter quarks, up (u), down (d) and strange (s), the quark current operators of the proton are given by

$$\hat{J}_\mu^\gamma \equiv \sum_q^{u,d,s} Q_q \bar{u}_q \gamma_\mu u_q, \quad \hat{J}_\mu^Z \equiv \sum_q^{u,d,s} g_V^q \bar{u}_q \gamma_\mu u_q, \quad \hat{J}_{\mu 5}^Z \equiv \sum_q^{u,d,s} g_A^q \bar{u}_q \gamma_\mu \gamma_5 u_q,$$

with  $Q$  being the electromagnetic charge,  $u$  the spinor and  $g_{V(A)}$  the vector (axial-vector) neutral-current couplings of the  $q = u, d, s$  quark (see Table 2.1). For polarized electron scattering from unpolarized protons, the parity violating asymmetry

$A^{PV}$  is defined by

$$A^{PV} = \frac{\vec{\sigma} - \overleftarrow{\sigma}}{\vec{\sigma} + \overleftarrow{\sigma}}, \quad (2.3)$$

where  $\vec{\sigma}$  ( $\overleftarrow{\sigma}$ ) is the cross-section for electrons scattering with spin polarized parallel (anti-parallel) to their direction of motion. Since the electron-proton scattering can involve either an exchange of a photon or a  $Z^0$ , the scattering cross-section is a summation and an interference of the two invariant amplitudes,

$$\sigma \approx |\mathcal{M}^\gamma + \mathcal{M}^Z|^2 = |\mathcal{M}^\gamma|^2 + |\mathcal{M}^Z|^2 + 2\mathcal{R}e(\mathcal{M}^\gamma)^*(\mathcal{M}^Z). \quad (2.4)$$

Due to the parity violating nature of the weak interaction and the  $|\mathcal{M}^Z| \ll |\mathcal{M}^\gamma|$ , the parity violating asymmetry for polarized electron scattering in terms of the invariant amplitudes is then written as

$$A^{PV} = \frac{2\mathcal{M}^\gamma\mathcal{M}^Z}{|\mathcal{M}^\gamma|^2}. \quad (2.5)$$

Combining all of these together, the parity violating asymmetry in polarized electron-proton scattering has the form [28, pgs 59-68]

$$A^{PV} = \frac{-G_F Q^2}{4\pi\alpha\sqrt{2}} \left[ \frac{\varepsilon G_E^{\gamma,p} G_E^{Z,p} + \tau G_M^{\gamma,p} G_M^{Z,p} + (1 - 4\sin^2\theta_w)\varepsilon' G_M^{\gamma,p} G_A^{Z,p}}{\varepsilon(G_E^{\gamma,p})^2 + \tau(G_M^{\gamma,p})^2} \right], \quad (2.6)$$

Table 2.1: Standard Model neutral-current couplings of the fermions given in terms of the weak-mixing angle  $\sin\theta_w$ , a fundamental parameter in the Standard Model.

Fermion	$g_V$	$g_A$
e	$-1 + 4\sin^2\theta_w$	1
u	$1 - \frac{8}{3}\sin^2\theta_w$	-1
d	$-1 + \frac{4}{3}\sin^2\theta_w$	1
s	$-1 + \frac{4}{3}\sin^2\theta_w$	1

with the kinematic factors

$$\tau = \frac{Q^2}{4M_p^2}, \quad \varepsilon^{-1} = 1 + 2(1 + \tau) \tan^2(\theta/2), \quad \varepsilon' = \sqrt{\tau(1 + \tau)(1 - \eta^2)},$$

where  $M_p$  is the mass of the proton and  $\theta$  is the scattering angle of the electron in the proton's rest frame. The weak-mixing angle  $\sin \theta_w$  enters in Equation 2.6 via the vector and axial-vector couplings of the electrons introduced in Equation 2.2. The functions  $G^{\gamma,p}(Q^2)$ ,  $G^{Z,p}(Q^2)$  and  $G_A^{Z,p}(Q^2)$  are the proton's electromagnetic, neutral-current vector and neutral-current axial-vector form factors respectively with the subscripts  $E/M$  standing for electric/magnetic.  $G_{E(M)}^{Z,p}$  is given in terms of the electromagnetic form factors of the proton and the neutron as

$$G_{E(M)}^{Z,p} = (1 - 4 \sin^2 \theta_w) G_{E(M)}^{\gamma,p} - G_{E(M)}^{\gamma,n} - G_{E(M)}^s, \quad (2.7)$$

where  $G_{E(M)}^s$  contains the contributions from the strange quarks. The neutral-current axial-vector form factor is given by

$$G_A^{Z,p} = -G_A^p + G_A^s, \quad (2.8)$$

where  $G_A^s$  is the contribution from the strange quarks.

At forward angle scattering and low momentum transfers where  $\theta \rightarrow 0$ ,  $\varepsilon \rightarrow 1$  and  $\tau \ll 1$ , Equation 2.6 reduces to [28]

$$A^{PV} = \frac{-G_F}{4\pi\alpha\sqrt{2}} [Q^2 Q_w^p + Q^4 B(Q^2)], \quad (2.9)$$

where the leading order term is the weak charge of the proton  $Q_w^p$  and the next-to-leading order term  $B(Q^2)$  contains the hadronic contribution in terms of the form factors. All of the form factors entering in  $B(Q^2)$  are well known experimentally. Therefore the extraction of the  $Q_w^p$  is independent of theoretical uncertainties associated with the hadronic structure. This will be discussed later in Subsection 2.1.5.

### 2.1.3 The Weak Charge of the Proton

The weak charge of the proton gives the coupling strength of the proton to the neutral-weak boson  $Z^0$ . It is defined in the Standard Model as

$$Q_w^p = 2g_V^u + g_V^d = 1 - 4 \sin^2 \theta_w. \quad (2.10)$$

From Equation 2.10, it is clear that the magnitude of  $Q_w^p$  depends on the magnitude of the weak-mixing angle  $\sin \theta_w$ . The weak-mixing angle  $\theta_w$  is a free-parameter of the Standard Model. It gives the mixing

$$g \sin \theta_w = g' \cos \theta_w = e,$$

between the weak couplings,  $g$  and  $g'$  and the electromagnetic coupling  $e$ . However, the magnitude of  $\sin \theta_w$  is not given in the Standard Model itself but is determined from precision neutral-current measurements done at the Z-pole ( $Q^2 = M_Z^2$ ). At the Z-pole, the masses of the W and Z bosons are proportional to their gauge interactions resulting in the tree-level relation

$$\sin^2 \theta_w = 1 - \frac{M_W^2}{M_Z^2}. \quad (2.11)$$

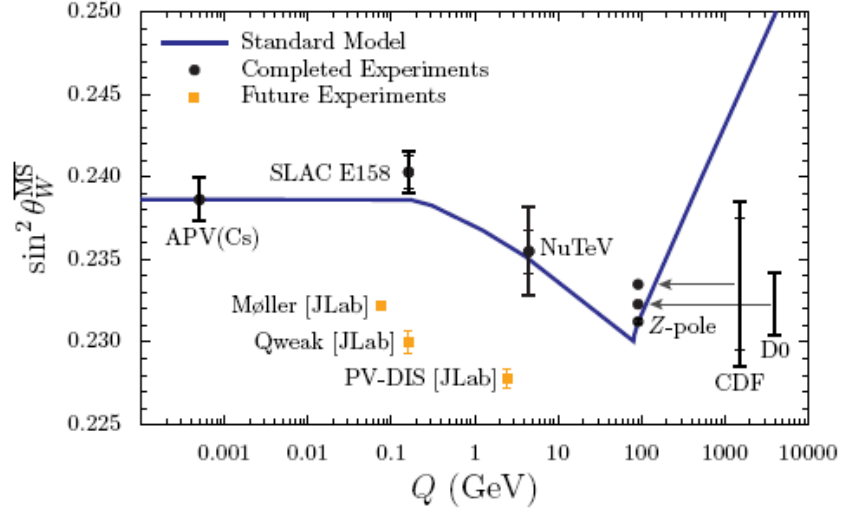


Figure 2.4: The Standard Model prediction of the running of the weak mixing angle in the  $\overline{MS}$  scheme [29] using measurements at the Z-pole (LEP and SLAC) [30]. The thickness of the curve reflects the theoretical uncertainty of  $7 \pm 10^{-5}$  due to hadronic contributions. The existing measurements are from the atomic parity violation (APV) in Cesium [31], deep inelastic  $\nu$  scattering (NuTeV) [32, 33], electron's weak charge from SLAC (E158) [34] and the electron-positron scattering measurements by LEP, SLAC [30], D0 [35] and CDF [36]. The predicted measurements are for  $Q_{\text{weak}}$ , Møller and PV-DIS experiments at Jefferson Lab. Figure from Ref. [32].

At momentum transfers above and below the Z-pole, the tree-level expression of  $\sin^2 \theta_w$  gets modified due to loop corrections on the electroweak couplings  $g$  and  $g'$ . This results in the *running* ( $Q^2$  evolution) of  $\sin^2 \theta_w$  (see Figure 2.4). The running of  $\sin^2 \theta_w$  depends on the renormalization scheme [37]. While there are several renormalization schemes [38] to consider, the  $Q_{\text{weak}}$  experiment uses the running of  $\sin^2 \theta_w$  performed [39] in the  $\overline{MS}$  scheme for several reasons. The definition of  $\sin^2 \theta_w$  in the  $\overline{MS}$  scheme uses the tree level formula in Equation 2.11 and the evolution is closely related to the evolution of the Quantum Electrodynamics coupling  $\alpha(\mu)$  in the  $\overline{MS}$  scheme which is fairly well established. These reasons help to improve the Standard Model prediction of low-energy observables, such as the weak charge of the proton, which depends on  $\sin^2 \theta_w$ . In addition, all the existing measurements of  $\sin^2 \theta_w$  shown in Figure 2.4 have utilized the  $\overline{MS}$  scheme. To be compared with the world data, the results from the  $Q_{\text{weak}}$  experiment needs to be quoted in the same renormalization scheme. In the  $\overline{MS}$  scheme,  $\sin^2 \theta_W^{\overline{MS}}(Q^2 = 0) = 0.23867 \pm 0.00029$  [39]. This leads to the Standard Model prediction of the weak charge of the proton

$$Q_w^p = 0.0705 \quad (Q^2 = 0). \quad (2.12)$$

#### 2.1.4 Motivation for a 4% Measurement of $Q_w^p$

The suppression of the weak charge due to the magnitude of  $\sin^2 \theta_w$ , is a unique property observed only in protons and electrons. Therefore, a precision measurement of either quantity presents a unique opportunity to test the Standard Model prediction of the weak-mixing angle and thereby the  $Q^2$  evolution of the neutral-current couplings of the fermions. While an agreement of such measurement with the Standard Model prediction provides strict constraints on  $\sin^2 \theta_w$ , a significant deviation would hint at new types of parity violating physics.

##### 2.1.4.1 Constraints on the Weak Mixing Angle and the Neutral-Current Quark Couplings

It can be seen from Figure 2.4, that previous experimental measurements over a range of  $Q^2$  have been successful in verifying the Standard Model prediction of the running of  $\sin^2 \theta_w$ . When published, a 4% measurement of the weak charge of the proton will result in a 0.3% measurement of  $\sin^2 \theta_W^{\overline{MS}}(0)$  making it the most precise measurement of this quantity at low  $Q^2$ . Even though the APV and E158 experiments have established the evolution of the  $\sin^2 \theta_w$  at low energies, due to the sensitivity of

the weak charge of the proton to new electron-quark couplings, the  $Q_{\text{weak}}$  experiment can provide constraints on possible extensions of the Standard Model as discussed below.

At  $Q^2 \ll M_Z$ , the weak interaction mediated by the exchange of a  $Z^0$  in electron-proton scattering, reduces to an effective four-Fermi interaction defined by [38]

$$\mathcal{L}^Z = -\frac{G_F}{\sqrt{2}} \sum_q [C_{1q} \bar{u}_e \gamma_\mu \gamma^5 u_e \bar{u}_q \gamma^\mu u_q + C_{2q} \bar{u}_e \gamma_\mu u_e \bar{u}_q \gamma^\mu \gamma^5 u_q], \quad (2.13)$$

where the tree-level vector and axial-vector neutral-current couplings of the electron and the quarks ( $g_V^{e,q}, g_A^{e,q}$ ) modified to  $g_A^e g_V^q \rightarrow C_{1q}$  and  $g_V^e g_A^q \rightarrow C_{2q}$ .  $C_{1q}, C_{2q}$  are called the renormalized neutral-current quark couplings or the effective quark couplings. In electron-hadron scattering, the linear combinations  $(C_{1u} + C_{1d})$  and  $(C_{1u} - C_{1d})$  give the coupling to the isoscalar and isovector hadronic neutral-currents [28]. The values of these linear combinations away from the Z-pole are extracted from the asymmetry measurements of atomic parity violation (isoscalar) and parity violating electron scattering (isovector) experiments. Figure 2.5 shows the current experimental limits on these couplings compared to the Standard Model value. The grey ellipse indicates the existing experimental bounds on the effective quark couplings are in good agreement with the Standard Model value. To-date, the APV experiments from large nuclei, such as Cs and Th, provide the most strict bounds on the isoscalar combinations. A 4% measurement of  $Q_w^p$ , which agrees with the Standard Model prediction, will provide the most strict bounds on the isovector combination. Together the two types of measurements will be able to provide further constraints on the possible extensions of the effective quark couplings.

#### 2.1.4.2 Sensitivity to New Parity Violating Physics

With a 4% overall precision, it is probable that a deviation observed in the  $Q_{\text{weak}}$  measurement from the Standard Model prediction

$$(Q_w^p)_{\text{New}} \equiv (Q_w^p)_{\text{Exp}} - (Q_w^p)_{\text{SM}},$$

can hint at the presence of new parity violating physics. By supposing this new physics interaction follows the dynamics of the Standard Model, the corresponding



low-energy effective Lagrangian of the electron-quark interaction takes the form [40]

$$\mathcal{L}_{NEW}^{PV} = -\frac{g}{4\Lambda^2} \bar{u}_e \gamma_\mu \gamma_5 u_e \sum_q h_V^q \bar{u}_q \gamma^\mu u_q, \quad (2.14)$$

where  $g$  is the coupling constant,  $\Lambda$  is the mass scale and  $h_V^q$  are the effective quark couplings associated with the new physics. Assuming the strength of the interaction is determined by the mass scale  $\Lambda$  with the coupling  $g$  of order 1, at a 95% C.L, a 4% measurement of  $Q_w^p$  is sensitive to new physics in the mass scale of

$$\Lambda = \frac{1}{\sqrt{2\sqrt{2}G_F}} \frac{1}{\sqrt{2\Delta Q_{Exp}^p}} \leq 2 \text{ TeV}, \quad (2.15)$$

(see Figure 2.6).

The new physics in Equation 2.14 could be a result of several particles and higher order loop corrections predicted by possible extensions to the Standard Model such as extra gauge bosons  $Z'$  in Grand Unified Theories (GUTs) [42], SUSY Loops and R-Parity violation (RPV) in Supersymmetric (SUSY) string theories [43] and

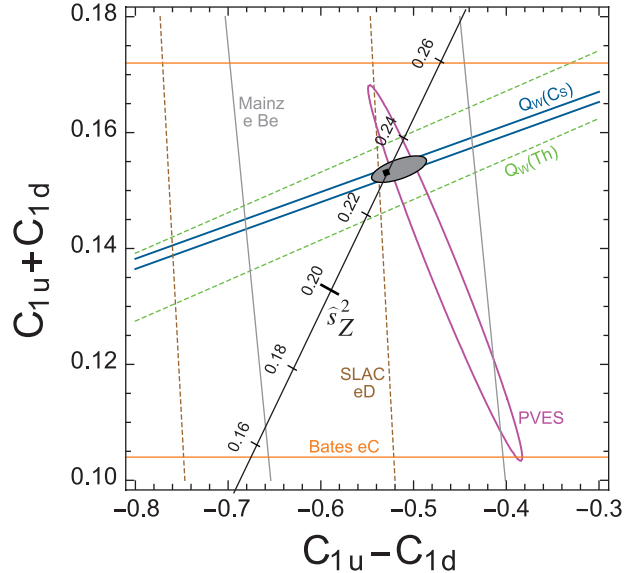


Figure 2.5: Constraints on the effective quark couplings  $C_{1u}$  and  $C_{1d}$  from the existing APV and PVES experiments. The grey filled contour represents the global fit at 90% C.L. The Standard Model prediction is given as a function of  $\hat{s}_Z^2 \equiv \sin^2 \theta_W^{MS}$ . The Standard Model best fit value at  $\hat{s}_Z^2 = 0.23116$  is also shown and is in excellent agreement with the current experimental bounds. Figure from Ref. [38].

leptoquarks [44]. While these particles can only be observed in direct searches carried out at high energy colliders, low energy parity violating measurements like  $Q_{\text{weak}}$  can also detect their presence as deviations in their measured observables. In an event these new interactions are observed by any of the high energy experiments, a precision measurement of  $Q_w^p$  will be able to provide limits on their weak charges and couplings to fermions [40].

Together with the measurements of the weak charge of the electron, a measurement of the weak charge of the proton will be able to distinguish between various new physics as summarized in Figure 2.7. While the weak charge of the electron is sensitive to new PV physics which couples to electron-electron vertices, the weak charge of the proton is sensitive to new PV physics which couples to electron-quark vertices (such as leptoquarks) making them excellent complementary probes of new physics. The E158 experiment made the first measurement of the weak charge of the electron which resulted in a  $Q_w^e = -0.053 \pm 0.011$  [45]. Although this measurement is consistent with the Standard Model value, their acquired precision is twice as much as the proposed error and larger than the shifts expected by new physics shown in Figure 2.7. The proposed MOLLER experiment [46] at the Jefferson Lab plans to make a 2.3% measurement of the  $Q_w^e$  ( $\pm 0.001$ ) which will be four times more sensitive to deviations caused by new physics shown in Figure 2.7.

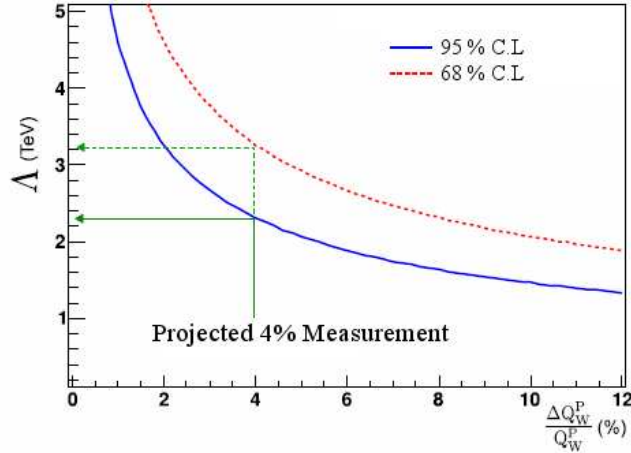


Figure 2.6: Sensitivity of the mass scale  $\lambda$  of new PV physics to the relative precision of the  $Q_w^p$  measurement. A 4% measurement of  $Q_w^p$  will rule out new particles with mass less than  $\approx 2.2$  TeV with 60% C.L. and mass less than  $\approx 3.2$  TeV with a 95% C.L. Figure from Ref. [41].

### 2.1.5 Theoretical Interpretability

As a probe of new physics, a precision measurement of  $Q_w^p$  needs to have the minimal theoretical uncertainties associated with radiative corrections and hadronic contributions. The use of the following technique to extract  $Q_w^p$  keeps the theoretical uncertainty on the measurement at the  $\approx 2\%$  level, well below the total anticipated uncertainty of 4%.

The  $Q^2$  dependence in Equation 2.9 indicates that at very low  $Q^2$ , the  $Q^2 Q_w^p$  term will dominate over the  $Q^4 B(Q^2)$  term. But then the physics asymmetry will be in the few ppb (parts per billion) range making it more difficult to measure. The strategy of the  $Q_{\text{weak}}$  experiment was therefore, to use an optimum  $Q^2$  of  $0.025 \text{ (GeV/c)}^2$  which can minimize  $B(Q^2)$  without minimizing the measurable asymmetry considerably. One can then use a fit on the world data on parity violating electron scattering from nucleons to minimize the theoretical uncertainty associated with  $B(Q^2)$ , namely the weak form factors. Figure 2.8 shows this anticipated method [47] of extracting  $Q_w^p$

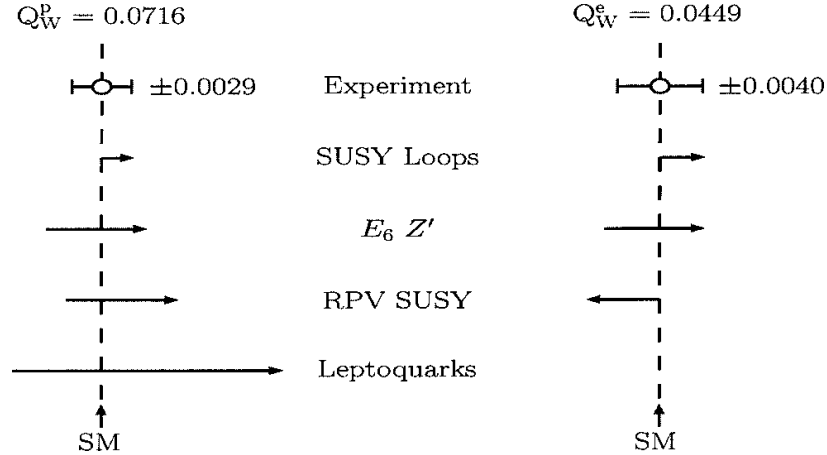


Figure 2.7: Expected deviations from the Standard Model predictions of the weak charge of the proton  $Q_w^p$  (left) and the weak charge of the electron  $Q_w^e$  (right) due to effects of new physics predicted by some of the Standard Model extensions in phase space allowed at 95% C.L by existing data. Figure from Ref. [40]. Note that the Standard Model value of  $Q_w^p$  used by authors of Ref. [40] for this work have since been updated with the improvements in electroweak loop corrections (see Subsection 2.1.5).

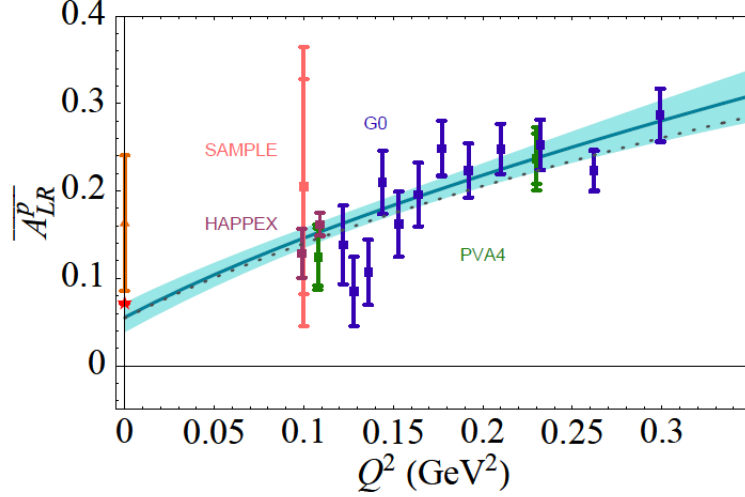


Figure 2.8: Anticipated methodology to extract  $Q_w^p$  by using existing world data on PVES from proton targets to constrain the hadronic term  $B(Q^2)$ . All the data points are normalized according to Equation 2.16 such that the extrapolation to  $Q^2 = 0$  will result in  $Q_w^p$ . The triangular data point (red) represents the previous experimental limit on  $Q_w^p$  using the APV Cesium measurement and the star represents the Standard Model prediction. The solid curve represents the best fit and the shaded region indicates the associated  $1\sigma$  error bounds on the global fit to all electroweak data. Figure from Ref. [47].

using world data on PVES. The normalized asymmetry is given by

$$\overline{A_{LR}^p} = \frac{A^{PV}}{Q^2 \left( \frac{-G_F}{4\pi\alpha\sqrt{2}} \right)} = Q_w^p + Q^2 B(Q^2). \quad (2.16)$$

The remaining theoretical uncertainties in the  $Q_w^p$  measurement comes from electroweak radiative corrections to the parity violating cross-section arising from vertex, self-energy, vacuum polarization and the interference of the one-photon and two-boson exchange processes which modify the scattering amplitudes as

$$\mathcal{M}^\gamma \rightarrow \mathcal{M}^\gamma + \mathcal{M}^{\gamma\gamma} \quad \text{and} \quad \mathcal{M}^Z \rightarrow \mathcal{M}^Z + \mathcal{M}^{\gamma Z} + \mathcal{M}^{Z\gamma}. \quad (2.17)$$

With these electroweak radiative corrections, the tree-level formula of  $Q_w^p$  given

in Equation 2.10 modifies to [40]

$$Q_w^p = [\rho_{NC} + \Delta_e][1 - 4\sin^2\theta_w^{\overline{MS}}(Q^2 = 0) + \Delta'_e] + \square_{WW} + \square_{ZZ} + \square_{\gamma Z}, \quad (2.18)$$

where  $\Delta\rho$  gives the modification to charge and neutral current couplings due to self-energy corrections,  $\Delta_e$  and  $\Delta'_e$  gives the vertex and external leg corrections to the Z boson axial-vector and photon couplings,  $\square_{WW}, \square_{ZZ}$  give the pure WW and ZZ box corrections and  $\square_{\gamma Z}$  gives the cross-box or interference corrections. Table 2.2 summarizes the magnitudes of these corrections.

Table 2.2: Electroweak radiative corrections applied on the weak charge of the proton in Equation 2.18 [41].

Electroweak Correction	Value
$\rho_{NC}$	1.047
$\Delta_e$	-0.001
$\Delta'_e$	-0.001
$\square_{WW}$	0.019
$\square_{ZZ}$	0.002
$\square_{\gamma Z}$	0.004

## 2.2 The Beam Normal Single Spin Asymmetry Measurement

The beam normal single spin asymmetry (BNSSA) generated by the scattering of polarized electrons from unpolarized protons is a possible false background asymmetry in parity violating electron scattering experiments (PVES). Theoretical calculations of the size of this parity conserving asymmetry indicates that it can be several orders of magnitude larger than the parity violating asymmetry. This prompted the  $Q_{\text{weak}}$  collaboration to make a dedicated measurement of the beam normal single spin asymmetry. But in its own perspective, a beam normal single spin asymmetry measurement provides direct access to the two-photon exchange process which is required to properly estimate the electron-nucleon scattering cross-sections beyond the Born approximation as discussed in the following subsections.

### 2.2.1 Electron Scattering in the Born Approximation

Usually, the scattering cross-section in elastic electron-nucleon scattering is derived to the first-order in the fine structure constant ( $\alpha$ ). This only involves the contribution of the single-photon exchange process (Figure 2.9a) which is known as the Born approximation. For the elastic electron (e) nucleon (N) scattering

$$e(k) + N(p) \rightarrow e(k') + N(p')$$

with the four-momenta  $k, p, k'$  and  $p'$ , the differential scattering cross-section in the Born approximation is given by

$$\left(\frac{d\sigma}{d\Omega}\right)_{Born} = \frac{\sigma_{Mott}}{\varepsilon(1+\tau)}\sigma_{Born}, \quad (2.19)$$

In Equation 2.19,  $\sigma_{Mott}$  is the cross-section for scattering of a point like fermion from another fermion and is given by [48]

$$\sigma_{Mott} = \frac{\alpha E' \cos^2(\theta/2)}{4E^3 \sin^4(\theta/2)},$$

where  $E(E')$  are the initial (final) energy of the electron,  $\theta$  is the scattering angle,  $\varepsilon$  (longitudinal photon polarization) and  $\tau$  are as defined in Equation 2.6 and

$$\sigma_{Born} = \varepsilon G_E^2(Q^2) + \tau G_M^2(Q^2), \quad (2.20)$$

is the reduced Born cross-section given in terms of the Sachs form factors.

In the Born approximation, higher-order processes involving more than one-

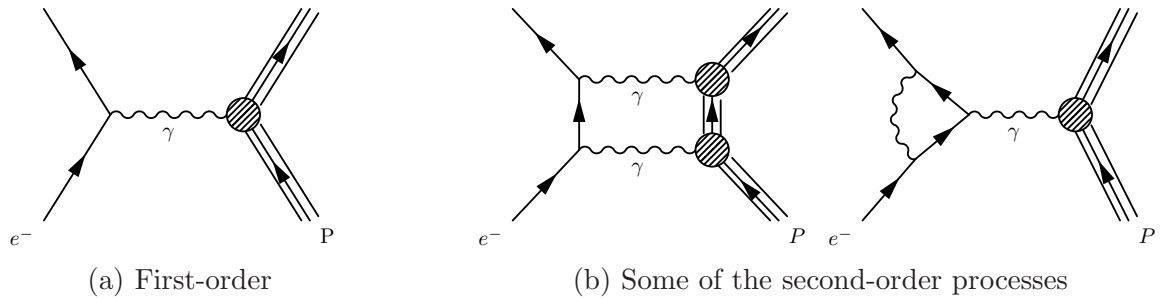


Figure 2.9: First-order and some of the second-order ( $\alpha^2$ ) Feynman diagrams in electron-proton scattering.

boson exchange and loop corrections (see Figure 2.9b) are treated as standard radiative corrections developed by Mo and Tsai [1] back in 1968. These higher order corrections modify the final cross-section as

$$\sigma = \sigma_{Born}(1 + \delta_{Virt.} + \delta_{Brems.}), \quad (2.21)$$

where  $\delta_{Virt.}$  is the correction for the particles exchanging a second virtual photon (self-energy, vertex energy and two-photon exchange) and  $\delta_{Brems.}$  is the correction for energy loss due to real photon emission. The largest correction comes from the  $\delta_{Virt.}$  which is dominated by soft processes<sup>2</sup>. Depending on the kinematics, the net radiative corrections are seen [49] to be as large as 30% of the uncorrected cross-section.

### 2.2.2 Scattering Beyond the Born Approximation

Using the kinematics introduced in the previous section, the total scattering amplitude for elastic scattering of two spin-half particles beyond one-photon exchange approximation can be parametrized [3] using six independent helicity amplitudes. Out of these helicity amplitudes, three do not involve a flip of the electron helicity and can be written as a linear combination of the form

$$T_{Non-flip} = \frac{e^2}{Q^2} \bar{u}(k', h') \gamma_\mu u(k, h) \times \bar{u}(p', \lambda'_N) \left( \tilde{G}_M \gamma^\mu - \tilde{F}_2 \frac{P^\mu}{M} + \tilde{F}_3 \frac{\gamma \cdot K P^\mu}{M^2} \right) u(p, \lambda_N). \quad (2.22)$$

The remaining three amplitudes do involve a flip of the electron helicity and are written as a linear combination of the form [50]

$$T_{flip} = \frac{e^2}{Q^2} \frac{m_e}{M} \left[ \bar{u}(k', h') u(k, h) \cdot \bar{u}(p', \lambda'_N) \left( \tilde{F}_4 + \tilde{F}_5 \frac{\gamma \cdot K}{M} \right) u(p, \lambda_N) + \tilde{F}_6 \bar{u}(k', h') \gamma_5 u(k, h) \cdot \bar{u}(p', \lambda'_N) \gamma_5 u(p, \lambda_N) \right], \quad (2.23)$$

where  $u(p)$ ,  $u(p')$  and  $u(k)$ ,  $u(k')$  are the spinors of the nucleon and the electron respectively and  $h(h')$ ,  $\lambda_N(\lambda'_N)$  are the initial(final) helicity of the electron and the nucleon respectively. The functions  $\tilde{G}_M$ ,  $\tilde{F}_2$ ,  $\tilde{F}_3$ ,  $\tilde{F}_4$ ,  $\tilde{F}_5$  and  $\tilde{F}_6$  are complex functions of  $\nu$  and  $Q^2$  where

$$\nu = K \cdot P \quad \text{with} \quad P = \frac{p + p'}{2} \quad \text{and} \quad K = \frac{k + k'}{2}$$

---

<sup>2</sup>The interaction of the virtual photon with the hadron occurs at vanishing momentum transfers.

and in the Born approximation they become the usual Pauli and Sachs form factors of the nucleon,

$$\tilde{G}_M^{Born}(\nu, Q^2) = G_M(Q^2), \quad \tilde{F}_2^{Born}(\nu, Q^2) = F_2(Q^2) \quad \text{and} \quad \tilde{F}_{3,4,5,6}^{Born}(\nu, Q^2) = 0. \quad (2.24)$$

Since  $\tilde{F}_{3,4,5,6}^{Born}$  and the  $\nu$  dependence of  $G_M$  and  $F_2$  vanish in the Born approximation, they carry contributions from higher order processes with at least two-photon exchange between the nucleon and the electron. The reduced scattering cross-section with contributions from processes beyond the Born approximation is then

$$\sigma = G_M^2 + \frac{\varepsilon}{\tau} G_E^2 + \frac{2\varepsilon}{\tau} G_E \mathcal{R}e \left( \delta \tilde{G}_E + \frac{\nu}{M^2} \tilde{F}_3 \right) + 2G_M \mathcal{R}e \left( \delta \tilde{G}_M + \frac{\varepsilon \nu}{M^2} \tilde{F}_3 \right) + \mathcal{O}(e^4),$$

where  $\mathcal{R}e$  denotes the real part,  $\tilde{G}_E \equiv \tilde{G}_M - (1 + \tau) \tilde{F}_2$  and the  $\nu$  dependence of the polarization parameter is given by

$$\varepsilon = \frac{\nu^2 - M^4 \tau (1 + \tau)}{\nu^2 + M^4 \tau (1 + \tau)}. \quad (2.25)$$

### 2.2.3 The Two-Photon Exchange Contribution

With precisions achievable by current and future elastic electron-nucleon scattering experiments, the standard radiative correction treatment for the contributions from higher order processes (embedded in the functions  $\tilde{G}_M$  and  $\tilde{F}_{2,3,4,5,6}$ ) is seen to be inadequate, most notably, in the calculation of the two-photon exchange contribution. The standard radiative corrections of Mo and Tsai [1] treat the two-photon exchange in the soft-photon approximation in which the interaction of the second photon with the hadron is occurring at vanishing momentum transfer neglecting the contribution from the hadronic structure. This results in an underestimate of the effective radiative corrections as it was first shown by Maximom & Tjon [49] and later by Blunden & Melnitchouk & Tjon [51] (see Figure 2.10).

#### 2.2.3.1 Experimental Evidence

The first experimental evidence for the importance of the proper treatment of the two-photon exchange correction was seen back in 2000 with the first measurement [5] of the proton's electric ( $G_E$ ) and magnetic form factor ( $G_M$ ) ratio using the polarization transfer technique [53]. This measurement, which is complementary to the Rosenbluth separation technique [54], yielded a  $G_E/G_M$  ratio which deviated from



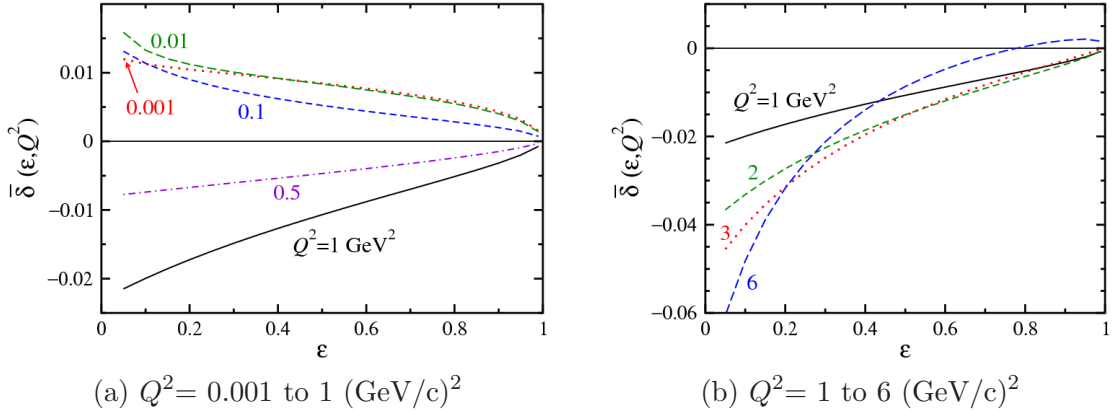


Figure 2.10: Difference  $\bar{\delta}$  between the size of the radiative corrections calculated using Blunden et al. treatment of the two-photon exchange and Mo & Tsai treatment (soft-photon approximation) of the two-photon exchange in electron-proton scattering for a range of  $Q^2$  values. The Blunden et al. calculation which includes hadronic structure differs from the Mo & Tsai calculation by as much as 1% to 6%. The differences are largest in backward angle scattering. Figures from Ref. [52].

the Rosenbluth results at  $Q^2$  above  $1$   $(\text{GeV}/c)^2$ . This was a surprising result as it contradicted the  $Q^2$  scaling of the  $G_E/G_M$  ratio predicted by the Rosenbluth results (see Figure 2.11a).

The Rosenbluth separation technique uses the  $\varepsilon$  dependence of the unpolarized elastic electron-proton scattering cross-section given in Equation 2.20 at fixed  $Q^2$  to extract  $G_M^2$  (from the intercept) and  $G_E^2$  (from the slope) separately. The polarization transfer technique on the other-hand uses the relationship

$$\frac{P_T}{P_L} = -\sqrt{\frac{2\varepsilon}{\tau(1+\varepsilon)}} \left( \frac{G_E}{G_M} \right), \quad (2.26)$$

in polarized elastic electron-proton scattering with  $P_{L(T)}$  being the longitudinal (transverse) polarization of the recoiling proton in Born approximation, to extract the ratio  $G_E/G_M$ . One can expect the two-photon effect to cancel out in the ratio  $G_E/G_M$  making the polarization transfer method insensitive to the two-photon exchange to a certain degree.

After eliminating systematics in both experimental techniques, attention is now being paid to the re-examination of the radiative corrections. What is required to explain the Rosenbluth discrepancy is an effect that increases as  $\varepsilon \rightarrow 0$  (backward angle scattering) where the momentum transfer from the electron to the proton is

large. Out of the standard radiative corrections, the two-photon exchange correction

$$\delta_{\gamma\gamma} = \frac{2\Re(\mathcal{M}^{\gamma*}\mathcal{M}^{\gamma\gamma})}{|\mathcal{M}^{\gamma}|^2}, \quad (2.27)$$

was shown [3, 51, 55] to have this required  $\varepsilon$  dependence. In Equation 2.27,  $\mathcal{M}^{\gamma\gamma}$  is the two-photon exchange contribution derived in the hard-photon treatment where the effect on the hadronic structure from the second exchanged photon is considered. In contrast, Mo & Tsai ignores the effect on the hadronic structure from the second exchanged photon, which leads to an under prediction of the two-photon correction. The Rosenbluth data corrected for the two-photon exchange correction in the hard-photon exchange treatment are seen to be in a reasonable agreement with the polarization transfer data (see Figure 2.11b).

However, the two-photon exchange calculations are not complete and have not been tested over a wider range of kinematics. Even though most of the Rosenbluth discrepancy is seen to be resolved at high  $Q^2$ , the effect of the two-photon exchange at lower  $Q^2$  is yet to be properly investigated. In addition, as observed (see Figure

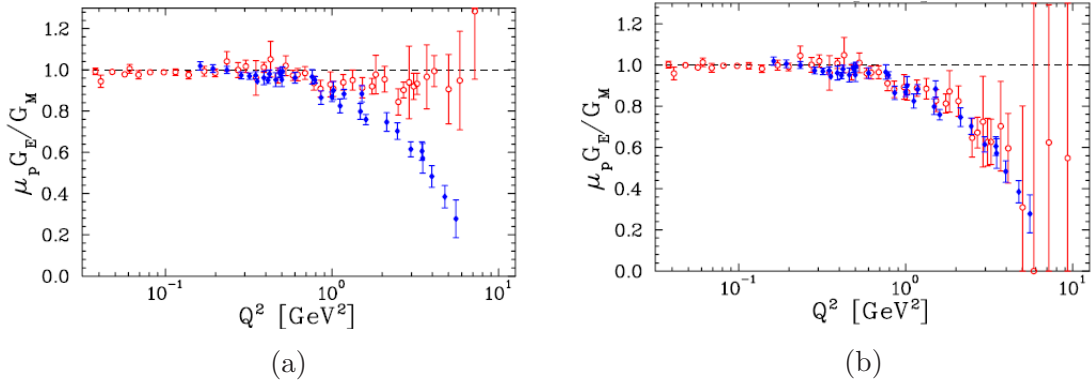


Figure 2.11: Resolving the Rosenbluth discrepancy using the two-photon exchange correction. (a) Proton's electric and magnetic form factor ratio  $\mu_p G_E/G_M$  ( $\mu_p$  is the protons magnetic moment) extracted from a global analysis of polarization transfer (blue diamonds) and Rosenbluth separation (red circles) data. The two sets of results start to deviate from each other above  $Q^2$  of  $1(\text{GeV}/c)^2$ . (b) Same set of data but after applying the two-photon exchange correction. The correction [4] has moved the Rosenbluth separation results closer to the polarization transfer results. The uncertainties in the two-photon corrected Rosenbluth separation data are partly due to how well the two-photon exchange is known at large  $Q^2$  and partly due to how the ratio is extracted from the data. Figures and analysis from Ref. [55].

2.12) by the GEp2 $\gamma$  experiment [56] recently, the two-photon exchange effects on the polarization transfer observables may not be negligible at forward angles as initially thought to be. Quoting authors in Ref. [52],

*“.. modern calculations of two-photon exchange corrections can resolve most of the observed form factor discrepancy and are consistent with all other experimental constraints; however, it will be important to test their validity over as large a range of observables and reactions as possible.”*

### 2.2.3.2 Two-Photon Effects in Other Reactions

Apart from the proton’s form-factor ratio, a proper interpretation of the two-photon exchange process benefits other types of reactions. Measurements of the cross-sections of these reactions are used to extract information on the hadron structure such as the form factors of the neutron, pion and heavy nuclei (deuteron and  $^3He$ ).

As an example, measurements of the neutron’s form factor ratio carried out at forward angles ( $\epsilon \approx 0.9$ ) and  $Q^2 = 1.45$  (GeV/c) $^2$  have shown [57] that the two-photon exchange correction on the cross-section is about 2.5%. Since the neutron electric form-factor is small compared to that of the proton, two-photon exchange contribution can be more prominent in the extraction of the neutron’s form factor

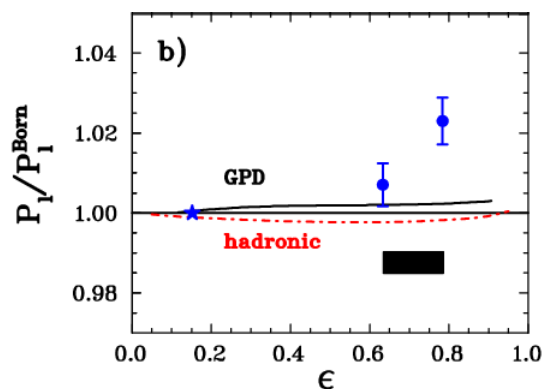


Figure 2.12: Ratio of the measured longitudinal polarization  $P_L$  to  $P_L^{Born}$  where  $P_L^{Born}$  is calculated using the Born approximation at a  $Q^2$  of 2.5 (GeV/c) $^2$ . The results show a  $2.3 \pm 0.6\%$  enhancement in  $P_L$  at large  $\epsilon$  relative to the Born approximation [56]. The curves are calculations of  $P_L$  with two-photon exchange correction from a GPD based model and a hadronic model. Theory curves indicate an increase in the two-photon exchange effect as  $\epsilon \rightarrow 1$  but under predicts the measurement. Figure from Ref. [56].

ratio. This then can effect a few percent precision extraction of the electric and magnetic form factors unless the two-photon exchange contribution is properly taken into account. In addition, the treatment of two-boson exchange (TBE) box corrections to parity violating electron scattering benefits from an understanding of the two-photon exchange mechanism which is similar in many ways [58]. In precision PV measurements (like  $Q_{\text{weak}}$ ) that tests the Standard Model, it is important to reduce the theoretical uncertainties associated with these TBE corrections as mentioned in Subsection 2.1.5. Moreover, the main physics analysis of this dissertation, the beam normal single spin asymmetry, is generated by the two-photon exchange process and is a systematic in parity violating electron scattering experiments (PVES). The model dependence of the two-photon exchange calculations prevents PVES from relying on calculations to determine the magnitude of the systematic due to the large theoretical uncertainties which can be as large as 50% (more on this will be discussed later).

Together with the form factor ratio measurements, all of these reactions provide compelling reasons to properly benchmark the two-photon exchange models using experimental inputs.

### 2.2.4 *Experimental Inputs of the Two-Photon Exchange*

Observables which provide direct access to the two-photon exchange process fall into two categories. Observables of the real part of the two-photon amplitude and observables of the imaginary part of the two-photon amplitude. The following are the well known examples of these categories.

#### 2.2.4.1 *( $e^-p$ ) and ( $e^+p$ ) Ratio*

The observable which provides direct access to the *real part* of the two-photon exchange amplitude is the ratio of electron-proton ( $e^-p$ ) and positron-proton ( $e^+p$ ) scattering cross-sections [4]

$$\frac{\sigma^{e^+p}}{\sigma^{e^-p}} \approx \frac{|\mathcal{M}_\gamma^{e^+}|^2 + 2\Re(\mathcal{M}_\gamma^{e^+*}\mathcal{M}_{\gamma\gamma}^{e^+})}{|\mathcal{M}_\gamma^{e^-}|^2 + 2\Re(\mathcal{M}_\gamma^{e^-*}\mathcal{M}_{\gamma\gamma}^{e^-})} = 1 - 2[\delta_{\gamma\gamma} - \delta_{IR}(MoT)], \quad (2.28)$$

where  $\delta_{\gamma\gamma}$  is as defined in Equation 2.27 and  $\delta_{IR}(MoT)$  is the IR divergent two-photon exchange correction determined in the Mo and Tsai [1] prescription. This observable was in fact used [59–62] to provide early experimental limits on the two-photon exchange correction to the Rosenbluth separation technique. These early

measurements (see Figure 2.13a) showed the two-photon correction was less than 1% over a range of  $Q^2$  from 0.01 (GeV/c)<sup>2</sup> to 5 (GeV/c)<sup>2</sup>.

A re-examination done on the same set of data, after the observation of the Rosenbluth discrepancy, indicates that the previous estimate might have been dominated by the low-precision high  $Q^2$  data (see Figure 2.13b). Moreover, these early measurements only have positron data with a full  $\varepsilon$  range below a  $Q^2$  of 2 (GeV/c)<sup>2</sup> where the Rosenbluth discrepancy is not significant. Still, an analysis [63] of the  $\varepsilon$  dependence of these low  $Q^2$  data shows a significant  $\varepsilon$  dependence of the ratio  $\frac{\sigma^{e^+p}}{\sigma^{e^-p}}$  which corresponds to a 2.8% partial increase in the observed Rosenbluth slope. Since the average  $Q^2$  of the data is about 0.5 (GeV/c)<sup>2</sup>, it is insufficient to make the full two-photon correction required to explain the Rosenbluth discrepancy above a  $Q^2$  of 2 (GeV/c)<sup>2</sup>. But recently completed high precision ( $\approx 1\%$ ) measurements [64, 65] of  $e^- + p$  and  $e^+ + p$  ratio are expected to make significant improvements to the two-photon correction estimate in the future<sup>3</sup>.

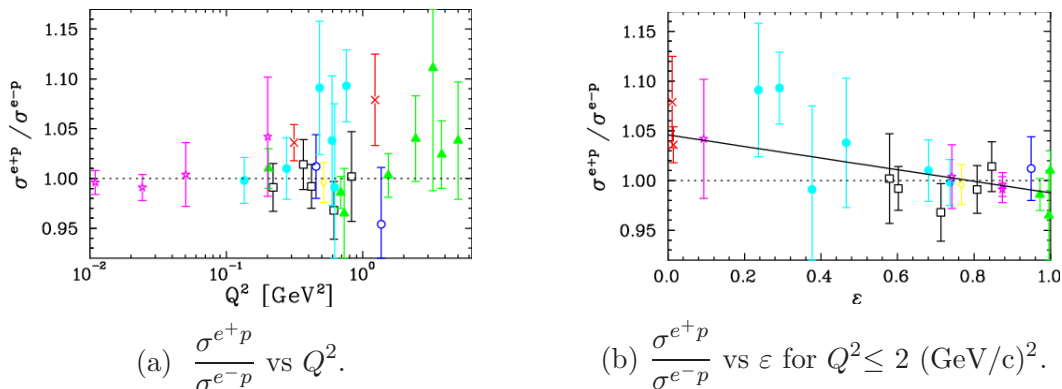


Figure 2.13: Measurements of the  $\frac{\sigma^{e^+p}}{\sigma^{e^-p}}$  ratio [59–62] (a) as a function of  $Q^2$  with the constant fit  $1.003 \pm 0.005$  and (b) as a function of  $\varepsilon$  for measurements with  $Q^2 \leq 2$ (GeV/c)<sup>2</sup> with a slope  $(5.7 \pm 1.8)\%$ . The constant fit in (a), driven by the small uncertainties on the low  $Q^2$  data, was thought to indicate the size of the two-photon exchange correction to be  $(0.15 \pm 0.25)\%$  [63]. However, the  $\varepsilon$  dependence of the low  $Q^2$  data analysis done 30 years later shown in (b) indicates there is a  $\varepsilon$  dependence in the ratio. The different colors indicates measurements by different experiments. Figures from Ref. [63].

<sup>3</sup>See Ref. [66] for the preliminary results from the measurement done by the CLAS collaboration.

### 2.2.4.2 Single Spin Asymmetries

An observable which is directly proportional to the *imaginary part* of the two-photon exchange amplitude is the single spin asymmetry measured in electron-nucleon scattering when either the target (target normal) or the electron (beam normal) is polarized normal to the scattering plane.

Both target and beam normal single spin asymmetries are time-reversal invariant, parity conserving observables which vanish in the Born approximation. They are generated by the interference of the one-photon and two-photon exchange processes and have the form [67]

$$A = \frac{\sigma \uparrow - \sigma \downarrow}{\sigma \uparrow + \sigma \downarrow} = \frac{\Im m \left[ \sum_{spins} (\mathcal{M}^\gamma)^* (Abs \mathcal{M}^\gamma) \right]}{\sum_{spins} |\mathcal{M}^\gamma|^2}, \quad (2.29)$$

where  $\sigma \uparrow$  ( $\sigma \downarrow$ ) denotes the scattering cross-section for spin parallel (anti-parallel) to a vector  $\hat{n} \equiv \frac{\vec{k} \times \vec{k}'}{|\vec{k} \times \vec{k}'|}$  normal to the scattering plane,  $\Im m$  is the imaginary part and  $Abs \mathcal{M}^\gamma$  is a sum over all the possible intermediate states in the two-photon exchange process. In terms of the amplitudes given in Subsection 2.2.2, the target normal single spin asymmetry is given by [68]

$$A_n = \sqrt{\frac{1\varepsilon(1+\varepsilon)}{\tau}} \left( G_M^2 + \frac{\varepsilon}{\tau} G_E^2 \right)^{-1} \quad (2.30)$$

$$\times \left[ -G_M \Im m \left( \delta \tilde{G}_E + \frac{\nu}{M^2} \tilde{F}_3 \right) + G_E \Im m \left( \delta \tilde{G}_M + \frac{2\varepsilon}{1+\varepsilon} \frac{\nu}{M^2} \tilde{F}_3 \right) \right] + \mathcal{O}(e^4),$$

and the beam normal single spin asymmetry is given by [50]

$$B_n = \frac{2m_e}{Q} \sqrt{2\varepsilon(1-\varepsilon)} \sqrt{1 + \frac{1}{\tau}} \left( G_M^2 + \frac{\varepsilon}{\tau} G_E^2 \right)^{-1} \quad (2.31)$$

$$\times \left[ -\tau G_M \Im m \left( \tilde{F}_3 + \frac{1}{1+\tau} \frac{\nu}{M^2} \tilde{F}_5 \right) - G_E \Im m \left( \tilde{F}_4 + \frac{1}{1+\tau} \frac{\nu}{M^2} \tilde{F}_5 \right) \right] + \mathcal{O}(e^4).$$

To calculate either quantity theoretically, one requires the knowledge of the invariant functions  $\tilde{F}_{3,4,5}$  and  $\tilde{G}_{M,E}$ . As mentioned in Subsection 2.2.2, these functions carry contributions from the higher order-processes like the two-photon exchange and are not readily available. The approach which is used to overcome this difficulty is to derive an expression for the right hand side of Equation 2.29 by modelling the

imaginary part of the two-photon exchange using well known experimental inputs on the Compton scattering. This modelling of the hadronic tensor gives rise to a model dependence in the single spin asymmetries.

### 2.2.5 Imaginary Part of the Two-Photon Exchange

The imaginary part of the two-photon exchange is modelled by treating the two-photon exchange with the nuclei as a Compton scattering of two virtual photons off of the nuclei also known as the Doubly Virtual Compton Scattering (DVVS) as shown in Figure 2.14. Using the DVVS tensor, the absorptive part of the imaginary part of the two-photon exchange is given by [69]

$$Abs\mathcal{M}^{\gamma\gamma} = e^4 \int \frac{|\vec{k}_1|^2 d\vec{k}_1 d\Omega_{k_1}}{2E_{k_1} (2\pi)^3} \bar{u}(k') \gamma_\mu (\gamma \cdot k_1 + m_e) \gamma_\nu u(k) \frac{1}{Q_1^2 Q_2^2} W^{\mu\nu}(w, Q_1^2, Q_2^2), \quad (2.32)$$

where  $k_1$  is the four-momentum of the intermediate electron,  $\Omega_{k_1}$  is the solid angle of the external electron,  $W^{\mu\nu}$  is the hadronic tensor,  $Q_{1(2)}^2 = -q_{1(2)}^2$  is the four-momentum transfer to the first (second) photon and  $w$  is the invariant mass of the intermediate hadronic state.

The hadronic tensor  $W^{\mu\nu}$  is the absorptive part of the DVVS tensor for all possible on-shell intermediate states X, where X = N (nucleon) for ground and X =  $\pi N, \pi\pi N, \dots$  for excited intermediate states. For the ground state,  $W^{\mu\nu}$  is exactly

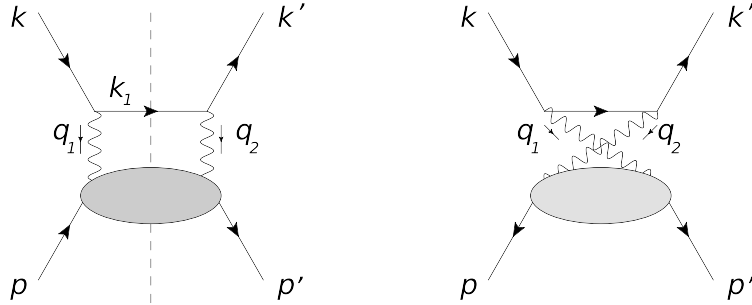


Figure 2.14: The Compton scattering treatment of the two-photon exchange process. Neglecting the electron line, the two sectors separated by the dash line can be thought of as Compton scattering of two virtual photons. The blob represents all the possible intermediate states (ground and excited) of the nucleus.  $k_1$  is the momentum of the intermediate electron and  $q_1 = k - k_1$  and  $q_2 = k_1 - k'$  are the four-momentums carried by the virtual photons.

calculable using on-shell electromagnetic form factors of the nucleon. For the excited states, the DVVS tensor depends on 18 invariant amplitudes [70]. But the resonance form factors of all the possible nucleon resonances are not known. Therefore to determine these invariant amplitudes, different methods have been used to relate the amplitudes to well known experimental inputs on Compton scattering. But these inputs depend on the kinematics (see Table 2.3). The calculated invariant amplitudes are used to determine the functions  $\tilde{F}_{3,4,5}$  and  $\tilde{G}_{M,E}$  which can then be used to determine  $B_n$  and  $A_n$ . There are several available models of single spin asymmetries as shown in Table 2.3. For a single kinematic, there may be several calculations available. One has to select which model is suitable to predict the single spin asymmetries at the desired kinematics. Since the calculations differ from one another due to either the types of inputs used or parametrization of the inputs, the uncertainty associated with the choice of model is large. This will be discussed in view of the beam normal single spin asymmetry in Subsection 2.2.6.1.

Based on model calculations, at few GeV electron energies, the target normal single spin asymmetries are in the order of  $10^4$  ppm and the beam normal single spin asymmetries are in the order of few ppm [72]. But unfortunately, there are no known measurements of the target normal single spin asymmetries for elastic electron scattering which is of interest for the two-photon correction on the cross-sections. All existing measurements [76, 77] of the target normal single spin asymmetries are

Table 2.3: Some of the available model calculations of single spin asymmetries, their experimental inputs and kinematics.

Model	$Q^2$ or E	Input
Diaconescu & Musolf [71]	$< 1$ GeV	This is an effective field theory calculation.
Pasquini & Vanderhaeghen [72]	$< 3$ GeV	MAID electroproduction amplitudes
Afanasev & Merenkov [73]	$Q^2 \rightarrow 0, E > 1$ GeV	Photoproduction cross-sections
Borisyuk & Kobushkin [74]	$\sin^2 \frac{\theta}{2} \ln \frac{Q^2}{m_e^2} \gg 1$	Photoproduction cross-sections
Gorchtein [75]	$Q^2 < 0.5(\text{GeV}/c)^2, E = 6-45$ GeV	Photoproduction cross-sections
Gorchtein & Guichon & Vanderhaeghen [50]	$Q^2 > 1(\text{GeV}/c)^2$ (partonic regime)	Generalized Parton Distributions



performed in the deep inelastic region. These resulted in asymmetries which are zero within the large uncertainties of the measurements. However, with the precision achievable with the present parity violating electron scattering (PVES) experiments, measurements of the beam normal single spin asymmetries have become possible as ancillary measurements. The parity violating electron scattering experiments use longitudinally polarized beams and therefore the only configuration change needed for a beam normal single spin asymmetry measurement is changing the beam polarization orientation from longitudinal to transverse.

### 2.2.6 Beam Normal Single Spin Asymmetry in Electron-Nucleon Scattering

The beam normal single spin asymmetry (BNSSA) is measured by scattering transversely polarized electrons off of unpolarized nucleons. The asymmetry measured in a detector placed in the scattering plane has an azimuthal angle dependence given by

$$B_n(\phi_e) = B_n \vec{S} \cdot \hat{n} = -B_n |\vec{S}| \sin(\phi_e - \phi_s), \quad (2.33)$$

where  $\vec{S}$  is the electron spin in the transverse direction,  $\hat{n}$  is a unit vector normal to the scattering plane,  $\phi_s$  is the azimuthal angle of  $\vec{S}$  and  $\phi_e$  is the azimuthal angle of the scattering plane (see Figure 2.15). Therefore, by placing a detector at  $\phi_e$ , the beam normal single spin asymmetry can be measured and extracted from the asymmetry measured in the detector.

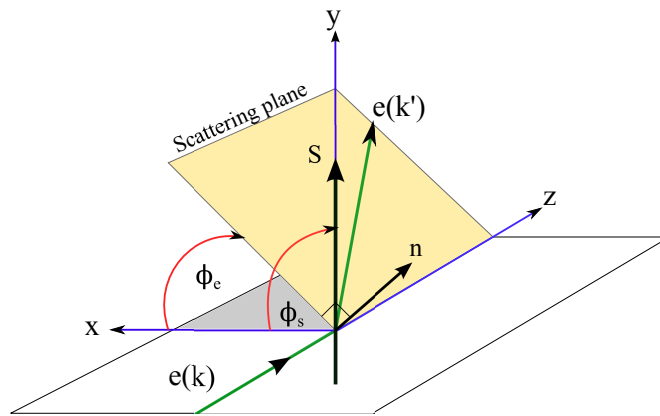
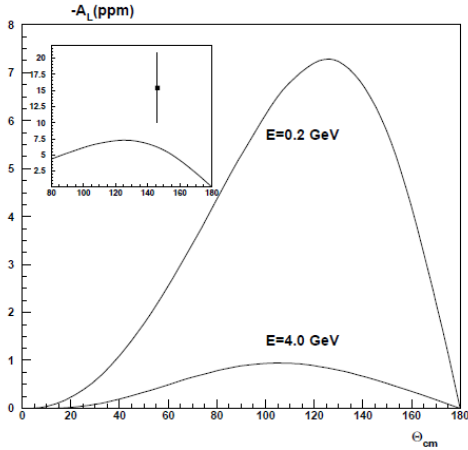


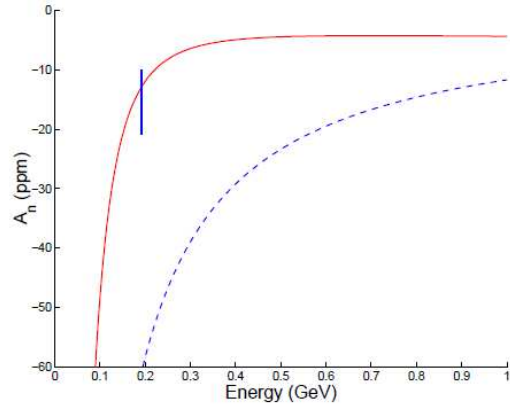
Figure 2.15: Kinematics of an electron spin polarized in the vertical transverse direction scattering from an unpolarized nucleon. The initial (final) momentum of the electron is given by  $k$  ( $k'$ ). See text for explanation.

### 2.2.6.1 Model Calculations

Subsection 2.2.5 presented a list of available models for single spin asymmetries. As noted before, these models are valid for specific kinematics and for a given kinematic, there may be more than one model calculation to choose from. This subsection will discuss the model dependence of the calculations and how the models compare with existing measurements. The first published model calculation of the beam normal single spin asymmetry was performed by Afanasev & Merenkov [78] (A&M) for very forward angles ( $Q^2 \ll s$ ) and high energies. They used the optical theorem to relate the Compton amplitude to the total photoproduction cross-section considering inelastic intermediate states of  $\pi N, \pi\pi N$ . This resulted in beam normal single spin asymmetry which are negative and are in the order of few ppm. The calculated asymmetries are large at backward angles. At higher energies, the total magnitude was dominated by the contributions from excited intermediate states. However, this model failed to match the first measurement of BNSSA by the SAMPLE experiment [79] (see Figure 2.16a).



(a) Afanasev &amp; Merenkov



(b) Diaconescu &amp; Musolf

Figure 2.16: Comparison of BNSSA measurement from the SAMPLE experiment to the calculation from models using only the nucleon intermediate state. (a) Dependence of BNSSA on the center of mass angle in the hadronic framework. (b) Dependence of the BNSSA at fixed scattering angle on the beam energy in an effective field theory with pions integrated out. Dashed line is the leading order result and the solid line is the full calculation. Data point is from the SAMPLE experiment with energy = 200 MeV and laboratory scattering angle =  $146.1^\circ$ . Figures (a) from Ref. [78] and (b) from Ref. [71].

Surprisingly, the Diaconescu & Musolf [71] (D&M) model using perturbation theory to estimate the elastic intermediate state contribution to second order in  $E_e/M$  (the pions were integrated out) were able to predict a value for BNSSA at SAMPLE kinematics (see Figure 2.16b). Since the SAMPLE measurement was carried out at the pion threshold, the inelastic states with the pions in the intermediate state should be accounted for in the full calculation of the BNSSA. None of the existing theoretical models using pion intermediates states have been able to explain this large asymmetry measured by the SAMPLE experiment yet.

Later calculations of the beam normal single spin asymmetry includes the Pasquini & Vanderhaeghen [72] (P&V) model for the resonance region below and around the two-pion threshold. Here, the imaginary part of the two-photon exchange is estimated by using the unitarity relation to express the Compton tensor in terms of the pion electroproduction amplitudes from MAID [80] assuming  $\pi N$  intermediate states. This model calculation failed to describe the SAMPLE result (see Figure 2.17a) but it was able to partially explain the forward angle measurement done by the A4 experiment and some of the backward angle measurements later done by the G0 and the A4 experiments [81] (see Figure 2.17b).

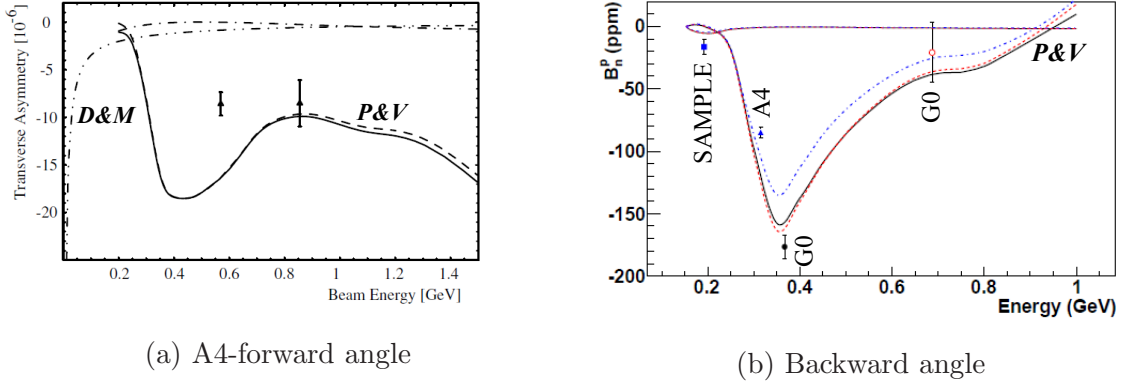


Figure 2.17: Comparing forward angle (a) and backward angle (b) scattering measurements of BNSSA to model calculations using  $\pi N$  in the excited intermediate state. (a) dash-dot-dot line is the calculation by Diaconescu & Musolf, dash-dot (dash) line is the contribution from the ground (excited) state as calculated by Pasquini & Vanderhaeghen and the thick line is the full calculation by Pasquini & Vanderhaeghen. (b) The three colors represents the Pasquini & Vanderhaeghen model predictions for  $\theta_{cm} = 120^\circ$  (black),  $\theta_{cm} = 130^\circ$  (red) and  $\theta_{cm} = 150^\circ$  (blue). The overlapping lines on the top, drawn close to zero, represents the ground state contribution and the lines on the bottom gives the full calculation. Figures from Ref. (a) [82] and (b) [81].

Since then, several model calculations [73–75] using the quasi-real Compton scattering approximation have pointed out the necessity to use multiple pion excitations in the excited intermediate states at energies around or above the two-pion threshold. These calculations, though using different parametrization of the photo-production cross-section, produced estimations for the G0-forward angle beam normal single spin asymmetry measurements which are similar to one another but larger than the measured value (see Figure 2.18). At 95% C.L, the  $20^\circ$  angle measurement indicates an under prediction from the Pasquini & Vanderhaeghen model and an over prediction from the Afanasev & Merenkov and Gorchtein models. Regardless of the measurements, the model calculations in the forward scattering kinematics are different from one another by at least a factor of two. From the preceding discussion, one can see that model calculations of the beam normal single spin asymmetry are dominated by the contributions from the excited intermediate states, the magnitude of the asymmetry depends on the types of intermediate states considered ( $\pi N$  over  $\pi\pi N$ ), some models are better at predicting BNSSA in backward angle high energy scattering than forward angle low energy scattering, and the uncertainty associated with the choice of model at forward angles can be about 50% of the size of the asymmetry. Overall, the model calculations are not complete due to the treatment of the two-photon exchange. This is the same difficulty observed in the determination of the two-photon exchange correction on the cross-section measurements discussed in Subsection 2.2.3. Although the large theoretical uncertainty is the driving factor for

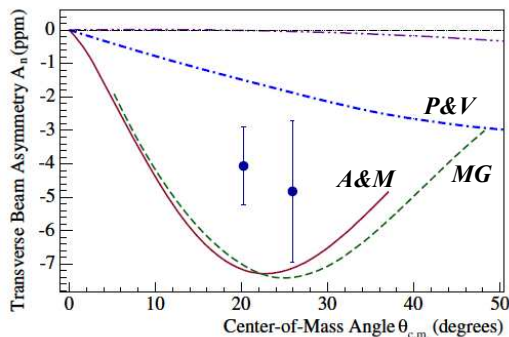


Figure 2.18: Comparing measurements of BNSSA to model calculations which use  $\pi\pi N$  in the inelastic intermediate state (MG, A&M) and Pasquini & Vanderhaeghen which use  $\pi N$  intermediate states. The measurements are from the G0-forward angle measurement at beam energies of 3 GeV [83]. Figure from Ref. [83].

beam normal single spin asymmetry measurements by PVES experiments, these measurements can be used to improve model calculations of the single spin asymmetries and the two-photon exchange process.

### 2.2.7 *As a False Asymmetry in PVES*

The beam normal single spin asymmetry becomes a false asymmetry in parity violating electron scattering experiments when there is residual transverse polarization in the electron beam and the azimuthal symmetry of the detector array is broken. This results in a small azimuthal modulating asymmetry in the measured asymmetry

$$A^{Msr} = P_L A^{PV} + B_n P_T \sin(\phi_e - \phi_s), \quad (2.34)$$

where  $P_{L(T)}$  stands for longitudinal (L) and transverse (T) polarization of the beam. Depending on the magnitude of the false asymmetry term, either a systematic correction or an uncertainty needs to be assigned to the parity violating asymmetry measurement to take this into account.

As an example, a 4% residual transverse polarization in the beam will result in an azimuthal modulating false asymmetry of

$$B_n P_T = -5 \text{ ppm} \times 0.04 = 0.2 \text{ ppm},$$

where -5 ppm is used as an estimate for the magnitude of the beam normal single spin asymmetry at  $Q_{\text{weak}}$  kinematics. If the detector array is perfectly symmetric in the azimuthal plane, then the contribution from this false asymmetry will be zero since

$$\int_0^{2\pi} \sin(\phi_e - \phi_s) d\phi_e = 0. \quad (2.35)$$

But realistically the modulating factor is not zero due to the difficulties associated with building a perfectly symmetric detector array. A modulating factor of  $\int_0^{2\pi} \sin(\phi_e - \phi_s) d\phi_e = 0.01$  (as an example) will generate a false asymmetry of

$$B_n P_T \times 0.01 = 0.002 \text{ ppm}, \quad (2.36)$$

which is called the leakage of the beam normal single spin asymmetry, or the BNSSA leakage. For the  $Q_{\text{weak}}$  parity violating asymmetry in the order of -0.2 ppm, this yields

a systematic correction of 1%. Unless the beam normal single spin asymmetry is well known, a 1% correction could accompany the systematic error which could affect the precision goal of the experiment.

Therefore, to properly correct for this false asymmetry, PVES experiments like  $Q_{\text{weak}}$  need to know the magnitude of the BNSSA at their kinematics, the size of the symmetry breaking in their detector array and the amount of residual transverse polarization in the beam. Since a measurement of beam normal single spin asymmetry can yield all of these factors, PVES experiments prefer to measure the beam normal single spin asymmetry as an ancillary measurement.

### 3 $Q_{\text{weak}}$ Setup Design and Implementation

This chapter summarizes the specific design and performance of the experimental setup in the context of  $Q_{\text{weak}}$ . Since the experiment was designed to measure a less than parts per million parity violating asymmetry, all that is discussed here attributes to the successful measurement of the order of magnitude larger beam normal single spin asymmetry.

The main technical challenge to the  $Q_{\text{weak}}$  measurement was the proposed 2.5% relative precision of the physics asymmetry of about -260 parts per billion (ppb) [84]. Table 3.1 shows the sources of statistical and systematic uncertainties associated with this measurement as well as their projected contributions to the measured asymmetry and the final weak charge measurement. In order to achieve these precision goals, the experiment was built upon technologies that already exist at Jefferson Lab as a result of previous parity violating experiments like G0 [83] and HAPPEX [85]. Since the  $Q_{\text{weak}}$  parity violating asymmetry and its absolute error is an order of magnitude smaller than any of these previous measurements, a dedicated design, additional control of systematics, and considerable modifications to hardware and software were needed to reach the precision goals summarized in Table 3.1.

Table 3.1: Proposed error budget of the  $Q_{\text{weak}}$  experiment [86]. This includes contributions from the different sources of error on both the parity violating asymmetry and the weak charge of the proton.

Source of Error	$\frac{\Delta A^{PV}}{A^{PV}}$	$\frac{\Delta Q_w^p}{Q_w^p}$
Counting Statistics	2.1%	3.2%
Hadronic Structure	-	1.5%
Beam Polarimetry	1.0%	1.5%
Absolute $Q^2$	0.5%	1.0%
Backgrounds	0.7%	0.7%
Helicity Correlated Beam Properties	0.5%	0.8%
<b>TOTAL:</b>	<b>2.6%</b>	<b>4.2%</b>

### 3.1 Design Parameters

The design parameters (see Table 3.2) of the experiment were chosen to achieve the proposed statistical precision with minimum contributions from systematics. A  $Q^2$  of  $0.025 \text{ (GeV/c)}^2$  ensures minimum contribution from the proton structure (see Equation 2.9) while providing an asymmetry large enough to measure with the quoted statistical precision in several thousand hours. Since counting statistics precision goes like

$$\sigma_{stat} = \frac{1}{\sqrt{N}},$$

with  $N$  being the total number of electrons collected, to reach the statistical goal the experiment collected data for about two years with a high event rate, high beam polarization, high beam current and a longer target. The high event rate also meant that integration<sup>1</sup> of signals was required for data acquisition instead of counting. This high-current running mode is known as the *integrating-mode* of the experiment. In addition, background and  $Q^2$  measurements were performed using low current (below  $2 \mu\text{A}$ ) beam where events were counted. This low-current running mode is known as the *tracking-mode* of the experiment. Both running modes of the experiment required separate data acquisition and analysis techniques which will be discussed in detail in Chapter 4.

Table 3.2: Design parameters of the  $Q_{\text{weak}}$  experiment [84, 86].

Parameters	Value
Full Current Production Running	2544 hours
Incident Beam Energy	1.160 GeV
Beam Polarization	88%
Beam Current	180 $\mu\text{A}$
Hydrogen Target Thickness	35 cm
Solid Angle	$\Delta\Omega=43 \text{ msr}$
Acceptance Averaged $Q^2$	$\langle Q^2 \rangle = 0.025 \text{ (GeV/c)}^2$
Nominal Scattering Angle	7.9 deg
Scattering Angle Acceptance	5.8 deg – 11.6 deg
Azimuthal Acceptance	49% of $2\pi$
Integrated Rate (all sectors)	6.5 GHz

<sup>1</sup>Collecting all the signals reported by the detectors within a given time period without any pre-event selection.



Figure 3.1 shows a Computer-Aided Design (CAD) diagram of the experimental setup indicating different subsystems used for the integrating-mode and the tracking-mode operations. During the experiment, polarized electrons were scattered off the target inside the target chamber. Elastically scattered electrons with a nominal scattering angle of  $7.9^\circ$  were selected and focused onto the array of Čerenkov main detectors using a combination of collimators and a toroidal magnet. In the tracking-mode, a tracking detector system consisting of drift chambers and a trigger scintillator were used to detect electrons in background and  $Q^2$  measurements (see Section 3.8). The following subsections will highlight the importance, utilization and performances of these subsystems.

### 3.2 Polarized Electron Beam at Jefferson Lab

The Superconducting Radio Frequency (SRF) Continuous Electron Beam Facility [87] at Jefferson Lab is one of the pioneering accelerator facilities in the world to provide electron beams of several GeV required for probing the nucleon structure.

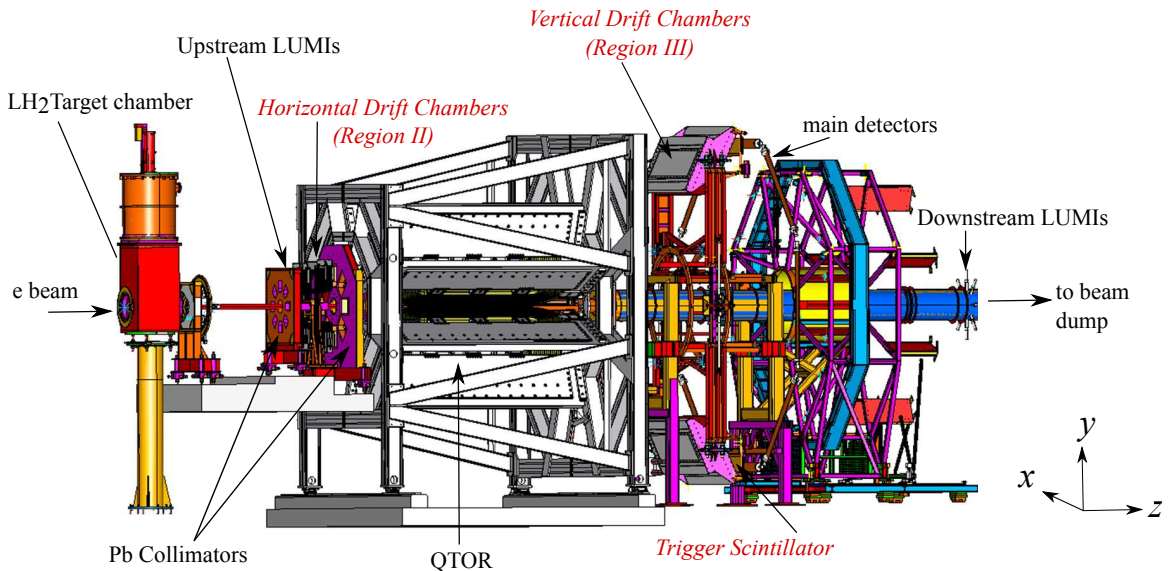


Figure 3.1: The CAD diagram of the side-view of the  $Q_{\text{weak}}$  apparatus highlighting the different subsystems used during the integrating-mode (black) and the tracking-mode (red/italic) operations. The distance along the beamline from the target center to the center of the main detector array is 12.2 m and the length of a main detector is 2 m. Figure from Ref. [84].

Figure 3.2 shows the layout of the Continuous Electron Beam Accelerator Facility (CEBAF) accelerator highlighting its main components relevant for this experiment. Three polarized electron beams corresponding to the three experimental halls are created at the polarized source where they are combined to form a bunched beam of 1.497 GHz. This beam is then sent through a series of spin rotators (see Subsection 3.2.3) located downstream of the polarized source to deliver the beam polarization orientation (longitudinal/vertical/horizontal) requested by the experimental halls. After spin manipulation, the beam is pre-accelerated to a 5 MeV energy and later up to 67 MeV before being injected into the North Linear Accelerator (LINAC). Each LINAC (North/South) provides 600 MeV of acceleration. Once the required energy is achieved by each beam, they are extracted at the end of the south LINAC and are transported into three experimental halls A, B and C. The remainder of the beam after the interaction with the targets is sent into the beam dump for proper disposal.

The  $Q_{\text{weak}}$  experiment was installed in the experimental Hall C and it utilized the full polarized electron capabilities of CEBAF. A huge effort was made by both the  $Q_{\text{weak}}$  Collaboration and the Jefferson Lab accelerator division to meet the parity quality electron beam requirements of the experiment. A major part of my research work was involved with achieving parity quality beam for the experiment by optimizing the polarized source performance. Therefore, in the following subsections more details are presented about the performance of the polarized electron source.

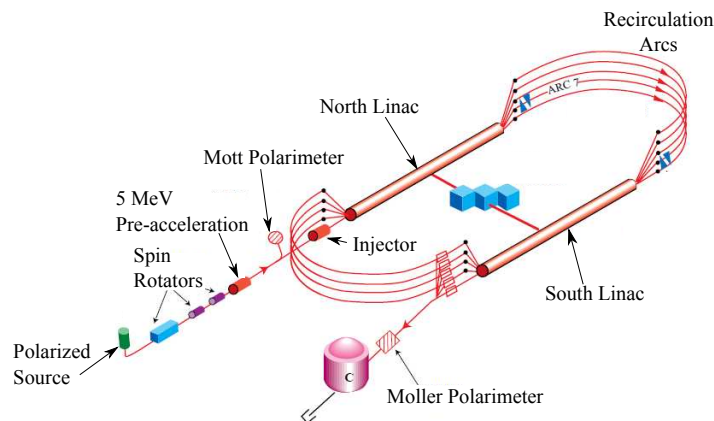


Figure 3.2: Layout of the CEBAF accelerator highlighting some of its components relevant to this experiment. Each linac is 1400 m in length. See text for explanation. Figure from Ref. [88].

### 3.2.1 Polarized Electron Source

Figure 3.3 contains a schematic of the CEBAF polarized electron source highlighting its main components, the electron gun and the laser table. The following subsections describe the features and performances of these two components.

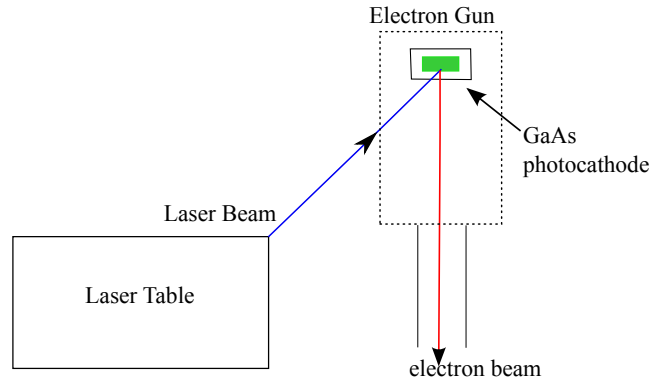


Figure 3.3: Schematic of the polarized electron source showing the paths of the laser beams and the electron beam before reaching the injector.

#### 3.2.1.1 The Inverted Electron Gun

The DC high voltage inverted electron gun [89, 90] at CEBAF, uses photo-injection [91] from a GaAs photocathode placed in an inverted insulator inside a vacuum chamber (see Figure 3.4) to generate photo-electrons. Compared to its predecessors [92], the inverted gun is designed to operate at a high bias voltage of 200 kV. A higher bias voltage is expected to improve the beam transmission through the injector thereby improving the parity quality of the beam. It is also expected to prolong the lifetime of the photocathode by minimizing the overhead associated with photocathode reactivation which affects the active running time of experiments.

However, field emission and operational limitations of some injector components [92], restricted the operational bias voltage of the gun to 130 kV during the  $Q_{\text{weak}}$  experiment. Under this operational condition, with a charge lifetime<sup>2</sup> of 70 C (see Figure 3.5a), the operation lifetime of the gun was about two weeks in a single illuminated area/laser spot [89]. Therefore, the laser spot needed to be moved (see Figure 3.5b) every two weeks during the running of the experiment. At this rate, a

---

<sup>2</sup>Charge lifetime denotes the total charge that can be collected from a photocathode before its quantum efficiency drops to  $1/e$  of its initial value.

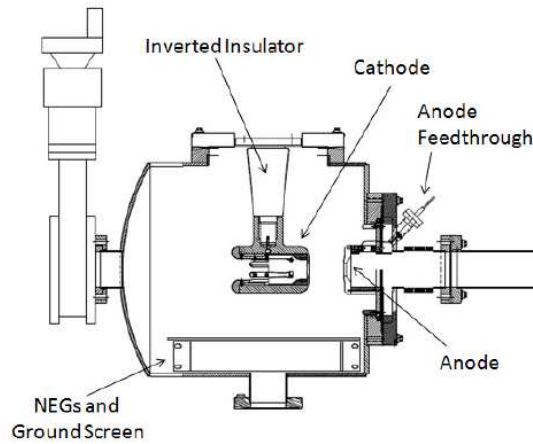


Figure 3.4: Cross section of the CEBAF 200 kV inverted electron gun. For scale, the cathode/anode gap is about 6 cm. Figure from Ref. [90].

single photocathode allowed three months of high beam current operation for  $Q_{\text{weak}}$  before running out of new spots and requiring reactivation. Since a reactivation requires about a week, this improvement done to the charge lifetime by the Jefferson Lab Polarized Source group was very helpful for maximizing  $Q_{\text{weak}}$  beam time.

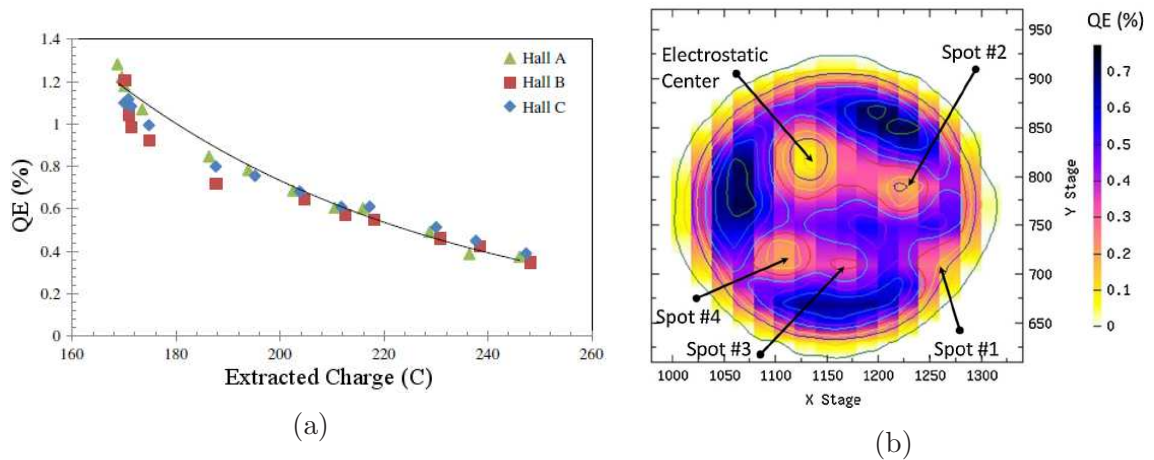


Figure 3.5: (a) QE efficiency curve from a single laser spot. From the fit, the charge life time is 70C. (b) QE efficiency map of the CEBAF photocathode with four used laser spots. Figures from Ref. [89].

### 3.2.1.2 The Laser Table

At the laser table, three fiber-lasers [93] are used to generate the electron bunches customized for polarization requirements of the three experimental halls. The laser beams are initially linearly polarized<sup>3</sup>, Radio Frequency (RF) pulsed at 499 MHz and combined with a  $120^\circ$  separation in space. The combined beams are then sent through a Pockels Cell (PC)<sup>4</sup> to convert their linear polarization to circular polarization before they shine upon the photocathode in the gun as shown in Figure 3.6. The PC axis is aligned along the laser beam axis with its birefringent axis at  $45^\circ$  to the vertical and horizontal axis. In order to convert linear polarization of the lasers to circular polarization, an appropriate high voltage (typically  $\pm 2.5$  kV) is applied to the anodes of the PC inducing a  $\pm 90^\circ$  relative shift between its birefringent axes. The direction of the resultant circular polarization is changed from left to right and vice versa by alternating the polarity of the anode voltages using an optically isolated Pockels Cell high voltage switch that is controlled by the helicity signal. The helicity

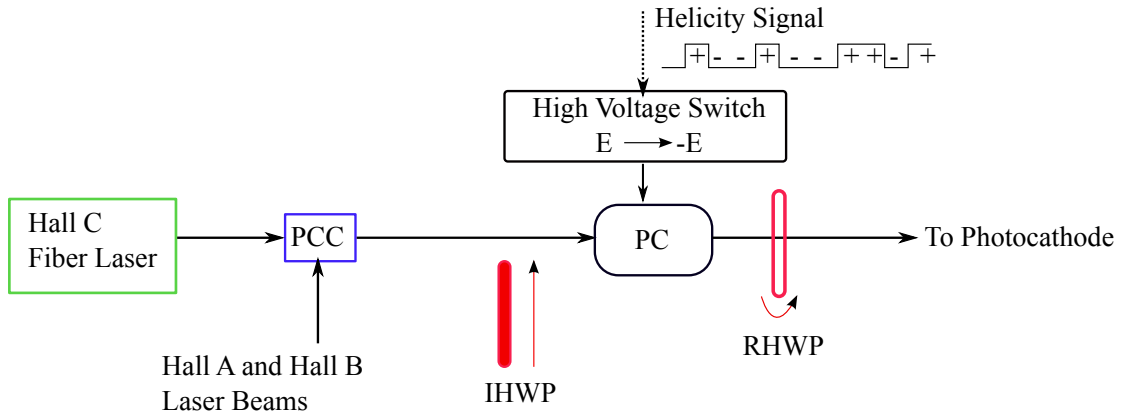


Figure 3.6: Schematic of the laser table with components relevant for this discussion. The three lasers are combined using a Polarized beam Combining Cube (PCC) before being sent to the Pockels cell (PC) to be converted to circular polarization. The PC high voltage is controlled by the helicity signal which decides the helicity of the electrons, positive (+) or negative (-). The Insertable Half Wave Plate (IHWP) and the Rotatable Half Wave Plates (RHWP) are used for controlling helicity correlated false asymmetries. See text for explanation.

<sup>3</sup>Hall A and B are linearly polarized in the horizontal plane and hall C is polarized in the vertical plane orthogonal to A and B.

<sup>4</sup>Basically a voltage controlled half wave plate used to convert linear polarization to circular or vice versa.

signal is a pulse signal varying between 0 V and 1 V. The positive (negative) going edge will control the PC to polarize the laser in right (left) circular direction which will result in the emission of electrons with spin  $-1/2$  ( $+1/2$ ) or negative (positive) helicity from the photocathode.

The Insertable Half Wave Plate (IHWP) and the Rotatable Half Wave Plate (RHWP) are birefringent elements which were used to minimize helicity correlated false asymmetries. The insertion of the Insertable Half Wave Plate (IHWP) changes the spin of the electrons by  $180^\circ$  independent of the helicity signal. Therefore, adding data sets with IHWP IN to the one with IHWP OUT provides the means to remove helicity correlated false asymmetries. For this purpose, during the experiment, the IHWP was inserted into the beam at time intervals of 8 hours called *slugs*. The RHWP was used with two predefined rotations for IHWP IN and OUT states to further minimize Helicity Correlated Beam Asymmetries (HCBA). These predefined angles are determined during dedicated laser table setup studies. Part of my work was to setup the laser table prior to running of the experiment. My work and the helicity correlated false asymmetries resulting from it will be discussed in Subsection 5.1.2.

### ***3.2.2 Helicity Generation and Fast Helicity Reversal***

The most important property of the beam for a parity experiment is the helicity reversal which produces the experimental asymmetry. In the Jefferson Lab polarized source, this is achieved by a pseudo-random helicity signal of 0 V and 1 V. As mentioned earlier, the helicity signal is used as the driver signal of the Pockels Cell to switch the polarization of the laser from left to right and vice versa. This change in the polarization direction causes the spin of the electrons to flip by  $180^\circ$  resulting in a helicity change. The helicity states are generated by a 30-bit pseudo-random generator (see Appendix D.4 for the algorithm) with a sequence that repeats every 50 days for a 1 kHz helicity reversal rate and a four state helicity pattern [94]. The randomness of the pattern ensures the cancellation of false asymmetries generated by background signals which can contribute in a periodical manner to the experimental signals.

The helicity signal can also induce a false asymmetry by leaking into experimental signals. In order to prevent this, the helicity generator is placed in an electrically isolated crate in the injector building and is powered by an isolated transformer. Moreover, the helicity information sent to the experiment's electronics, for recording

purposes, is delayed by a fixed number of patterns (see Figure 3.7). This was a method adopted historically by experiments running at Jefferson Lab, but to our knowledge, the benefits were never quantified. In Section 5.2, I will present my findings from a study carried out for  $Q_{\text{weak}}$  to determine the amount of false asymmetry induced by the helicity signal at the parts per billion level.

To form an asymmetry, one requires a combination of helicity states (a pattern) which can be either a pair, a quartet, an octet or a sextuplet and so on. The choice of helicity pattern is based on the desired magnitude of systematic cancellation required by an experiment. Based on various types of studies and tests [95] done prior to the experiment,  $Q_{\text{weak}}$  chose to use quartets (either  $+ - - +$  or  $- + + -$ ) with a helicity reversal rate of 960 Hz and a two pattern delay in order to suppress common mode noise coming from target boiling, power line harmonics and other noise sources.

### 3.2.3 Spin Manipulation with the Double Wien

As electrons travel through the accelerator, the spin precesses in the horizontal plane. A spin manipulation system made out of two Wien filters [96] and two solenoids (see Figure 3.8) located in the injector is used to ensure the spin orientation in the experimental hall matches the experimental requirement. The vertical Wien filter is used to rotate the spin in the vertical plane vertically up or down. The two solenoids located after the vertical Wien filter are used to rotate the spin in the transverse plane<sup>5</sup> by a  $\pm 90^\circ$ , each solenoid adding  $\approx \pm 45^\circ$  rotation. Finally, a horizontal Wien filter is used to rotate the spin in the horizontal plane with respect to the direction of motion of the electron beam.

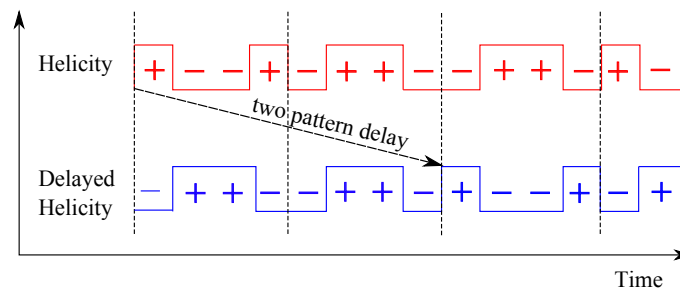


Figure 3.7: Timing diagrams of the true and delayed helicity signals. In the illustration, the helicity signal is delayed by two quartets before being sent to the data acquisition electronics.

<sup>5</sup>The plane normal to both the vertical and horizontal planes.

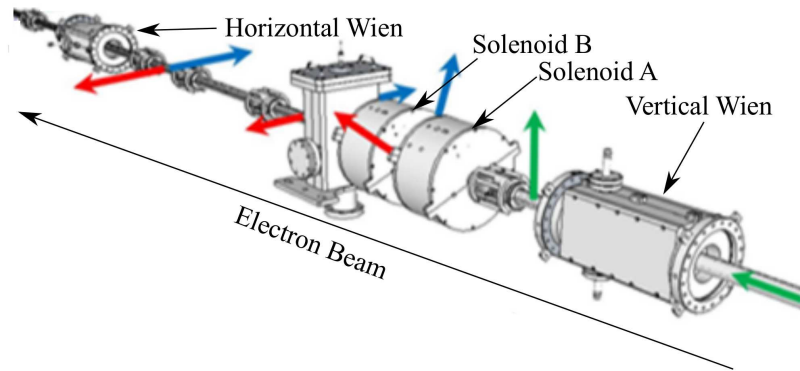


Figure 3.8: Schematic of the double Wien spin manipulating system. The incident spin orientation out of the electron gun is shown in green. Red (blue) indicates spin orientation when the solenoids are set to flip the spin to beam right (left). Figure from Ref. [97].

To get full longitudinal or full transverse polarization using this setup, the two Wien filters and the solenoids are used with appropriate pre-calibrated rotation angles. However, during the  $Q_{\text{weak}}$  experiment, using these pre-calibrated Wien angles resulted in considerably different beam properties in the beam between the left and right Wien flips. In addition, it was noted [98] during the preparations of the first transverse measurement done in February 2011, that the vertical Wien had a  $2^\circ$  offset which resulted in about 2% residual transverse polarization in the beam during the  $Q_{\text{weak}}$  commissioning period. A  $2^\circ$  to  $3^\circ$  offset is typically the uncertainty associated with the Wien angle. Considering the beam parameter goals (see Section 3.4) and the residual transverse polarization requirements of the experiment (see Chapter 7), it was deemed necessary to recalibrate both the solenoids and the Wien filters for both left and right flip settings. This recalibration was done using both the Hall C Møller polarimeter and the Mott polarimeter [99] in the injector. The Mott polarimeter measures the transverse polarization in the beam at the injector. Studies carried out using the combination of the two polarimeters provided the optimized angles shown in Table 3.3.

During the experiment, the two solenoids were used to flip the spin from left to right for time periods known as *Wiens* which spanned over several weeks. In principle, Wien flips should cancel helicity correlated false asymmetries on a longer time scale compared to the slugs (8 hour) introduced in Section 3.2.1. Since a Wien flip is carried out using a magnetic field, it potentially provides non-invasive means



Table 3.3: The Wien filter and solenoid angle settings used by the experiment. Run II longitudinal settings are from January 13th 2012. Run I vertical transverse settings are from February 8th, 2011 and Run II are from February 16th, 2012. Run II horizontal transverse settings are from February 17th, 2012. The - (+) sign in the solenoid angle indicates the electron spins are flipped to the left (right).

Configuration	Vertical (deg.)	Solenoids (deg.)	Horizontal(deg.)
Run II Longitudinal (left)	90.00	-91.95	-60.85
Run II Longitudinal (right)	90.00	+88.71	-60.85
Run I Vertical	87.10	0.00	-63.22
Run II Vertical	90.00	0.00	-60.85
Run II Horizontal	90.00	-91.95	29.15

to cancel helicity correlated false asymmetries generated by birefringence of optical elements in the laser table.

### 3.3 Beam Polarimetry

The dominant experimental systematic uncertainty to the final parity violating asymmetry measurement is expected to come from a 1% absolute error on beam polarization (see Table 3.1). To help achieve this goal, two polarimeters were used: the Hall C Møller polarimeter and the Compton polarimeter. The Hall C Møller polarimeter is able to provide accurate absolute polarization measurements but it is a low-current (about  $1\mu\text{A}$ ) invasive measurement. Therefore, for continuous beam polarization measurements at high current, the experiment also relied on the newly built Compton polarimeter.

#### 3.3.1 *Basel-Hall C Møller Polarimeter*

The Hall C Møller polarimeter [100] uses the process of  $e^- + e^- \rightarrow e^- + e^-$  (Møller scattering) to determine the polarization of the electron beam. Since this is a pure Quantum Electrodynamics (QED) process, its cross-section can be calculated accurately leading to a precision measurement of the beam polarization. Figure 3.9 shows the layout of the Hall C Møller polarimeter. The Møller polarimeter was built to measure beam polarization with an absolute precision less than 1% in 5 minutes with a 0.47% systematic uncertainty [100]. It was designed to operate with currents lower than  $8\mu\text{A}$ . During the experiment, Møller measurements were done invasively

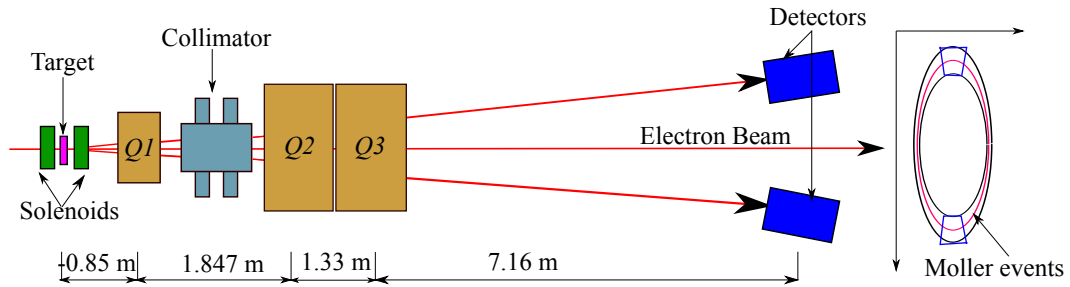


Figure 3.9: Layout of the Hall C Møller polarimeter. During the experiment, Q3 was powered off; only Q1 and Q2 were used. The plot on the right shows the scattered electron profile overlaid with the acceptance of the detectors.

at low currents ( $1\mu\text{A}$ ) three times a week. The typical longitudinal polarization measured throughout the experiment was about 88%.

### 3.3.2 Hall C Compton Polarimeter

The Hall C Compton polarimeter [101] uses the process of Compton scattering of polarized electrons from circularly polarized photons to provide two semi-independent measurements of the beam polarization. An electron detector is used to measure the asymmetry of the scattered electrons while a photon detector is used to measure the asymmetry of the back-scattered photons (see Figure 3.10). Each polarization measurement was complementary to the Møller measurements. Due to commissioning, the Compton polarimeter was only available to provide polarization measurements starting from April 2011.

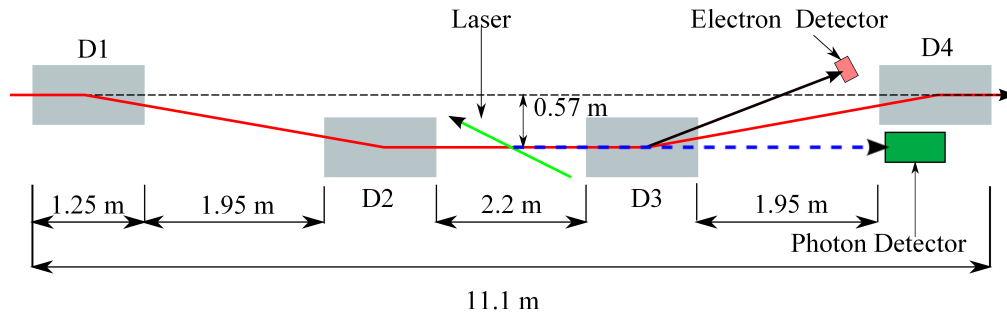


Figure 3.10: Layout of the Hall C Compton polarimeter. The electron beam is presented in red, the scattered electrons are in black and the scattered photons are in blue.

### 3.4 Electron Beam Monitoring

Helicity correlated beam parameter differences are known to generate false asymmetries into the measured asymmetries due to changes in the scattered electron profile on the detectors. In principle, knowing the beam parameter differences accurately enables experiments to remove these false asymmetries with the help of linear regression (see Subsection 6.4.3). Therefore, an accurate determination of the beam charge, position, angle and energy differences at the target was an essential part of the overall setup. For this purpose, the experiment monitored several beam monitors installed along the beamline (see Figure 3.11). The following subsections contain brief descriptions of beam monitors which were essential for the experiment.

#### 3.4.1 Beam Position

Beam position monitoring is carried out by the use of Beam Position Monitors (BPM). All the BPMs monitored by the experiment were transport style Switched

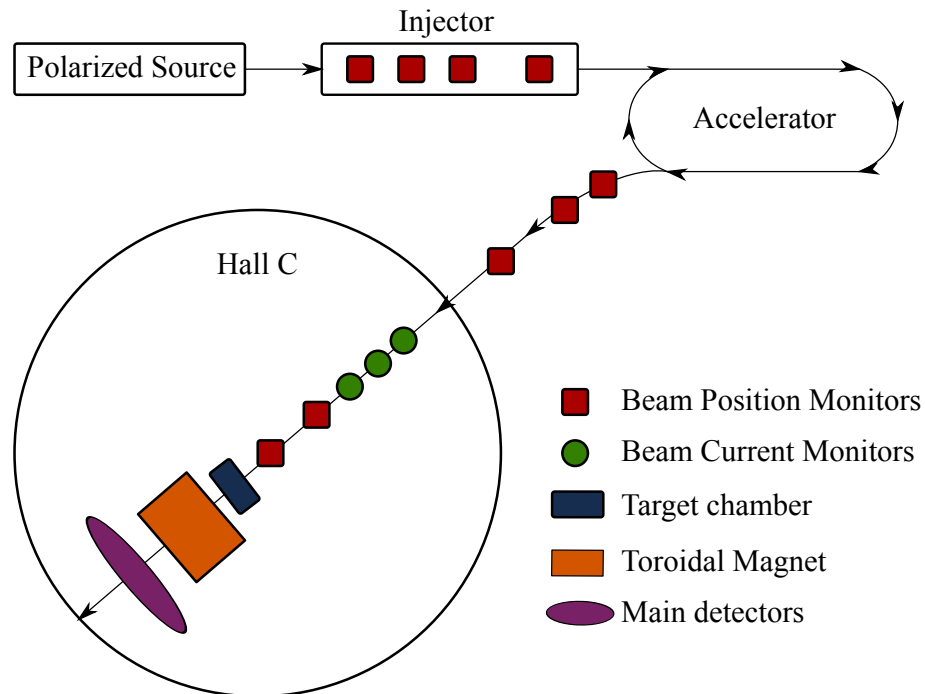


Figure 3.11: Schematic of the beamline from the polarized source to Hall C showing the types of beam monitors used during the experiment (not to scale). Also shown are the target, magnet and the main detectors for reference.

Electrode Electronics (SEE) Beam Position Monitor (BPM)s [102] out of which twenty four were located in the injector beamline and twenty three were located in the Hall C beamline. Appendix A.1 lists all BPMs used by the experiment, their location in the beamline and geometry settings. Since beam position monitoring was one of my main responsibilities, this section will contain a detailed account of the type of BPMs used by the experiment and the work done on them to meet the beam position requirements.

### 3.4.1.1 SEE Beam Position Monitors

For beam position and energy monitoring, CEBAF uses two types (SEE) BPMs [103]: the linac style and the transport style. Both are able to operate at beam intensities ranging from 50 nA up to 2 mA. In addition to regular position and energy monitoring, these devices are also used as part of a Fast Feedback System (FFB) [104] in order to suppress position and energy jitter along the beamlines leading to Hall A and Hall C.

The signal processing chain of an SEE BPM consists of a BPM canister with four-wire stripline antennas connected to the beamline, a Radio Frequency (RF) module located in the beamline tunnel, an Intermediate Frequency (IF) module and a Sample and Hold (S/H) module located in a service building 10 feet above the beamline tunnel (see Figure 3.12).

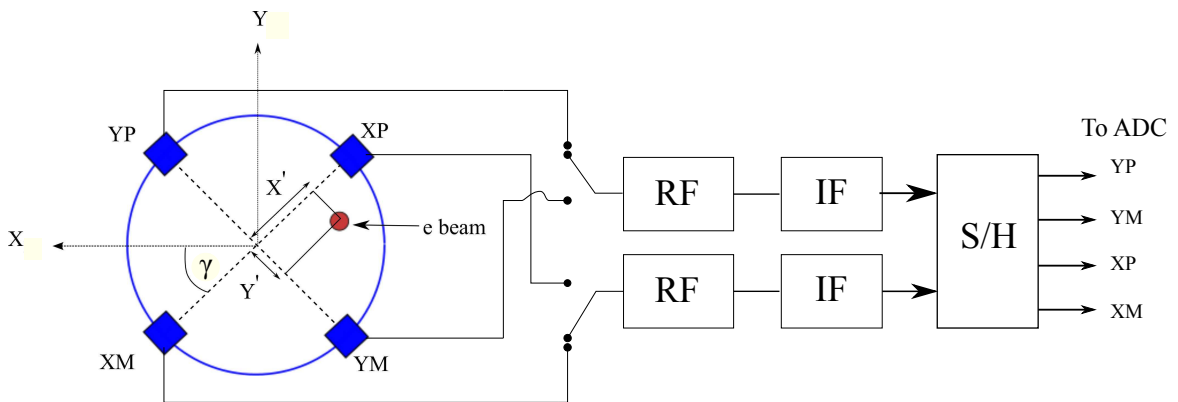


Figure 3.12: Electronics chain of the transport style SEE BPM. The blue circle represents the BPM canister with blue filled blocks representing the antennas. See text for explanation.

As the electron beam passes through the BPM, signals are induced in the four-wire stripline antennas placed transverse to the direction of motion of the beam. The amplitudes of the signals are proportional to the distance of the beam centroid from the antenna and the frequencies are the same as the electron beam frequency of 1.497 GHz. The RF module switches between the positive and negative antenna pair at a rate of 120 kHz [105] multiplexing the signals in the time-domain to generate a one-signal conditioning chain ( $X+, X-, X+, X-, \dots$  or  $Y+, Y-, Y+, Y-, \dots$ ). The use of multiplexing allows opposite antennas of X and Y to use the same RF chain thereby avoiding gain drifts which can result in faulty reported positions. The multiplexed signals are down converted from 1.497 GHz to 45 MHz before transmitting to the IF module where they are amplified with a three stage amplifier having a digitally controlled gain. The amplified signals are down converted into a baseband signal of 14.8 kHz before being sent to the S/H modules. In the S/H modules, the X and Y signals are de-multiplexed as a sequence of  $X+, Y+, X-, Y-, \dots$  signal before being transmitted to ADCs to be read out via the experiment.

During nominal operations, the IF gain system maintains the output from the IF module between 1V and 4V regardless of the beam position in what is called the auto gain mode. This avoids the input to the S/H module and the ADCs thereafter, from fluctuating beyond operational limits due to fluctuations in the beam. During BPM calibrations (see Subsection 3.4.1.4), the BPM gains are fixed at settings which are typically suitable for the range of operational currents.

### 3.4.1.2 *Beam Position Construction*

From the antenna signals digitized by the ADCs, the beam positions  $X'$  and  $Y'$  in the BPM-coordinate system are determined from [106]

$$\begin{aligned} X' &= k \left[ \frac{(XP - XP_{off}) - \alpha_X(XM - XM_{off})}{(XP - XP_{off}) + \alpha_X(XM - XM_{off})} \right], \\ Y' &= k \left[ \frac{(YP - YP_{off}) - \alpha_Y(YM - YM_{off})}{(YP - YP_{off}) + \alpha_Y(YM - YM_{off})} \right], \end{aligned} \quad (3.1)$$

where  $k$  is the conversion factor for the BPM signals to position units of millimetres and the subscript *off* indicates beam off pedestal values of the wires. The gain factors  $\alpha_X$ ,  $\alpha_Y$  take into account the difference between the positive and negative wire signals. Ideally, for an SEE type BPM,  $\alpha$  should be unity since both the positive and negative wires use the same electronics chain (see Figure 3.12). But due to

geometrical imperfections in the system, it was noted [107] that  $\alpha$  can vary from about 0.8 to 1.0 introducing an offset into the measured beam position. However, for  $Q_{\text{weak}}$ , we are only concerned about position differences. The offset introduced by the error on  $\alpha$  drops out of the difference (see Appendix A.2) without having any effect on the position difference calculations.

To avoid the distortion from synchrotron radiation present in the horizontal and vertical planes, the BPMs in the beamline are typically<sup>6</sup> rotated in the anticlockwise direction around the beam axis by an angle  $\gamma$  w.r.t the hall coordinate system. Therefore, the beam position in the hall coordinates is obtained by rotating the BPM readings using

$$X = X' \cos \gamma + Y' \sin \gamma \quad \text{and} \quad Y = X' \sin \gamma - Y' \cos \gamma. \quad (3.2)$$

Figure 3.13 shows the typical beam position constructed from a BPM in the Hall C beamline using above equations. The typical standard deviation of a reconstructed beam position is about  $10 \mu\text{m}$ . But it depends on the beam jitter and the resolution of the BPM. Since beam jitter averages over long periods of time, the BPM resolution was the limiting factor for how well the experiment was able to identify changes in the beam position.

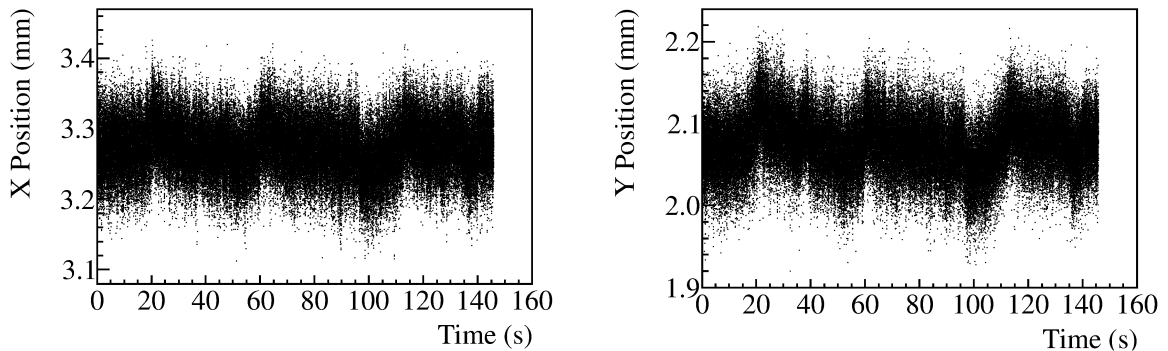


Figure 3.13: Constructed X and Y beam positions in the hall coordinates from BPM 3H07C. The jagged structure is caused by the Fast Feedback system adjusting the beam path to stabilize it. Each data point corresponds to a time interval of 1 ms.

---

<sup>6</sup>BPMs in the injector beamline are not rotated.

### 3.4.1.3 BPM Resolution

According to laboratory testing, the position resolution of a SEE BPM changes from  $1000 \mu\text{m}$  to  $10 \mu\text{m}$  for beam current changing from  $1 \mu\text{A}$  to  $100 \mu\text{A}$  [102]. Above a current of  $100 \mu\text{A}$  the resolution remains stable at  $10 \mu\text{m}$ . This behaviour is governed by the signal-to-noise ratio at the input and the output of the device [102]. The  $Q_{\text{weak}}$  experiment used several current ranging from  $26 \mu\text{A}$  for the background measurements to  $150 \mu\text{A}$  -  $180 \mu\text{A}$  for the main measurement. Therefore, it was necessary to verify the behaviour of the BPM resolution under these realistic conditions. Using selective data samples that span the two year period of the experiment, I reproduced the current dependence of the BPM resolution using the following method.

Let  $(X_1^M, Z_1)$ ,  $(X_2^M, Z_2)$  and  $(X_3^M, Z_3)$  be the measured beam position and BPM location along  $Z$  axis for three BPMs, BPM1, BPM2 and BPM3 located in the drift region<sup>7</sup> of the Hall C beamline (see Figure 3.14). Using BPM2 and BPM3, the projected beam position at BPM1 is

$$X_1^P = \left( \frac{Z_1 - Z_3}{Z_2 - Z_3} \right) X_2^M - \left( \frac{Z_1 - Z_2}{Z_2 - Z_3} \right) X_3^M. \quad (3.3)$$

If the measured beam position at BPM1 is given by  $X_1^M = X_1^T + r_1$ , where  $X_1^T$  is the true beam position and  $r_1$  is from the distribution with the standard deviation = resolution, then the difference between the measured and the projected beam position

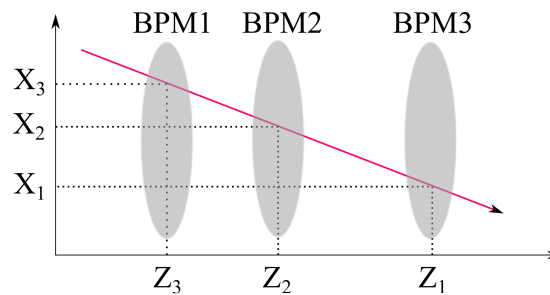


Figure 3.14: Schematic of the arrangement used to determine the resolution of BPM1 with the use of BPMs 2 and 3. The filled ellipses represent the BPM cans.

<sup>7</sup>The region of the beamline free of active elements such as dipoles and quadrupoles which are used for steering the beam. To be able to make a linear fit through the BPMs, the beam needs to be moving freely in the fit region.

is  $\delta X_1 = X_1^M - X_1^P$  and the corresponding helicity correlated difference<sup>8</sup> is

$$\begin{aligned}
d(\delta X_1) &= [(X_1^M - X_1^P)^+ - (X_1^M - X_1^P)^-] \\
&= [(X_1^{M+} - X_1^{M-}) - (X_1^{P+} - X_1^{P-})] \\
&= \left[ (\Delta X_1^T + \Delta r_1) - \left( \frac{Z_1 - Z_3}{Z_2 - Z_3} \right) (\Delta X_2^T + \Delta r_2) - \left( \frac{Z_1 - Z_2}{Z_2 - Z_3} \right) (\Delta X_3^T + \Delta r_3) \right].
\end{aligned} \tag{3.4}$$

Performing error propagation on Equation 3.4 leads to

$$\sigma_{\delta X_1}^2 = \left[ \sigma_{\Delta X_1^T}^2 + \sigma_{\Delta r_1}^2 + \left( \frac{Z_1 - Z_3}{Z_2 - Z_3} \right)^2 (\sigma_{\Delta X_2^T}^2 + \sigma_{\Delta r_2}^2) + \left( \frac{Z_1 - Z_2}{Z_2 - Z_3} \right)^2 (\sigma_{\Delta X_3^T}^2 + \sigma_{\Delta r_3}^2) \right],$$

where  $\sigma_{\Delta X_i^T}^2$  is the standard deviation of the true beam position differences at the  $i^{\text{th}}$  BPM and  $\sigma_{\Delta r_i}$  is the resolution of the  $i^{\text{th}}$  BPM.

The true helicity correlated differences in the drift region should be the same at each BPM since it is a property of the beam that does not depend on the device i.e  $\sigma_{\Delta X_1^T}^2 = \sigma_{\Delta X_2^T}^2 = \sigma_{\Delta X_3^T}^2$ . In addition, the intrinsic resolution of the three BPMs should be the same since it is a property of the device i.e  $\sigma_{\Delta r_1}^2 = \sigma_{\Delta r_2}^2 = \sigma_{\Delta r_3}^2 = R$ . Under these assumptions, Equation 3.5 reduces to

$$\sigma_{\delta X_1} = R \sqrt{1 + \left( \frac{Z_1 - Z_3}{Z_2 - Z_3} \right)^2 + \left( \frac{Z_1 - Z_2}{Z_2 - Z_3} \right)^2},$$

and the resolution of BPM1 becomes

$$R = \frac{\sigma_{\delta X_1}}{\sqrt{1 + \left( \frac{Z_1 - Z_3}{Z_2 - Z_3} \right)^2 + \left( \frac{Z_1 - Z_2}{Z_2 - Z_3} \right)^2}}. \tag{3.5}$$

For my BPM resolution analysis, I chose the BPMs in the Hall C drift region 3H07B, 3H07C and 3H09. Equation 3.5 was used to extract the resolution of 3H07B at each beam current. The measured resolutions are shown in Figure 3.15. The dependence of the measured resolution of the beam current follows an exponential behaviour which is presumably an indication of the behaviour of the signal-to-noise ratio of the device. However, my analysis shows that the resolution of the SEE BPMs

---

<sup>8</sup>Helicity correlated difference in a parameter is the difference between the positive (+) and negative (-) helicity states. Subsection 4.2.1 describes how this quantity is calculated for the Q<sub>weak</sub> experiment.



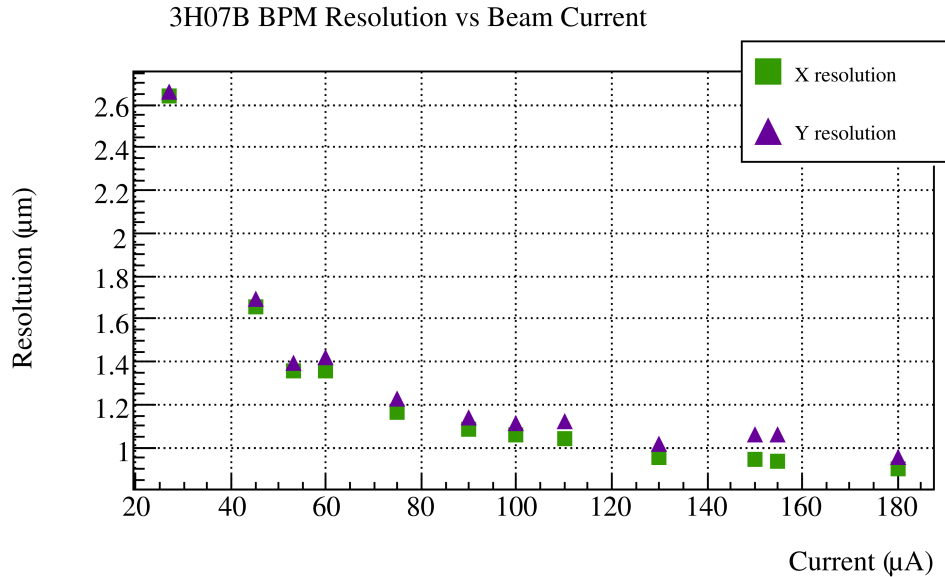


Figure 3.15: Dependence of the measured resolution of BPM3H07B on the beam current. See Appendix A.3 for the corresponding table.

above beam currents of  $100 \mu\text{A}$  are about  $1 \mu\text{m}$  compared to the  $10 \mu\text{m}$  observed in Ref. [102] under different conditions.

#### 3.4.1.4 BPM Calibrations

BPM calibrations are dedicated measurements carried out to determine the pedestals of the BPMs introduced in Equation 3.1. These pedestals are not necessarily similar to the readings of the BPM when the beam is off, due to the non-linearity of the BPM signals at low beam currents. Therefore dedicated measurements are required to determine the size of the pedestals. The pedestal are known to be stable at a few percent level (see Appendix A.4) with negligible contributions to the position differences. Therefore BPM calibrations were only carried out once at the beginning of each of the two running periods of the experiment. During calibrations, the BPMs are switched to fixed gain mode when the beam current is at its nominal value. This fixes the BPM gains enabling wire signals to increase linearly with changing current. Then the beam current is varied from a value that is 10% of the nominal beam current up to a value that is 105% of the nominal beam current. The offset of the graph of beam current vs ADC counts of each BPM wire gives the pedestals of the wires (see Figure 3.16).

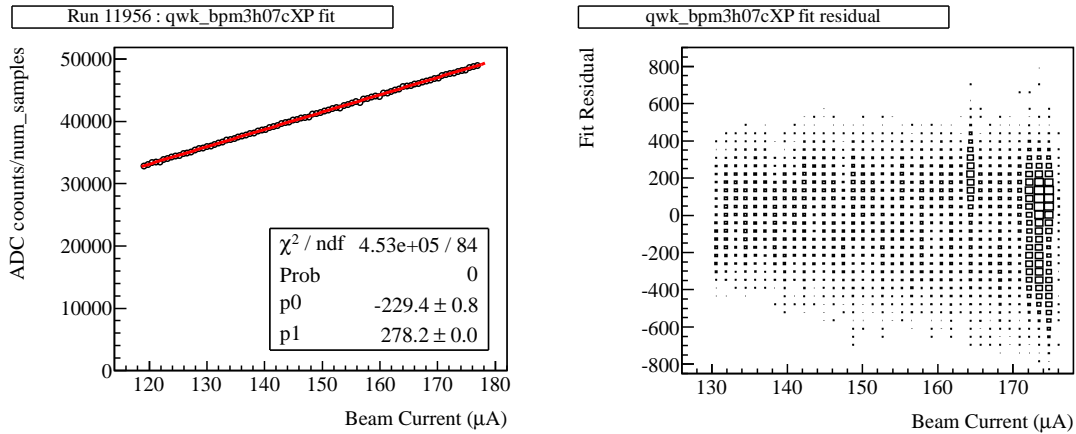


Figure 3.16: Calibration plot of BPM3H07C XP wire vs beam current (left) and fit residual plot (right) from calibration run 11956. The wire output is in units of ADC counts per num\_samples (ADC samples per second). At 960 Hz this was 464 (see Appendix D.3.1). The linear fit over the data points is shown in red. The slope of the fit is given by the parameter  $p1$  and the pedestal is given by  $p0$ . Residuals centered around zero indicate an even spread of data points in the region of  $130 \mu\text{A}$  to  $172 \mu\text{A}$ .

### 3.4.1.5 Beam Position and Angle At The Target

The last BPM in the Hall C beamline was located about 1.5 m upstream of the  $Q_{\text{weak}}$  target. Relying on position measurements from this BPM alone could have potentially introduced a displacement of the beam at the target. Therefore, the electron beam position and angle at the target were determined by an event by event linear least squares fit of the form  $\mathbf{X} = \mathbf{Z}\mathbf{a} + \mathbf{b}$  (see Appendix A.5) over a set of BPMs located in the drift region in front of the target. This allowed the incorporation of more than two BPMs to get a better position resolution while avoiding possible beam displacements at the target.

For the linear fit,  $\mathbf{a}$  and  $\mathbf{b}$  parameters were calculated separately on an event by event basis using a single weight<sup>9</sup> of 1. Then the beam positions in X and Y at the target were estimated by using

$$X_{Tgt} = aZ_{Tgt} + b. \quad (3.6)$$

Under the small angle approximation, the slope  $\mathbf{a}$  is used as the beam angle in radians.

<sup>9</sup>We can do this assumption since the resolution of the BPMs are similar.

Table 3.4 shows the list of BPMs used for this purpose and the error associated with the calculation of position and angle for beam operations at currents above  $100 \mu\text{A}$ . Figure 3.17 shows the propagation of helicity correlated beam position differences along the set of BPMs used for beam projection at target in Run II. This shows the nice agreement between the beam position differences at the target and at the BPMs.

### 3.4.1.6 Differential Non-linearity

A differential non-linearity between the BPMs used to project the beam position on the target can create angle differences which are not real. As an example, with a 100 nm helicity correlated position difference at BPM3H07A, a differential non-linearity of 10% between BPM3H07A and BPM3H09B (separated by a distance of 8945 mm) can create a false angle difference of

$$\frac{100 \text{ nm} \times 0.1}{8945 \text{ mm}} \approx 1 \text{ nrad}. \quad (3.7)$$

This is larger than the 0.2 nrad helicity correlated angle differences observed during the experiment. Using correlation plots, the differential non-linearity was seen to vary between 5% and 15% in the set of BPMs given in Table 3.4. For the proper interpretation of angle differences, an additional factor  $X/Y$  is used to remove the differential non-linearity when calculating the beam position from the four-wire signals. This modifies Equation 3.1 to  $X'' = X' \times X_{non-linear}$  and  $Y'' = Y' \times Y_{non-linear}$ . Appendix A.7 contains the method used to extract these multiplicative factors and their stability over different beam current ranges. Figure 3.18 shows the improvement in the non-linearity with the use of these new factors.

Table 3.4: BPM combinations used to determine the beam position and angle at the target and the error associated with the calculation (see Appendix A.6 for the error calculation). BPM3H09B was removed from run 14487 onwards due to malfunctioning.

Time period	BPMs combination	Error	
		Position	Angle
up to run 14486	3H07a, 3H07b, 3H07c, 3H09, 3H09B	$0.98 \mu\text{m}$	$0.13 \mu\text{rad}$
From run 14487	3H07a, 3H07b, 3H07c, 3H09	$1.72 \mu\text{m}$	$0.21 \mu\text{rad}$

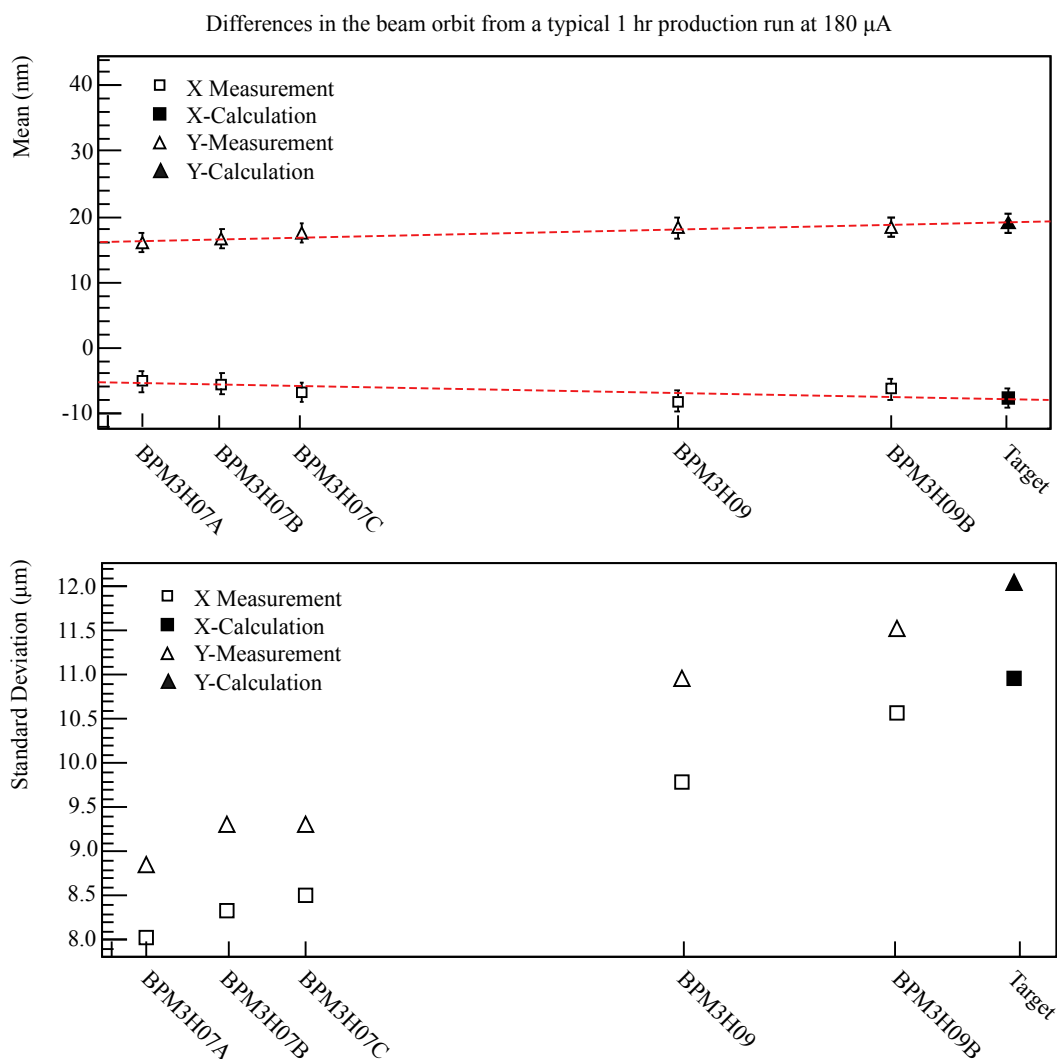


Figure 3.17: Propagation of beam position differences in the drift region up to the target. Top - X and Y position difference measurements from the five BPMs in the drift region in front of the target (open symbols). The error bars represent the  $1.0 \mu\text{m}/\sqrt{\text{quartets}}$  where  $1.0 \mu\text{m}$  is the resolution of the BPMs. Also included are the projected beam positions to the target center for a typical 1 hour long run at  $180 \mu\text{A}$  (solid symbols). The horizontal axis represents the location of the BPMs in meters along the Hall C beam line. There are 10 meters between BPM3H07A and the target. Bottom - The corresponding standard deviations from the X and Y position differences. Open and closed symbols are as in the previous plot. The slight but steady increase in the standard deviation is due to the increase in magnification as the electron beam leaves its tight focus in the upstream Compton polarimeter collision region.

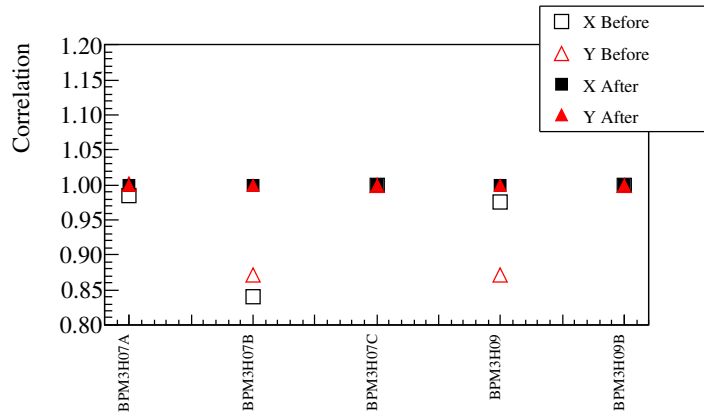


Figure 3.18: Improvements in the differential non-linearity between the BPMs before and after applying the multiplicative factors  $X_{non-linear}$  and  $Y_{non-linear}$ . The differential non-linearity which was as large as 15% in some BPMs, has dropped to an acceptable value of less than 2%. This particular dataset was taken at a beam current of  $163 \mu\text{A}$ .

### 3.4.2 Beam Current

Since the Čerenkov detector yields were charge normalized to remove charge fluctuation effects, beam current monitoring using a Beam Current Monitor (BCM) with a low noise and linear response was a high priority requirement of the experiment. The experiment used up to six RF cavity type BCMs (see Figure 3.19) which provided continuous and non-invasive measurements of the beam current. These cylindrical cavities were made out of stainless steel and were resonant in the  $\text{TM}_{010}$  mode at 1.497 GHz. BCM1 and BCM2 were the only BCMs available during the first part of the experiment. BCMs 5-8 were later built with lower noise digital receivers than BCM1 and BCM2. The new BCMs were commissioned during the first part of the experiment and were available full time during the second part.

Similar to the BPMs, the BCMs required calibrations to determine the beam off pedestals. Since the signal from the cavity is proportional to the beam current and is not an absolute measurement of the current itself, the BCMs were calibrated against an Unser [109] monitor<sup>10</sup>. An absolute current calibration was required to measure the maximum amount of charge delivered to the experiment during its active period. The Unser calibration was done once prior to the experiment while the BCM calibrations were done a couple of times during the experiment to check the stability

<sup>10</sup>The Unser monitor provides absolute calibration, but was too noisy for routine charge normalization.

of the pedestals and the linearity of the BCM signals. During these dedicated BCM calibrations, the current is varied from a 20% nominal to 105% nominal, and the measured currents from the BCMS are plotted against the readings from the Unser monitor to obtain the slopes and the offsets which give the inverse gain and the pedestal of the BCMS, respectively.

Lots of effort [108] were put into minimizing the standard deviations of the charge asymmetry distributions which can couple to the non-linearity of the BCMS and increase the standard deviation of the Čerenkov detector asymmetry distributions during charge normalization. As an example, a 500 ppm charge asymmetry width combined with a 2% BCM non-linearity increases the standard deviation of the normalized detector asymmetry by an undesirable amount of  $500 \text{ ppm} \times 0.02 = 10 \text{ ppm}$ . Therefore, the standard deviation of the charge asymmetry and the device intrinsic noise were closely monitored throughout the experiment. The standard deviation of a charge asymmetry distribution measured by a BCM depends on the

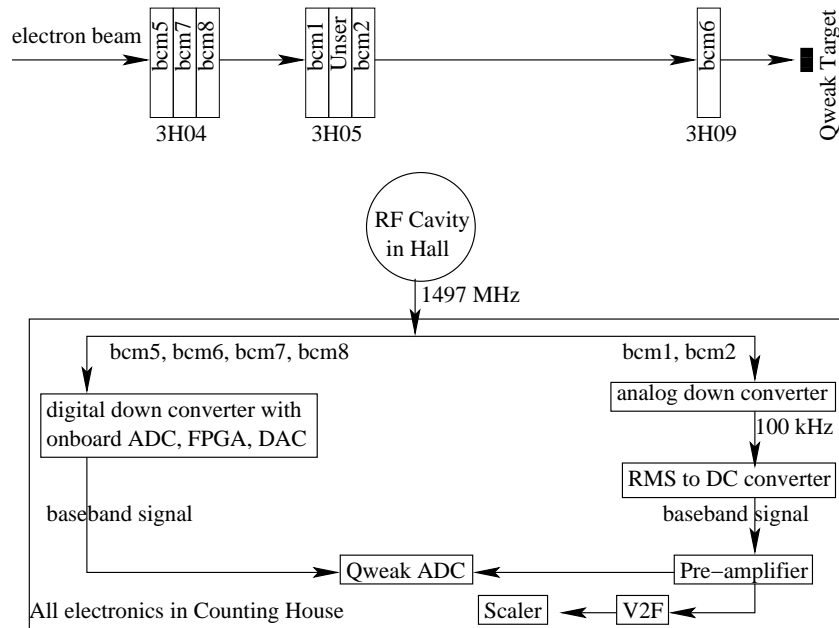


Figure 3.19: Top - BCMS used by the experiment and their locations in the beamline. Bottom - The BCM electronics chain. The resonant energy of the cavity is read out by an antenna inside the cavity generating a output signal which is proportional to the amount of charge in the beam. The output signal of 1.497 GHz is down-converted to a lower frequency of 100 KHz, filtered and converted to a DC voltage readable by the experiments custom ADCs. Figure from Ref. [108].

beam noise and the device intrinsic noise such as electronic noise. While beam noise was minimized by achieving good transmission through the accelerator, minimizing device noise required the use of low noise electronics and matching the bandwidths of all the BCMs to that of the Čerenkov detectors. The device intrinsic noise was measured by taking the difference between charge asymmetries measured by pairs of BCMs (see Figure 3.20b). BCM1 and BCM2 had a typical double difference width of about 110 ppm while BCM7 and BCM8 had a double difference width of 62 ppm. With these minimized double differences and good beam transmission, the typical standard deviation achievable through out the experiment was about 300 ppm - 500 ppm (see Figure 3.20a).

### 3.4.3 Beam Energy

Two types of beam energy measurements were required for the experiment. An absolute beam energy measurement for the initial energy of the electrons (before scattering) and the energy asymmetry measurements to remove false asymmetries generated by helicity correlated energy fluctuations.

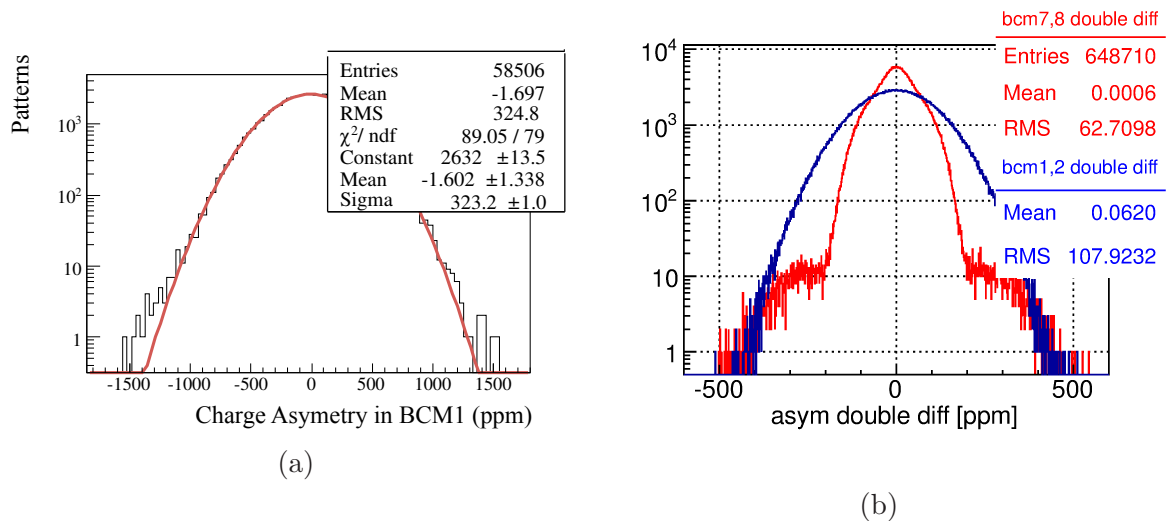


Figure 3.20: (a) Charge asymmetry measured by BCM1. (b) Double difference in BCM pair BCM1 and BCM2 and pair BCM7 and BCM8. By taking the difference, noise common to both devices (like beam related noise) cancels out leaving only the device intrinsic noise. The difference between BCM1 and BCM2 compared to 7 and 8 is in the different electronics used. Figures from Ref. [108].

### 3.4.3.1 Absolute Beam Energy

The absolute beam energy measurements were carried out by utilizing the Hall C arc beamline as a spectrometer [110]. In that case the momentum  $P$  of the beam is given by [111]

$$P = \frac{e}{\Theta} \int Bdl, \quad (3.8)$$

where  $\Theta$  is the bend angle in the arc and  $\int Bdl$  is the magnetic field integral over the electron path. During beam energy measurements, the eight 3 m long dipoles in the arc beam line are activated and the other magnetic elements (such as quadrupoles and corrector magnets) are turned off. The bend angle is then determined by measuring the beam position and direction at the entrance, middle and the exit of the Hall C arc by using three pairs of super harp-scanners [112]. The magnetic field integral is matched to the central momentum by varying the current in the set of eight magnets until the orbit is approximately centered.

### 3.4.3.2 Energy Asymmetry

The helicity correlated beam energy asymmetry was determined by using the reading of BPM3C12 located in the region of highest dispersion in the Hall C arc. The horizontal (X) beam position differences measured at BPM3C12 are sensitive to position, angle and energy differences. Therefore, using the first order beam transport matrix between BPM3C12 and the target, relative energy differences at the target can be obtained from

$$\frac{\Delta P}{P} = \frac{1}{M15} \Delta X_{3C12} - \frac{M11}{M15} \Delta X_{target} - \frac{M12}{M15} \Delta \theta_{target}^X, \quad (3.9)$$

where the subscripts indicate the beam position at 3C12/target,  $\theta_{target}^X$  represents the beam angle in X at the target and M11, M12, M15 are the transport matrix elements for beam propagation between 3C12 and the target. The OPTIM based values of the transport matrix elements used for this calculation are  $M11 = 0.69$ ,  $M12[\text{cm rad}^{-1}] = -9.28$  and  $M15[\text{cm}] = 411$  [113]. The helicity correlated difference of  $\Delta P/P$  gives the energy asymmetry  $\Delta E/E$  at the target.

However, there was often a large amount of residual dispersion at the target and coupling between X and Y positions. Therefore X differences at the target were not purely caused by beam motion in X. This made it impossible to relate X differences



at BPM3C12 to X differences at the target as given by Equation 3.9. The calculation in Equation 3.9 is only valid under the assumption that when taking helicity correlated differences, contributions coming from Y motion cancels out leaving only beam energy differences. Under this assumption, the typical energy asymmetry measured at the target was about 0.001 ppm in a 1 hour long data sample and was at the upper limit of the energy asymmetry requirement of the experiment.

### 3.5 The Primary Target

The primary Liquid Hydrogen target of the experiment was a 35 cm long target with a conical target cell (see Figure 3.21a). A longer target provided more scattering electrons per unit volume contributing to the statistics of the experiment. The conical shape of the target cell accommodated the  $7.9^\circ$  scattering angle selection. During operations, the beam was rastered [114] across a rectangular area on the surface of the upstream target window to avoid excessive heating. A  $4\text{ mm} \times 4\text{ mm}$  rastered electron beam of  $180\text{ }\mu\text{A}$  deposited about  $2120\text{ W}$  of power on the liquid volume and a  $2500\text{ W}$  of cooling power was required to remove this amount of heat load in order to prevent target warming. In addition, as shown in Figure 3.21b, the transverse flow with the unique cell design keeps a high flow of Liquid Hydrogen ( $\text{LH}_2$ ) on the target windows preventing localized target boiling. The  $\text{LH}_2$  target operated under a 35 psi pressure at 20 K with a transverse flow of  $1.2\text{ kg/s}$ . A cryogenic target pump was used

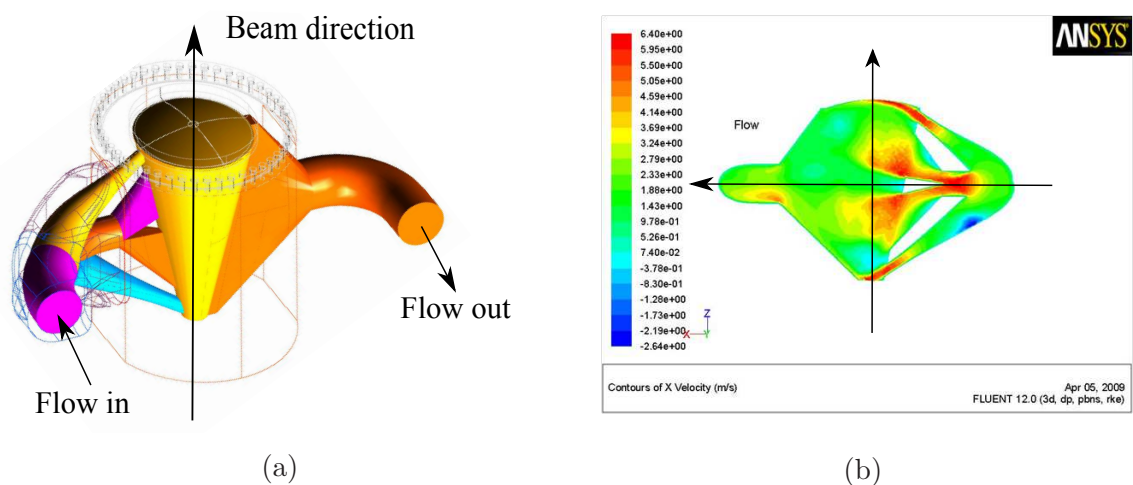


Figure 3.21: (a) Conical shaped target cell design. (b) Simulation of the velocity contours inside the cell corresponding to flow of liquid hydrogen.

to recirculate the  $\text{LH}_2$  inside the cell. A novel heat exchanger which used a mixture of a 4K and 15K coolant was used to maintain the temperature inside the target cell at a constant 20K. During beam off periods, a high power heater was used to replace the beam heat load preventing the target from freezing up. The target exit and entrance windows were made of a high strength aluminum alloy. The exit window was 0.02 inch thick with a 10 inch radius of curvature. A 0.005 inch nipple was designed in the very center of the window where beam exits the target to minimize backgrounds.

Density fluctuations which occur due to the temperature changes in the liquid Hydrogen create fluctuations in the scattered electron rates. These fluctuations which occur randomly produce additional noise in the asymmetry distribution. These are known as target noise. The  $Q_{\text{weak}}$   $\text{LH}_2$  target design requirement was to limit target noise to less than 50 ppm. With a typical  $4 \times 4 \text{ mm}^2$  raster and a  $182 \mu\text{A}$  current used during the experiment, the target noise was measured to be about 46 ppm (see Figure 3.22), well below the requirement of the experiment.

### 3.6 The Toroidal Magnet and the Collimator System

The  $Q_{\text{weak}}$  Toroidal (QTOR) Magnet was used as a magnetic spectrometer to bend and focus the elastically scattered electrons onto the Čerenkov detectors while bending away the inelastics (see Figure 3.23). During the elastic asymmetry

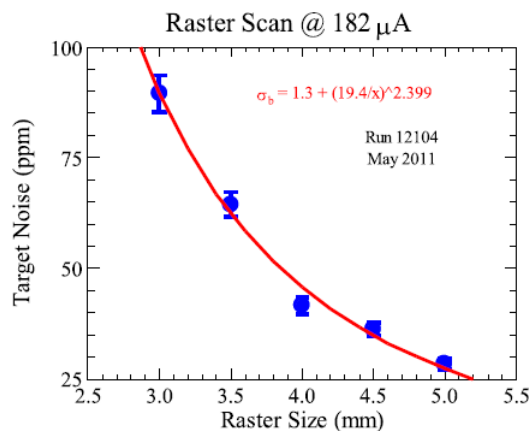


Figure 3.22: Target noise at  $182 \mu\text{A}$  as a function of raster size. Figure from Ref. [86].

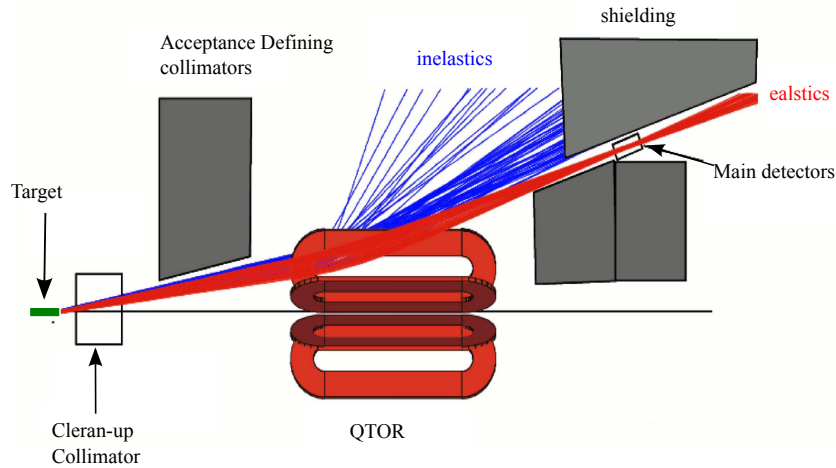


Figure 3.23: A GEANT simulation of the QTOR steering elastic and inelastic electrons. High energy elastic electrons (red) are focused onto the Čerenkov detectors while the low energy inelastic electrons (blue) are steered away from them.

measurement, the QTOR was operated at 8921 A in Run I and 8900 A in Run II<sup>11</sup>. For inelastic  $N \rightarrow \Delta$  asymmetry measurements, it was operated at 6700 A.

While the objective of the QTOR was to focus and separate elastics from the inelastics, the objective of the collimator system located upstream of the QTOR was to define the  $Q^2$  acceptance of the measurement. This was done by using a set of three lead (Pb) collimators placed between the target and the QTOR (see Figure 3.24) to select the scattered electrons with the nominal scattering angle. Collimator 2 acted as the acceptance defining collimator selecting 4% of  $\pi$  in  $\theta$  and 49% of  $2\pi$  in the azimuthal plane. The remaining two collimators acted as clean-up collimators. Each collimator had eight symmetric apertures that were designed to optimize the imaging of the elastically scattered electron envelope onto the Čerenkov detector bars at the focal plane while keeping the largest possible acceptance. The symmetry of the collimator system with the target, QTOR and the Čerenkov detector system is important when applying corrections for the beam motion sensitivities of the asymmetries.

<sup>11</sup>The difference in the settings was due to the slight decrease in the beam energy of 1159 MeV in Run I to 1156 MeV in Run II.

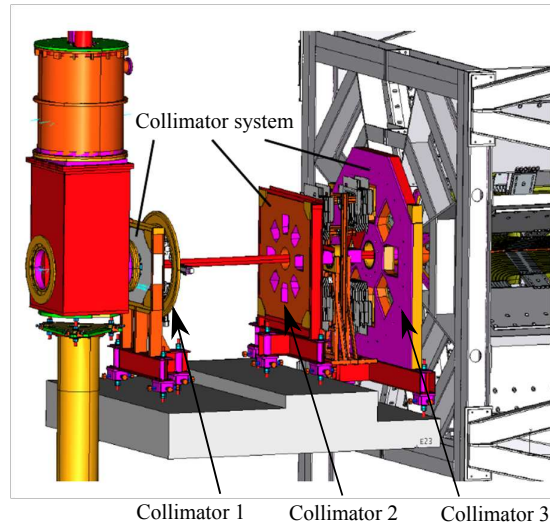
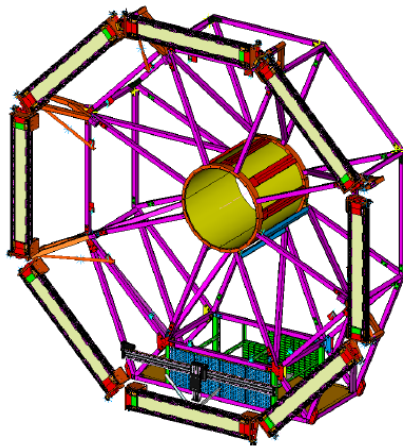


Figure 3.24: CAD drawing showing the location of the collimator system in the setup. Figure from Ref. [115].

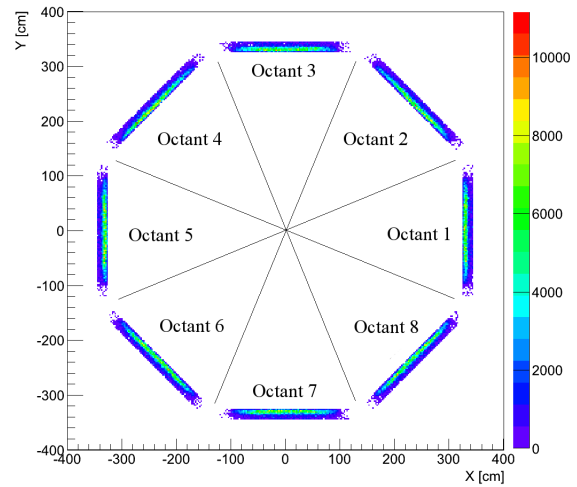
### 3.7 The Čerenkov Detector Array

The Čerenkov detector array provided efficient detection of electrons at the focal plane. It consisted of eight fused silica quartz bars placed azimuthally around the beamline as shown in Figure 3.25a. The detector material, Spectrocil 2000 [116], was chosen for its radiation hardness and low sensitivity to low energy photon backgrounds while providing the maximum number of photo electrons (pe) per scattered electron. Each bar was made out of two 100 cm long quartz pieces with an optical glue joint in the middle. A bar has an active area of 200 cm x 18 cm for detecting all of the elastic profile (see Figure 3.25b). A set of 2 cm thick lead tiles, called pre-radiators, were installed in front of each bar to reduce low energy backgrounds.

The detection of electrons via a quartz bar is done by collecting the Čerenkov light generated in the bar when an electron passes through it. The light propagates through the bar due to total internal reflections and is collected by two Photomultiplier Tubes (PMT)s connected to the either end of the quartz bar. The signals from the PMT are amplified using a custom built low noise voltage amplifier before they are sent for processing. Performance wise, due to light transportation loss, the light yield along a bar dependence on the location of the bar where electrons interact (see Figure 3.26). This required the PMTs in a single bar to be gain matched (see Appendix C). For the high current running using a 180  $\mu\text{A}$  beam, a 813 MHz electron



(a) Main detector array



(b) Scattered electron profile

Figure 3.25: (a) CAD drawing of the Čerenkov detector array mounted on the support frame. Figure from Ref. [116]. (b) A GEANT simulation showing the upstream view of the elastic electron profile on the bars. At  $180 \mu\text{A}$  current, the electron rate on a single detector is about 813 MHz. Figures from Ref. [117].

rate on a single Čerenkov detector was expected to generate an asymmetry distribution with a standard deviation of 600 ppm when digitized at 960 Hz acquisition rate. The measured asymmetries indeed show this statistical noise within  $\pm 2$  ppm fluctuations. More information on main detector design, construction and performance

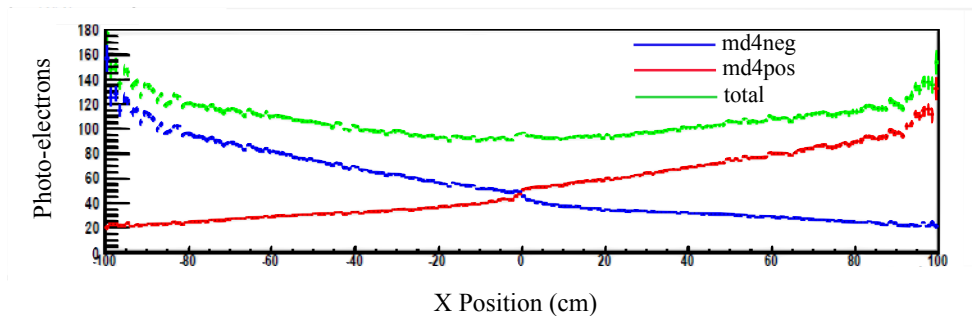


Figure 3.26: Light yield variation along the pre-radiated Čerenkov main detector 4 (md4) using tracking-mode data [116]. The signal collected at either end of the bar (negative and positive pmt) shows strong position dependence. The sum of the two PMTs is flatter. The small dip in the light yield in the middle of the bar is caused by the glue joint. Figure from Ref. [116].

can be found in the dissertation of P.Q.Wang [116].

### 3.8 Tracking Detector System

The approximate proportionality of the parity violating asymmetry to  $Q^2$  in  $Q_{\text{weak}}$  kinematics, required a 0.5% measurement of the acceptance-weighted  $Q^2$  in order to reach the proposed precision of the experiment. For this purpose, a separate detector system (tracking detector system) was used to make a dedicated measurement of the  $Q^2$  in the acceptance of the experiment using the relation

$$Q^2 = 4E_i E_f \sin^2 \frac{\theta}{2}, \quad (3.10)$$

where  $\theta$  is the scattering angle at the scattering vertex and  $E_{f/i}$  is the final/initial energy of the electron. Using the tracking data, the reconstructed  $Q^2$  of the experiment can be determined to an accuracy of 0.1% [118] More on the tracking detectors and the methodology can be found in the dissertation of Jie Pan [118].

## 4 Data Acquisition and Analysis Software

Data acquisition of the signals sent from the experimental setup is an integral part of an experiment. It provides the means to convert physical signals such as currents, voltages, rates, etc, into digitized quantities that are easier to handle and store for later analysis. As a member of the Data Acquisition (DAQ) group, a better part of my work involved building and maintaining the integrating-mode data acquisition system and the related analysis tools of the experiment. This chapter summarizes the  $Q_{\text{weak}}$  data acquisition system, analysis software, and other analysis tools development I was actively involved in.

### 4.1 The Data Acquisition System

The experiment relied on two modes of data acquisition called the *integrating-mode* and the *tracking-mode* in relation to the two modes of running introduced in Chapter 3. These were based on the CEBAF Online Data Acquisition System (CODA) [119] and were implemented as two independent systems with separate read-out electronics and analysis software.

#### 4.1.1 CEBAF Online Data Acquisition

The CEBAF Online Data Acquisition is a data acquisition toolkit designed for nuclear physics experiments at Jefferson Lab. CODA is composed of hardware and software from which a data acquisition system can be built such that it can manage acquisition, monitoring and storage of data. A typical data acquisition system is constructed using programs which are embedded in processors and have the primary function of collecting data, processing them and passing the result to an output.

Figure 4.1 shows the basic architecture of CODA [119]. The analog signals from the detectors are sent into front-end data readout modules controlled by the Readout Controllers (ROCs). A Readout Controller (ROC) has a Central Processing Unit (CPU) which uses the real time operating system VxWorks [120] for communicating with the Event Builder (EB) and other ROCs. The data transport between multiple ROCs is carried out by using commercial network hardware, such as ethernets with standard network protocols. The Event Builder (EB) collects incoming

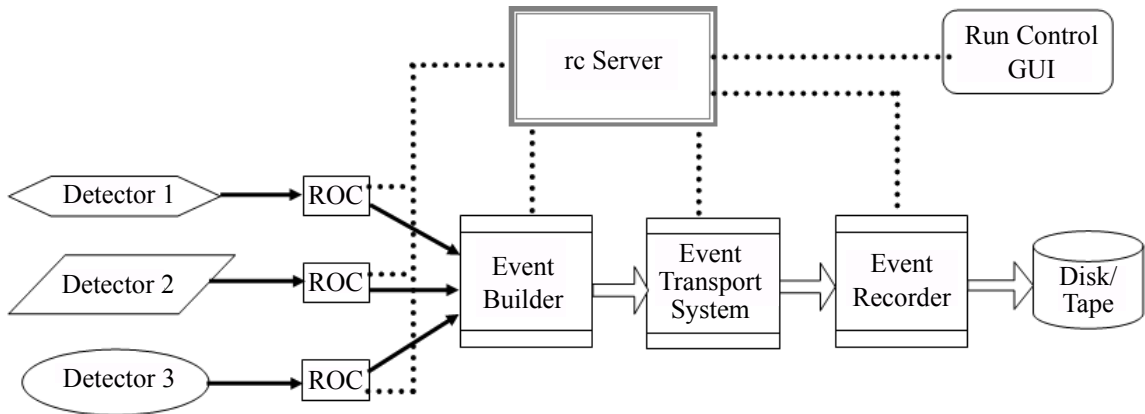


Figure 4.1: Basic architecture of CODA. See text for explanation.

data from different ROCs and group them such that data belonging to a single event appear together in the data storage file. Event data formatted in this manner are sent into the Event Transport (ET) system which permits users and analysis tools access for data filtering and monitoring purposes. An Event Recorder (ER) then writes the data onto a storage disk. The configuring and controlling of all these systems is done via a RunControl program with a graphical user interface (GUI) known as the RunControl GUI and the rcServer. The RunControl GUI provides access to various data collection operations such as run-start and run-end. At a given time, for a single rcServer, multiple copies of the RunControl GUI can be executed to control the data taking operations which is very useful for off-site DAQ monitoring and trouble-shooting.

#### 4.1.2 *Integrating-Mode DAQ*

The CODA based integrating-mode DAQ of the experiment was used for monitoring and saving data from the Čerenkov detectors, beamline monitors and other control and diagnostic devices at an optimized acquisition rate of 960 Hz. Within the 1 ms duration of a helicity window, all the information sent by the setup is read and stored in an integrating manner without any predefined event selections.

Overall, three types of data were collected and stored by the integrating mode DAQ; Detector signals, event information and configuration information. Detector signals were required for extracting physics asymmetries. These include Čerenkov detectors, luminosity monitors, BPMs and BCMs. Event information contained event number, pattern number and helicity. Configuration information is information re-



lated to the experimental setup and the injector setup such as target location, QTOR current, Wien filter settings, helicity rate etc. These were provided by the Jefferson Lab Experimental Physics and Industrial Control System (EPICS) [121, 122]. See Appendix D.1 for the full list of signals digitized by the integrating-mode DAQ. During operations, all of these channels were read out at a rate of  $5.6 \text{ MBs}^{-1}$  (see Appendix D.2 for the calculation).

#### 4.1.2.1 Layout

Figure 4.2 shows the layout of the integrating mode DAQ. The DAQ was built with readout electronic modules (see Table 4.1) mounted on VME64Bus (VersaModular Eurocard Bus) [123] crates with high speed programmable ROCs for parallel data readout. A Trigger Supervisor (TS) [124] was used to handle the triggering of the data readout and to communicate with the four ROCs used to collect data from detectors in the experimental setup, Hall C beamline and injector beamline.

The primary readout modules used by the DAQ were Analog-to-Digital Converter (ADC) modules custom built by TRIUMF [125] to perform the integration of the signals. These VME  $Q_{\text{weak}}$  (VQWK) ADC modules [126] played an important

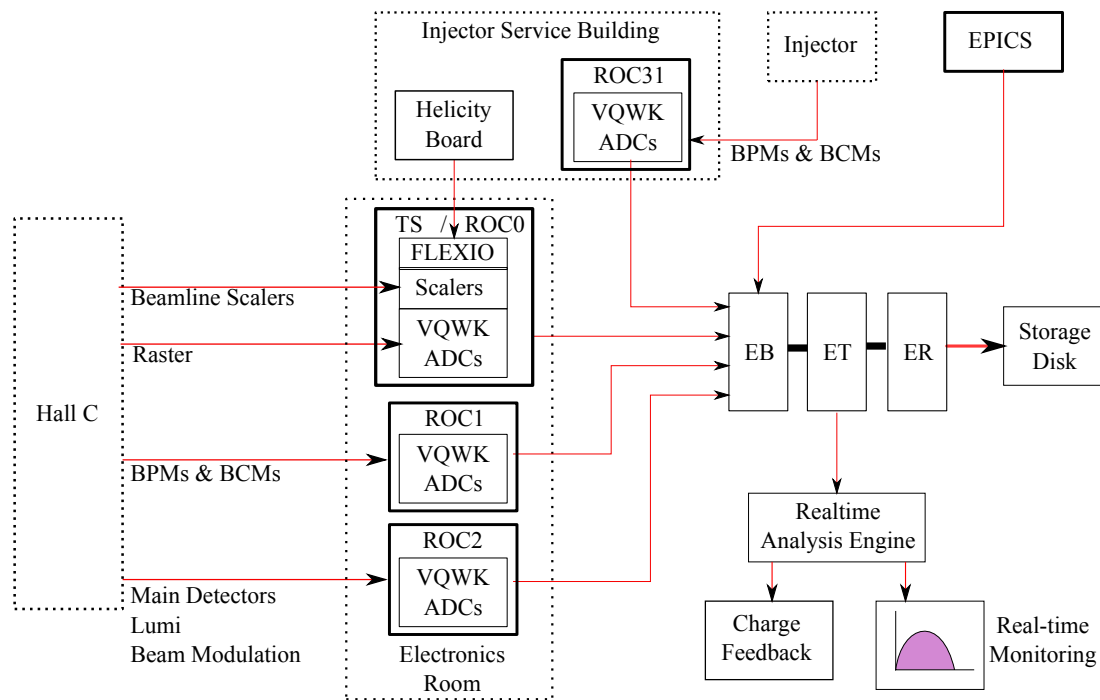


Figure 4.2: Integrating-mode DAQ layout. See text for explanation.

Table 4.1: Read-out modules used in the integrating-mode DAQ.

ROC	VQWK	Scaler
TS/ROC0	1	2
ROC1	13	-
ROC2	7	-
ROC31	12	-

role in contributing to the accuracy of the experiment. Each module has eight 18-bit AD7674 ADCs with a digitization rate of 500 kSPS (kilo samples per second). The 18-bit provide an effective 27-bit precision for digitization of analog signals within the signal range of  $\pm 10$  V with a resolution of  $76.29 \mu\text{V}$ . A signal is integrated by summing the samples within the event window. For a 960 Hz event rate, this resulted in summing over 464 samples. The samples were stored in the channel memory on First-In-First-Out (FIFO) basis to avoid data loss due to delayed read-cycles. In addition to the sum of samples within an event, the VQWK ADCs have the ability to produce the sum of the samples over four equal sub-blocks within an event. This sub-block feature of the ADCs was particularly useful for diagnostic purposes since it provided the means to observe signal variations within an event. For each event, an ADC channel stores the sum of the digitized samples, the sum of the samples in the four sub-blocks and the number of digitized samples into its registers to be read by the CPUs in the ROCs. The ADC data handling routines and VME back-end communications with the ROCs were carried out by an Altera Cyclone FPGAs.

In addition to the ADCs, beamline scalers such as Halo monitor rates were collected via SIS3801 [127] scaler module. A STR7200 [128] scaler module was used for collecting event information sent from the helicity board via Fiber Optics. These include the MPS (Macro-Pulse) signal which indicates the beginning of a new event, the pattern-sync signal which indicates the beginning of the new pattern (for  $Q_{\text{weak}}$  it was quartets or QRT) and the helicity signal which was delayed by two quartets. Configuration information from the experimental setup and the accelerator were also readout via the EPICs Input Output Controller (IOC)s.

The integrating-mode DAQ had the capability provided by CODA to view the data from different subsystems in real-time. This was done by setting up a version of the  $Q_{\text{weak}}$  analyzer (see Subsection 4.2.1) known as the real-time analysis engine with selected functions to perform the analysis of selected subsystems such as the

Čerenkov detectors and the beamline devices. The real-time analysis engine was capable of producing analysed detector asymmetries, beam position differences, charge asymmetry which were some of the critical diagnostic parameters of the experiment.

#### 4.1.2.2 Triggering

The integrating-mode DAQ was triggered by the MPS signal which indicates the beginning of a new helicity state. The MPS signal consists of a  $T_{Stable}$  period and a  $T_{Settle}$  period (see Figure 4.3). The  $T_{Settle}$  period is the time required by the high voltage of the Pockels cell to complete transitioning from positive to negative or vice versa during a helicity flip. During this transition period, the fluctuations in the Pockels cell crystal can result in 3% to 5% residual linear polarization in the beam. Therefore it is necessary to provide a settling time for the system during which the signals from the detectors should be ignored. The signals from the detectors are only collected within the  $T_{Stable}$  time. The transition to  $T_{Stable}$  from the  $T_{Settle}$  time occurs

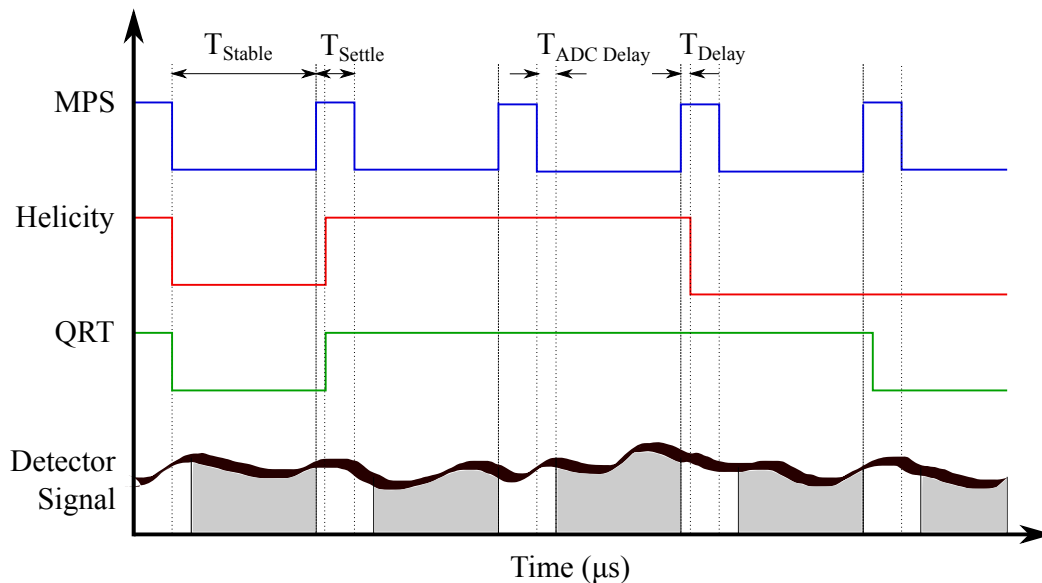


Figure 4.3: Triggering and readout timing diagram of the integrating-mode DAQ. The ADCs were triggered by the MPS signal. At the 960 Hz event rate,  $T_{Stable} = 70 \mu s$  and  $T_{Settle} = 971.67 \mu s$  are set by the helicity board.  $T_{Settle}$  transition occurs  $T_{Delay} = 1 \mu s$  ahead of the QRT and helicity signals to allow the DAQ to prepare to receive the next event. A delay of  $T_{ADC\ Delay} = 42.5 \mu s$  allowed the ADCs to prepare for data acquisition after detecting the new event. The shaded area in the detector signal indicates the signal region digitized by the ADCs.

1  $\mu\text{s}$  ahead of the QRT and the helicity signal. The ADCs required an additional delay of 43.5  $\mu\text{s}$  (see Appendix D.3.1) to prepare for data acquisition. With these time settings, at the 960 Hz event rate, 99.9% of the experiment's signals within the  $T_{\text{Stable}}$  period were readout by the ADCs and scalers in the integrating-mode DAQ.

### 4.1.3 Tracking-Mode DAQ

The tracking-mode DAQ was implemented for collecting signals from the tracking detectors, horizontal and vertical drift chambers, trigger scintillator, quartz scanner, the Čerenkov detectors and two spare scintillator detectors. All these detectors were readout via QDCs (Charge-to-Digital Converters), TDCs (Time-to-Digital Converters) and scalers. The tracking-mode DAQ hosted the capability to handle multiple triggers generated by the trigger scintillator, Čerenkov detectors and the scanner as individual triggers or combination of triggers simultaneously. At each trigger, which is a voltage pulse indicating the interaction of a particle with the detector volume, the data from the QDCs, TDCs and scalers are readout and stored in CODA files. These data carry information about the location of the electron interaction in the detector volume and the event rates on the detector which can be used to track individual electrons through the setup for the  $Q^2$  measurement. A detailed description of the tracking-mode DAQ layout and triggers can be found in the dissertation of Rakitha Beminiwattha [41].

## 4.2 QwAnalysis Software

The QwAnalysis ( $Q_{\text{weak}}$  Analysis) is the data analysis framework used by the  $Q_{\text{weak}}$  Collaboration for processing digitized signals into physical quantities, such as detector yields. It is an object-oriented application software framework written in C++ utilizing multiple-inheritance, polymorphism, encapsulation and abstraction features of the language to carry out the analysis of the experiment's 270+ data channels in a robust manner. The analyzed data are stored into CERN ROOT [129] and MySQL [130] structures for later use.

Even though the CODA decoding routines for data from the integrating-mode and tracking-mode detectors are similar, their end results are very different. As an example, the integrating-mode data from the Čerenkov detectors provide asymmetries while the tracking-mode data from drift chambers provide timing information related to electrons passing through the chambers. Due to this difference, integrating-mode

and tracking-mode data are analysed using separate analysis modules, the Parity Analysis Engine (QwParity) and the Tracking Analysis Engine (QwTracking).

Figure 4.4 shows the class inheritance diagram of the QwAnalysis outlining the parity analysis and tracking analysis classes. All subsystems in the QwAnalysis inherit from the abstract base class `VQwSubsystem` which defines the routines required for data decoding, analysing and storage. The analysis routines specific for parity and tracking data are defined in the virtual classes `VQwSubsystemParity` and `VQwSubsystemTracking` which are the base classes of the relevant subsystems such as `QwBeamline` and `QwDriftchamber`. Some subsystems, such as `QwScanner`, inherit from both base classes. The inheriting classes are responsible for actually performing the data decoding and analysis according to their specific requirements. As an example, the `QwBeamline` class is responsible for retrieving beam position information, such as beam current and position from the classes `QwBCM` and `QwBPMStripline`, and writing them to ROOT trees. The `QwHelicity` class on the other hand is responsible for decoding event information such as helicity, event number, pattern number, and for forming asymmetries and differences and storing them into ROOT trees.

Whereas the `VQwSubsystem` is responsible for managing the data and analysis routines, the `VQwDataElement` is an abstract base class which is responsible for defining the operations (sum,difference, ratio, etc) required to carry out the analysis. For example, adding data from two VQWK ADCs, say BCM1 and BCM2, requires summing over six data words<sup>1</sup>. Adding two scalers on the other-hand required summing of a only a single data word. Therefore, depending on the readout module, `VQwDataElement` and its inheriting classes define appropriate operations required to calculate signal asymmetries, differences and yields. Together, the `VQwSubsystem` and the `VQwDataElement` and their inheriting classes provide the analysis flow of the parity analysis and the tracking analysis engines described in the following subsections.

#### 4.2.1 Parity Analysis Engine

The parity analysis Engine is responsible for processing raw data to extract event based and pattern based detector yields, differences and asymmetries. I was involved in the development of the parity analysis engine therefore this section will contain a somewhat detailed explanation of its functionality.

Figure 4.5 shows the simplified flowchart of the parity analysis engine. At the

---

<sup>1</sup>The sum of the digitized samples in the event, individual sum of the four sub-blocks and the number of digitized samples per-block.

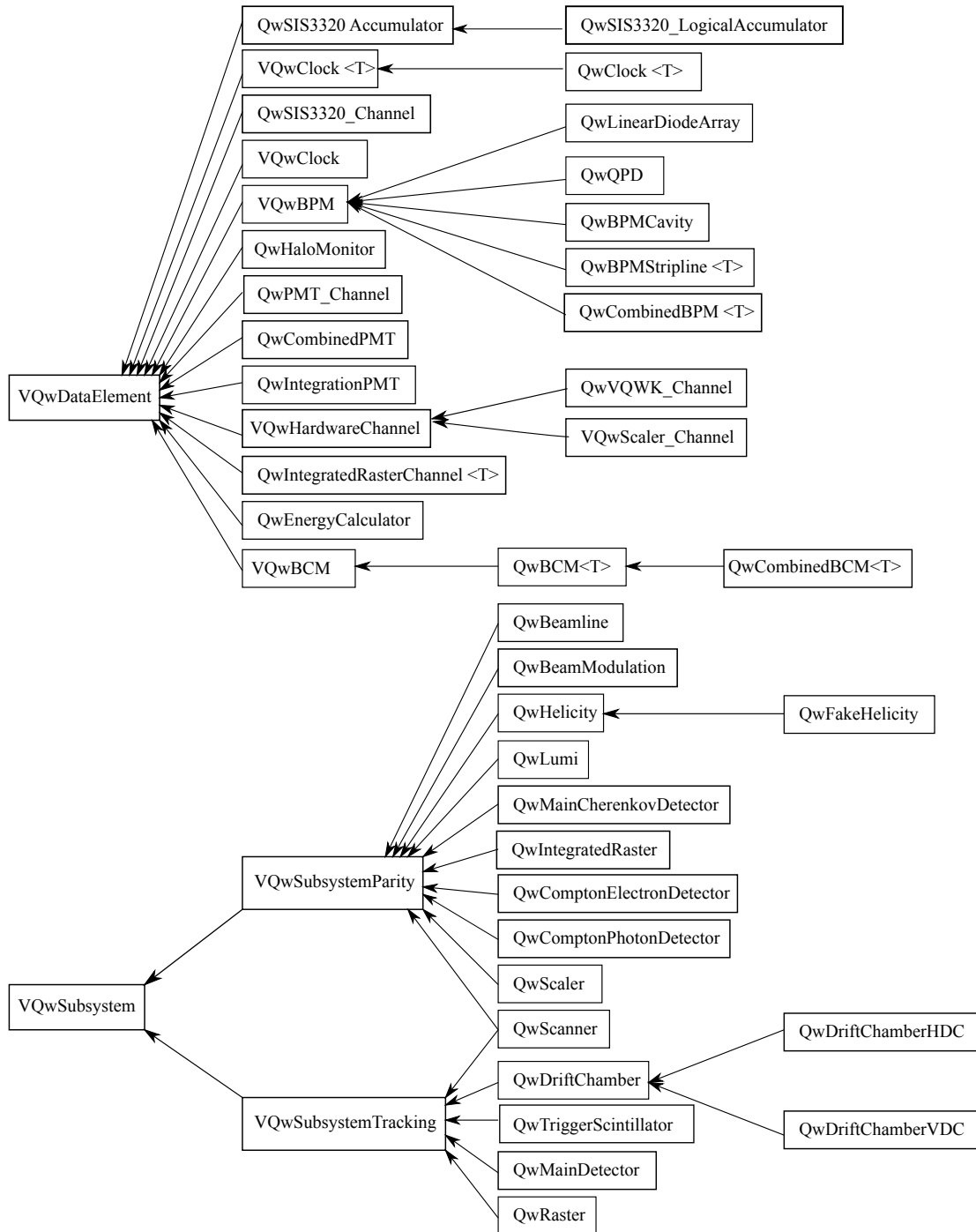


Figure 4.4: Main class inheritance diagram of the QwAnalysis outlining the classes used for parity and tracking analysis. Shown only are the classes relevant for the material discussed in this dissertation. See Ref. [131] for the full class hierarchy.  $\langle T \rangle$  denote template classes which define common set of functions to handle different types of data such as scaler type or ADC channel type. See text for explanation.

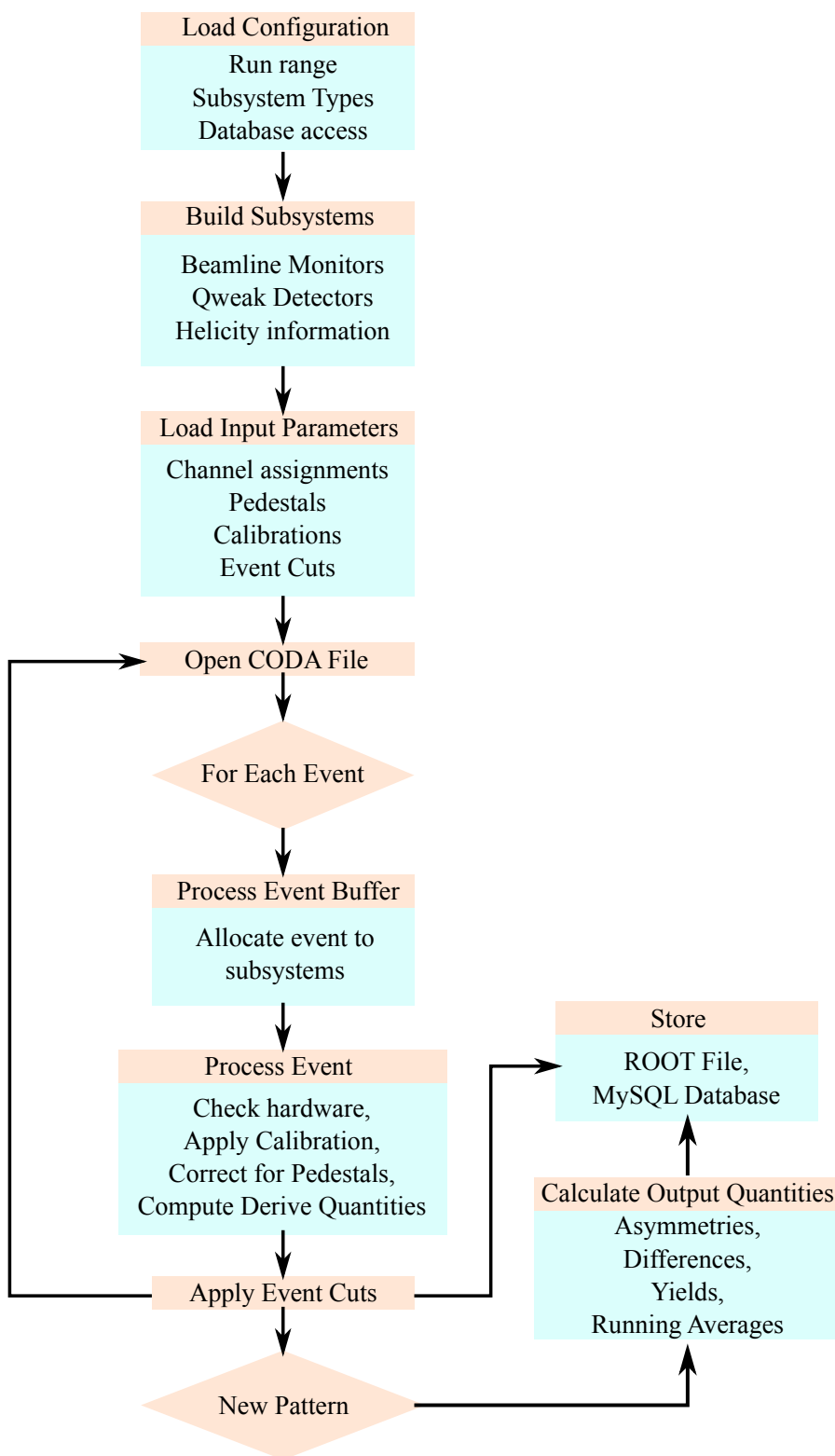


Figure 4.5: Simplified flow chart of the QwAnalysis parity analysis engine.

beginning of an analysis, the analyzer reads a set of configuration information about the particular run such as the run number, run type, detector subsystems, database access etc. These configuration information allow the analyzer to identify special data types with different analysis requirements and perform the analysis accordingly. As an example, a BPM calibration run will only need the analysis routines in the Qw-Beamline subsystem and it does not need to be written into the database<sup>2</sup>. Setting the appropriate configuration allows the analysis of a BPM calibration to be performed faster. Once the configurations are read in, subsystem objects are created to handle data processing of each group of instruments used. In the next step, configuration information of the DAQ, such as channel assignments in the ROCs, calibration factors, detector pedestals, event cuts and histogram parameters (names, ranges, etc) are read in. After loading the input parameters, the CODA file is opened and for each event, all the information is read and allocated to the relevant subsystems. The parts of the CODA event belonging to different detectors are processed by each detector subsystem object separately by first checking for hardware failures and then applying calibration factors and correcting for pedestals. Derived quantities such as beam position at the target, average charge, sum of all the main detector PMTs, etc, are also calculated during this step.

Events processed in this manner are then checked for predefined set of data qualities or event cuts [132]. Each detector subsystem has its own set of event cuts. For example, the beamline subsystem checks for low beam currents (lower event cut), beam trips and saturation of the BPMs (upper event cut). Typically, the event cuts used during the first analysis of the data, which took place parallel to data taking, were flexible. This was done intentionally to understand the behaviour of the experimental setup (beam parameters, etc). With the knowledge of the first analysis, the event cuts used in the next analysis cycles (or passes) are tightened up such that only events that meet certain set of requirements are passed for the final asymmetry analysis.

Table 4.2 shows the event cuts used in the parity analysis engine of QwAnalysis software version 3.04, which was used for the pass-five analysis of the data presented in this dissertation. A lower current cut of  $100 \mu\text{A}$  was required<sup>3</sup> to remove low current beam which were seen [41] to shift the Čerenkov detector asymmetries in a non-statistical way. The upper event cut on the BPM wires removes saturation which

---

<sup>2</sup>The database only contains information relevant for parity asymmetry analysis.

<sup>3</sup>For aluminum running at a  $70\mu\text{A}$  beam current, this limit was lowered to  $50\mu\text{A}$ .



Table 4.2: Event selection criteria used in the parity analysis engine of QwAnalysis software version 3.04.

Parameter	Bounds	Stability
Beam Current (qwk_charge)	$> 100 \mu A$	$2 \mu A$
BPM wire signals (all BPMs)	$> 0.7 \text{ V}$ and $< \approx 7\text{V}$	–
Beam position (all BPMs)	within $\pm 10 \text{ mm}$	–
Beam position at the target (qwk_target)	within $\pm 10 \text{ mm}$	0.15 mm
Main detector 1 and 7 barsums	$< 0.05 \text{ V}/\mu A$	$0.0001 \text{ V}/\mu A$
Main detector PMT adc counts	$\pm 1000000$	-
Main detector barsums adc counts	$\pm 1000000$	–
Background detectors adc counts	$\pm 1000000$	–

occurs during beam ramps and can cause false beam angles at the target. The lower event cut on the BPMs is used to remove events where a BPM can malfunction and produce noise which can be mistaken as position information. The upper and lower bounds on the Čerenkov detector PMTs, sum of the PMTs (barsum) and background detectors are used as a precautionary measure to remove non-physical signals that can be generated due to hardware failures or software failures<sup>4</sup>. The stability cuts remove sudden beam fluctuations which can generate non-physical responses in the detectors. These are applied to the standard deviation of the signal distributions and they are based on the values typically observed during the data taking period.

All events which fail event cuts are flagged with an error code which carries information about the detector name and the failed event cut type (lower or upper). These error codes are later stored as a device specific error code which can be used to select usable events for the final analysis. Events which pass data and hardware quality checks are then tested for the correct pattern number, event sequence and helicity pattern. A set of internal counters compare the information on MPS, QRT and delayed helicity to determine if the event has the correct event number and pattern number. A discrepancy between the internal counters and the signals can arise due to counter malfunction in the helicity generator. This happens rarely but as a precaution, the checks applied on the event information provide the means to properly match the events to the correct helicity. The true helicity pattern is generated inside the analyzer (see Appendix D.4) using the same 30-bit pseudo-random generator used in the injector. This was required because the DAQ only records the delayed

<sup>4</sup>Such as using wrong pedestals and/or gain factors

helicity signal and not the true helicity signal. By knowing the pattern delay in the delayed helicity signal sequence, one can predict the true helicity of the events. Both the delayed-helicity and the actual-helicity are stored in the rootfile for diagnostic purposes. Events which pass the event and pattern number checks are grouped into patterns of four events, known as quartets and the pattern based asymmetries, differences and yields are computed as shown in Table 4.3. Additionally, for diagnostic purposes, there are several options (see Table 4.4 and Table 4.5) available to form the asymmetries and yields from the individual Čerenkov detectors and the full detector array. For all the pattern based asymmetries, yields and differences calculated from different detectors and beam monitors, a running average, a running sum and the error on the running average are also calculated in parallel using an algorithm developed by the Sandia National Laboratories [133] for statistical moment calculations of large scale data sets.

During the final step of the analysis process, the analyzer saves the event based and pattern based processed data into a set of pre-defined histograms and ROOT trees. Event based yields are saved into the Mps\_Tree and pattern based asymmetries, average yields and the differences are saved into the Hel\_Tree. In addition, event based EPICs values are stored into a ROOT tree named Slow\_Tree. For diagnostics and quality checks, the configuration used by the analyzer and its version are also stored into the rootfile. Finally, the running averages, running sums, errors on the running averages and the slow control values (QTOR current, target position, etc.) read in via EPICS are written into the MySQL databases.

Table 4.3: Pattern based formation of asymmetries, differences and yields. The subscripts indicate the event sequence in a quartet pattern defined as 1,2,3,4 with helicity + - - +. The physical quantities are  $D_{14}$  and  $A_{14}$  and the rest of the combinations are used for diagnostic purposes. The ROOT stems are the file stems used to store the variables in the rootfiles. Detector list contains the type of detectors which have these quantities calculated and stored in the rootfiles.

Quantity	Equation	ROOT Stem	Detector
Differences	$D_{14} = \frac{(Y_1^+ + Y_4^+) - (Y_2^- + Y_3^-)}{2}$	diff_	BPMs, Combined BPMs, Energy calculator
	$D_{12} = \frac{(Y_1^+ + Y_2^-) - (Y_3^- + Y_4^+)}{2}$	diff1_	
	$D_{13} = \frac{(Y_1^+ + Y_3^-) - (Y_2^- + Y_4^+)}{2}$	diff2_	
Yields	$Y = \frac{(Y_1^+ + Y_4^+) + (Y_2^- + Y_3^-)}{2}$	yield_	All the detectors
Asymmetry	$A_{14} = \frac{(Y_1^+ + Y_4^+) - (Y_2^- + Y_3^-)}{(Y_1^+ + Y_4^+) + (Y_2^- + Y_3^-)}$	asym_	PMTs, Lumis, BCMs, BPM effective charge
	$A_{12} = \frac{(Y_1^+ + Y_2^-) - (Y_3^- + Y_4^+)}{(Y_1^+ + Y_2^-) + (Y_3^- + Y_4^+)}$	asym1_	
	$A_{13} = \frac{(Y_1^+ + Y_3^-) - (Y_2^- + Y_4^+)}{(Y_1^+ + Y_3^-) + (Y_2^- + Y_4^+)}$	asym2_	

Table 4.4: Options available to form the asymmetry from a single Čerenkov detector. Yield based which uses the yields of the left/right PMTs ( $Y_{L/R}$ ) or the asymmetry based which uses the asymmetry of the left/right PMTs ( $A_{L/R}$ ).  $W_{L/R}$  represents the weights of the two PMT's which is the  $1/Y_{L/R}$  from a stable run and it is used to equalize the left and right PMT yields by removing gain mismatches. See Appendix C for the weights estimations for the transverse running period.

Quantity	Yield and Asymmetry
barsum	$Y_{barsum} = \frac{W_L Y_L + W_R Y_R}{W_L + W_R} \rightarrow A_{barsum}$ calculated using yields as shown in table 4.3.
pmtavg	$A_{pmtavg} = \frac{1}{2} (A_L + A_R)$ where $A_{L/R}$ is calculated from PMT yields as shown in table 4.3.

Table 4.5: Options available to form the asymmetry from the full Čerenkov detector array using either yields, weighted yields of left/right PMTs ( $Y_{L/R}$ ) or the average asymmetry of the left/right PMTs ( $A_{L/R}$ ).

Quantity	Yield and Asymmetry
mdallbars	$Y_{allbars} = \frac{1}{8} \sum_i Y_{barsum}^i \rightarrow A_{allbars}$ is calculated using yields as shown in Table 4.3
mdallbarsavg	$A_{barsavg} = \frac{1}{8} \sum_i A_{barsum}^i$
mdallpmtavg	$Y_{pmtavg} = \frac{1}{16} \sum_i (Y_L^i + Y_R^i) \rightarrow A_{allpmtavg}$ is calculated using yields as shown in Table 4.3

## 5 False Asymmetries and Random Noise

False asymmetries generated by background physics processes, helicity correlated beam asymmetries, and the leakage of helicity control signals potentially could change the asymmetry measured by the  $Q_{\text{weak}}$  experiment. On the other hand, random noise generated by electronics and target boiling could increase the standard deviation of the asymmetry distribution decreasing the precision of the experiment. Therefore, in order to reach the goal of a 4% measurement of the weak charge of the proton, it was important to minimize contributions from both false asymmetries and random noise. I was part of the group of  $Q_{\text{weak}}$  collaborators who worked with the Jefferson Lab polarized electron source group to control the sources of helicity correlated changes in electron beam properties. In addition, I performed the first measurement of the helicity leakage on the  $Q_{\text{weak}}$  DAQ setup at the part per billion level, and determined the random noise content in the Čerenkov detector electronics. This chapter contains a discussion of these studies.

### 5.1 Helicity Correlated Beam Asymmetries

Helicity correlated beam asymmetries (HCBA) are generated by the differences in beam properties between the left and right helicity states. These originate at the polarized electron source due to various effects which will be shortly discussed in Subsection 5.1.1. Table 5.1 shows the beam parameters which generate HCBA and

Table 5.1: Specifications on the helicity correlated beam asymmetries and differences for the full  $Q_{\text{weak}}$  data set. With these limits, the HCBA contribution to the final parity violating asymmetry is expected to be 0.5% assuming the sensitivities given in Ref. [84].

Beam Parameter	Max. run-averaged helicity correlated value (2544 hours)	Max. noise during a quartet (4 ms)
Position Differences	$\langle \Delta X \rangle < 2 \text{ nm}$	$7 \mu\text{m}$
Angle Differences	$\langle \Delta \theta \rangle < 30 \text{ nrad}$	$100 \mu\text{rad}$
Charge Asymmetry	$A_Q < 0.1 \text{ ppm}$	$< 300 \text{ ppm}$
Energy Asymmetry	$\Delta E/E \leq 0.001 \text{ ppm}$	$\leq 3 \text{ ppm}$

the specifications set on their values to limit the relative contribution to the final  $Q_{\text{weak}}$  parity violating asymmetry to 0.5%. Starting with the sources of HCBA, the following subsections will discuss the techniques used by the experiment to reach the goals shown in Table 5.1. I will also summarize the work done at the polarized source to minimize HCBA during the commissioning period and the beginning of Run I (from September 2010 to February 2011), during which I was actively involved with the polarized source setup work.

### 5.1.1 Sources of HCBA

As mentioned in the previous section, correlations of the electron beam properties with the helicity signal is generated at the polarized source. This is due to the different responses of the optical properties of elements in the laser table and of the photocathode to the polarization state of the laser beam. Following is a brief discussion of the known sources of HCBA.

#### 5.1.1.1 Residual Linear Polarization

The coupling of residual linear polarization in the laser beam with the optical properties of elements in the laser table and the photocathode is the dominant cause of helicity correlated beam parameters. Residual linear polarization in the laser beam arises when converting linear polarization to circular polarization using the Pockels cell (PC).

According to Ref. [134], the phase shift  $\omega$  induced by the Pockels cell to convert linear polarization to circular polarization can be parametrized by the two parameters  $\alpha$  and  $\Delta$  which take into account the difference between a perfect  $90^\circ$  phase shift and the applied phase shift,

$$\omega_+ = -\left(\frac{\pi}{2} + \alpha\right) - \Delta \quad \text{and} \quad \omega_- = +\left(\frac{\pi}{2} + \alpha\right) - \Delta, \quad (5.1)$$

where  $\omega_+(\omega_-)$  is the phase shift for positive (negative) helicity. Both non-zero  $\alpha$  and  $\Delta$  represent contributions from residual linear polarization. However, residual linear polarization from a non-zero  $\alpha$  contributes with opposite sign to both helicity states while residual linear polarization from a non-zero  $\Delta$  contributes with the same sign to the two states. This results in polarization ellipses for the two helicity states which

are  $90^0$  out of phase with each other. The  $\alpha$  phase depends on the birefringence<sup>1</sup> of the PC and can be adjusted by selecting an appropriate voltage difference between the electrodes (see subsection 5.1.2). But the  $\Delta$  phase represents phase contributions coming from any birefringent object in the optic transport line including the Pockels cell itself, and the stressed vacuum windows between the photocathode and the laser table enclosure. The method used to adjust the  $\Delta$  phase will be described in Subsection 5.1.2.

### ***5.1.1.2 Optical Analysing Power***

An optical element is said to have an analysing power when one polarization state is transmitted with better efficiency than the others. This is a result of the transmission axis of linear polarization in one helicity state aligning with the high efficiency transmission axis of the optical element. It generates an asymmetry in the laser light intensity between the two helicity states which are known as Polarization Induced Transport Asymmetries (PITA) [135]. PITA can be controlled by adjusting the Pockels cell voltages as described in Section 5.1.2. Optical elements in the laser table after the Pockels cell also possess an analysing power and can contribute a PITA asymmetry.

### ***5.1.1.3 Photocathode Analysing Power***

In addition to the analysing power of the optical elements in the laser table, the photocathode crystal has a Quantum Efficiency (QE) analysing power. When polarization ellipses are incident on the photocathode with their major axis parallel to the analysing power, they will generate more charge in one helicity state than the other state (see Figure 5.1 a). The charge difference in the two states then creates a helicity correlated charge asymmetry. This type of charge asymmetry, generated by the coupling of the residual linear polarization to the analysing power of the photocathode, can be minimized by rotating the polarization ellipses (see Figure 5.1 b).

---

<sup>1</sup>Refractive index that depends on polarization and the direction of propagation of light within an optical element.

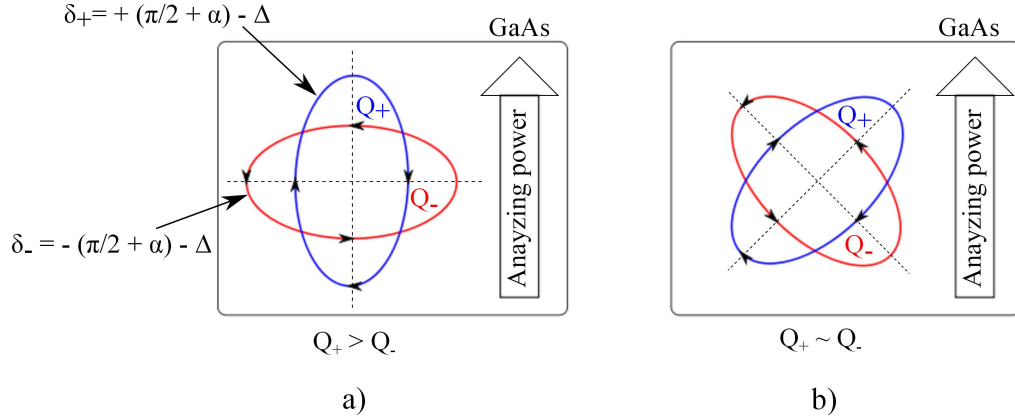


Figure 5.1: Charge asymmetry generated by the analysing power of the Pockels cell and the analysing power of the photocathode. (a) Orientation of the polarization ellipses with respect to the analysing power of the photocathode that can generate the maximum charge asymmetry. Since the + ellipse is aligned with the analysing power of the photocathode, the charge  $Q_+$  generated in the + helicity state (blue) is larger than  $Q_-$  generated in the - helicity state (red). (b) Alignment of the polarization ellipses for the minimum charge asymmetry ( $Q_+ \approx Q_-$ ).

#### 5.1.1.4 Phase Gradients

When the birefringence of the Pockels cell varies across its surface, it creates a gradient of the  $\Delta$  phase across the area of the incident laser beam. If the  $\Delta$  gradient is linear (see Figure 5.2 a), it creates a shift in the beam centroid between the two helicity states (see Figure 5.2 b). This results in a beam position difference which is correlated to the helicity. While the derivative of the  $\Delta$  phase generates helicity correlated position differences, the second derivative of the  $\Delta$  phase can generate beam spot size asymmetries [134].

The gradient of the photocathode QE analysing power coupled with a constant non-zero  $\Delta$  phase can also create position differences. A photocathode QE gradient arises when the analysing power across the photocathode increase due to the increasing QE anisotropy. The increasing QE causes the centroid of the beam to shift from its nominal position (similar to the case of the  $\Delta$  phase gradient) and this induces a helicity correlated position difference which is dependent on the  $\Delta$  phase.



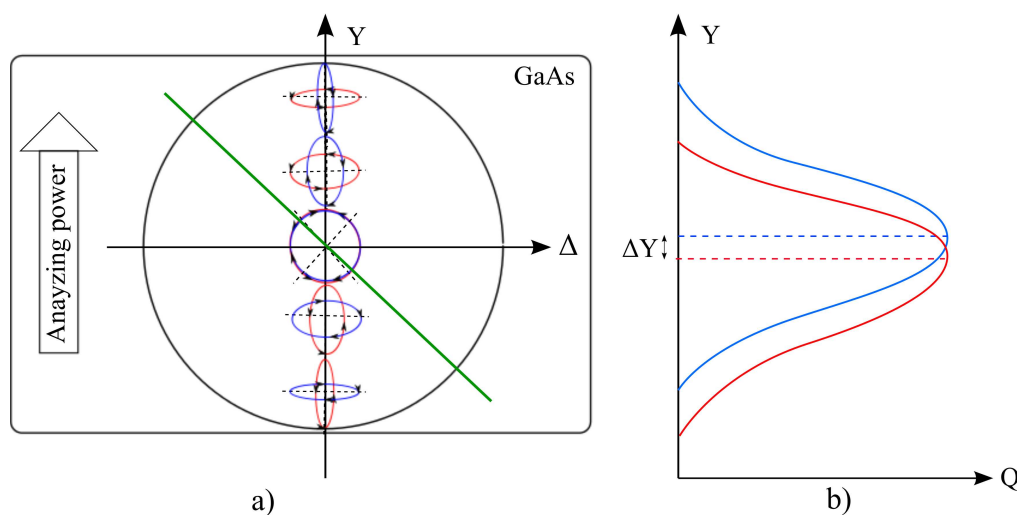


Figure 5.2: Helicity correlated vertical (Y) Position differences generated from a linear  $\Delta$  phase gradient across the laser spot. (a) The  $\Delta$  phase is linearly decreasing from bottom right to top left across the laser spot (green line). This causes the ellipticity of + and - polarization states to change across the laser spot. (b) Effect in (a) causes the beam intensity distributions between the two helicity states to shift. It appears as a shift in beam centroid along Y and that causes a position difference in Y. Similar effect can be observed in horizontal position differences due to  $\Delta$  gradients along the horizontal direction.

#### 5.1.1.5 Pockels Cell Steering

When the direction of the electric field across the Pockels cell is changed in order to change the direction of the circular polarization of the laser from left to right, it generates a pulsing effect in the crystal. This makes the Pockels cell behave like a converging or a diverging lens to laser light that pass through it. If the laser is not centered on the optical axis of the Pockels cell, the laser beam will be steered from its nominal path, resulting in a helicity correlated position difference [134].

#### 5.1.1.6 Other

Other known sources of helicity correlated beam properties at Jefferson Lab include cross talk between the three laser beams and beam clipping on apertures along the injector beamline.

### 5.1.2 Minimizing HCBA in the Commissioning Period and Run I

The minimization of helicity correlated beam asymmetries was carried out in two steps. The first step was focussed on proper setup of the laser table optics to minimize sources of HCBA and the second step was focussed on using slow helicity reversal and feedback on HCBA throughout the duration of the experiment for active cancellation. The following is a summary of the general steps taken to minimize helicity correlated beam asymmetries in the  $Q_{\text{weak}}$  commissioning period and Run I. These are the end results of a series of polarized source studies done between September 2010 and January 2011. Additional details on the principles of HCBA minimization techniques can be found in the dissertation of Rupesh Silwal [136].

#### 5.1.2.1 Pockels cell ringing

On 01-06-2011, Pockels cell ringing was measured [137] at the laser table using base voltages<sup>2</sup>  $+HV = 45950$ ,  $-HV = 38270$ , PITA offset of 120 V and the RHWP angle set at 4100 (see Figure 5.3). The ringing at the rising edge of the helicity signal is about 11 V peak-to-peak and at the falling edge it is about 9 V. This was larger than what has been measured before and generated about 3% residual linear polarization in the beam.

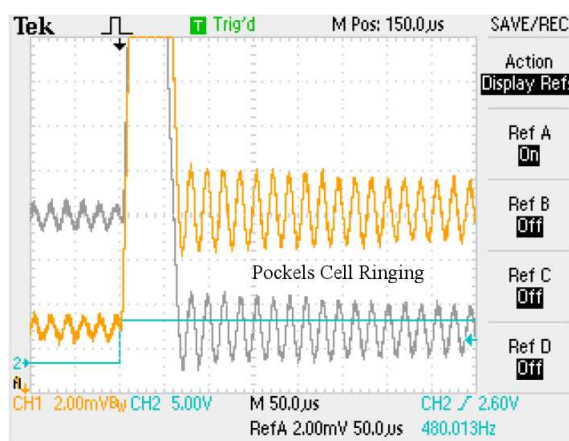


Figure 5.3: Pockels cell ringing observed at the falling (ash) and rising (orange) edges of the helicity signal (light-blue) using an oscilloscope.

<sup>2</sup>The Pockels cell HV range is  $\pm 4000$  V which is set using a DAC with a range of 65535.

### 5.1.2.2 *Pockels cell base voltages for reducing the $\alpha$ phase offset.*

A spinning linear polarizer and a photodiode placed downstream of the Pockels cell were used to measure the residual linear polarization in the laser beam. The Pockels cell electrode voltages which give a minima in the photodiode output indicates the minimum residual linear polarization in the beam generated by the  $\alpha$  offset. Table 5.2 shows the values used for the commissioning period and Run I.

Table 5.2: Pockels cell base voltages for minimum  $\alpha$  phase measured on 12-29-2010. 1 DAC = 0.06 V. Also shown are the amounts of residual linear polarization in the laser beam measured after the  $\alpha$  phase adjustment.

IHWP	PC HV+ (DAC)	PC HV- (DAC)	Linear Polarization in Positive Helicity	Linear Polarization in Negative Helicity
OUT	42300	41800	1.8%	3.3%
IN	42800	41200	1.8%	3.7%

### 5.1.2.3 *Pockels Cell placement for minimum beam steering.*

To remove steering of the laser beam, the optimum horizontal and vertical placements of the Pockels cell are selected by performing translation scans. The position sensitivities measured from these scans are used to adjust the location of the Pockels cell in the vertical and horizontal planes in order to provide the minimum helicity correlated position differences. Figure 5.4 shows the results of the last set of PC translational scans done prior to the beginning of the commissioning period. Based on the measured sensitivities, the PC was set at X = 5.4 mils (horizontal) and Y = -47.5 mils (vertical) for minimum or no laser beam steering<sup>3</sup>.

### 5.1.2.4 *Optimized RHWP Angle*

In principle, a Rotatable Half Wave Plate (RHWP) removes helicity correlated charge asymmetries generated by the photocathode analysing power by rotating the incident polarization ellipses such that their axes are at a  $45^{\circ}$  angle to the analysing power of the photocathode (see Figure 5.2). However, in practice, the ellipses are rotated leaving a small PITA sensitivity to the charge asymmetry. This sensitivity

---

<sup>3</sup>mils = 0.001 inch

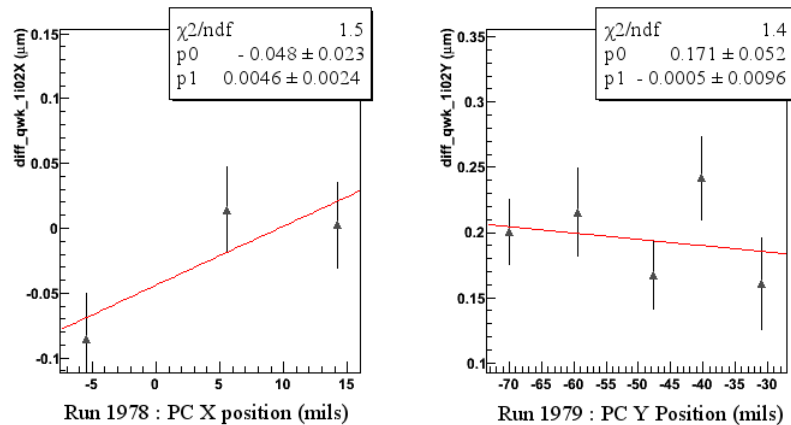


Figure 5.4: PC translation scans taken at the end of polarized source studies done on 01-06-2011. The position differences were measured by the first BPM in the injector, BPM1I02. In the linear fits, p0 gives the offset and p1 gives the slope.

is later used to adjust the PITA offset in order to remove the  $\Delta$  phase generated by the optics between the photocathode and the vacuum window. Choosing a RHWP angle at which the PITA slope is small additionally allows for the minimization of helicity correlated position differences that occur due to birefringent gradients of the photocathode and the vacuum window [134].

A RHWP angle which satisfies the above conditions was chosen for the commissioning period by performing RHWP scans (see Figure 5.5). During the RHWP scans, the charge asymmetry and position differences were measured over the full range of RHWP angles and they were fitted<sup>4</sup> with an equation of the form [136]

$$f(\theta) = \underbrace{a}_{\text{Optics downstream}} + \underbrace{b \sin(2\theta + c)}_{\text{RHWP}} + \underbrace{d \sin(4\theta + e)}_{\text{Optics upstream}}, \quad (5.2)$$

with  $\theta$  being the angle between the RHWP fast axis and the horizontal plane. Each term in Equation 5.2 represents the charge asymmetry generated by the coupling of the photocathode analysing power to the  $\Delta$  phase of the optics upstream/downstream of the RHWP (see Figure 3.6). Since the source in this case is the linear polarization, the resultant HCBA are expected to flip sign with the insertion of the IHWP. To determine the optimized angle, RHWP scans are repeated for a PITA of 120 V and the measured charge asymmetry and position differences (constant terms) from both

<sup>4</sup>Here we assume the position differences generated from the charge asymmetry gradients follow the same behaviour.

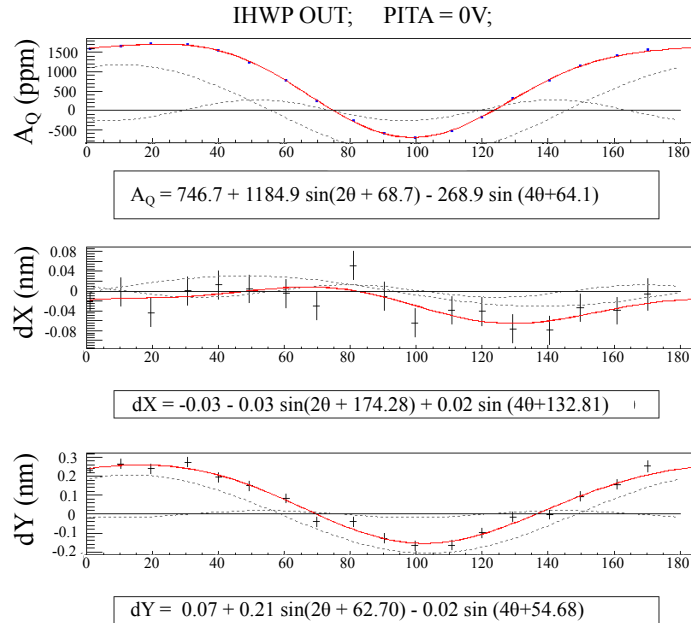


Figure 5.5: A RHW scan taken on 01-06-2010. The charge asymmetry ( $A_Q$ ) and position differences ( $dX, dY$ ) are from the first BPM in the injector, BPM1I02. The dashed lines are fits of the individual sine terms in Equation 5.2. See text for explanation.

fits are used to determine the PITA slope associated with each angle. These PITA slopes are then used to project position differences at each angle when the PITA offset is adjusted to zero the charge asymmetry (see Figure 5.6). The RHW angle which gives a small charge asymmetry sensitivity and the minimum position differences in each IHWP state was then selected as the optimized angle.

For the time period under consideration, based on the RHW optimization done on 01-06-2011, a RHW angle of  $79^\circ$  (DAC 3950) with a PITA slope of 14 ppm/V chosen as the optimized angle setting. The PITA slope of 14 ppm/DAC was used by the  $Q_{\text{weak}}$  charge feedback mechanism (see Subsection 5.1.2.6) to minimize the charge asymmetry to zero. However, starting from the 16th of March 2011,  $Q_{\text{weak}}$  moved to using two optimized RHW angles and PITA slopes for each of the two IHWP states to further reduce helicity correlated beam position differences. Table 5.3 shows the HCBA measured in the injector after completing the polarized source setup on 01-06-2011.

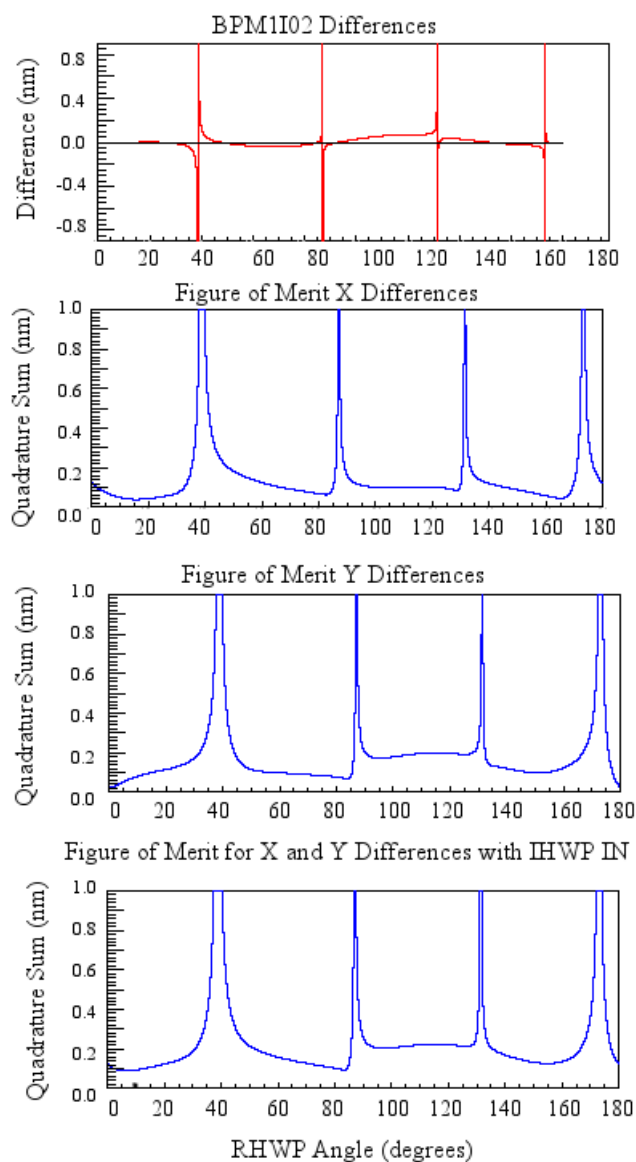


Figure 5.6: RHPW optimization plots for IHWP IN projected using the measured PITA slope. The first plot shows X position differences achievable at each RHPW angle using the PITA slopes extracted from the RHPW scans (similar to the ones in Figure 5.5). The second and third plots are the figure of merit plots for the position differences in the injector. They show the quadrature sum of the X and Y differences of the first 6 BPMs in the injector. The fourth plot is the figure of merit for both X and Y. It contains the quadrature sum of values in plots 2 and 3. Comparing the minima of the fourth plot for IHWP IN and OUT states, the RHPW angle at  $3950$  ( $79^{\circ}$ ) gives the minimum X and Y differences with zero charge asymmetry.

Table 5.3: HCBA measured at the injector after completing the polarized source setup on 01-06-2011. The RHWP angle is  $79^{\circ}$  (3950 DAC). The PITA slope is 14 ppm/DAC.

IHWP	$A_Q$ (ppm)	dX (nm)	dY (nm)
IN	-67.4	200	100
OUT	35.4	200	300

### 5.1.2.5 *Slow helicity reversal*

Slow helicity reversal removes helicity correlated false asymmetries generated by both polarization and non-polarization<sup>5</sup> effects.  $Q_{\text{weak}}$  used two slow helicity reversal techniques: the Insertable Half Wave Plate (IHWP) reversal and the Wien reversal.

The IHWP is located just before the Pockels cell and it is used for slow helicity reversal on short time scales. The insertion of the IHWP causes a  $180^{\circ}$  spin reversal changing the actual helicity of the electrons w.r.t the helicity signal. This causes the asymmetries and position differences that depend on the polarization to change sign while the sign of false asymmetries and differences that are independent of the polarization remain unchanged. Adding data taken with the IHWP in the beam (IN) and out of the beam (OUT) provides cancellation of these polarization independent, helicity correlated false asymmetries. During the experiment, the IHWP is inserted into the laser beam every 8 hours.

The Wien reversal is provided by the double Wien system located at the injector (see Subsection 3.2.3). The solenoids located inbetween the two Wien filters are used to flip the spin of the electrons to either beam left or right. This is known as the Wien reversal/flip and it provides a cancellation of slow varying helicity correlated false asymmetries, such as spot size asymmetry, which are independent of the polarization. The non-invasive slow helicity reversal via the double Wien is a relatively new technique which was introduced in 2010 during the PREX experiment in Hall A. During the experiment, a Wien reversal/flip was typically done every 3 to 4 weeks of beam time known as a Wien period. Table 5.4 shows how the combination of these two processes provides an effective cancellation of HCBA for the physics asymmetry measured from the full data set.

---

<sup>5</sup>Not caused by residual linear polarization in the beam.

Table 5.4: HCBA cancellation with slow helicity reversal. HCBA generated by polarization effects ( $A^{Pol}$ ) are only sensitive to the IHWP reversal whereas the physics asymmetry ( $A^{Phys}$ ) is additionally sensitive to the Wien reversal. This introduces a relative sign change between these two quantities which depends on polarization. The HCBA generated by non-polarization effects ( $A^{Non-Pol}$ ) are only sensitive to the helicity signal and therefore are not effected by either process. Summing the difference between the IHWP states in a Wien cancels both types of HCBA.

IHWP	Wien flip	Asymmetry in the hall	Sum	Difference
OUT	Right	$A^{Phys} + A_{HC}^{Pol} + A_{HC}^{Non-Pol}$	$A_{HC}^{Non-Pol}$	$A^{Phys} + A_{HC}^{Pol}$
IN	Right	$-A^{Phys} - A_{HC}^{Pol} + A_{HC}^{Non-Pol}$		
IN	Left	$A^{Phys} - A_{HC}^{Pol} + A_{HC}^{Non-Pol}$	$A_{HC}^{Non-Pol}$	$A^{Phys} - A_{HC}^{Pol}$
OUT	Left	$-A^{Phys} + A_{HC}^{Pol} + A_{HC}^{Non-Pol}$		
Sum of the differences				$A^{Phys}$

### 5.1.2.6 Charge Feedback

The magnitude of charge asymmetry achievable at the target after configuring the polarized source was of the order of 1 to 2 ppm. But the charge asymmetry requirement for  $Q_{weak}$  was less than 0.1 ppm (see Section 3.4). Therefore, an active charge feedback system was used to bring down the charge asymmetry at the target to this desirable level. The charge feedback system operated by measuring the charge asymmetry periodically and adjusting the Pockels cell voltages using a PITA offset to null it. The PITA slope measured during the polarized source setup, was used to calculate the required PITA offset. This process was repeated every 80 s causing the charge asymmetry to converge to zero as  $1/n$ , within the accuracy of the asymmetry determination<sup>6</sup> (see Figure 5.7). An alternative method would have been to apply the PITA offset at the beginning of each run (which was about 1 hour long) instead of at 80 s time intervals. But the 80 s interval ensures that the majority of the data is taken with a charge asymmetry which is less than 0.1 ppm. This was essential to minimize charge related systematics such as charge non-linearity (see Subsection 6.5.3).

---

<sup>6</sup> $n$  is the number of quartets collected inside the 80 s time window.



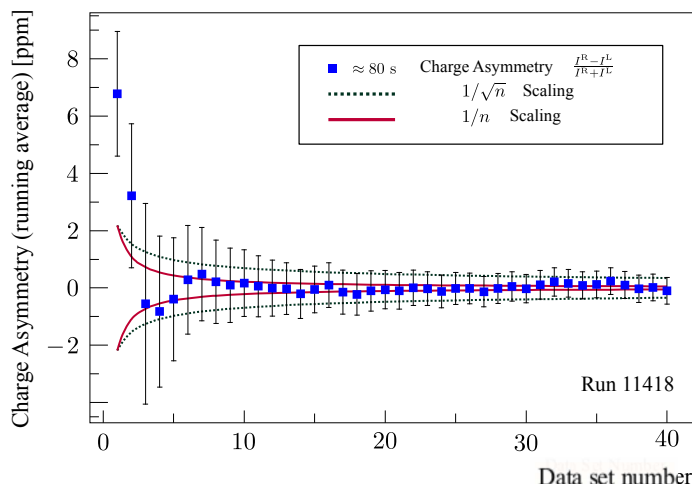


Figure 5.7: Running charge asymmetry showing the effect of charge feedback applied over 80 s time intervals. The horizontal axis shows the number of 80 s intervals. The blue data points are the average of charge asymmetry measured within a single interval. The red solid curve represents the  $1/n$  expectation. The dotted black line is the  $1/\sqrt{n}$  statistical expectation shown here for comparison. Figure from Ref. [41].

### 5.1.2.7 Position Feedback

Position differences achievable in the injector from configuring the polarized source are typically of the order of 100 nm. The adiabatic damping<sup>7</sup> of the beam in the accelerator is expected to bring down these position differences to a few nano meters by the time the beam reaches the experimental halls. But during different beam tunes in the accelerator, the beam emittance can change along the beamline interfering with the process of adiabatic damping. This results in position differences in the hall which can be as large as 100 nm. In situations where the beam position differences at the target are large and are not adjustable via beam tuning in the accelerator, a position feedback was used to reduce the position differences. This was not an active feedback and required operator intervention. The position feedback system uses a set of helicity magnets located in the injector to kick the beam horizontally and vertically in a helicity correlated manner. Therefore, these magnets are used for position feedback by generating helicity correlated position differences cancelling out differences generated by other sources in the injector beamline. The initial testing of the magnets done in November 2011, showed that their response was slower than the

<sup>7</sup>Adiabatic damping is the decrease in beam emittance in accelerating beams. This requires a perfect optics matching between beam configuration from one accelerating point to the the other in the beamline [138].

helicity reversal rate of 960 Hz (see Appendix E for the results from these tests) used by the experiment. But with necessary hardware changes and proper calibrations [139], the position feedback was operational in Run II as a passive feedback system. Figure 5.8 shows an instance where large position differences present at the target were brought down to  $Q_{\text{weak}}$  specifications using the position feedback system.

## 5.2 False Asymmetry Due to Helicity Control Signals

The helicity signal is an important part of a parity experimental setup. As discussed in Subsection 3.2.2, the helicity signal controls the direction of the electron spin required for the formation of the experimental asymmetry. But there are effects from the helicity signal which are undesirable for an experiment. One such effect is the helicity correlated beam asymmetries discussed in the previous section and the other effect is the potential leakage into the experiments signals.

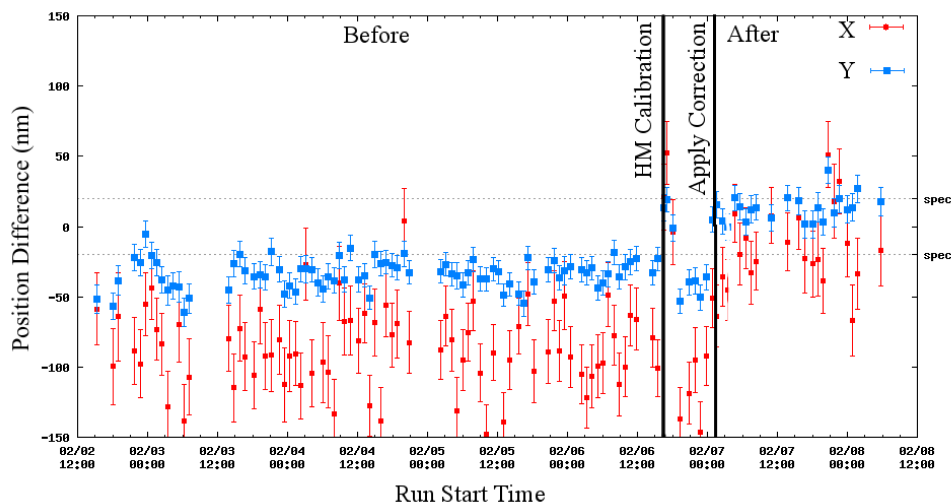


Figure 5.8: Position feedback using helicity magnets. The vertical axis shows the date and the starting time of the data collecting periods. Each point corresponds to an average over about 25000 quartets. The dotted lines indicate the limits of position difference specifications for  $Q_{\text{weak}}$  (not taking into account the cancellation coming from the IHWP). The X position differences at the beginning of this particular running period were of the order of 100 nm. Starting from 02-07-2012, the position feedback was applied using the two helicity magnets 0L01V and 0L03V which caused the position differences to drop to acceptable values. Figure from Ref. [140].

### 5.2.1 The Delayed Helicity Signal

Indeed the helicity signal can be picked up by electronics in the injector and in the Hall C electronics room resulting in a shift of the detector base line voltages. This generates a helicity correlated false asymmetry. To avoid this leakage from the helicity signal, the true helicity signal (i.e the signal used in the injector to control the Pockels cell voltages) is delayed by a fixed number of patterns, before being sent to readout electronics. By delaying the helicity signal, the leakage on the electronics is randomized averaging to zero (see Figure 5.9). The delayed helicity signal from the injector is carried into the electronics rooms of the experimental halls via optical fibers. The signal is then converted into a Nuclear Instrument Module (NIM) signal via a Fiber Translator (FT) module before being readout via a scaler module (input register). So the only route taken by the helicity signal inside the electronics room is from the FT module to the scaler module. With the precision of the  $Q_{\text{weak}}$  physics asymmetry being in the ppb range, it was necessary to check the magnitude of the false asymmetry due to helicity leakage at the ppb level. It was also important to check the sensitivity of the VQWK ADC's to the delayed helicity signal and to confirm that the DAQ electronics were well isolated from the helicity leakage. The following sections describe the tests I conducted for these purposes.

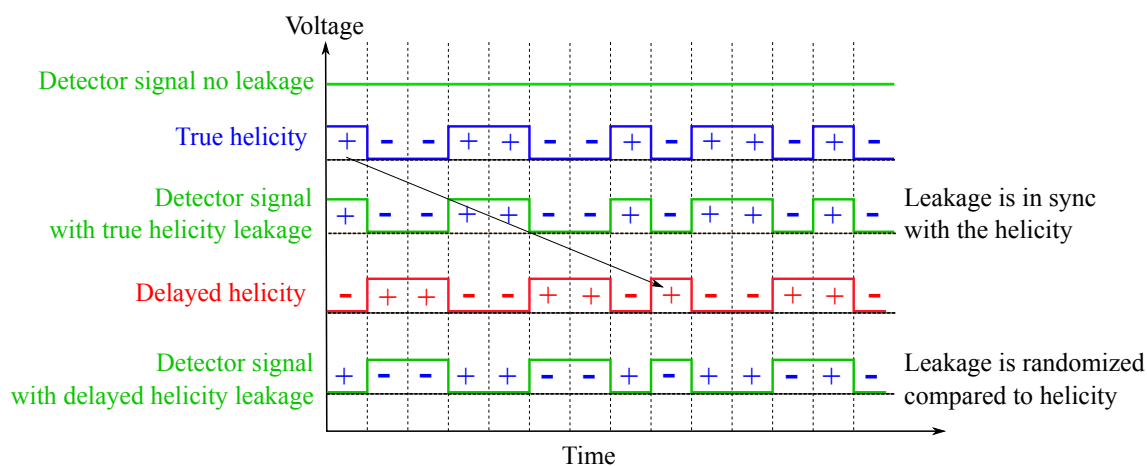


Figure 5.9: Representation of the leakage on the detector signals from true (blue) and delayed (red) helicity signals. The vertical axis gives the magnitude of the signals and the horizontal axis gives the time. The true helicity leakage is in sync with the helicity leading to a false asymmetry. But the leakage from the delayed helicity is randomized leading to a false asymmetry which averages to zero.

### 5.2.2 Helicity Signal Leakage Measurements

The helicity signal leakage measurements were carried out prior to the beginning of the experiment in November 2009. In each measurement setup, the helicity leakage was measured using one of two test signals : a 6V battery as a best-case of a low-noise voltage source, and a low-noise current source constructed from a battery and a resistor. The current signal was sent to a current-to-voltage converter and then to a  $Q_{\text{weak}}$  preamplifier module powered by a Topward DC power supply. Both sources were RF shielded and were isolated from the ground effects. The two signal sources were placed in Hall C near the patch panel used for carrying detector signals to the electronics room located about six stories below the electronics room. In the electronics room, the signals were connected to a VQWK ADC module with the voltage signal plugged into channel 1 and the preamplified current signal plugged into channel 2. The VQWK ADC module was read out via the same VME crate [141] which was later used for the Čerenkov detector signal digitization.

#### 5.2.2.1 Setup

The helicity signal leakage measurements explored three different scenarios :

1. *Normal* :

During normal operations, at any place in between the helicity board and the scaler module used to read out the helicity signal in the electronics room, the signal could leak into the DAQ electronics. The setup shown in Figure 5.10a was used to measure the helicity signal leakage under this scenario.

2. *Via Ground* :

All the electronics in the electronics room share a common ground signal. Therefore, there was a possibility that the helicity signal could be picked up by the ground signal. The setup shown in Figure 5.10b was used to induce a leakage on the ground signal by routing a copy of the helicity signal through a 757 Fan In Fan Out (FIFO) NIM module.

3. *Worst Case* :

The worst case scenario determines the amount of helicity signal leakage when the helicity signal itself is plugged into an ADC by accident. This scenario will induce the maximum leakage on the detector signals. The setup used to measure this leakage used a 757 FIFO NIM module to obtain two copies of the delayed

helicity signal (see Figure 5.10c). One copy was sent to the scaler module and the other was plugged into the ADC channel 2 of the VQWK module containing the voltage and current signals<sup>8</sup>.

Data were collected from each setup for approximately 1 hour at a time using a two quartet helicity delay. The helicity reversal rate used for these measurements was 30 Hz as the measurements were performed while the PVDIS experiment was running in Hall A. Having these measurements done at a smaller helicity rate than 960 Hz had no effect on the interpretation of the results since we were looking for shifts in the means of the asymmetry distributions and not in the standard deviations.

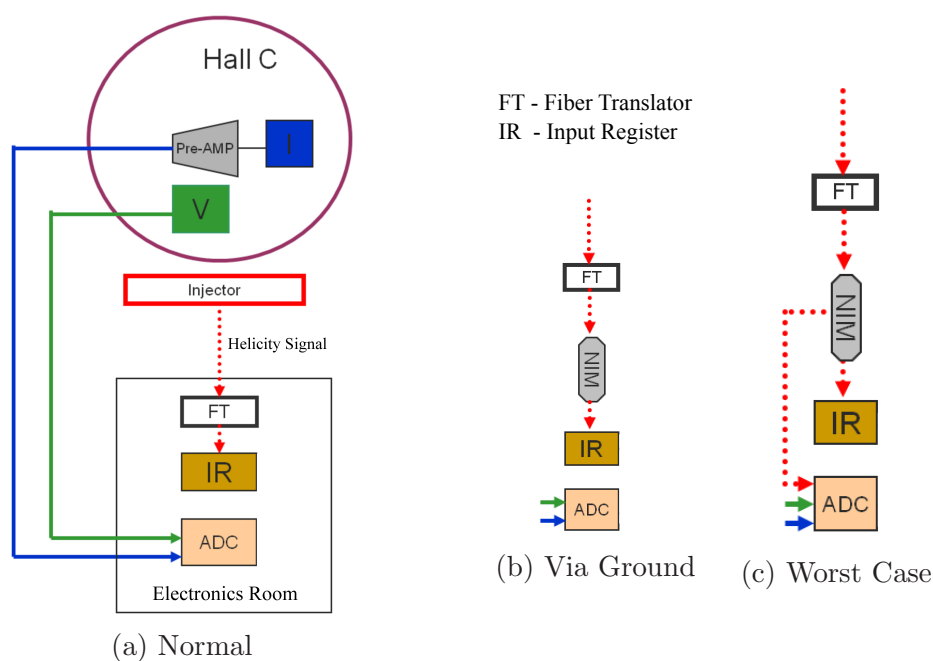


Figure 5.10: Setups used for the helicity signal leakage measurements. Each setup uses a preamplified current source (I) and a reference voltage source (V) to mimic a low noise detector signal. The red dotted line represents the helicity signal coming from the helicity board in the injector building via optical fibers. The signal is then converted to NIM signal via a Fiber Translator (FT) and NIM copies are sent into the Input Register (IR). (a) The full setup in the hall and the electronics room. (b) The helicity signal is routed through a NIM module and (c) the delayed helicity signal is plugged directly into the ADC. (b) and (c) only show the changes done to the setup in the electronics room. The setup in the hall was the same as in (a).

<sup>8</sup>The voltage signal was moved to the ADC channel 3.

### 5.2.2.2 *Data analysis*

The goal of the analysis was to identify the shifts in the current and voltage source asymmetries due to the helicity signal leakage. To observe these shifts, each data set was analyzed twice under two assumptions.

1. *The helicity signal in the electronics room is the true helicity signal used in the injector.*

Setting the helicity pattern delay in the QwAnalysis to zero provides the helicity pattern required for the asymmetry formation.

2. *The helicity signal in the electronics room is the delayed helicity signal.*

Setting the helicity pattern delay in the QwAnalysis to four patterns provides the helicity pattern required for the asymmetry formation.

The following subsections contain the findings of this analysis.

### 5.2.2.3 *Effect of using delayed helicity*

Table 5.5 shows the asymmetries extracted using the two analysis methods mentioned in the previous section. In the absence of leakage from background signals, both the voltage and current sources should measure zero asymmetries since they are constant DC sources. From Table 5.5, one can see that both current and voltage sources in the *normal* and the *via ground* setups measured asymmetries which are probably consistent with zero at the level of 11 ppb whenever the delayed or the true helicity signal are present in the electronics room. There is however a clear difference between the amount of shifts observed in the two scenarios (-27 ppb versus 12 ppb and -19 ppb versus -10 ppb). In contrast, in the *direct* setup, both sources measured non-zero helicity leakage from the true helicity signal. The largest leakage of -71 ppb with a 6.5 sigma deviation from zero is seen on the preamplified current source which goes to zero for the delayed helicity signal. Although normal wiring configurations found no helicity signal leakage at the level of  $\pm 11$  to  $\pm 13$  ppb, this measurement demonstrated how a false asymmetry produced with direct/pathological wiring could be cancelled using a delayed helicity reporting. But for purpose of  $Q_{\text{weak}}$  experiment, further tests were needed to clarify the amount of helicity leakage at the 1 ppb level. The relevant measurement and the analysis are discussed in the next subsection.

Table 5.5: Helicity leakage observed in an hour long measurement from delayed and true helicity signals. See text for an explanation on the analysis method. The voltage signal chain was a bit noisier than the preamplified current signal chain. This explains the 2 ppb difference between the statistical errors.

Setup	True Helicity (ppb)	Delayed Helicity (ppb)
Pre-amplified Current Source		
Normal (Run 1042)	$12 \pm 11$	$-27 \pm 11$
Via Ground (Run 1041)	$-10 \pm 11$	$-19 \pm 11$
Direct (Run 1043)	$-71 \pm 11$	$4 \pm 11$
Voltage Source		
Normal	$6 \pm 13$	$-8 \pm 13$
Via Ground	$-4 \pm 13$	$0 \pm 13$
Direct	$-36 \pm 13$	$-8 \pm 13$

#### 5.2.2.4 *A parts per billion measurement of the helicity leakage*

The ppb level measurement of the helicity leakage was performed using a setup similar to the one shown in Figure 5.10c. The only change was the order in which the current, voltage and helicity signals were connected to the VQWK ADC module. In this setup, the voltage signal was connected to channel 1, the preamplified current signal was connected to channel 2, and the copy of the delayed helicity signal was connected to channel 3. Data were collected for 10 hours using a 240 Hz helicity reversal rate<sup>9</sup> with a two quartet delay. The techniques described in the previous section were then used to extract the leakage from the delayed and the true helicity signals. Table 5.6 shows the results from this analysis. A non-zero asymmetry is observed in the preamplified current signal only for the true helicity signal. The asymmetry of  $-88.6 \pm 1.3$  ppb measured in this case gives the magnitude of the helicity signal leakage from the true helicity signal. One explanation for the lack of leakage in the voltage signal is that to feel the full effect of the helicity signal (or similar) the source signal needs to be in the adjacent ADC channel. This observation suggests that even under direct contact with the signal handling crate, the helicity signal leakage is only present in the adjacent ADC channels of the VQWK module. It could be attributed to how well the ADC channels are isolated from one another.

---

<sup>9</sup>This was the helicity reversal rate available at the time of this measurement due to the PREX experiment running in Hall A.

Table 5.6: Helicity leakage observed in a 10 hour long measurement.

Source	Delayed Helicity (ppb)	True Helicity (ppb)
Preamplified Current Source	$-0.4 \pm 1.3$	$-88.6 \pm 1.3$
Voltage Source	$-0.5 \pm 0.8$	$-0.3 \pm 0.8$

Therefore, from this analysis, it can be concluded that without pathologically inane wiring conditions, the helicity signal leakage is zero with a sensitivity of 1 ppb. Furthermore, the leakage is only present in the ADC channels adjacent to the channel containing the helicity signal in a VQWK module. But as long as the helicity is delayed in the electronics, this leakage will average out to zero.

### 5.2.3 MPS and QRT Signal Leakage Measurements

The MPS and QRT signals (introduced in Subsection 4.1.2) are periodic signals with frequencies of 960 Hz and 240 Hz which are indicators of the beginning of a new event and pattern, respectively. Similarly to the helicity signal, both signals are sent into the electronics room via fiber optical cables and the signals are converted to NIM using the Fiber Translator. But unlike the helicity signal, both of these signals were used in the  $Q_{\text{weak}}$  DAQ electronics to form the ADC gates and the event and pattern counters in the fake MPS generator<sup>10</sup> (see Figure 5.11). Since both signals are varying voltage signals, there was a possibility they would leak into the detector signals. The following is a discussion of the set of leakage measurements carried out in July 2012 after the end of the data taking period of the experiment to determine the sizes of these leakages.

#### 5.2.3.1 Setup

The setup is similar to the one used in Section 5.2.2 for the helicity signal leakage measurements. However, in this case, a 5.4 V source was placed inside the electronics room rather than in Hall C. The output was connected to a VQWK ADC in the VME crate used for the main detector signal digitization. For these measurements, two possible leakage scenarios<sup>11</sup> were considered:

<sup>10</sup>Used for systematic studies which require different helicity reversal rates.

<sup>11</sup>From the results of the helicity leakage measurements presented in Subsection 5.2.2, it was clear that the *Normal* and *Via Ground* yielded similar results.



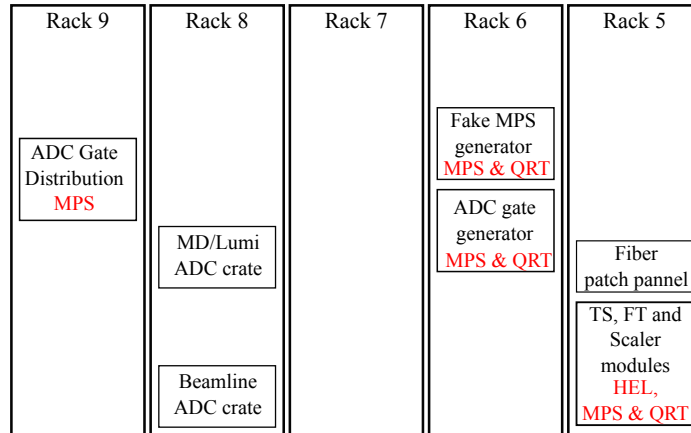


Figure 5.11: Schematic (not to scale) showing the distribution of Helicity (HEL), MPS and QRT signals in the  $Q_{\text{weak}}$  electronics racks. Each block represents a VME crate. Both MPS and QRT signals are plugged into combination of modules in order to generate the ADC gates and the fake MPS required for tracking and other background measurements.

1. *Via Ground* :

MPS/QRT leakage via the ground signal. A copy of the MPS/QRT signal is plugged into an empty NIM module placed in a VME crate in rack 6 (see Figure 5.11). The difference between this setup and the normal use of MPS/QRT in the NIM modules for ADC gate and Fake MPS generation is that the output channel of the NIM module was not terminated, doubling the size of the NIM signal.

2. *Worst Case* :

The MPS/QRT signal leakage under direct contact with a VQWK ADC. In this setup, the MPS/QRT signal was plugged into the adjacent channel of the voltage signal.

### 5.2.3.2 Results

For each signal and setup, data were collected for 12 hours at a time using a helicity rate of 960 Hz with a two quartet delay. The data were then analyzed using the QwAnalysis standard configuration which yielded the results shown in Table 5.7. The results suggest that there was no significant leakage from either the MPS or the QRT signals at the 1 to 2 ppb level.

Table 5.7: MPS/QRT leakage observed in a 12 hour long measurement.

Setup	Runs	Leakage (ppb)	
		from MPS	from QRT
via Ground	18983,18979,18978	$4 \pm 2$	$1 \pm 2$
Worst Case	18985,18982,18980	$2 \pm 1$	$-2 \pm 1$

#### 5.2.4 *Quartet Polarity Dependence of the Helicity, MPS, QRT Leakage*

During the experiment, it was discovered [142] that a 50 ppb false asymmetry was present on the voltage source which was being used as a background detector in the electronics room. This false asymmetry changed sign depending on the polarity<sup>12</sup> of the quartet used to form the asymmetries. At the time, it was believed that the cause of this false asymmetry was the QRT signal leaking into the voltage source. This was an interesting hypothesis since a cancelling false asymmetry from the QRT signal had never been observed before.

To test this hypothesis, I used the data taken from the *via Ground* setup in the previous section. In addition to the QRT signal, I also looked into the MPS and helicity signals for completeness. To extract the quartet polarity dependence of the leakage, asymmetries from quartets with positive and negative polarity were grouped together. Additionally, to eliminate Pockels cell hysteresis effect<sup>13</sup> as a possible cause, each group was separated based on the polarity of the previous quartet. This resulted in four asymmetry distributions for each signal containing quartets with polarity  $+, +, +$ ,  $-, -, +$ ,  $-, -$  where the first (second) sign indicates the polarity of the previous (current) quartet. Figure 5.12 shows the results of this analysis. At first glance, the asymmetries in all three signals depend on the current quartet polarity and not on the polarity of the previous quartet. This seems to eliminate the Pockels cell hysteresis effect as the cause of the false asymmetry<sup>14</sup>. On closer observation, there is a significant pattern polarity dependent false asymmetry generated in the voltage signal in the MPS and the helicity signal. In comparison, the asymmetry generated by the QRT signal is consistent with zero at the 95% C.L. This observations confirms

<sup>12</sup>The polarity of a quartet is the helicity of the first event in the quartet.

<sup>13</sup>Due to hysteresis of the Pockels cell, a given helicity state can carry the helicity of the previous state.

<sup>14</sup>Asymmetries caused by Pockels cell hysteresis effect would show a dependence on the sign of the previous pattern polarity.

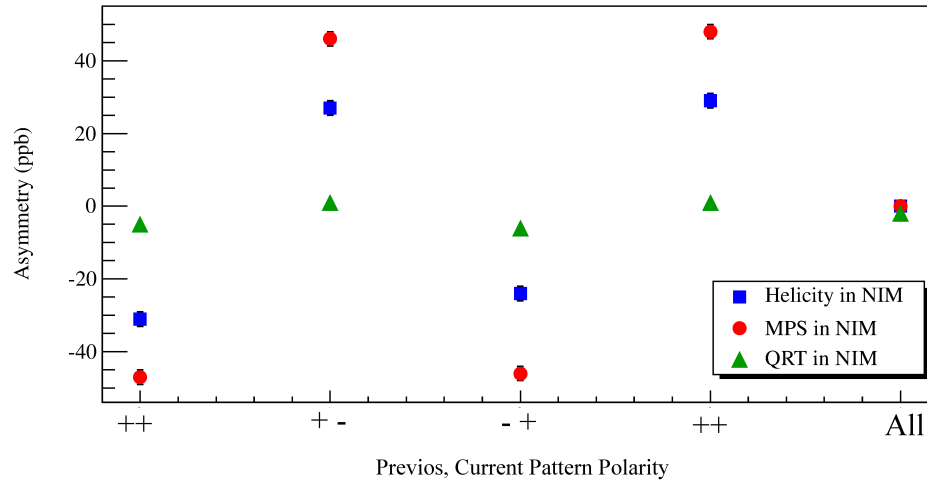


Figure 5.12: Quartet polarity dependence of the MPS, QRT and helicity leakage in the *Via Ground* setup. The horizontal axis shows the asymmetry distributions based on the polarities of the previous and current patterns. The vertical axis gives the measured asymmetry. Error bars are not visible at this scale.

that the quartet polarity dependent false asymmetry seen on the background detector during the experiment could not have been generated by the QRT signal alone. It maybe be a result of the combined leakages from all three signals. Further insight into the exact generator of this leakage was gained by using the sub-block feature of the VQWK ADCs (see Subsection 4.1.2). The next section presents the results of the sub-block analysis of the quartet polarity dependant leakage.

#### 5.2.4.1 *Sub-block dependence of the MPS, QRT leakage*

The sub-block analysis was performed on the data presented in the previous section. The asymmetry distributions relevant to the three signals, MPS, QRT and helicity, were separated into groups with positive and negative quartet polarities. My findings are summarized in Table 5.8 and Figure 5.13. From the table and the figure, one can clearly see that there is a false asymmetry of the order of 150 ppb present in sub-block 0 of the MPS signal data set. It drops to 50 ppb in sub-block 1 and then to zero in sub-blocks 2 and 3. In comparison, the QRT signals have a smaller asymmetry in sub-block 0. This type of leakage can only be generated by an effect present at the beginning of each event in a quartet. The observation that it is dominant for the helicity and the MPS signal suggests that the observed leakage is generated by a combination of MPS, QRT and helicity signal leakages. Since during, normal

Table 5.8: Sub-block dependence of the leakage from the MPS, helicity and QRT signals when each signal is plugged into an NIM module in the DAQ setup. +(-) indicates the polarity of the quartets used in the signal distributions are positive (negative).

Block	Asymmetry (ppb)					
	MPS		Helicity		QRT	
	+	-	+	-	+	-
0	$-148 \pm 2$	$148 \pm 2$	$-23 \pm 2$	$20 \pm 2$	$-91 \pm 2$	$91 \pm 2$
1	$-36 \pm 2$	$36 \pm 2$	$1 \pm 2$	$-3 \pm 2$	$-26 \pm 2$	$23 \pm 2$
2	$-2 \pm 2$	$4 \pm 2$	$2 \pm 2$	$-8 \pm 2$	$1 \pm 2$	$0 \pm 2$
3	$1 \pm 2$	$0 \pm 2$	$-1 \pm 2$	$-4 \pm 2$	$4 \pm 2$	$-2 \pm 2$

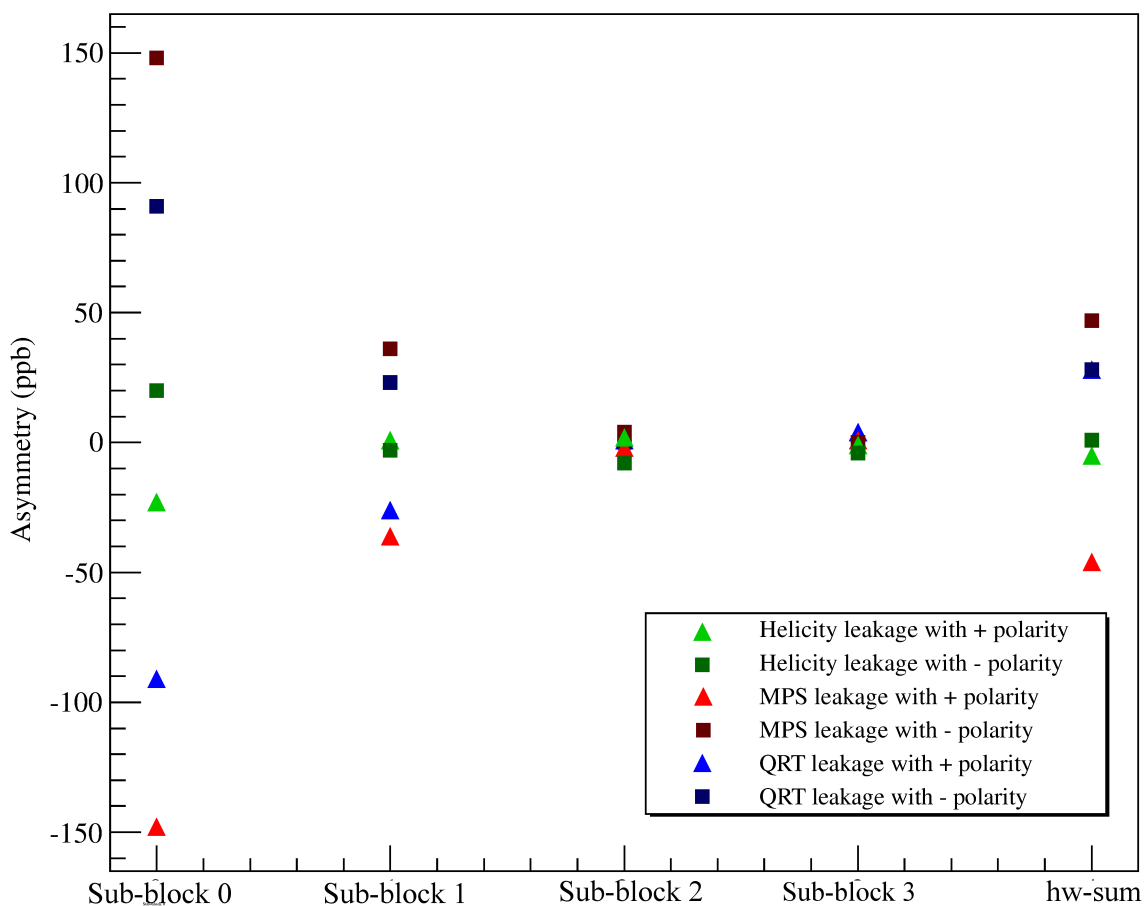


Figure 5.13: Graphical representation of the sub-block dependence of the leakage from the MPS, helicity and QRT signals given in Table 5.8. The leakage in the first block is as large as 150 ppb. For reference, the leakage from the sum of the sub-blocks (hw-sum) is also shown.

operations, only the MPS and QRT signals are spread throughout the electronics modules, the quartet polarity dependent leakage observed in the background detector must have been generated by a combination of MPS and QRT leakages. The MPS can leak into the voltage signal at the beginning of all events but the QRT signal can leak into the beginning of only the first event in a quartet. The coupling of the falling edge of the QRT signal to the rising edge of the MPS would create an imbalance in the leakage resulting in a false asymmetry that depends on the polarity of the quartet as observed in Subsection 5.2.4.

This is an important aspect of the electronics setup that should be kept in mind when doing quartet polarity specific analysis of the data. But for the overall analysis, using quartets with opposite polarities helps to cancel out the leakage making the final detector asymmetries insensitive to the effects of MPS and QRT signals.

### 5.3 Random Noise

The overall statistical error of an asymmetry measurement depends on the number of samples. This is expressed by

$$\Delta A_{Stat}^{Exp} = \frac{\sigma^{Exp}}{\sqrt{N}}, \quad (5.3)$$

where  $\sigma^{Exp}$  is the precision of a single asymmetry measurement and  $N$  is the number of asymmetry measurements. It is clear from Equation 5.3 that for a fixed number of measurements,  $\Delta A_{Stat}^{Exp}$  depends on the magnitude of  $\sigma^{Exp}$ . In an ideal situation,  $\sigma^{Exp}$  will be limited by the counting statistics,  $\sigma^{Stat}$ . But in reality, it gets contributions from random noise sources such as electronic noise, fluctuations in the number of photo-electrons per scattered electron and target density fluctuation caused by target boiling. This dependence of the  $\sigma^{Exp}$  can be expressed as

$$\sigma^{Exp} = \sqrt{\sigma_{Stat}^2 + \sigma_{Electronics}^2 + \sigma_{PE}^2 + \sigma_{Target}^2 + \dots} \quad (5.4)$$

With  $\sigma_{Stat}$  limited by the fixed time allowed for data taking in order to achieve the experiments precision goal, the contributions from random noise sources indicated in Equation 5.4 were required to be well below the statistical uncertainty of  $\Delta A_{Stat}^{Exp} = 5$  ppb. At full luminosity, the standard deviation of the asymmetry distribution of a single Čerenkov detector was about 600 ppm. Therefore, it was important to constrain the contributions from random noise sources to well below 600 ppm. Studies

were conducted prior to the experiment and during the data taking period of the experiment to achieve this goal. The studies done prior to the experiment include measurements of electronic noise from data acquisition electronics. The following sections discuss the electronic noise measurements carried out during the experiments commissioning period and their results.

### ***5.3.1 Electronic Noise Measurements Under Realistic Conditions***

The most notable sources of electronic noise which were expected to contribute to the experiments signals are

- ADC channel noise,
- Noise in cables and connectors,
- 60 Hz line noise and harmonics,
- Preamplifier noise,
- Noise from preamplifier power supplies, and
- Other electronic noise sources in the hall related to beam operations.

The noise measurements done in October 2009 to determine the electronic noise in the Čerenkov detector electronics chain were sensitive to all of these sources.

#### ***5.3.1.1 Setup and analysis***

In their final configuration, the Čerenkov detector electronics chains consisted of TRIUMF preamplifiers, DC power supplies, coaxial cables and BNC connectors. DC power supplies were used to power the preamplifiers and coaxial cables were used to carry the amplified signals from the PMTs to the VQWK ADCs located in the electronics room. These coaxial cables were connected into the Hall C patch panel<sup>15</sup> which was routed through several isolated patch panels to the patch panel located in the upstairs electronics room. The noise measurements done in October 2009 used this same signal path.

The noise measurement setup (see Figure 5.14) used two RF-shielded, isolated current sources of  $4.7 \mu\text{A}$  (a 9 V transistor battery across a 2M $\Omega$  resistor [143])

---

<sup>15</sup>The cable patch panel located inside the Hall C near the High Momentum Spectrometer (HMS).

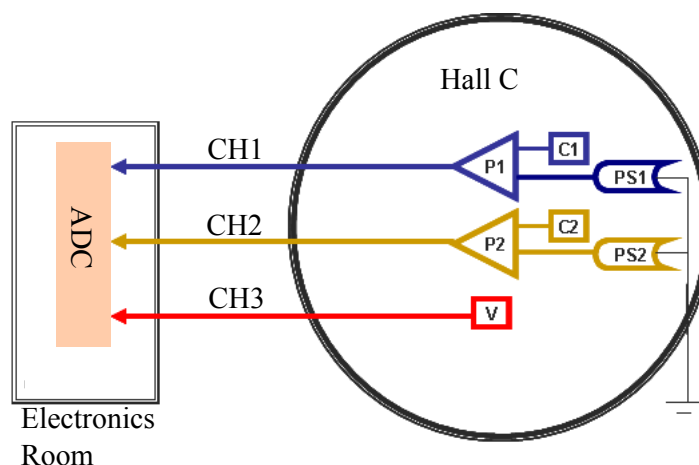


Figure 5.14: Schematic of the setup used for measuring electronic noise content in the Čerenkov detector signal chain. PS stands for Power Supply, C for Current source and P for Preamplifier. The different colors identify the three different signal chains. Out of the three, two contains preamplified current signals. The third is a voltage source. All the signals were read out using the same VQWK ADC module.

and a 9 V reference voltage source. The current signals were preamplified up to 5.5 V using TRIUMF preamplifiers powered by two DC power supplies from two different manufacturers (Texico and Topward)<sup>16</sup>. The two preamplified current sources represented two different detector signal chains. *Chain 1* used the Topward DC power supply and *Chain 2* used the Texico DC power supply. The two power supplies were connected to the same AC power outlet in the hall in order to make sure they have a common ground. All three signals were connected to the Hall C patch panel via coaxial cables. *Chain 1* was patched through channel 410 in the Hall C patch panel, *Chain 2* used channel 412 and the voltage source used channel 414. In the electronics room, the signals were sent into three consecutive channels of a VQWK module and data were collected using a fake 1 kHz reversal rate<sup>17</sup>. At the time, 1 kHz was the reversal rate  $Q_{\text{weak}}$  had planned to use.

During these noise measurements, Hall C was actively being used by the Hyper Nuclear Spectroscopy (HKS) [144] experiment. This provided realistic conditions in the hall similar to what was expected during the data taking period of the  $Q_{\text{weak}}$  experiment. Except for the helicity leakage (discussed in Section 5.2), this setup was

<sup>16</sup>Two power supplies were used to identify the DC power supply with the lowest noise contribution.

<sup>17</sup>The actual event rate at the time was 30 Hz as required by the HAPPEX III experiment. However, as mentioned before,  $Q_{\text{weak}}$  DAQ had the capability to generate fake ADC gate signals inside the electronics room for commissioning purposes like this.

sensitive to all possible noise sources listed at the beginning of this subsection. Data taken from the setups for the different configurations discussed below, were analyzed using the fake helicity generator available in the QwAnalysis software which generated the 1 kHz helicity pattern required for the asymmetry calculations internally. At the time, the fake helicity pattern generator inside the analyzer used the 24-bit helicity generator which was being used by the helicity board before it was upgraded to the 30-bit generator. This however does not affect the interpretation of the following results.

### 5.3.1.2 60 Hz line frequency and harmonics

The presence of 60 Hz line harmonics in the electronics chains was confirmed with the use of a spectrum analyzer. The Fast Fourier Transforms (FFT) of the signals obtained via the spectrum analyzer at the inputs to the ADCs are shown in Figure 5.15. There was no beam in the hall at the time these FFTs were taken. In addition to the three signals coming from the hall, a preamplifier placed inside the electronics room was used as a reference to differentiate between the harmonics from the coaxial

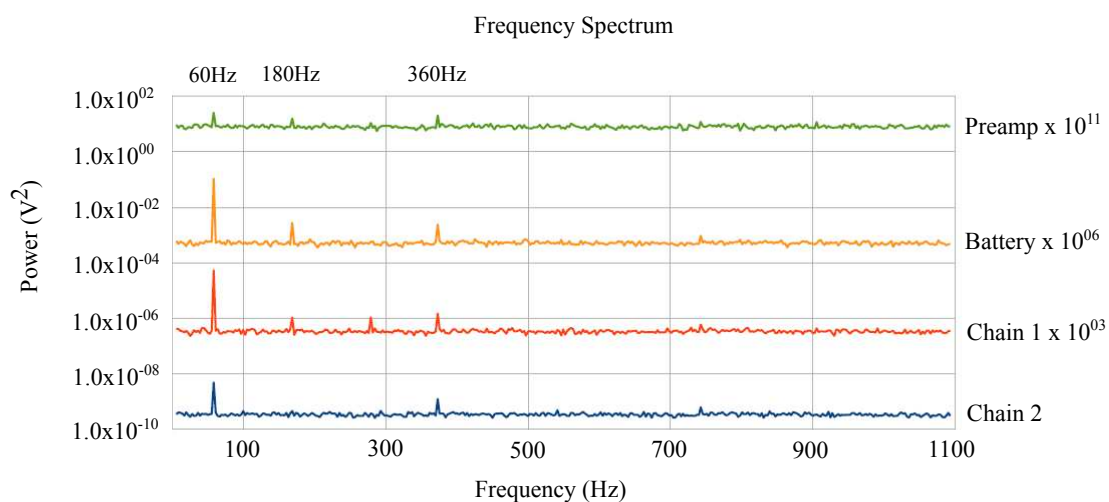


Figure 5.15: Frequency spectra of the preamplified current signals and the voltage signal from the setup in Figure 5.14. The preamp is an independent preamplifier located in the electronics room. All the spectra are in same units but are shifted along the vertical axis for comparison. The 60 Hz power line frequency and its harmonics are clearly present in all of the signals but they are more prominent in the signals coming from the hall (blue, red and orange) compared to the reference preamplifier signal located in the electronics room (green).



cables and the preamplifiers. The preamplified current signals from the hall are sensitive to both noise from the preamplifiers and the 60 Hz power line frequency in the coaxial cables. In comparison, the preamplified signal in the electronics room had a shorter coaxial cable and was dominated by preamplifier electronics noise rather than by 60 Hz. The frequency peak at 60 Hz and its multiples indicate the presence of power line harmonics in all four signals. The difference in the magnitude of the spectra of preamplifiers in the electronics room and the hall is presumably coming from power line harmonics in the coaxial cables. Chain 1 has a lower line harmonic content than chain 2. The difference in the magnitude between the 60 Hz and its harmonics in chain 1 and 2 could be due to a combination of coaxial cable noise and the quality of regulation between the two DC power supplies.

### ***5.3.1.3 Noise from cables, preamplifiers and power supplies***

The noise contribution from the preamplifiers and the power supplies was measured by switching the power supplies/preamplifiers between the two signal chains, chain 1 and chain 2, and observing the differences in the standard deviations of the measured signal distributions (see Appendix F.2). Overall, the difference observed between the two cases were below 0.1 ppm. Old cables and corroded connectors were identified to be the largest noise contributor. Replacing the cables and connectors reduced the standard deviations of the asymmetry distributions in chain 1 to about 3.6 ppm from 10 ppm (see Table 5.9). Since the noise from the cables and the connectors is often overlooked, the fact that they can contribute a noise content in the order of 10 ppm was an eye opener. With this observation, the experiment made sure to use good quality cables and connectors to transport detector signals. According to Table 5.9, under realistic conditions, using good cables and connectors, the measured noise levels on the voltage and current signals were in the 5 ppm level. This is two orders of magnitude smaller than a Čerenkov detector asymmetry distribution width at full luminosity. Therefore these measurements eliminated electronic noise coming from the detector electronics chain as a possible contributor to the experiments error.

### ***5.3.1.4 VQWK ADC channel noise***

Early table top measurements [145] carried out by Des Ramsey and Bill Roberts back in 2008 at TRIUMF using a 6 V voltage supply showed the noise in the VQWK ADC channels was in the range of 45  $\mu V$  to 90  $\mu V$ . The measurement

Table 5.9: Improved noise levels (identified by the RMS of the asymmetry distributions) when using new cables and connectors. The noise levels in chain 1 dropped to 3.6 ppm from about 10 ppm (see Appendix F.2, Table F.2.1). There was no beam in the hall during these measurements. The results are also given in terms of noise per root Hertz = (Average Signal $\times$ Asymmetry Std.)/VQWK ADC input bandwidth, for ease of conversion for different bandwidths associated with different event rates. The bandwidth of a VQWK ADC at 1 kHz rate is 130.21 Hz.

Channel	Signal (V)	Signal RMS ( $\mu V$ )	Asymmetry RMS (ppm)	Noise per root Hertz ( $\mu V/\sqrt{Hz}$ )
0	5.5	53.2	4.2	2.0
1	5.5	51.5	3.6	1.7
2	7.8	114.0	2.6	1.8

presented here used a separate setup where three 9 V voltage sources placed in the electronics room were used to measure the noise in the VQWK ADC channels. The results from this measurement are presented in Table 5.10. The noise levels measured in the three ADC channels are in agreement with the values presented in Ref. [145]. The contribution from channel noise into the standard deviation of the asymmetry distribution is about 1.5 ppm. This is well below the 660 ppm Čerenkov detector asymmetry widths at full luminosity.

### 5.3.2 Electronic Noise in the Detector Electronic Chains

During the commissioning period of the experiment in July of 2010, I measured the noise present in the 16 electronic chains<sup>18</sup> corresponding to the 16 Photomultiplier

Table 5.10: Results from the VQWK ADC channel noise measurement using 9 V voltage sources. The noise in the ADC channels is the standard deviation  $\sigma$  of the asymmetry distributions of the voltage sources.

Channel	Signal (V)	Signal $\sigma$ ( $\mu V$ )	Asymmetry $\sigma$ (ppm)	Noise per root Hertz ( $\mu V/\sqrt{Hz}$ )
0	9.1	44.3	1.2	1.1
1	8.1	36.4	1.5	1.1
2	8.9	47.9	1.2	0.9

<sup>18</sup>The electronic chains included the preamplifiers, coaxial cables, patch panels and the ADCs.

tubes (PMT's) of the Čerenkov detectors in their final configuration. The measurement setup used  $4.5 \mu A$  current sources with TRIUMF preamplifiers resulting in 9 V signals. The outputs from the preamplifiers were connected to coaxial cables which were patched through low noise channels<sup>19</sup> of the Hall C patch panel into the electronics room. In the electronics room they were read out via VQWK ADC modules assigned for the Čerenkov detector signal digitization. Two sets of data were collected with a 1 kHz rate and a four day gap in between them. The first data set was taken with the preamplified current sources connected to the electronics chains assigned for positive PMTs. The second data set was taken with the preamplified current sources connected to the electronics chains assigned for the negative PMTs.

The expected standard deviation of the asymmetry distribution from a  $4.5 \mu A$  current signal integrated for a 0.004 s is<sup>20</sup>

$$\sigma = \frac{1}{\sqrt{I \times t \times N_e}} = \frac{1}{\sqrt{4.5 \mu A \times 0.004 s \times 6.241 \times 10^{18}}} = 3 \text{ ppm.}$$

Table 5.11 shows that the measured average standard deviations of the signal chains are indeed about 3 ppm. The negative PMT chains are slightly noisier than the positive PMT chains. This could be explained by the increased activity in Hall C (construction work associated with  $Q_{\text{weak}}$  commissioning) during the time in which data were collected from the negative PMT chains. The negative PMT chain data were taken four days before the positive PMT chain data. However, both chains give standard deviations in the asymmetry distributions below 4 ppm. This observation confirmed that the as built Čerenkov detector electronics chains have contributions from electronic noise that are at the level of a few ppm.

At full beam luminosity, the statistical standard deviation of an asymmetry distribution from a single Čerenkov detector was expected to be around 600 ppm. The few ppm electronic noise in the signal chains was therefore negligible compared to 600 ppm and was not expected to contribute to the overall standard deviation of the measured asymmetries.

---

<sup>19</sup>The low noise channels in the Hall C patch panel chosen specifically for the use of  $Q_{\text{weak}}$  and the amount of noise in them based on my measurements are given in Appendix F.1.

<sup>20</sup>At 960 Hz, 1 event is about 1 ms. A quartet is 4 ms.

Table 5.11: Noise measured in the Čerenkov detector electronics chains using preamplified current sources. Results are given for both positive PMT and negative PMT chains in each detector. The standard deviation of the asymmetry distributions is about 3 ppm. All the channels measure zero asymmetries as expected. Slightly more data were collected for positive PMT compared to the negative PMT chains which explains the difference between the statistical errors.

Detector	Asymmetry (ppm)			
	Positive PMT Chain		Negative PMT Chain	
	Mean	$\sigma$	Mean	$\sigma$
1	0.012±0.011	2.46	-0.007±0.008	2.13
2	-0.003±0.012	2.72	-0.010±0.007	1.99
3	-0.005±0.013	3.00	-0.003±0.008	2.17
4	-0.004±0.014	3.30	-0.006±0.008	2.20
5	0.000±0.015	3.49	-0.008±0.008	2.04
6	0.007±0.016	3.68	-0.017±0.007	2.00
7	-0.001±0.017	3.92	-0.004±0.007	2.00
8	0.007±0.016	3.73	-0.011±0.008	2.12

### 5.3.3 Noise in LED driven PMTs

In April 2010, using a PMT connected to a Light Emitting Diode (LED) and a  $4.7 \mu\text{A}$  reference current source, I measured the noise in the PMTs used to collect the light from the Čerenkov detectors. The PMT and the LED were placed inside a black box to isolate them from background light sources. Both the current signal and the LED driven PMT signal were preamplified up to 4.5 V using TRIUMF preamplifiers. Both were patched through the Hall C patch panel to be read out by VQWK ADCs in the electronics room. The asymmetries and noise measured from the setup during a 10 hour long run are shown in Table 5.12. In the absence of excess noise in the LED+PMT system, the noise magnification between the  $4.7 \mu\text{A}$  current source and the 30.5 nA cathode current<sup>21</sup> from the LED should be 12.4 [143]. From the results in Table 5.12, this factor is 18.5. Therefore, there is an excess noise of

$$\sqrt{26.1^2 - (18.5 \times 1.4)^2} = 3.2 \text{ ppm},$$

present in the PMT+LED system which is presumably coming from either the PMT or the LED.

<sup>21</sup>Measured anode current was  $10 \mu\text{A}$  and the gain was 328.

Table 5.12: Noise in LED driven PMTs. Also shown is the noise in the reference current source of  $4.7 \mu\text{A}$ . Both signals are pedestal subtracted. Figure 5.16 shows the relevant asymmetry distributions.

Source	Average Signal (V)	Signal $\sigma$ (mV)	Asymmetry $\sigma$ (ppm)
PMT with LED	4.5	3.3	26.1
Current Source	4.3	0.1	1.4

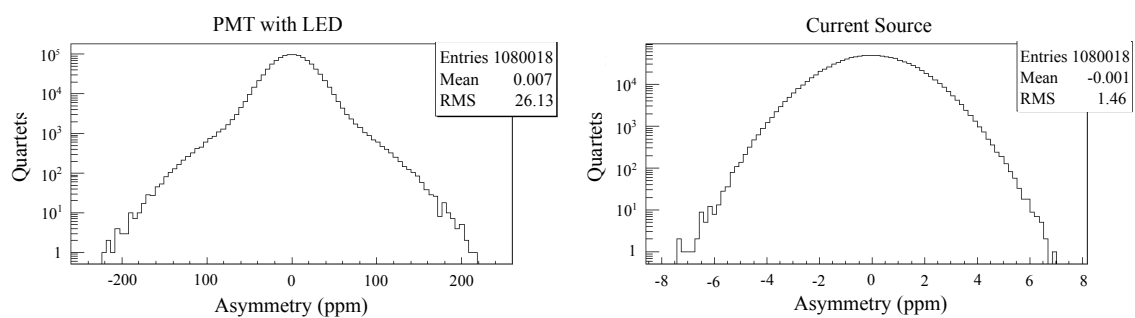


Figure 5.16: Asymmetry distributions of the LED driven PMT (left) and the current source (right) corresponding to Table 5.12. The non-gaussian shape of the PMT+LED asymmetry distribution indicates the presence of excess noise.

## 6 Beam Normal Single Spin Asymmetry Analysis

The  $Q_{\text{weak}}$  beam normal single spin asymmetry (BNSSA) (a.k.a the transverse asymmetry) measurements were performed during the two running periods of 2-8-2011 to 2-10-2011 (Transverse\_Run I) and 2-18-2012 to 2-20-2012 (Transverse\_Run II). I was responsible for the development and execution of the run plans and for carrying out the initial data analysis and asymmetry extraction. But for my dissertation, I will only concentrate on the full analysis of the beam normal single spin asymmetry from elastic electron-proton scattering. This chapter contains the details of the analysis.

### 6.1 Experimental Setup and the Full Data Set

The beam normal single spin asymmetry measurements used an identical setup to the parity violating asymmetry measurement with the obvious changes done at the injector to change the electron beam polarization to fully vertical/horizontal from the standard longitudinal orientation using the double Wien setup. Each adjustment in the double Wien was followed by a Mott measurement at the injector carried out by the Jefferson Lab polarized source group to confirm the magnitude and the orientation of the polarization<sup>1</sup>.

Two transverse spin orientations, vertical and horizontal, were used to study the leakage of beam normal single spin asymmetry into the parity violating asymmetry. Using vertical and horizontal transverse polarization allows to check for the asymmetry cancellation between the Čerenkov detectors 1 & 5 and 3 & 7. Since any polarization component in the transverse plane can be separated into a vertical and a horizontal component, data taken with these two polarization orientations provide a good estimate on the BNSSA leakage due to the broken symmetry of the Čerenkov detector array. A dedicated discussion on this estimation is presented in Chapter 7. At each spin orientation, events were collected from liquid hydrogen (LH2-cell), 4% thick downstream aluminum foil (DS4Al) and a 1.6% thick downstream carbon foil<sup>2</sup>

---

<sup>1</sup>Due to the small magnitude of the parity violating  $Q_{\text{weak}}$  asymmetry, a spin dance was not required to setup the Wien to avoid residual longitudinal polarization in the beam. A spin dance is a polarization measurement which uses the polarimeters in the experimental halls to identify the Wien angle which gives a maximum (zero) polarization in the longitudinal direction for longitudinal (transverse) polarization setup.

<sup>2</sup>The carbon data are not required for  $Q_{\text{weak}}$ . The intention here is to provide a measured asymmetry which will help to benchmark model calculations of two-photon exchange in heavy nuclei.

(C12) using a beam energy of 1.160 GeV. Table 6.1 shows the beam currents used on these targets. The Insertable Half Wave Plate (IHWP) was used for slow helicity reversal at intervals of about 2 hrs (see Appendix G.1 for the durations and the slug numbers).  $Q_{\text{weak}}$  also performed the first known measurements of the inelastic beam normal single spin asymmetries with a  $\Delta(1232)$  in the final state from all of these targets.

Table 6.1: Beam currents used on different targets during transverse running period. During Transverse\_Run I a 3.5 mm x 3.5 mm beam raster was used to scan the beam on the target but it was increased to 4.5 mm x 4.5 mm in Transverse\_Run II to minimize target boiling as the experiment reached its designed beam current goal of 180  $\mu\text{A}$ . The increase in beam current on DS4Al was to increase the statistics required for the aluminum background measurement of the main experiment.

Target	Beam Current ( $\mu\text{A}$ )	
	Transverse_Run I	Transverse_Run II
LH2-cell	145	170
DS4Al	24	70
C12	–	70

Out of the total data collected, the amount of usable data available for the analysis after hardware and software quality checks (see Subsection 4.2.1) are shown in Table 6.2. Roughly 1 % of the data were removed by hardware and software quality checks. From the total usable data in Table 6.2, the data used in the analysis presented in this dissertation are marked by a †. The analysis of the remaining data are still under way and will not be covered in this dissertation.

## 6.2 General Analysis Considerations

The general method used to extract asymmetries from the Čerenkov detector signals was explained in Subsection 4.2.1 of Chapter 4. Due to the azimuthal modulation behaviour of the beam normal single spin asymmetry, the analysis of the transverse asymmetries will focus on the azimuthal dependence of the Čerenkov detector asymmetries. When the beam is polarized transversely, the Čerenkov detectors

Table 6.2: Amount of transverse data available for analysis after quality cuts in terms of the total charge collected. A QTOR current of 8901 A represents elastic data while the rest represents inelastic data taken around the inelastic peak at a QTOR current of 6700 A. A dagger ( $\dagger$ ) marks the data used for the analysis in this dissertation.

Target	Polarization	QTOR (A)	Usable Data in Coulombs	
			T_Run I	T_Run II
LH2-cell	Vertical	6700 $\dagger$	–	1.9
		8901 $\dagger$	8.4	3.1
	Horizontal	6000	–	1.5
		6700 $\dagger$	–	1.8
		7300	–	2.0
8901 $\dagger$	–	8.6		
DS4A1	Vertical	6700 $\dagger$	–	0.4
		8901 $\dagger$	0.5	0.4
	Horizontal	6700 $\dagger$	–	0.8
		7300	–	0.9
		8901 $\dagger$	–	0.8
C12	Horizontal	6700	–	0.6
		8901	–	0.6

measure an azimuthal modulation of the asymmetry that can be parametrized by

$$A^T(\phi) = A^V \cos(\phi^V + \phi_0^V) + A^H \sin(\phi^H + \phi_0^H) + C, \quad (6.1)$$

where  $\phi$  is the azimuthal angle in the plane transverse to the beam direction with  $\phi = 0$  being at beam left,  $\phi_0$  is a phase offset in  $\phi$ ,  $A$  is the amplitude of the azimuthal modulation generated by BNSSA and  $C$  is a constant representing monopole asymmetries such as the parity violating asymmetry generated by residual longitudinal polarization in the beam. The superscripts V/H stand for vertical/horizontal components. In the two specific transverse polarization configurations, Equation 6.1 simplifies to

$$f(\phi) = \begin{cases} A^V \cos(\phi^V + \phi_0^V) + C^V & \text{Vertical,} \\ A^H \sin(\phi^H + \phi_0^H) + C^H & \text{Horizontal.} \end{cases} \quad (6.2)$$

Broadly speaking, the analysis of the different transverse data sets presented in this chapter will use Equation 6.1 as the azimuthal fit of the asymmetries measured from the detector array, the average of the two PMT asymmetries for the asymmetry



from a single detector and the error weighted average of the asymmetries from 5 min long data samples (runlets)<sup>3</sup> as the average asymmetry from a given data set.

### 6.3 Azimuthal Dependence of the Raw Asymmetry

Figure 6.1 shows the azimuthal dependence of the raw Čerenkov detector asymmetries (not corrected for backgrounds, polarization or other experimental related systematics) extracted from the LH2-cell target. As discussed in the figure, the average of the PMT asymmetries is a good representation of the asymmetry for the full Čerenkov detector. A -4.5 ppm azimuthal modulation seen in the raw asymmetries indicates the beam normal single spin asymmetry in  $Q_{\text{weak}}$  kinematics is a factor of 20 larger than the parity violating asymmetry. The raw asymmetries measured using vertical and horizontal transverse polarization are shown in Figure 6.2. As expected from the azimuthal dependence of the beam normal single spin asymmetry, there is a  $90^\circ$  phase offset between the two modulations.

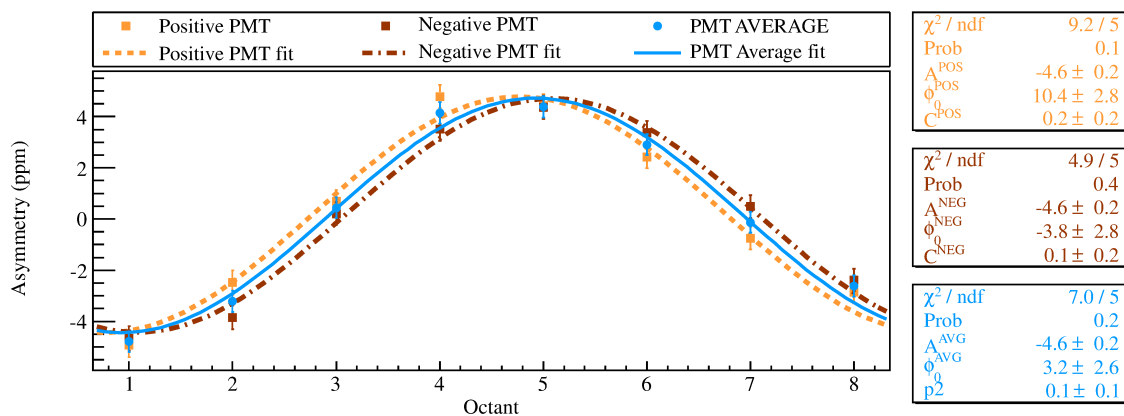


Figure 6.1: Azimuthal dependence of the raw asymmetries from the LH2-cell target from a 2 hour long measurement with vertical transverse polarization. The PMT AVERAGE is the average asymmetry of the positive (POS) and negative (NEG) PMTs. As expected for beam normal single spin asymmetry from a vertical transverse polarized beam, the asymmetries have a cosine modulation with the Čerenkov detectors in octants 1 & 5 measuring a maximum asymmetry and Čerenkov detectors in octants 3 & 7 measuring a null asymmetry. The  $6^\circ$  phase shift between the positive and negative PMT asymmetries is expected as a result of the averaging in the azimuthal angle. This will be discussed later in Subsection 6.5.1.

<sup>3</sup>During data collections, run segments were broken down into 5 min short samples for ease of data acquisition and analysis.

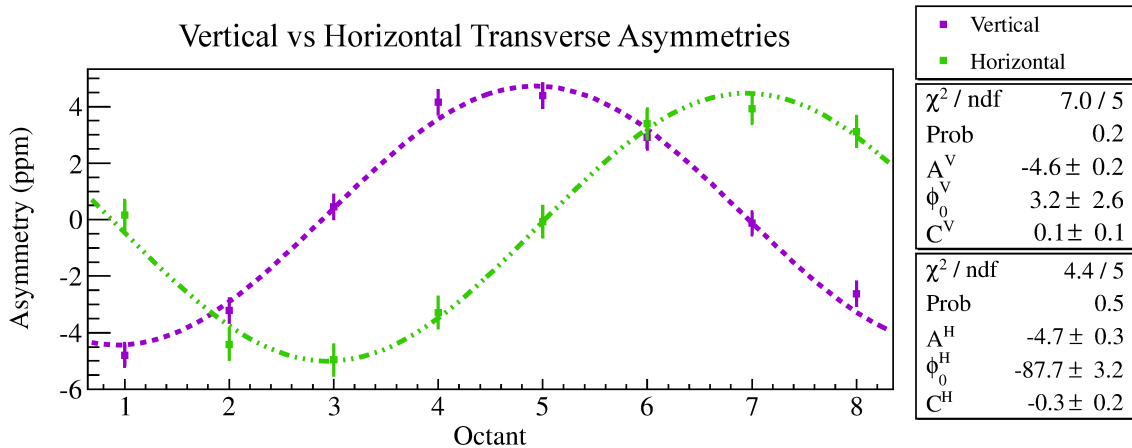


Figure 6.2: Comparing the azimuthal dependence of the raw asymmetries from the LH2-cell target with vertical and horizontal transverse polarization. Each data set is a 2 hour long measurement. The cosine fit used over the asymmetries in each case clearly shows  $90^\circ$  phase offset expected between vertical and horizontal configurations.

#### 6.4 Beam Asymmetry Correction Using Linear Regression

Before extracting the physics asymmetry, the raw asymmetries need to be corrected for beam asymmetries generated by helicity correlated beam parameters. Beam asymmetries are a type of false asymmetry generated into the Čerenkov detector asymmetry due to helicity correlated changes in the electron beam energy, position and angle which change the effective scattered angle and energy of the electrons in the detector acceptance. A multi-variable linear regression [133] is used to remove the beam asymmetries from the raw Čerenkov detector asymmetries such that

$$A_j^{Reg} = A_j^{Raw} - \sum_i \left( \frac{\partial A_j^{Raw}}{\partial B_i} \right) \Delta B_i, \quad (6.3)$$

where  $A_j^{Reg}$  is the regressed asymmetry of the  $j^{th}$  Čerenkov detector and  $\frac{\partial A_j^{Raw}}{\partial B_i}$  is the sensitivity of the raw asymmetry  $A_j^{Raw}$  to the  $i^{th}$  beam asymmetry/difference  $\Delta B_i$ .

The asymmetries presented in this dissertation are regressed against five-beam parameters: vertical and horizontal position differences, vertical and horizontal angle differences and the energy asymmetry. The amount of correction applied to the raw asymmetries depends on the size of the helicity correlated beam asymmetry  $\Delta B_i$  and the sensitivity  $\frac{\partial A_j^{Raw}}{\partial B_i}$  and is discussed in more detail in the following subsections.

### 6.4.1 Helicity Correlated Beam Asymmetries Measured at the Target

The typical time variations of the charge ( $A_Q$ ) and the energy ( $A_E$ ) asymmetries observed during the transverse running period are shown in Figure 6.3. These particular asymmetries are stable within the measurement period and similar stability was observed with the horizontal and vertical beam position and angle differences (see Figure G.3 in Appendix G.2). The distributions of the HCBA are shown in Figure 6.4.

As a reminder from Subsection 5.1.1, the slow helicity reversal applied by the IHWP provides a cancellation of HCBA generated by polarization effects (see Table 5.4 in Subsection 5.1.2.5). These HCBA contribute with the same sign to the two IHWP states and can be determined from the average  $(\text{IN}+\text{OUT})/2$  of data taken with IHWP IN/OUT of the beam. The net HCBA which contribute to the measured Čerenkov detector asymmetries are obtained by correcting the data for

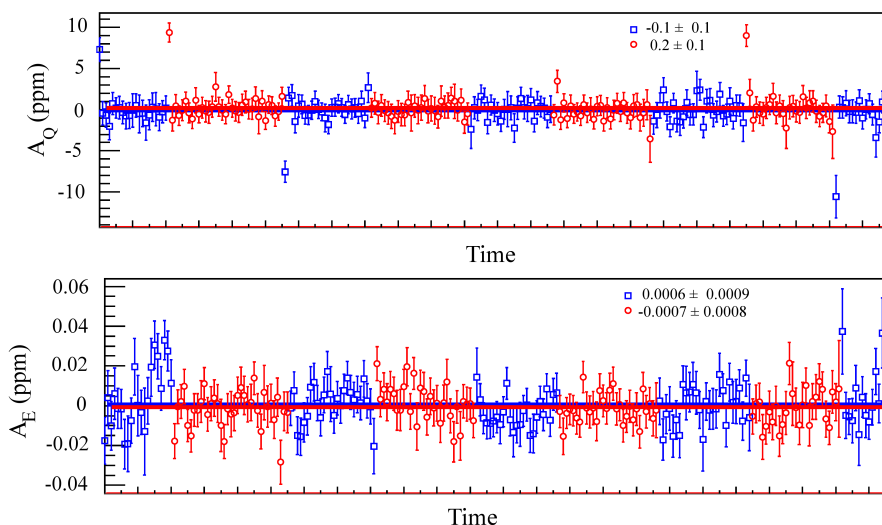


Figure 6.3: Typical helicity correlated charge and energy asymmetries at the target. Each data point represents a 5 minute data sample and the full panel represents about 14 hours of beam time. Red (blue) are data with IHWP OUT (IN). The printed values give the results from the constant fits over the two IHWP data sets. The asymmetries are stable within the measurement period and the averages are consistent with zero. The outliers at the beginning of each new IHWP period in the charge asymmetry plot are associated with the charge feedback operation (see Ref. [41] for the details).

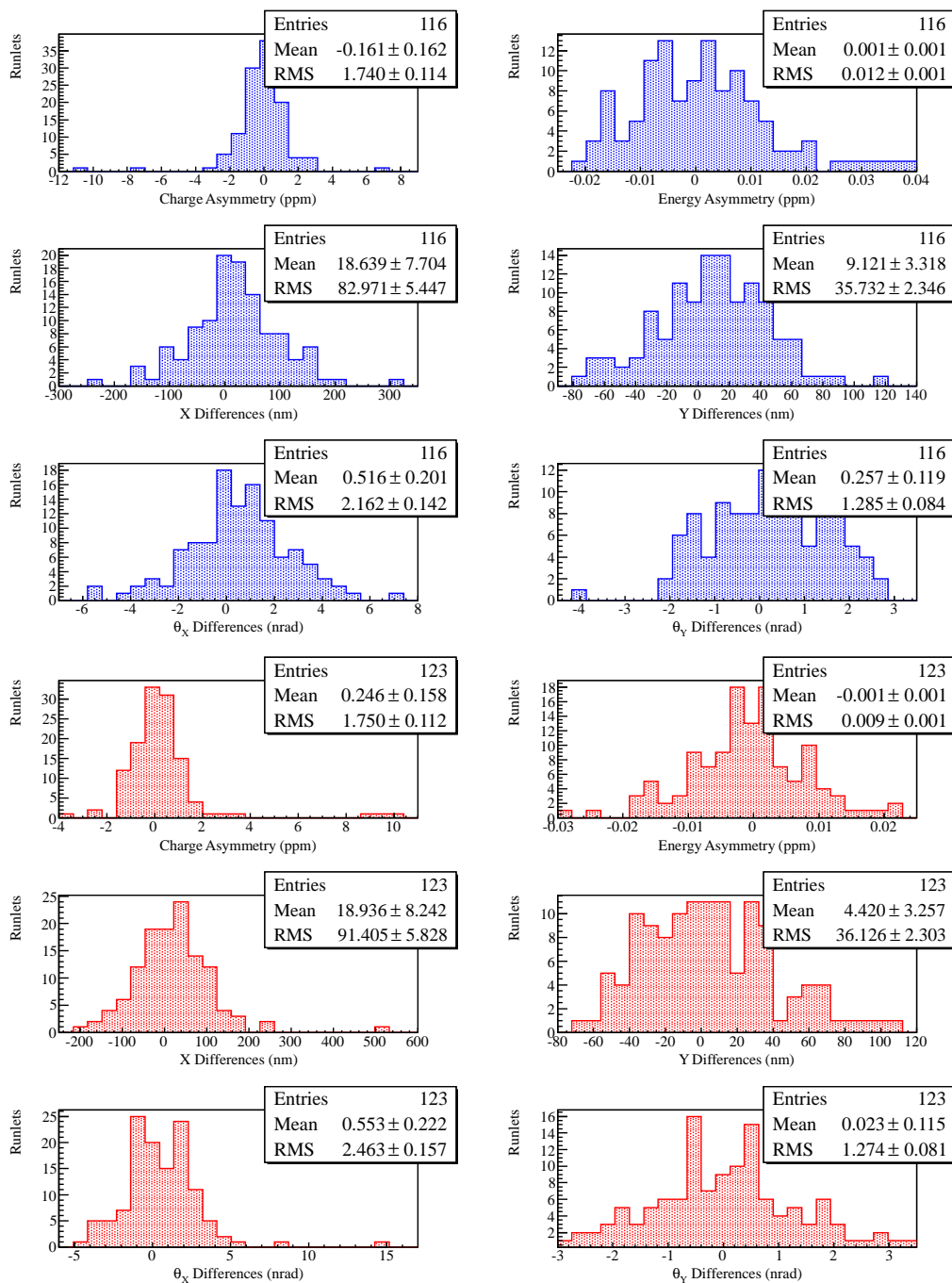


Figure 6.4: Helicity correlated beam asymmetry distributions from the high current LH2-cell period. The IHWP IN (OUT) data are shown in blue (red). Each entry is a 5 minute long measurement. The distributions are generally Gaussian with one or two outliers. The means are consistent with zero except in X position differences which are slightly large ( $\approx 2.5$  sigma deviation) and does not change sign with the IHWP.

the IHWP reversal<sup>4</sup> and taking the error weighted average between IN and -OUT, denoted by AVG(IN,-OUT). Table 6.3 shows these two quantities in the vertical and horizontal transverse running periods. The difference between Transverse\_Run I and Transverse\_Run II HCBA can be attributed to the different beam transportation configurations used in the accelerator for beam delivery with vertical and horizontal transverse polarization.

### 6.4.2 Detector Sensitivities to HCBA

The sensitivity of the Čerenkov detectors to helicity correlated beam asymmetries has the azimuthal dependence shown in Figure 6.5. This behaviour is a result of the changes in the scattered electron profile as mentioned earlier, and is not spe-

Table 6.3: Average helicity correlated beam asymmetries measured during the vertical and horizontal transverse running periods with the LH2-cell target. Transverse\_Run I has the relatively worst HCBA content dominated by X position differences and can be expected to provide the largest beam asymmetry correction to the Čerenkov detector asymmetries. Notice that even though dX is large in both IN and OUT data for Transverse\_Run I and Transverse\_Run II, the dX in Transverse\_Run II are generated from non-polarization effects and therefore gets cancelled out in the AVG(IN,-OUT).

Parameter	IN	OUT	(IN+OUT)/2	AVG(IN, -OUT)
Transverse Run I with Vertical Polarization				
$A_Q$ (ppm)	$0.8 \pm 0.4$	$-0.2 \pm 0.4$	$0.3 \pm 0.4$	$0.5 \pm 0.3$
$A_E$ (ppm)	$0.003 \pm 0.001$	$-0.014 \pm 0.001$	$-0.006 \pm 0.001$	$-0.009 \pm 0.001$
$dX$ (nm)	$-45.2 \pm 4.5$	$33.8 \pm 4.8$	$-5.7 \pm 3.3$	$-39.8 \pm 3.3$
$dY$ (nm)	$36.8 \pm 4.8$	$9.5 \pm 6.0$	$23.2 \pm 3.8$	$18.5 \pm 3.8$
$d\theta_X$ (nrad)	$-0.9 \pm 0.1$	$0.3 \pm 0.1$	$-0.3 \pm 0.1$	$-0.6 \pm 0.1$
$d\theta_Y$ (nrad)	$1.6 \pm 0.2$	$0.4 \pm 0.2$	$0.1 \pm 0.1$	$0.8 \pm 0.1$
Transverse Run II with Horizontal Polarization				
$A_Q$ (ppm)	$0.3 \pm 0.2$	$-0.2 \pm 0.16$	$0.1 \pm 0.2$	$0.2 \pm 0.1$
$A_E$ (ppm)	$-0.004 \pm 0.001$	$0.001 \pm 0.001$	$-0.002 \pm 0.001$	$-0.003 \pm 0.001$
$dX$ (nm)	$18.9 \pm 8.2$	$18.6 \pm 7.7$	$18.8 \pm 5.6$	$-1.1 \pm 5.6$
$dY$ (nm)	$4.4 \pm 3.3$	$9.1 \pm 3.3$	$6.8 \pm 2.3$	$-2.2 \pm 2.3$
$d\theta_X$ (nrad)	$0.6 \pm 0.2$	$0.5 \pm 0.2$	$0.5 \pm 0.2$	$0.0 \pm 0.1$
$d\theta_Y$ (nrad)	$0.0 \pm 0.1$	$0.3 \pm 0.1$	$0.2 \pm 0.1$	$-0.1 \pm 0.1$

<sup>4</sup>For the transverse data, IHWP OUT asymmetries needs to be sign corrected for the IHWP reversal. See Appendix D.5 for the details.

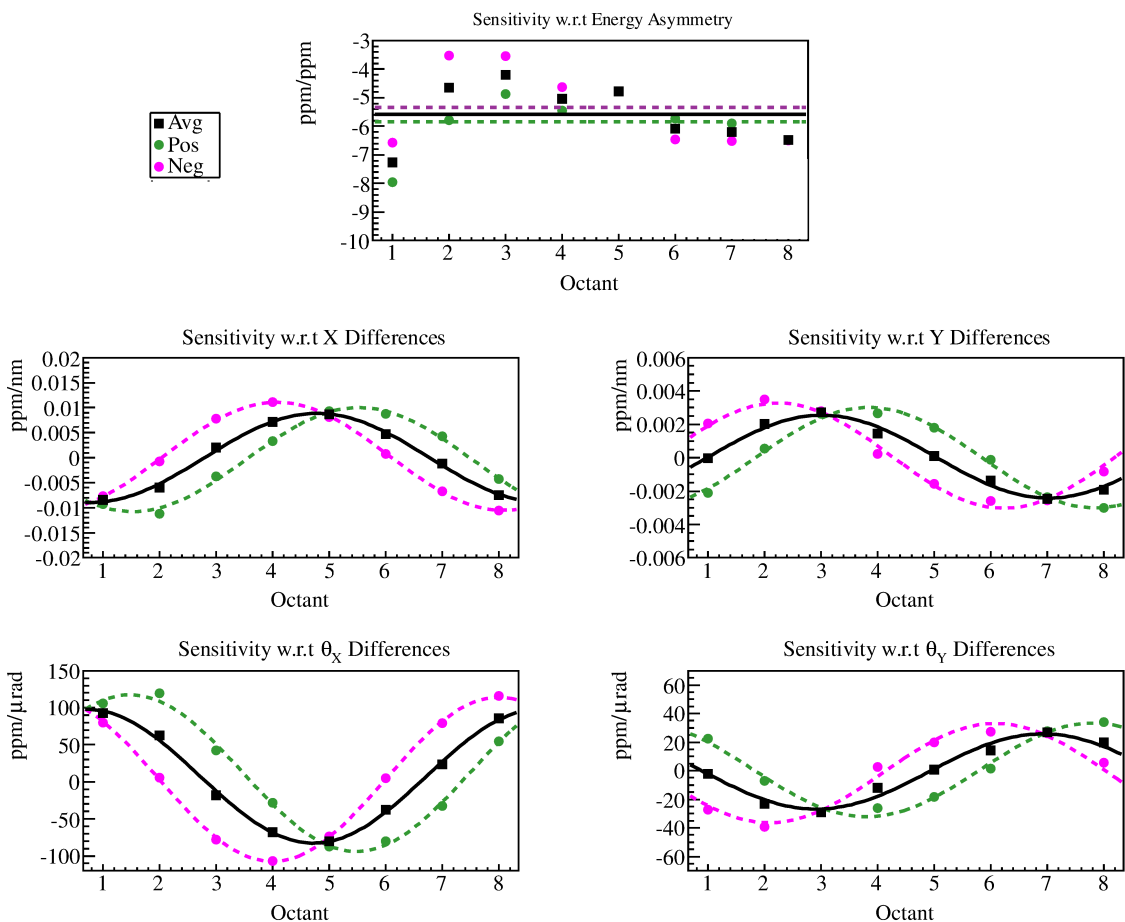


Figure 6.5: Azimuthal dependence of the Čerenkov detector sensitivities to HCBA in the horizontal LH2-cell transverse data set. For comparison, the sensitivities of the positive and negative PMTs are also shown. See text for explanation. See Appendix G.3 for the sensitivities from other transverse data sets.

cific to the beam normal single spin asymmetry measurement. The behaviour of the position and angle sensitivities are a result of the movement of the scattered electron profile across the bars which changes the effective scattering angle of the detected electrons. Čerenkov detectors which are normal (parallel) to the fluctuations in the scattered electron profile experience large (no) changes in the acceptance. The energy sensitivity is not expected to have an azimuthal dependence since it does not change the acceptance. However, the energy asymmetry calculation (see Subsection 3.4.3), which relies on position and angle changes to extract the energy, is not perfect and is known to be correlated to position and angle differences in X. Moreover, X and Y positions are known to be correlated at the target due to residual dispersion in the

beam. Both of these phenomena explain the observed azimuthal dependence of the energy sensitivities in terms of the azimuthal dependence of the X and Y sensitivities.

### 6.4.3 Beam Asymmetry Correction

The amount of correction to be applied on the raw Čerenkov detector asymmetries to remove the Čerenkov detector sensitivities to HCBA can be estimated by taking the difference between the regressed asymmetries and the raw asymmetries (see Figure 6.6). Using this method, the largest correction applied on a Čerenkov detector is observed to be about 0.3 ppm and it is smaller than the 0.4 ppm statistical error on an asymmetry measurement at the slug scale (2 hours). As expected from the discussion in Subsection 6.4.1, the azimuthal dependence of the corrections indicate the dominance of the beam asymmetry generated by horizontal (X) position differences. The differences between the total correction applied on the vertical and horizontal transverse asymmetries are explained by the differences between the relative magnitudes of the measured HCBA in the two running periods. Figure 6.7 shows the changes in the azimuthal fits over the raw asymmetries after applying above discussed beam asymmetry corrections. Due to the size of the measured asymmetry, the 0.3 ppm beam asymmetry correction applied on the raw asymmetries do not have a significant effect on the amplitude of the azimuthal fit. Note that this obser-

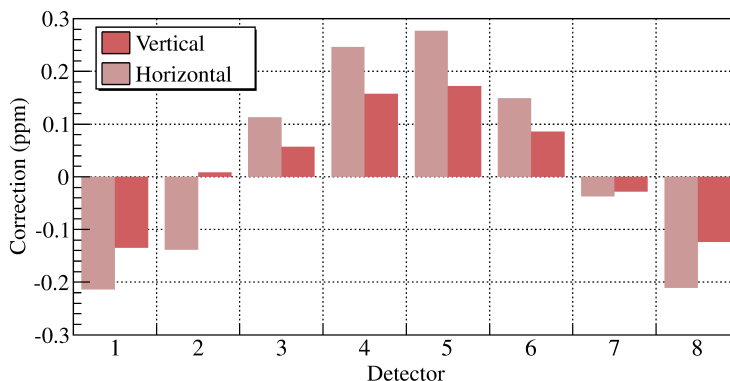
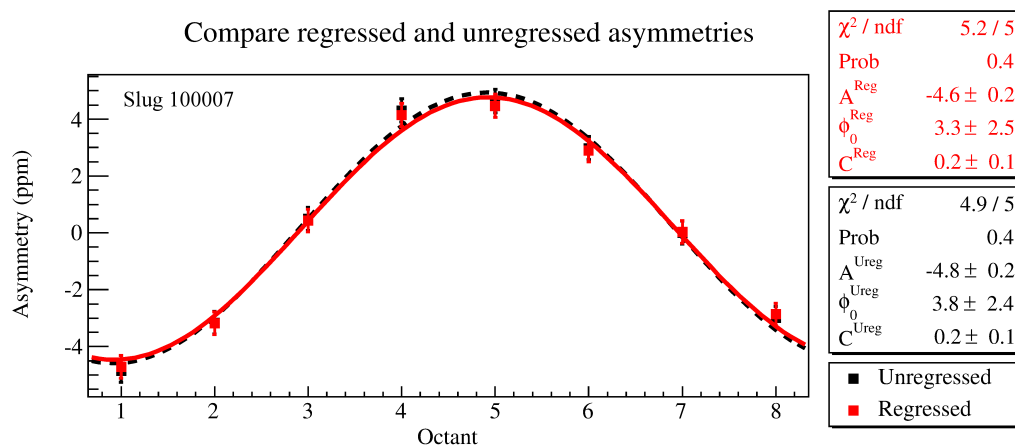
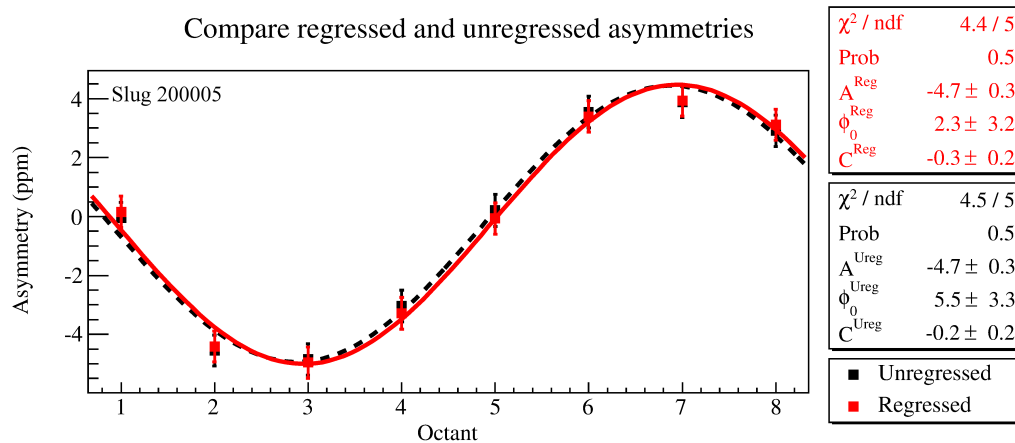


Figure 6.6: Total beam asymmetry corrections applied on the raw Čerenkov detector asymmetries measured from the LH2-cell target in Transverse\_Run II. The correction is the difference between the raw asymmetry  $A^{Raw}$  and the five-parameter regressed asymmetry  $A^{Reg}$ . The largest correction applied on a Čerenkov detector is about 0.3 ppm. Each data set is about 2 hours long.

vation prompted the use of Čerenkov detectors for residual transverse polarization monitoring as discussed in Chapter 7.



(a) Vertical Transverse



(b) Horizontal Transverse

Figure 6.7: Effect of linear regression on the azimuthal dependence of the Čerenkov detector asymmetries. The data set is a 2 hour long measurement from the LH2-cell target in Transverse\_Run II. Each data point represents about 2 hours worth of data. Applying regression does not effect the amplitude of the fits but it does improve the phase offset.



## 6.5 Azimuthal Modulating Physics Asymmetry

The azimuthal modulating physics asymmetry is extracted using the five-parameter regressed Čerenkov detector asymmetries. But prior to extracting the physics asymmetry from the LH2-cell target, the regressed asymmetries measured in the IHWP configurations need to be sign corrected for the extra spin flip and averaged together after checking for the IHWP cancellation of the false asymmetries. Figure 6.8 shows that overall, the IHWP cancellation or  $(IN+OUT)/2$  of the regressed asymmetries from the LH2-cell target are zero within the measurement errors. This indicates the azimuthal modulating component in both IHWP IN and OUT asymmetries are similar and the non-polarization dependent false beam asymmetries were successfully removed by regression. With this observation, the two data sets are averaged as  $AVG(IN,-OUT)$  to extract the physics asymmetry as shown in Figure 6.9 are summarized in Table 6.4. After incorporating the asymmetry averaging over the detector acceptance, detector non-linearity and regression scheme dependence (all of which are discussed in the following subsections), the physics asymmetry measured from the full LH2-cell target data set is

$$A_{LH2-cell}^{Phys} = -4.835 \pm 0.057_{Stat} \pm 0.102_{Sys} \text{ ppm}, \quad (6.4)$$

where the subscripts Stat (Sys) identifies the statistical (systematic) error.

Table 6.4: The physics asymmetry extracted from the LH2-cell target using the fits shown in Figure 6.9. Due to similar beam energy, polarization and  $Q^2$  (discussed later), the average of the three running periods will be used as the physics asymmetry from the combined LH2-cell target data set.

Transverse_Run	Polarization	Physics Asymmetry (ppm)
I	Vertical	$-4.807 \pm 0.090$
II	Vertical	$-4.701 \pm 0.142$
	Horizontal	$-4.841 \pm 0.085$
Error weighted average		$-4.805 \pm 0.057$ (stat)

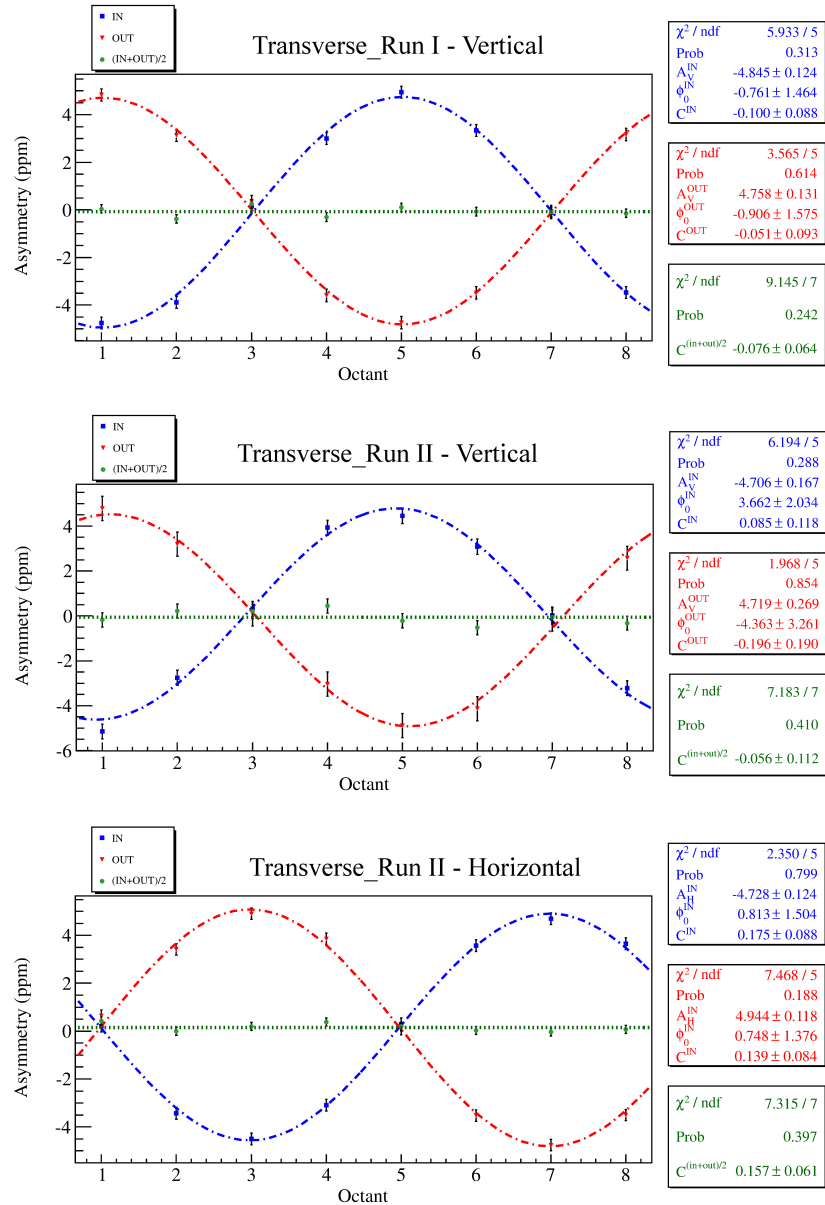
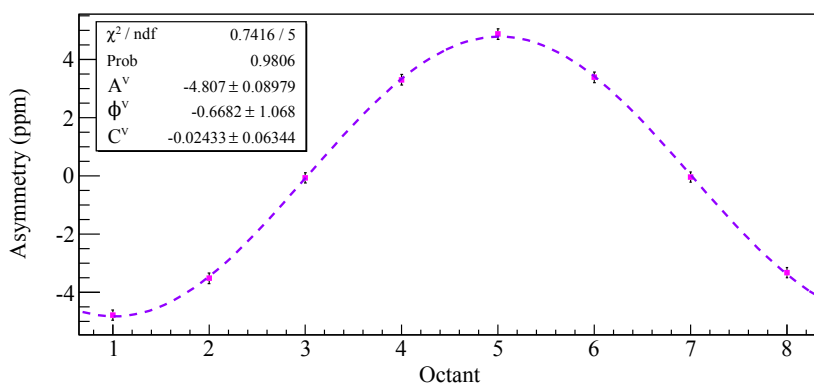
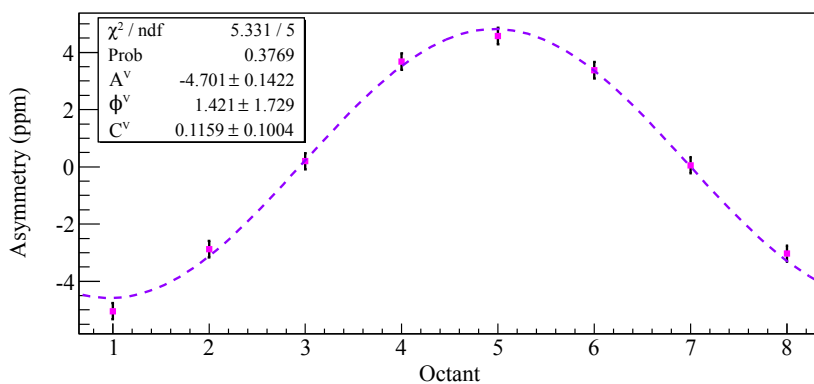


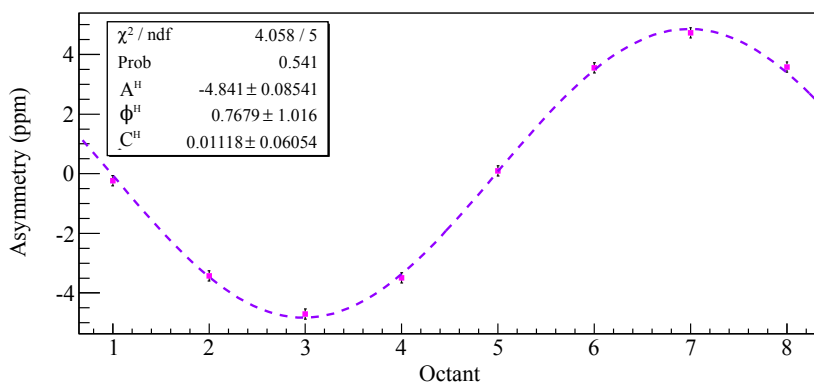
Figure 6.8: Azimuthal dependence of the  $(\text{IN}+\text{OUT})/2$  of regressed asymmetries grouped by the three distinct running periods in the LH2-cell target elastic configuration. For comparison, asymmetries for IN and OUT data are also shown. As expected from spin dependent asymmetries, the regressed asymmetries change sign with the insertion of the IHWP with comparable amplitudes. The  $(\text{IN}+\text{OUT})/2$  of the eight Čerenkov detectors, given by  $C^{(\text{In}+\text{Out})/2}$  is compatible with zero except in the horizontal data set. But what is relevant for the BNSSA extraction is the amplitudes in the fits and by comparison one can see that IN and OUT amplitudes are compatible with one another.



(a) With vertical transverse polarization in Transverse\_Run I



(b) With vertical transverse polarization in Transverse\_Run II



(c) With horizontal transverse polarization in Transverse\_Run II

Figure 6.9: Azimuthal depending physics asymmetry from the LH2-cell target. Each data point is the AVG(IN,-OUT) of the five-parameter regressed asymmetry from the relevant data set.

### 6.5.1 Detector Acceptance Correction

By design, the acceptance of a single Čerenkov detector is only 49% of an octant. Therefore the reported asymmetry from a detector is an average asymmetry over a  $22^\circ$  azimuthal angle. To take into account the averaging over the acceptance, a correction is applied to the extracted physics asymmetry following the prescription in Ref. [146].

Consider a Čerenkov detector centered at an azimuthal angle of  $\phi_0$  spanning  $\phi_0 - \Delta\phi$  and  $\phi_0 + \Delta\phi$  in the azimuthal plane (see Figure 6.10). Assuming that each half of the Čerenkov detector has equal weighting, the azimuthal averaging of the cosine over the range  $\phi_0 - \Delta\phi$  to  $\phi_0 + \Delta\phi$  is,

$$\overline{\cos \phi} = \frac{\int_{\phi_0 - \Delta\phi}^{\phi_0 + \Delta\phi} \cos \phi d\phi}{(\phi_0 + \Delta\phi) - (\phi_0 - \Delta\phi)} = \cos \phi_0 \frac{\sin \Delta\phi}{\Delta\phi}, \quad (6.5)$$

and similarly  $\overline{\sin \phi} = \sin \phi_0 \frac{\sin \Delta\phi}{\Delta\phi}$ . Hence the averaging over the azimuthal angle scales the measured asymmetry in each Čerenkov detector by a factor of  $\frac{\sin \Delta\phi}{\Delta\phi}$ . Therefore, for  $\Delta\phi = \pm 11.03^\circ$ , the physics asymmetry extracted from the azimuthal fits should be scaled by a factor of 0.9938 yielding

$$A_{LH2-cell}^{Phys} = -4.805/0.9938 = -4.835 \text{ ppm}. \quad (6.6)$$

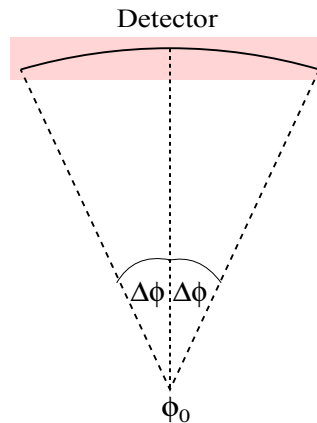


Figure 6.10: Illustration of the azimuthal ( $\phi$ ) averaging of a Čerenkov detector located at the azimuthal angle  $\phi_0$ . The asymmetry measured by this detector will be an average asymmetry over the electrons scattered into the  $2\Delta\phi$  angle spanned by the detector.

This is the method available at the time to apply this correction. A conservative error of 50% will be applied on the correction.

### 6.5.2 Regression Scheme Dependence

The beam asymmetry correction applied on the Čerenkov detector asymmetries are seen to have a small dependence on the type of beam monitors used to measure helicity correlated beam asymmetries with. These changes are typically generated by the differences in the intrinsic properties of the beam monitors such as the intrinsic resolution, non-linear response, etc.

To identify these types of systematics associated with beam asymmetry correction, the  $Q_{\text{weak}}$  collaboration currently uses 12 types of regression schemes with different combinations of beam monitors. Out of these 12 schemes, to study the beam monitor (or regression scheme) dependence of the transverse data set, I chose the five schemes (see Table 6.5) that contain beam monitors<sup>5</sup> which are common to both Transverse\_Run I and Transverse\_Run II. On average, the corrections applied by the different regression schemes on an individual Čerenkov detector asymmetry are comparable at the  $\pm 0.10$  ppm level and are smaller than the  $\pm 0.17$  ppm statistical uncertainty of the data set. But below 0.1 ppm level, one can see a difference between the corrections which are resulting from the choice of beam monitors (see Figure 6.11). These changes appear in the physics asymmetries below the 0.04 ppm level as shown in Table 6.6.

Table 6.5: Regression schemes used to study the regression scheme dependence of the beam asymmetry corrections.

Scheme	Independent Variables		
	Position and angle	Energy	Charge
on	qwk_target	qwk_energy	-
on_5+1	qwk_target	qwk_energy	qwk_charge
on_set3	qwk_target	qwk_bpm3c12	qwk_charge
on_set7	qwk_bpm3h09, qwk_bpm3h04	qwk_bpm3c12	-
on_set8	qwk_bpm3h09, qwk_bpm3h04	qwk_bpm3c12	qwk_charge

<sup>5</sup>Note that, in Transverse\_Run I, the combination of BPMs used for the beam projection on the target (see Subsection 3.4.1.5) includes the 3H09B BPM but in Transverse\_Run II it does not. Also, the average beam charge in Run I was obtained from the average of BCM1 and BCM2 where as in Run II it was obtained from BCM8.

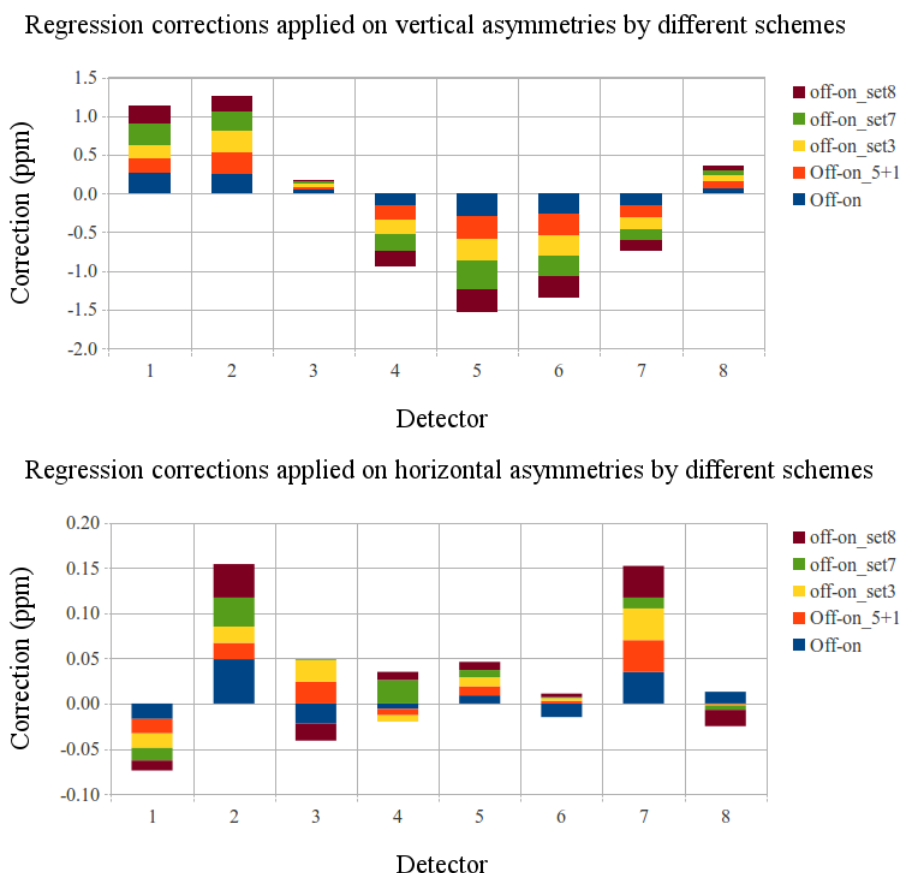


Figure 6.11: Comparing beam asymmetry corrections applied by different regression schemes on the LH2-cell vertical (top) and horizontal (bottom) data. Correction = unregressed average asymmetry ("off") - regressed asymmetry (see Appendix G.8 for the values). Making this calculation is possible since all the regressed and the raw asymmetries have the same statistics. The corrections from the different schemes are comparable to each other at the 0.1 ppm level. Note the corrections from different schemes are stacked on top of one another for easy comparison and the vertical scales on the two plots are different. The Transverse\_Run I dataset with the large horizontal position differences have similar correction from all of the regression schemes. The horizontal dataset measured in Transverse\_Run II have corrections which are an order of magnitude smaller than the previous dataset. Recall from Table 6.3, the HCBA in this particular data set was statistically compatible with zero. Therefore the differences between the corrections from the different schemes in this data set are dominated by the subtle differences coming from the choice of beam monitors.

The beam monitor dependence of the physics asymmetry extracted from the different regression schemes are shown in Table 6.7 and Figure 6.12. The choice of regressing the detector asymmetry against the charge asymmetry, changes the physics

Table 6.6: Regression scheme dependence of the physics asymmetry from the LH2-cell target. The physics asymmetries are comparable with each other at the 0.04 ppm level. The azimuthal dependent raw asymmetry ("off") is also shown for comparison.

reg. scheme	Physics Asymmetry (ppm)	
	Vertical	Horizontal
off	$-4.539 \pm 0.090$	$-4.844 \pm 0.086$
on	$-4.807 \pm 0.090$	$-4.840 \pm 0.085$
5+1	$-4.804 \pm 0.090$	$-4.845 \pm 0.085$
set3	$-4.804 \pm 0.090$	$-4.845 \pm 0.085$
set7	$-4.836 \pm 0.090$	$-4.854 \pm 0.085$
set8	$-4.801 \pm 0.090$	$-4.842 \pm 0.085$

asymmetry by as much as 0.005 ppm. In theory, the detector asymmetries should not be sensitive to the charge asymmetry since the detector yields are charge normalized prior to forming the asymmetries. But in practice, due to the non-linearity of the experimental signal, higher order effects could be present in the charge normalized Čerenkov detector asymmetries, leaving a small sensitivity to the charge asymmetry. The exact relationship between the charge asymmetry and the charge normalized regressed Čerenkov detector asymmetries is not properly understood yet. Therefore, the analysis of the transverse data presented here does not use charge asymmetry in regression. Instead, the charge asymmetry dependence of the regressed detector asymmetries will be addressed as a systematic uncertainty in Subsection 6.5.3.

Moving onto the remaining beam parameters, the differences between "on-5+1" and "on-set3" indicate the choice of energy variable has no noticeable effect on the physics asymmetry. The largest difference between the schemes are seen for the choice of monitor used for beam position and angle estimations. From "on-set7", using the two BPMs compared to the five BPM target combination causes the physics asymmetry to shift by as much as 0.029 ppm. Surprisingly though, "on-set8" shows that with charge regression, this shift goes down to about 0.006 ppm. This charge sensitivity of the beam position and angle differences is a known effect which is currently being investigated.

Using 3H04 and 3H09 BPMs to estimate the beam position and angle at the target provides twice as much angle resolution in the measured angle than what is

provided by the `qwk_target` BPM<sup>6</sup>. However, there are certain aspects of BPM 3H04 (resolution, non-linearity) that needs to be adjusted and understood prior to using it to determine the level of angle sensitivity required by  $Q_{\text{weak}}$ . In addition, there is a set of magnets located between 3H04 and 3H09 which are used to move the beam vertically by approximately 2 cm to get it into the plane of the Hall C. The effect of these magnets on the linear fit over 3H04 and 3H09 is still unknown and needs to be investigated.

Due to the large physics asymmetry and the small size of the scheme dependence compared to the measurement uncertainty (0.029 ppm compared to 0.08 ppm), the transverse analysis does not require further improvements in the regression. Therefore, the regression of the transverse asymmetries is performed using five-parameter or the "on" regression scheme with the combinations of beam moni-

Table 6.7: Differences between the LH2-cell physics asymmetry extracted from five-parameter regression and other regression schemes. See Figure 6.12 for the illustration. The largest difference comes from the use of the composite BPM (target BPM) vs the BPM pair 3H09 and 3H04 for beam position and angle measurements at the target.

	"on" - "5+1"	"on" - "set3"	"on" - "set7"	"on" - "set8"
vertical	-0.003	-0.003	0.029	-0.006
horizontal	0.005	0.005	0.014	0.002

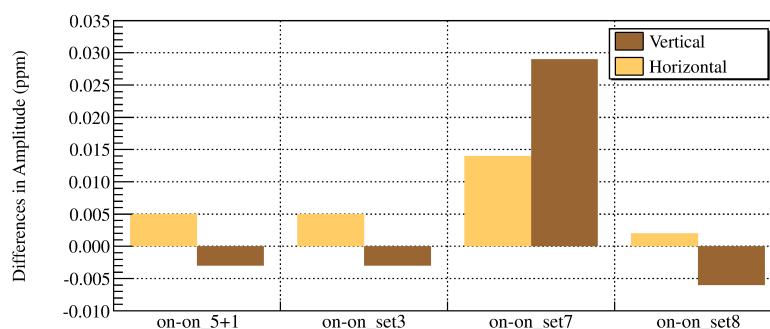


Figure 6.12: Figure relevant to Table 6.7 showing the differences between the LH2-cell physics asymmetries extracted using five-parameter regression and the other regression schemes.

<sup>6</sup>3H04 and 3H09 have a 16 m separation compared to the 9 m separation between the end BPMs in the target BPM combination.



tors (qwk\_target and qwk\_energy) to determine the beam position, angle and energy at the target. However, to take into account the choice of using "on" regression scheme over any of the other regression schemes,  $(dA^{Phys})_{\text{Reg.}} = \pm 0.029$  ppm will be assigned as a systematic uncertainty on the extracted physics asymmetry  $A^{Phys}$ .

### 6.5.3 Non-linearity of the System

The non-linearity of the BCM electronics, the Čerenkov detector electronics and target density fluctuations can induce non-linear distortions in the physics asymmetry and the charge asymmetry [147]. This non-linearity of the system is seen in the non-zero correlation between the regressed Čerenkov detector asymmetries and the charge asymmetry shown in Figure 6.13. Attempts [86] have been made to remove this non-linearity by adjusting (or optimizing) the pedestals of the BCMs. But the pedestals could only be adjusted within a small current range and they were time dependant due to drifts in the BCM electronics. In the transverse data analysis, optimized pedestals were only used for the analysis of Al27 data taken in Transverse\_Run I with the small beam current of  $24 \mu\text{A}$ . It is a well known fact that at lower beam currents, the BCMs are highly non-linear. Therefore it was necessary to use optimized pedestals for the analysis of these low current Al27 data (see Subsection 6.6.2.1).

As of Summer 2013, there is no clear method for separating the non-linearity distortions of the physics asymmetry and the charge asymmetry. However, with the use of charge normalized Čerenkov detector signals and the active charge feedback

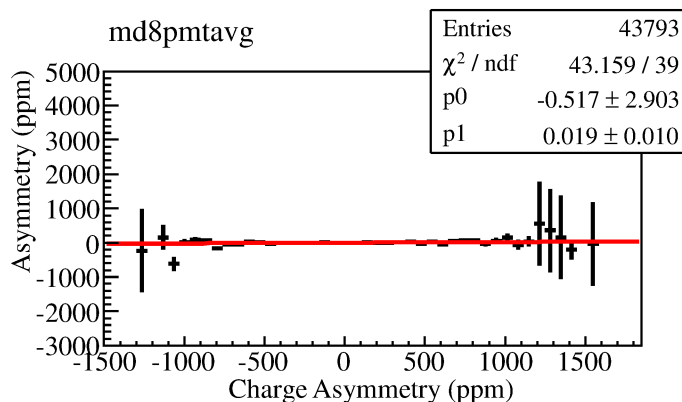


Figure 6.13: Correlation between the five-parameter regressed Čerenkov detector asymmetry and charge asymmetry in a runlet (5 min data sample) showing a 2% non-linearity.

restricting the charge asymmetry to below 1 ppb, the dominant contribution to the non-linearity can be expected to come from the distortions in the physics asymmetry. Until a proper method of handling the physics asymmetry distortion is available, the charge sensitivity of the raw Čerenkov detector asymmetries will be used as an indicator of the non-linearity of the system. Figure 6.14 shows the non-linearity of the full detector array. Even though this data set shows a maximum detector non-linearity of 1.3%, on going analysis of the full  $Q_{\text{weak}}$  data suggests it maybe as large as 2%. Therefore, for the LH2-cell asymmetry analysis, a non-linearity of 2% will be used to apply a systematic uncertainty on the measured asymmetry. Similarly a non-linearity of 4% will be used for the aluminium asymmetry. i.e.

$$(dA^{Phys})_{Non-lin.} = A^{Phys} \times \text{Non-linearity} = \begin{cases} \pm A_{LH2-cell}^{Phys} \times 0.02 & \text{for LH2-cell,} \\ \pm A_{Al27}^{Phys} \times 0.04 & \text{for Aluminum.} \end{cases} \quad (6.7)$$

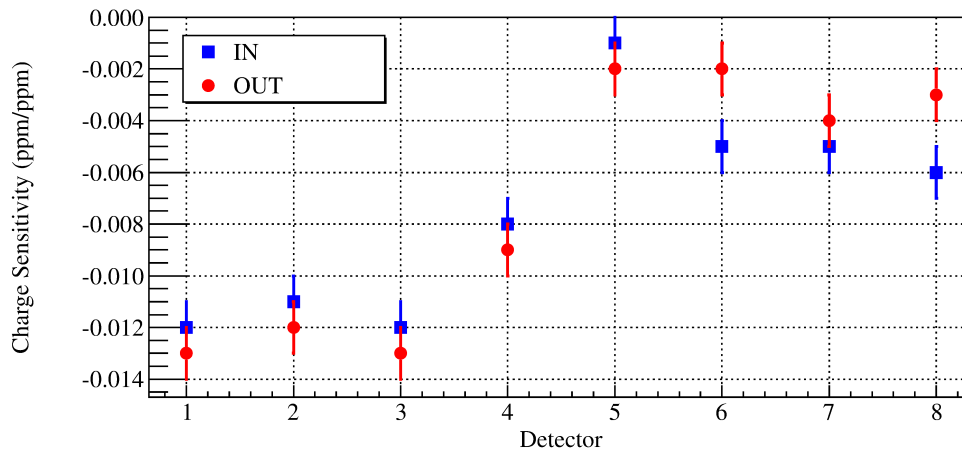


Figure 6.14: Average charge sensitivities of the raw Čerenkov detector asymmetries extracted from the six-parameter (charge+five-parameter) regression at a beam current of  $170 \mu\text{A}$ . Red (Blue) represents the sensitivity of the IHWP IN (OUT) data which are consistent with each other as expected. The sensitivities of the eight Čerenkov detectors vary from -0.1% to -1.3% and are stable within the running period. The differences between the Čerenkov detectors may be attributed to the different response of the detector signal chains.

## 6.6 The Extraction of the Beam Normal Single Spin Asymmetry

The beam normal single spin asymmetry from elastic electron-proton scattering is embedded in the physics asymmetry measured from the LH2-cell target. To extract it, the physics asymmetry needs to be corrected for systematics such as beam normal single spin asymmetry from background processes, beam polarization, radiative processes and other experimental bias effects. With these corrections, the beam normal single spin asymmetry from electron-proton scattering has the form

$$B_n = R \left[ \frac{\left( \frac{A^{Phys}}{P_{Beam}} \right) - \sum_i A_i^{Bkg} f_i}{\sum_i (1 - f_i)} \right], \quad (6.8)$$

where  $R$  is a correction factor for the experimental bias and radiative effects,  $P_{Beam}$  is the beam polarization and  $A_i^{Bkg}$  is  $i^{th}$  background asymmetry with dilution<sup>7</sup>  $f_i$ . The following subsections contain the analysis of these additional systematic corrections on the physics asymmetry and the associated uncertainties.

### 6.6.1 Beam Polarization

Beam polarization measurements in the experiment were carried out using both the Hall C Møller polarimeter and the Compton polarimeter. However, the Compton polarimeter was being commissioned at the beginning of the experiment and around the time the first transverse data set was taken and was not available for polarization measurements. Therefore, only the Møller polarimeter measurements will be used for the transverse data analysis.

By design, the Møller polarimeter is only sensitive to longitudinal polarization. To determine the beam polarization in the transversely polarized beam, the experiment relied on Møller measurements done with the longitudinally polarized beam close to the transverse data taking period. Since the quantum efficiency of a laser spot on the cathode is good for up to two weeks (see Subsection 3.2.1), the polarization in the beam within one to two days of the transverse measurements are similar to the beam polarization in the transverse running period. With this assumption, Transverse\_Run I uses the beam polarization estimated [148] for the  $Q_{weak}$  21 % result from the commissioning period (see left panel in Figure 6.15). The Transverse\_Run I data

---

<sup>7</sup>Fraction of backgrounds in the total detector acceptance.

were taken right after the commissioning period and at the same beam spot<sup>8</sup>. Following the suggestion of the Møller polarimeter group [149, 150], Transverse\_Run II analysis uses the results of the Møller measurements done on February 20th, 2012 (see right panel on Figure 6.15). Table 6.8 shows the polarization results from both of these cases and the final beam polarization used for the transverse analysis.

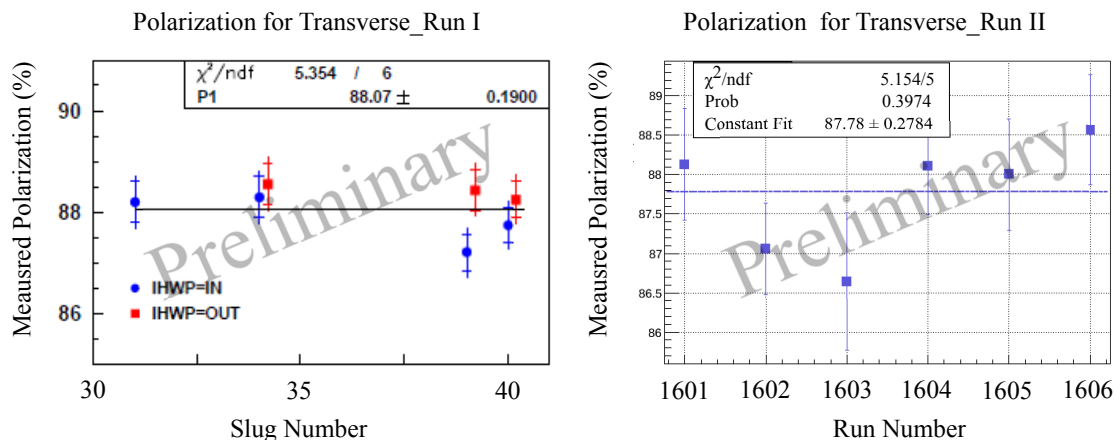


Figure 6.15: Beam polarization in Transverse\_Run I and Transverse\_Run II based on Møller measurements. The data points are corrected for IHWP reversal. Left - Polarization results from the commissioning period used for Transverse\_Run I. A data point is the average of the runs in a given IHWP setting in a given day. Data taken with IHWP IN (OUT) are shown in blue (red). The inner error bars represent the statistics and the outer error bars represent an additional point-to-point error of  $dP/P=0.37\%$  on each data point. Figure from Ref. [148]. Right - Polarization results used for Transverse\_Run II based on the Møller measurements performed on February 20th, 2012. A data point is the average over a 10 min long run. The errors are pure statistical. Although not shown in the figure, the final error will include a point-to-point error of  $dP/P=0.37\%$  similar to what was used in the commissioning period (plot on the left). Figure from Ref. [149]. In both cases, the measurements are stable and the fits over the data points are a good representation of the data.

<sup>8</sup>One thing to note here is that during the commissioning period and part of  $Q_{\text{weak}}$  Run I, one of the quadrupoles (Q3) of the Møller polarimeter was malfunctioning. This malfunction required adding an additional systematic error to the polarization result estimated for the commissioning period. This additional systematic is not included for Run II polarization measurements since the quadrupole was fixed by then.

Table 6.8: Beam polarization in Transverse\_Run I and Transverse\_RunII based on the measurements shown in Figure 6.15. The  $\square$  indicates the additional systematic error related to the Q3 is added linearly with the rest of the errors. The two measurements are statistically compatible. Therefore, they are combined together to get the beam polarization required for the full transverse data set.

Transverse_Run	Beam Polarization %
I	$88.95 \pm 0.19_{Stat} \pm 0.93_{Sys} [\pm 0.89_{Q3-sys}]$
II	$87.78 \pm 0.28_{Stat} \pm 0.95_{Sys}$
Error weighted average	$P_{Beam} = 88.04 \pm 0.87$

### 6.6.2 Backgrounds

The largest known background source in the Čerenkov detector acceptance is the electrons scattering from aluminum target windows. In addition, there are relatively small fraction of inelastic electrons and soft backgrounds in the acceptance<sup>9</sup>. Following subsections present the analysis of the background asymmetries and their contributions to the electron-proton asymmetry.

#### 6.6.2.1 Electrons scattering from aluminum target windows

The correction required for electrons scattering from the aluminum target windows is estimated by performing an asymmetry analysis of the DS4Al target data similar to what was done on the LH2-cell target data. The physics asymmetries extracted from the three data sets are shown in Table 6.9. The average of the three asymmetries is used as the physics asymmetry from the DS4Al target. This asymmetry is then scaled by a 0.9938 for acceptance averaging (see Subsection 6.5.1) and an additional systematic error of  $0.04 \times A^{Phys}$  is assigned for the system non-linearity (see Equation 6.7) resulting in the corrected aluminum physics asymmetry of

$$A_{DS4Al}^{Phys} = -8.985 \pm 0.340_{Stat} \pm 0.358_{Sys} \text{ ppm.} \quad (6.9)$$

Even at this preliminary stage, one can see that the beam normal single spin asymmetry from the electron-aluminum nuclei scattering is a factor of 2 larger than the beam normal single spin asymmetry from the LH2-cell.

---

<sup>9</sup>More information on the background sources in the  $Q_{weak}$  acceptance can be found in K.Myers dissertation [86].

Table 6.9: Physics asymmetry extracted from the DS4Al target. The (IN+OUT)/2 in the three data sets are compatible with zero (see Appendix G.5 for the figures.). The physics asymmetries given by AVG(IN,-OUT) are a factor of two larger than the asymmetry measured from the LH2-cell target. The relevant plots are shown in Figure 6.16.

Transverse_Run	Polarization	(IN+OUT)/2 (ppm)	AVG(IN-OUT) (ppm)
I	Vertical	$-0.290 \pm 0.604$	$-9.791 \pm 0.604$
II	Vertical	$0.838 \pm 0.727$	$-8.619 \pm 0.727$
	Horizontal	$-0.008 \pm 0.521$	$-8.486 \pm 0.499$

For the background correction of the LH2-cell asymmetry,  $A_{DS4Al}^{Phys}$  needs to be corrected for the acceptance difference between the upstream and downstream target windows. GEANT4 simulations have shown [86] this acceptance difference causes a 20% relative difference between the mean  $Q^2$  of the electrons coming from the upstream target window compared to the downstream target window such that

$$Q_{US}^2 = 0.8 \times Q_{DS}^2. \quad (6.10)$$

Theoretical models [151, 152] of the beam normal single spin asymmetry from nuclei suggest at very forward angle scattering, the asymmetry is proportional to  $\sqrt{Q^2}$ . Therefore, in terms of the asymmetry measured from the downstream DS4Al target, the asymmetry of the upstream aluminum target window would be

$$A_{Al}^{US} = \sqrt{0.8} A_{DS4Al}. \quad (6.11)$$

From GEANT4 background simulations, both downstream and upstream aluminum target windows are expected to contribute equally to the aluminum dilution in the Čerenkov detectors resulting in an effective aluminum asymmetry of

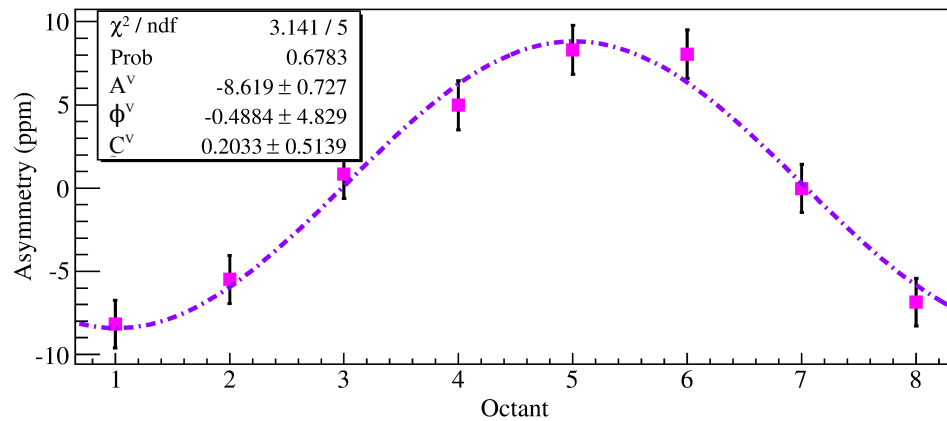
$$A_{Al}^{Phys} = \frac{A_{Al}^{DS} + A_{Al}^{US}}{2} = -8.510 \text{ ppm}. \quad (6.12)$$

This is a 0.474 ppm correction on the asymmetry measured from the DS4Al target. In order to take into consideration the theoretical uncertainty associated with the  $Q^2$  dependence of the beam normal single spin asymmetry, a  $\pm 50\%$  systematic uncertainty of 0.237 ppm is assigned to this correction. With the beam polarization

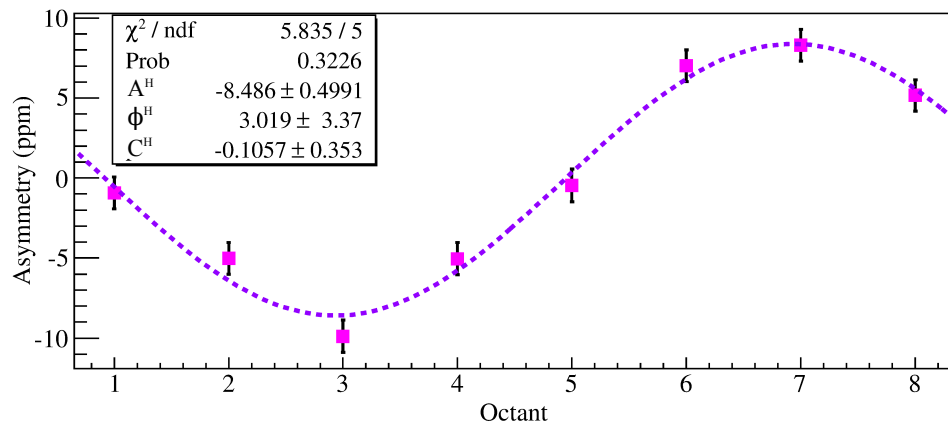
correction, the final aluminum asymmetry is

$$A_{Al} = \frac{A_{Al}^{Phys}}{P_{Beam}} = \frac{-8.5104}{0.8804} = -9.667 \pm 0.603 \text{ ppm} \quad (6.13)$$

where  $P_{Beam}$  is the beam polarization given in Subsection 6.6.1. See Appendix G.9.2 for the error analysis. The extraction of the beam normal single spin asymmetry from electrons scattering from aluminum nuclei requires additional corrections on Equation 6.13 for inelastics, quasi-elastics and many body interactions which are beyond the



(a) Vertical



(b) Horizontal

Figure 6.16: Azimuthal depending physics asymmetry from the DS4Al target. The errors are pure statistical. The octant dependence in either polarization orientation are similar to what was observed for the LH2-cell. But the physics asymmetry is a factor of two larger than the LH2-cell asymmetry.

scope of this dissertation. What is required for the background correction of the LH2-cell physics asymmetry is the result in Equation 6.13 as it is. The aluminum background correction and the associated uncertainty on the beam normal single spin asymmetry from the proton, extracted using this value are shown in Table 6.10.

Table 6.10: Aluminum target window background correction for the LH2-cell physics asymmetry.

Background	Asymmetry (A) (ppm)	Dilution (f)	Correction (-fA) (ppm)
Aluminum windows	$-9.667 \pm 0.603$	$0.033 \pm 0.002$ [153]	0.319

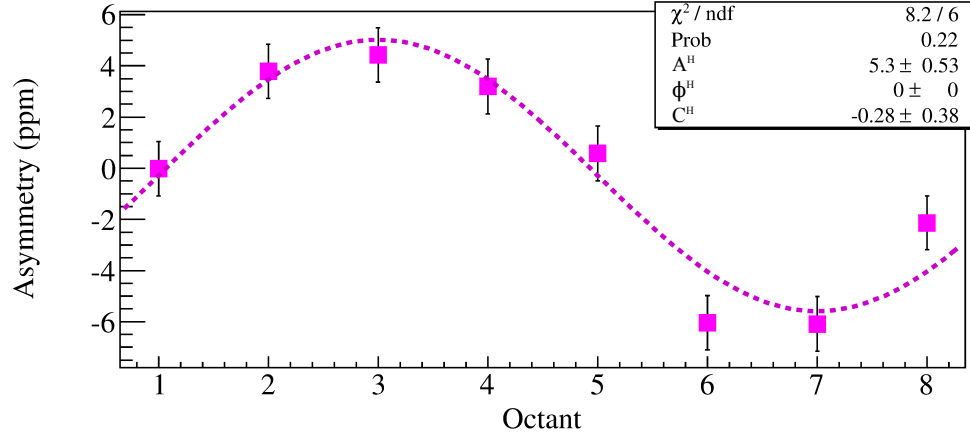
### 6.6.2.2 Inelastic electrons from $N \rightarrow \Delta$ reaction

The background correction for the inelastic electrons in the acceptance is estimated from the transverse data collected at the inelastic peak (QTOR = 6700A) in Transverse\_Run II. The analysis procedure is similar to what was done in the LH2-cell and DS4Al data analysis. The five-parameter regressed Čerenkov detector asymmetries are used to extract the physics asymmetry after confirming the false asymmetry cancellation with the IHWP. The results are summarized in Table 6.11. As discussed in the table, the inelastic physics asymmetry from the LH2-cell is similar in magnitude to the elastic asymmetry but has the opposite sign.

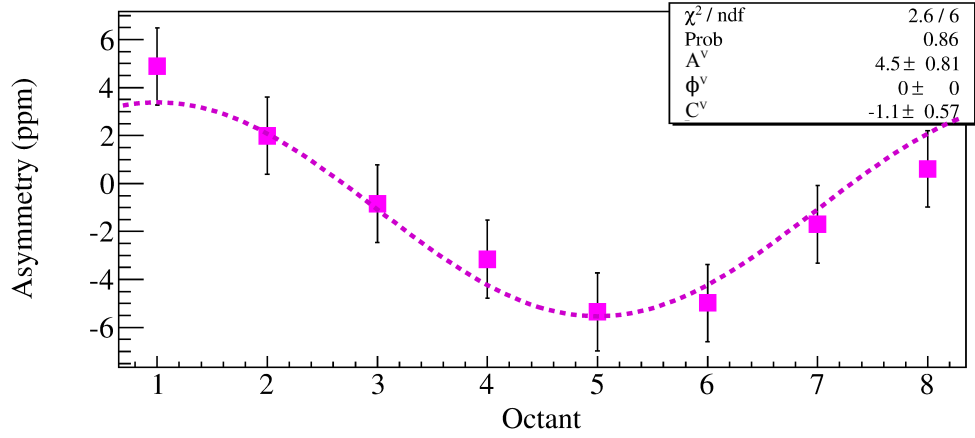
Table 6.11: Inelastic asymmetry from the LH2-cell target. The (IN+OUT)/2 in both data sets are consistent with zero (see Appendix G.6.1 for the figures). The physics asymmetry extracted from AVG(IN,-OUT) fits has the same magnitude but the opposite sign of the elastic asymmetry (see Figure 6.17).

Polarization	(IN+OUT)/2 (ppm)	AVG(IN,-OUT) (ppm)
Vertical	$-0.499 \pm 0.817$	$4.457 \pm 0.807$
Horizontal	$-1.103 \pm 0.534$	$5.303 \pm 0.533$





(a) Horizontal



(b) Vertical

Figure 6.17: Azimuthal depending inelastic physics asymmetry from the LH2-cell target. The amplitudes are similar in magnitude to that of the elastic asymmetry (see Figure 6.9) but have the opposite sign.

Since all the data were taken within one to two days of each another, they have similar beam energy and polarization and can be averaged to get the physics asymmetry of  $5.046 \pm 0.445$  ppm for the full data set. With the 0.9938 acceptance correction and the 2% non-linearity uncertainty, the inelastic physics asymmetry from the LH2-cell target is

$$A_{LH2-cell}^{ie} = 5.078 \pm 0.445_{Stat} \pm 0.103_{Sys}. \quad (6.14)$$

To get the inelastic electron-proton asymmetry,  $A_{LH2-cell}^{ie}$  needs to be corrected for

beam polarization, the aluminum background ( $A_{Al}^{ie}$ ) with a  $f_{Al}^{ie} = 0.033 \pm 0.002$  [153] dilution and the elastic radiative tail ( $A_{ep}^e$ ) with a  $f_{ep}^e = 0.669 \pm 0.067$  [86] dilution using

$$A_{ep}^{ie} = \frac{\frac{A_{LH2-cell}^{ie}}{P_{Beam}^I} - A_{Al}^{ie} f_{Al}^{ie} - A_{ep}^e f_{ep}^e}{1 - f_{Al}^{ie} - f_{ep}^e}. \quad (6.15)$$

For the calculation in Equation 6.15, the inelastic aluminum background is determined from the inelastic aluminum data taken at the inelastic peak (QTOR = 6700 A). The analysis is similar to that of the elastic aluminum asymmetry presented in Subsection 6.6.2.1 and is summarized in Appendix G.6.2. It resulted in an inelastic aluminum asymmetry of  $A_{Al}^{ie} = 9.141 \pm 1.156$  ppm. Using a -5 ppm estimate<sup>10</sup> for the asymmetry at the elastic peak (QTOR = 8901 A) and using the modelled  $Q^2$  dependence of the beam normal single spin asymmetry at forward angles, the magnitude of the elastic proton asymmetry at the inelastic peak (QTOR = 6700 A) is

$$(A_{ep}^e)_{6700A} \approx (A_{ep}^e)_{8901A} \times \sqrt{\frac{Q_{6700A}^2}{Q_{8901A}^2}} = -5 \text{ ppm} \sqrt{\frac{0.021}{0.025}} = -4.6 \pm 2.3 \text{ ppm} \quad (6.16)$$

where a 50% systematic uncertainty was assigned in order to take into account the theoretical uncertainty associated with the  $Q^2$  dependence of the elastic asymmetry. Using the beam polarization in Transverse\_Run II,  $P = 0.8778 \pm 0.0099$  and the inelastic aluminum and elastic proton asymmetries derived before in Equation 6.8, the inelastic proton asymmetry is

$$A_{ep}^{ie} = 28.67 \pm 7.77 \text{ ppm}. \quad (6.17)$$

The resulting inelastic background correction for the LH2-cell physics asymmetry estimated using  $A_{ep}^{ie}$  is shown in Table 6.12.

Table 6.12: Inelastic background correction for the LH2-cell physics asymmetry.

Background	Asymmetry (A) (ppm)	dilution (f)	Correction (-fA) (ppm)
Inelastics	$28.67 \pm 7.77$	$0.0002 \pm 0.0001$ [86]	-0.0058

<sup>10</sup>Based on the LH2-cell physics asymmetry extracted in Subsection 6.5.

### 6.6.3 Electromagnetic Radiative Corrections

Electromagnetic radiation (EM) causes energy loss and depolarization [154] of the electrons. To extract the beam normal single spin asymmetry at the effective  $Q^2$  and beam polarization of the experiment, the measured BNSSA needs to be corrected for these EM radiative effects. The leading order radiative effects on the electron is real Bremsstrahlung photons and virtual photon loops which can occur either outside (external) or inside (internal) of the field of the nuclei (see Figure 6.18). In addition, there could be second order effects resulting from multiple scattering and pair production.

Following the prescription in Ref. [155, 156], the EM radiative corrections on the BNSSA are applied by treating the energy loss due to internal bremsstrahlung (IB), external bremsstrahlung (EB) and the depolarization separately. The GEANT3 simulation developed for the  $Q_{\text{weak}}$  experiment was used to obtain the average  $Q^2$  at the scattering vertex when corrected for energy loss due to internal and external bremsstrahlung separately. These are shown in Table 6.13. Then using the modelled [73] behaviour of  $B_n \propto \sqrt{Q^2}$  at forward angles, the energy loss correction on the measured asymmetry is

$$R_x = \frac{(B_n)_{No-rad}}{(B_n)_{Measured}} = \sqrt{\frac{(Q^2)_{No-rad}^{Sim}}{(Q^2)_x^{Sim}}}, \quad (6.18)$$

where  $(Q^2)_x^{Sim}$  is the simulated  $Q^2$  of the elastic electrons, including the energy loss due to  $X = \text{IB, EB}$  and  $(Q^2)_{No-rad}^{Sim} = 0.02501 \text{ (GeV/c)}^2$  is the simulated  $Q^2$  without radiative effects. A 50% systematic uncertainty will be applied on this correction to take into account the theoretical uncertainty in the  $Q^2$  dependence of the BNSSA. Table 6.14 shows the correction factors estimated for each of the two cases.

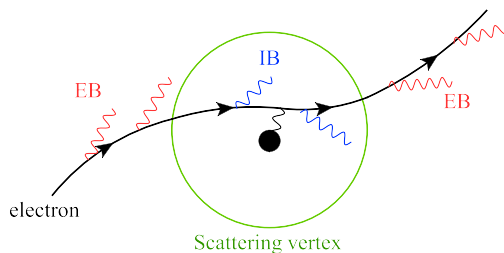


Figure 6.18: Illustration of external (EB) and internal (IB) Bremsstrahlung radiation emission in electron scattering near the scattering vertex.

Table 6.13: Simulated  $Q^2$  at the scattering vertex with corrections for the energy loss due to EM radiation [156]. See text for explanation.

$Q^2$	$(\text{GeV}/c)^2$
$(Q^2)_{No-rad}^{Sim}$	0.02501
$(Q^2)_{EB}^{Sim}$	0.02490
$(Q^2)_{IB}^{Sim}$	0.02471

Table 6.14: Energy loss correction factors for the different radiative effects. The values were estimated using Equation 6.18.

Energy loss due to	Correction factor R
External bremsstrahlung	$1.0022 \pm 0.0011$
Internal bremsstrahlung	$1.0061 \pm 0.0030$

From Ref. [154], depolarization of a transversely polarized electron is 3/2 times the depolarization of a longitudinally polarized electron. The depolarization of longitudinally polarized electrons in the  $Q_{\text{weak}}$  acceptance was estimated in Ref. [157] which showed the difference between depolarization of electrons with external and internal bremsstrahlung is negligible. Considering both cases, a  $0.0011 \pm 0.0005$  was used as the depolarization of the longitudinally polarized electrons due to both internal and external bremsstrahlung radiation. Therefore the depolarization of the transversely polarized electrons in  $Q_{\text{weak}}$  acceptance is  $0.0017 \pm 0.0008$  and the measured beam normal single spin asymmetry needs to be corrected by a factor of  $1.0017 \pm 0.0008$  to take this effect into account.

Taking all of the above correction factors together, the correction which needs to be applied on the measured BNSSA to remove EM radiative effects is

$$R_{RC} = R_{IB} \times R_{EB} \times R_{Depolarization} = 1.010 \pm 0.004. \quad (6.19)$$

### 6.6.3.1 Detector Bias

Detector bias includes systematic effects specific to the Čerenkov detectors such as the light-collection bias and the  $Q^2$  variation over the detectors. Both of these effects modifies the measured asymmetry and need to be accounted for in the final asymmetry extraction.

The light-collection bias, first introduced in Section 3.7, affects the measured asymmetries which are computed using the Čerenkov light yield. Therefore, a correction factor of the form

$$R_{Det} = \frac{B_{No-bias}^{Sim}}{B_{Bias}^{Sim}} = \sqrt{\frac{(Q^2)_{No-bias}^{Sim}}{(Q^2)_{Bias}^{Sim}}} = 0.988 \pm 0.001, \quad (6.20)$$

will be applied on the asymmetry to correct for the light collection bias. In the above equation  $B^{Sim}$  is the simulated asymmetry with (Bias) and without (No-Bias) the light-collection bias.

Simulations [158] and data [159] have shown a non-uniform  $Q^2$  variation over the Čerenkov detector array due to changes in the magnetic field and the beam angle (see Figure 6.19). These relative changes are expected to induce relative changes in the beam normal single spin asymmetry of the form

$$\frac{dB_n}{d(Q^2)} \propto \frac{1}{2\sqrt{Q^2}} \implies \frac{dB_n}{B_n} = \frac{d(Q^2)}{2Q^2} \quad (6.21)$$

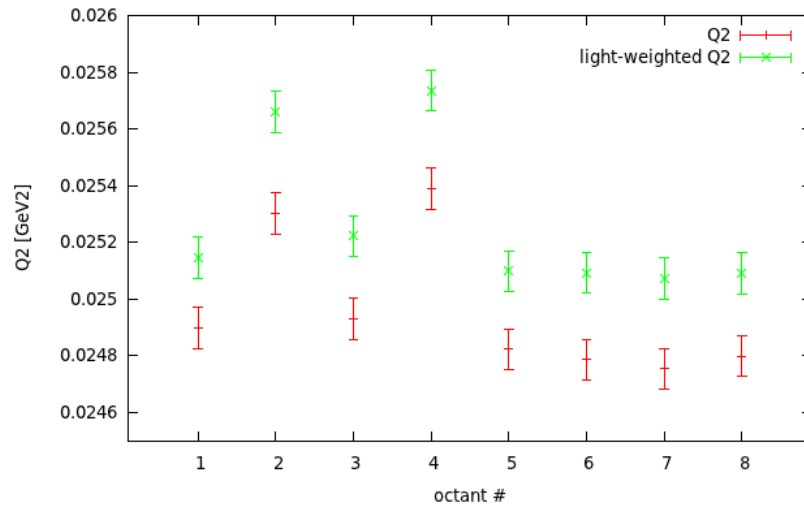


Figure 6.19: Simulated  $Q^2$  variation of elastic events over the Čerenkov detectors. The octant variation is dominated by magnetic field changes across the Čerenkov detectors. The light weighted  $Q^2$  takes into account the Čerenkov detector light collection bias. Note that the outliers in octants 2 and 4 are believed [160] to be caused by the presence of the vertical and horizontal tracking drift chambers and therefore will not be included in the analysis. Neglecting octants 2 and 4, the average light weighted  $Q^2$  over the detectors is  $0.0251 \text{ (GeV/c)}^2$ . Figure from Ref. [160].

For the  $Q^2$  variation shown in Figure 6.19, Equation 6.21 predicts a 0.02% (see Appendix G.7) variation in the measured beam normal single spin asymmetry in each detector. But when taking into consideration the azimuthal dependence of beam normal single spin asymmetry at a given transverse polarization orientation, the effect of  $Q^2$  variation is not observed in the amplitudes of the fits of the measured asymmetries generally at the 0.04% level (see Figure 6.20). Therefore, a factor of

$$R_{Q^2} = 1.000 \pm 0.0004$$

will be applied to the measured beam normal single spin asymmetry to take into account the  $Q^2$  bias of the Čerenkov detectors.

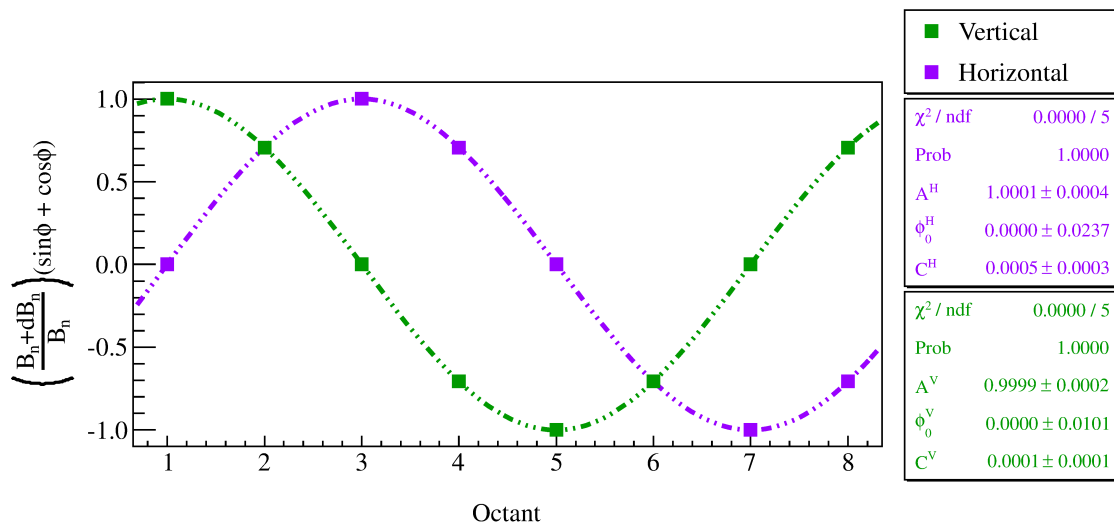


Figure 6.20: Simulated changes in the vertical and horizontal transverse asymmetry fits (assuming the presence of elastic  $B_n$  only) due to  $Q^2$  variation in the Čerenkov detector array.  $B_n$  is the magnitude of the elastic beam normal single spin asymmetry expected at a nominal  $Q^2$  of  $0.025 \text{ (GeV/c)}^2$  and  $dB_n$  is the change expected from the  $Q^2$  changes shown in Figure 6.19. The amplitudes of the fits are consistent with zero at the 0.04% level.

## 6.7 Beam Normal Single Spin Asymmetry from the Proton

To summarize, the analysis presented so far estimated the quantities

$$\begin{aligned}
 A_{LH2-cell}^{Phys} &= -4.835 \pm 0.057_{Stat} \pm 0.102_{Sys} \text{ ppm} \\
 R &= R_{RC} \times R_{Det} \times R_{Q^2} = 0.9979 \pm 0.004 \\
 P_{Beam} &= 0.8804 \pm 0.0087 \\
 A_{Al} &= -9.667 \pm 0.603 \text{ ppm} \\
 f_{Al} &= 0.033 \pm 0.002 \\
 A_{ep}^{ie} &= 28.67 \pm 7.77 \text{ ppm} \\
 f_{ie} &= 0.0002 \pm 0.0001
 \end{aligned}$$

which are required to extract the beam normal single spin asymmetry from the transverse data using

$$B_n = R \left[ \frac{\left( \frac{A^{Phys}}{P_{Beam}} \right) - \sum_i A_i^{Bkg} f_i}{\sum_i (1 - f_i)} \right].$$

In cooperating all of the above gives the beam normal single spin asymmetry in elastic electron-proton scattering

$$\boxed{B_n = -5.350 \pm 0.067_{stat} \pm 0.137_{Sys} \text{ ppm}} \quad (6.22)$$

for the effective kinematics of acceptance averaged electron energy of  $\langle E \rangle = 1.155 \pm 0.003$  GeV,  $\langle Q^2 \rangle = 0.0250 \pm 0.0006$  (GeV/c)<sup>2</sup> and a average scattering angle  $\langle \theta_s \rangle = 7.9 \pm 0.3^\circ$  [41]. Table 6.15 shows the breakdown of corrections applied on the physics asymmetry to extract  $B_n$  using the above equation.

The contributions from the different error sources into the final measurement error are summarized in Table 6.16. The dominant correction to the asymmetry comes from beam polarization whereas the dominant error on the asymmetry is the system non-linearity.

Table 6.15: Summary of systematic corrections applied on the physics asymmetry  $A_{LH2-cell}^{Phys}$ , to yield  $B_n$ . See Appendix G.9.1 for the relevant formulas.

Systematic	Correction
Beam polarization	-0.678 ppm
Aluminum window background	0.329 ppm
Experimental bias	-0.156 ppm
Inelastic background	-0.006 ppm

Table 6.16: Error summary of the elastic beam normal single spin asymmetry extraction. Measurement systematic contains the systematic uncertainties related to the extraction of the physics asymmetry such as regression, nonlinearity and acceptance averaging.

Error Source	Relative Contribution (%)
Statistics	1.25
Systematics	
System non-linearity	2.13
Beam polarization	1.05
Regression scheme dependence	0.64
Aluminum dilution	0.39
Aluminum asymmetry	0.38
Acceptance averaging	0.37
Experimental bias	0.36
Inelastic dilution	0.06
Inelastic asymmetry	0.03
Systematics only	2.57
Total	2.86



## 7 Beam Normal Single Spin Asymmetry Leakage

The beam normal single spin asymmetry (BNSSA) in electron-proton scattering can become a source of false asymmetry into the parity violating asymmetry measurements when the azimuthal symmetry of the detector array is broken and there is residual transverse polarization in the electron beam. The transverse measurement discussed in the previous chapter was used to determine both of above quantities. They were then used to assign a systematic uncertainty for the parity violating asymmetry to take into account the false asymmetry generated by BNSSA. In addition, the physics asymmetry measured from the transverse data was used to implement an online monitoring of the transverse polarization in the electron beam. This chapter describes my work on monitoring the transverse polarization in the electron beam and estimating the systematic uncertainty for BNSSA leakage into the  $Q_{\text{weak}}$  parity violating asymmetry.

### 7.1 BNSSA Leakage Due to Symmetry Breaking in the Detector Array

The amount of beam normal single spin asymmetry which contributes to the parity violating asymmetry (a.k.a. BNSSA leakage) is extracted from the fit

$$A^T(\phi) = A^V \cos \phi - A^H \sin \phi + C, \quad (7.1)$$

over the detector asymmetries measured in transverse running. Here the constant term is

$$C = A^{PV} P^L + C_{\text{BNSSA Leakage}}, \quad (7.2)$$

where  $A^{PV}$  is the parity violating asymmetry,  $P^L$  is the residual longitudinal polarization in the transversely polarized electron beam and  $C_{\text{BNSSA Leakage}}$  is the BNSSA leakage due to the broken symmetry of the detector array. By neglecting the  $A^{PV} P^L$  term<sup>1</sup>,

$$C \rightarrow C_{\text{BNSSA Leakage}}. \quad (7.3)$$

---

<sup>1</sup>The parity violating  $Q_{\text{weak}}$  asymmetry is about 0.2 ppm compared to the -5 ppm beam normal single spin asymmetry. Therefore, the leakage of the parity violating asymmetry into the beam normal single spin asymmetry measurement due to a few percent residual longitudinal polarization is negligible.

The magnitude of  $C_{\text{BNSSA Leakage}}$  can be determined using either actual transverse data or simulations. Although both methods are reasonable, the choice of which method to use depends on how well the BNSSA leakage is determined and the contribution of the uncertainty in the estimation into the uncertainty of the parity violating asymmetry measurement. More on this choice will be discussed later in Subsection 7.3. The estimations of the  $C_{\text{BNSSA Leakage}}$  from measurements and simulations are presented in the following subsections.

### 7.1.1 Leakage via Transverse Measurements

The azimuthal fits over the LH2-cell asymmetries from the transverse data were presented in the beam normal single spin asymmetry analysis discussion in Subsection 6.5. The BNSSA leakage (the constant term) extracted from those fits are shown in Table 7.1. The measured BNSSA leakages in each data set are consistent with zero at the 0.1 ppm level. As mentioned in Chapter 6, the motivation behind the horizontal and vertical transverse measurements was to check for the leakage from the vertical (3 & 7) and horizontal (1 & 5) detector pairs. Since any transverse polarization orientation can be decomposed into vertical and horizontal components, the BNSSA leakage can be quoted in terms of the leakages observed in the vertical and horizontal transverse measurements. From the Vertical I and Horizontal II transverse data sets, one can conclude the cancellation between the detectors in octants 1 & 5 and 3 & 7 is consistent with zero at the  $\pm 60$  ppb level. A more precise measurement of this quantity at the few ppb level could not be carried out due to the time constraints on the main  $Q_{\text{weak}}$  measurement.

Table 7.1: BNSSA leakage extracted from the LH2-cell target transverse data set presented in Subsection 6.5. The leakages are obtained from the constant terms in the fits over the five-parameter regressed asymmetries in Figure 6.9. On average, the measured BNSSA leakage is compatible with zero at the 0.1 ppm level.

Configuration	BNSSA leakage (ppm)
Vertical I	$-0.024 \pm 0.064$
Vertical II	$0.116 \pm 0.108$
Horizontal II	$0.011 \pm 0.061$

### 7.1.2 Leakage via Simulations

A simulation of the BNSSA leakage considers all possible scenarios in which the symmetry of the Čerenkov detector array can be broken. A detector array is said to have a broken symmetry when there are relative shifts between the placements of the opposite detectors. There are three possible ways in which this could happen. A displacement in the azimuthal angle, the radial direction or the polar angle (see Figure 7.1). A displacement in either the radial direction or the polar angle will result in a  $Q^2$  bias between the two detectors due to the shifts in the scattered electron envelope across the detectors. Subsection 6.6.3.1 discussed this effect of  $Q^2$  bias on the measured asymmetry. From Figure 6.20 in Subsection 6.6.3.1, one can see the effect of  $Q^2$  bias on the constant term is consistent with zero at the 1 ppb level. Therefore, the simulation discussed in this subsection will only investigate the BNSSA leakage coming from shifts in the azimuthal angle.

The simulation uses the surveyed vertical and horizontal locations of the individual PMTs w.r.t the QTOR coordinate system to calculate the azimuthal angles of the Čerenkov detectors (see Table ??). The calculated shifts from the ideal azimuthal angle vary between  $0.003^0$  and  $0.2^0$ . What is of interest here is the relative shifts between the opposite detectors in the azimuthal plane which are shown in Table 7.3. These non-zero relative shifts indicate the broken symmetry of the detector array. The

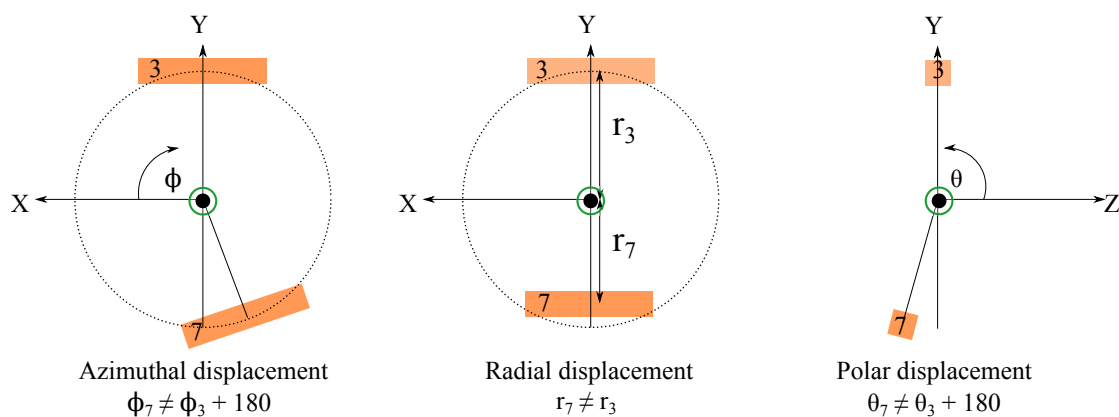


Figure 7.1: Illustration of the scenarios for a broken symmetry in the detector array due to the broken symmetry of opposite detectors. For simplicity, only the pair of detectors in octants 3 and 7 are shown here. Detector 7 is displaced from its ideal azimuthal angle (left), radial direction (middle) and polar angle (right) resulting in a broken symmetry between the pair.

Table 7.2: Azimuthal angles of the Čerenkov detectors w.r.t the left-handed coordinate system with the origin at the QTOR (see Appendix B). The angles are calculated from the as found vertical and horizontal locations from the post-experiment survey done on 25th October 2012. X and Y represent the horizontal and vertical locations of the center of the detector in the QTOR coordinate system. The absolute value of  $\tan^{-1}(Y/X)$  gives the azimuthal angle  $\phi$  of the detector measured clockwise w.r.t to the horizontal axis.  $d\phi$  is the shift of the detector in the azimuthal plane from the ideal angle.

Octant	X (m)	Y (m)	$\phi$ (deg.)	Ideal $\phi$ (deg.)	$d\phi$ (deg.)
1	3.437	-0.004	-0.057	0	-0.057
2	2.437	2.428	44.914	45	-0.086
3	-0.000	3.435	89.997	90	-0.003
4	-2.436	2.425	135.115	135	0.115
5	-3.441	-0.004	180.057	180	0.057
6	-2.425	-2.446	225.257	225	0.257
7	0.002	-3.444	270.040	270	0.040
8	2.422	-2.444	314.743	315	-0.257

amount of BNSSA leakage expected from this broken symmetry is estimated with the help of a simple simulation<sup>2</sup> written by me. The simulation considers a large number of transverse measurements which are  $t$  hrs long. For each  $t$  hr long measurement, the physics asymmetry of  $A^{Phys} = -4.8$  ppm measured from the LH2-cell target with transverse polarization is used to generate the asymmetry in the individual detectors

Table 7.3: Relative azimuthal shifts between pairs of detectors in opposite octants using data given in Table B. The non-zero shifts indicate the broken azimuthal symmetry of the detector array.

Octant pair	Relative shift in $\phi$ (deg)
1 & 5	0.11
2 & 6	0.34
3 & 7	0.04
4 & 8	0.37

<sup>2</sup>The simulation code can be found under the  $Q_{weak}$  software repository directory `Qwanalysis/Extensions/Macros/Transverse`

using a Gaussian random generator with

$$A^T(\phi) = A^{Phys}[P^V \cos \phi - P^H \sin \phi] \text{ ppm}, \quad \sigma(\phi) = \frac{\sigma(\phi)_{\text{Detector}}}{\sqrt{t \times 3600s \times \frac{960Hz}{4}}} \text{ ppm}.$$

Here,  $P^V, P^H$  are vertical (V),horizontal (H) transverse polarization which were either set to 0 or 1 for the relevant transverse configuration. The azimuthal angles calculated from the survey results (see Table ??) were used for the  $\phi$  angle of each detector and  $\sigma(\phi)_{\text{Detector}}$  is the typical 660 ppm standard deviation of the asymmetry distribution of a Čerenkov detector. The measurement length t was set to 500 hours to provide a good statistical accuracy for a single leakage measurement (similar to the actual transverse measurement). The process was repeated for 30000 times (see Figure 7.2) to simulate the statistical precision of many number of measurements. The BNSSA leakage extracted from these simulations are

$$\text{BNSSA Leakage} = \begin{cases} -0.0002 \pm 0.0005 \text{ ppm} & \text{for vertical,} \\ 0.0519 \pm 0.0005 \text{ ppm} & \text{for horizontal.} \end{cases} \quad (7.4)$$

The leakage with the vertical transverse polarization is negligible at the 0.0005 ppm level. The leakage with the horizontal transverse polarization is however 0.052 ppm. By comparing the relative differences in the azimuthal angles of the opposite

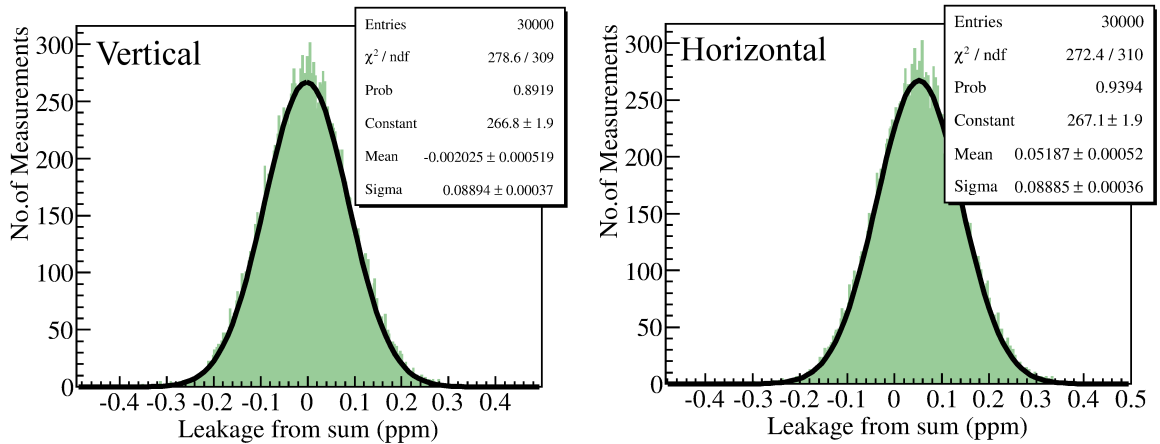


Figure 7.2: Simulated leakages due to the broken azimuthal symmetry in the detectors array and the -4.8 ppm azimuthal modulating asymmetry. The leakage in horizontal (vertical) transverse polarization are given by the distribution on the right (left).

detectors 1 & 5 and 3 & 7 (see Table 7.3), one can see the size of the leakage is determined by the broken symmetry of the detector pairs measuring the null asymmetry. Even though the detector pairs 2 & 4 and 6 & 8 have the largest broken symmetry, their contribution to the leakage generated by both vertical and horizontal transverse polarization is the same.

## 7.2 Residual Transverse Polarization in the Electron Beam

The amount of residual transverse polarization present in the longitudinally polarized electron beam provided by the Jefferson Lab accelerator has several contributing factors.

- ***The accuracy of the Wien filters***

The known accuracy with which the Wien filters (horizontal and vertical) can rotate the spin direction is about  $\pm 2^0$ . This can generate a 3% ( $\sin(2^0) = 0.034$ ) residual transverse polarization in the beam in either the vertical or the horizontal directions.

- ***Difference between the injector and the Hall C planes***

The Mott polarimeter in the Jefferson Lab injector is used to null the vertical transverse polarization component in the beam by Wien angle adjustments. A null vertical transverse polarization measurement in the plane of the injector may not necessarily indicate a null vertical transverse polarization in the Hall C. It can therefore lead to a residual vertical transverse polarization in the beam.

- ***Energy drifts that result in an energy imbalance in the linear accelerators***

Even after a proper configuration of the Wiens to deliver full longitudinal polarization to the Halls, an energy imbalance in the two linear accelerators (linacs) that keep the energy delivered to the halls constant, can cause a spin precession in the horizontal plane resulting in residual horizontal transverse polarization. According to the energy model used for the Jefferson Lab accelerator [161], a 10 MeV energy imbalance in the two linacs can create a  $2^0$  spin precession in the horizontal plane and a 2 MeV energy difference between the injector and the linacs can create a  $2^0$  spin precision in the horizontal plane.

Out of these factors, the dominant source of residual transverse polarization for the  $Q_{\text{weak}}$  experiment was the accuracy of the Wien angle. Since the experiment relied

on the double Wien system for slow helicity reversal (see Subsection 5.1.2.5), each Wien filter adjustment induced a potential 2% to 3% residual transverse polarization in the beam. In addition, Wien angle drifts caused by the drifts in the electric and magnetic fields of the Wien filter are known to affect the reproducibility of the Wien. Without direct indicators of residual transverse polarization in the beam, these changes are harder to observe. Other than the passive Mott measurement, there are no known online monitors of transverse polarization in the beam at the Jefferson Lab accelerator. However, with the knowledge gained from the transverse measurements in Transverse\_Run I, for the purpose of the  $Q_{\text{weak}}$  experiment, the Čerenkov detector array was used as a transverse polarization monitor for both online and offline transverse polarization monitoring<sup>3</sup>.

### 7.2.1 Transverse Polarization Monitoring

The amount of residual transverse polarization in a longitudinally polarized beam is extracted by fitting the Čerenkov detector asymmetries using the fit

$$A^L(\phi) = -4.8 \text{ ppm} \times [P^V \cos \phi - P^H \sin \phi] + C, \quad (7.5)$$

(see Figure 7.3) where  $P^{V/H}$  is the residual vertical/horizontal transverse polarization in the beam and -4.8 ppm is the physics asymmetry measured from the transverse measurements. This procedure was repeated on data accumulated for approximately 3 day time period (see Figure 7.4) to identify non-zero  $P^V$  and  $P^H$  at 99.7% C. L. Figure 7.5 shows an example of the successful use of transverse monitoring to reduce residual horizontal transverse polarization in the beam. In this particular case, the transverse monitoring at the end of Wien 6 (2 to 3 weeks of data) period shows a residual horizontal transverse polarization in the beam of about  $-4.6 \pm 0.8\%$ . For a 88% longitudinally polarized beam, this indicates a  $3.5^\circ$  shift in the Wien filter from its optimized longitudinal angle. This observation was confirmed by a super spin dance<sup>4</sup> [162] done at the end of Wien 6 which showed the horizontal Wien was off

---

<sup>3</sup>Historically, parity violating electron scattering experiments which ran at the Jefferson Lab have utilized luminosity monitors to monitor residual transverse polarization in the beam due to their high resolution. Even though the  $Q_{\text{weak}}$  setup was equipped with luminosity monitors, backgrounds and noise prevented them from being used as transverse polarization monitors.

<sup>4</sup>A super spin dance is a calibration of the Wien filter done using the Møller polarimeters in the halls. For left-flip and right-flip spin configurations, the Wien angle is optimized to deliver full longitudinally polarized beams into the halls. The optimized direction of the polarization is confirmed using the Møller polarimeter.

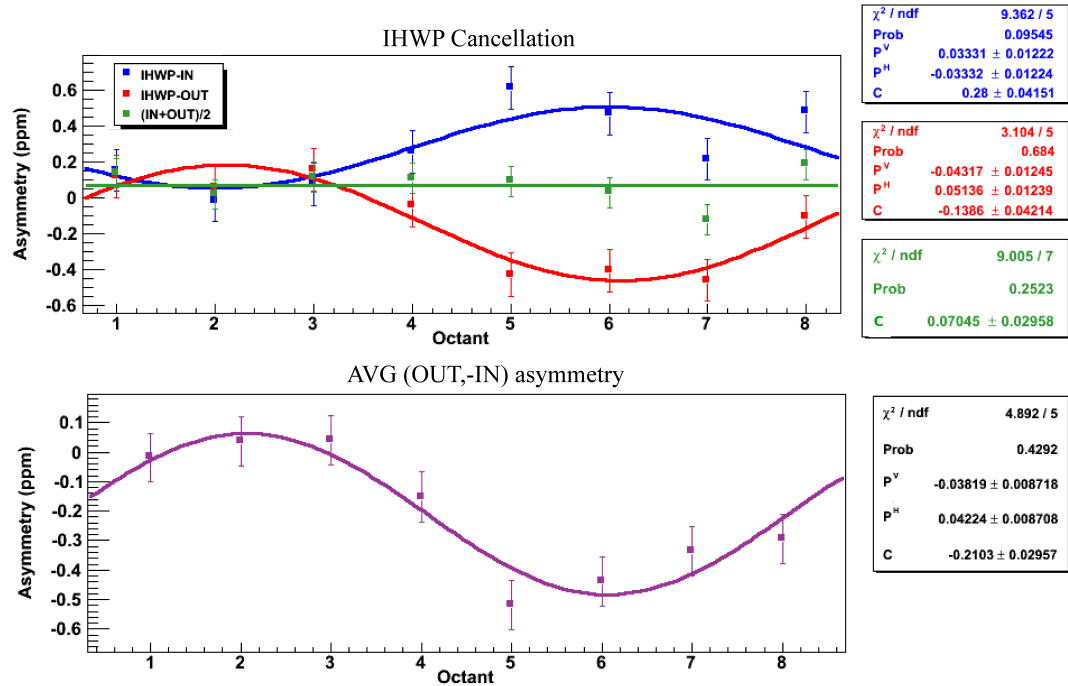


Figure 7.3: Residual transverse polarization in the longitudinally polarized electron beam during the  $Q_{\text{weak}}$  commissioning period extracted using the fit in Equation 7.5 over the Čerenkov detector asymmetries. Top - Asymmetries from IHWP IN and OUT data are fitted separately to check for the IHWP cancellation. Bottom - The physics asymmetry of the average of IN and sign corrected OUT data are fitted to extract the residual vertical ( $P_V$ ) and horizontal ( $P_H$ ) transverse polarization components. Error bars are statistical only.

from the optimal position by  $+3.7 \pm 0.3^\circ$ . In the Wien flip which followed afterwards, the Wien angle was adjusted to  $0.0 \pm 0.3^\circ$ , and the transverse monitoring of the data taken afterwards shows the residual transverse polarization in the beam was then consistent with zero.

However, not all azimuthal modulations observed from transverse monitoring were corrected by adjusting the Wien filter due to several reasons. This was the first time a transverse polarization feedback was attempted on the double Wien setup which is a relatively new system. There is a  $2^\circ$  error in the Wien filter that can lead to an over or under prediction of the optimal angle required for the correction. Currently, the optimal way to do this correction is to do a mini-spin dance using the Møller polarimeter. This process can take 4-8 hours to complete and interferes with the beam delivery. Even if the Wien angle was optimized, it can drift over time requir-



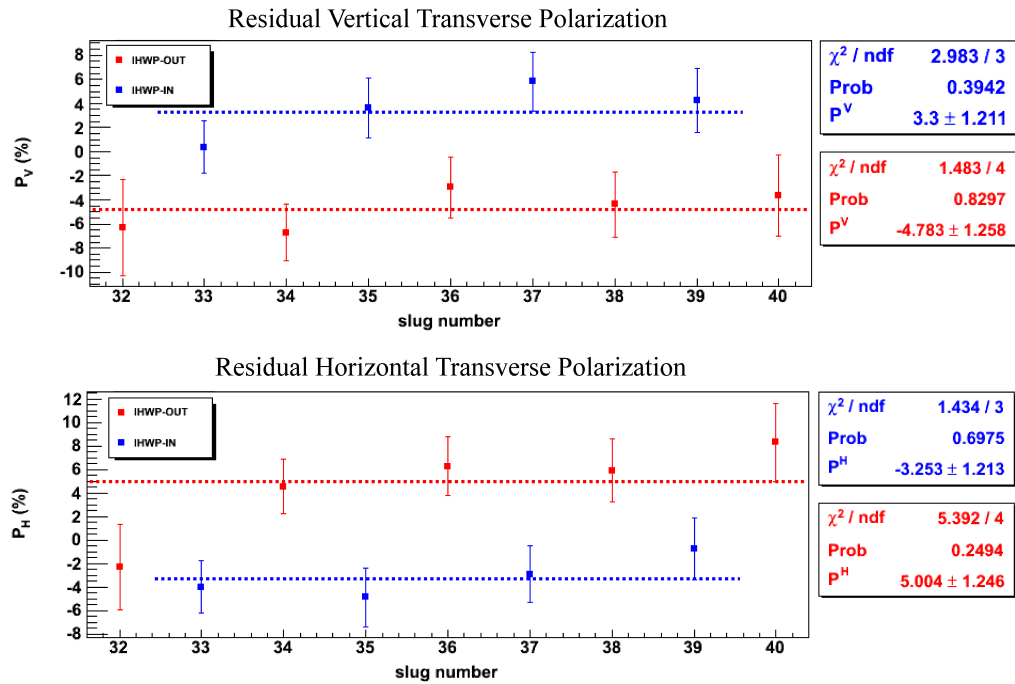


Figure 7.4: Residual transverse polarization monitoring results from the  $Q_{\text{weak}}$  commissioning data set. Both plots show about a 3-4% residual vertical and horizontal transverse polarization in the beam. The data points are not corrected for the IHWP reversal. Each data point represents a 8 hr long measurement (slug). The error bars are statistical only.

ing the correction to be applied more frequently than acceptable, such as once every week. Since  $Q_{\text{weak}}$  was under a strict time schedule, losing this amount of beam time once a week in addition to all the other allocated beam losses was not acceptable. It was a trade-off between minimizing the BNSSA leakage correction/uncertainty to the parity violating asymmetry and losing the statistical precision on the parity violating asymmetry measurement. Another reason to avoid correcting all indicators of azimuthal modulations was the correlations between asymmetry modulations generated by the BNSSA and residual helicity correlated beam asymmetries (see Appendix H.1). Due to systematics, which are currently under investigation [163], linear regression of detector asymmetries are seen not to completely remove beam asymmetries generated by helicity correlated beam parameter differences. For a proper deconvolution of the two types of asymmetry modulations, the false asymmetries generated by

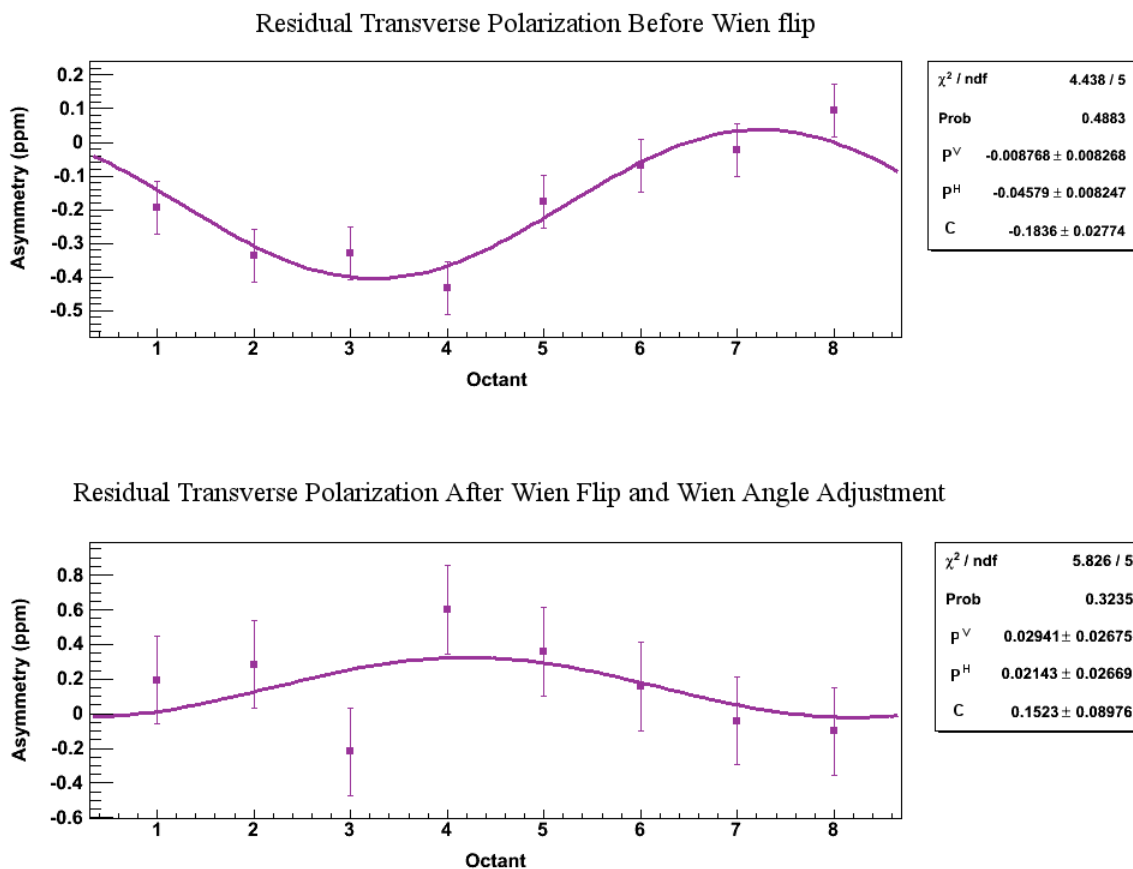


Figure 7.5: The successful use of transverse monitoring to identify and correct the residual transverse polarization in the beam. Top - Residual horizontal transverse polarization in the beam in Wien 6 (flip right) is about  $-4.6 \pm 0.8\%$ . Bottom - After adjusting the Wien angle in the Wien flip (left) setting, the residual horizontal transverse polarization in the beam is consistent with zero.

beam parameters<sup>5</sup> should be relatively small compared to the precision of the measured detector asymmetries. If not, the correction applied on the Wien angle based on the azimuthal modulations could probably induce a transverse polarization in the beam.

All of the above mentioned reasons prevented the experiment from relying on the full capability of the Čerenkov detector array for transverse polarization monitoring at all times. But the attempts made at online transverse monitoring and feedback lead to the discovery [164, 165] of the 1% non-linearity in the Wien filter calibration.

<sup>5</sup>The beam position and angle sensitivities of the detectors show an azimuthal dependence similar to the beam normal single spin asymmetry (see Subsection 6.4.2).

This and all other lessons learned from  $Q_{\text{weak}}$  will facilitate better control of residual transverse polarization in the beam at Jefferson Lab and the proper implementation of transverse polarization monitoring in future precision parity violating experiments.

### 7.3 BNSSA Leakage on Parity Violating Asymmetry

Due to systematics associated with the corrections to beam position and angle false asymmetries, at this time, residual transverse polarization monitored via the Čerenkov detectors during the longitudinal polarization measurement can not be interpreted as pure residual transverse polarization. Therefore, applying a correction for BNSSA leakage on the parity violating asymmetry could inadvertently introduce a false asymmetry. To avoid this BNSSA leakage will be treated as a systematic uncertainty only. In the following subsections I will present the estimate for the systematic uncertainty used on the parity violating asymmetry from the commissioning data set used for the 19%  $Q_w^p$  measurement whose result was released in the fall of 2012 as a proof of concept of the  $Q_{\text{weak}}$  experiment. I will then propose the BNSSA leakage systematic uncertainty for the full  $Q_{\text{weak}}$  data set for the 4% measurement of  $Q_w^p$ .

#### 7.3.1 Systematic Uncertainty for the 19% $Q_w^p$ Measurement

From the fits in Figure 7.3, the amounts of residual transverse polarization in the beam during the  $Q_{\text{weak}}$  commissioning period is

$$\begin{aligned} P^H &= -3.8 \pm 0.9\%, \\ P^V &= 4.2 \pm 0.9\%. \end{aligned} \tag{7.6}$$

Following the description in Subsection 7.1.1, with five-parameter and charge asymmetry regression<sup>6</sup>, the BNSSA leakages in the two transverse settings are

$$\begin{aligned} C^V &= 0.008 \pm 0.072 \text{ ppm}, \\ C^H &= 0.004 \pm 0.064 \text{ ppm}. \end{aligned} \tag{7.7}$$

---

<sup>6</sup>These results are based on the preliminary analysis [166] of the transverse data set with less strict event cuts. At the time of the analysis of the commissioning data set, the full analysis of the transverse data set with updated event cuts, presented in the Chapter 6 of this dissertation was not available. However, the differences in the quality cuts does not effect the final systematic uncertainty as it is an upper bound.

Using 7.6 and 7.7, the amount of BNSSA leakage into the parity violating asymmetry in this particular longitudinal data set is

$$C_{\text{Commissioning}}^L = |C^V * P^V| + |C^H \times P^H| = 0.0005 \pm 0.0039 \text{ ppm}, \quad (7.8)$$

the upperbound of which

$$(dA^{Phys})_{\text{BNSSA leakage}}^{\text{Commissioning}} = \pm(0.0005 + 0.0039) = \pm 0.0044 \text{ ppm}, \quad (7.9)$$

was assigned as the systematic uncertainty for BNSSA leakage. This is a 2% contribution to the total error of the acceptance corrected parity violating asymmetry.

### 7.3.2 Systematic Uncertainty for the Final $Q_w^p$ Measurement

To determine the BNSSA leakage systematic uncertainty for the full  $Q_{\text{weak}}$  data set I will first try to use the residual transverse polarization extracted from the individual Wien periods (2-3 weeks) similar to what was shown in Figure 7.3. These results are summarized in Table 7.4 and Figure 7.6. As discussed in the figure, the large values of the horizontal component observed between Wien 4 to 7 were not thought to be generated by the transverse polarization only due to the large horizontal position differences presented at the time. Looking at the overall behaviour of the horizontal component, one can see that even after being sign corrected for the Wien flip, the sign of the horizontal values changes from one Wien to the other going from Wien 4 to Wien 7. This is a characteristic of helicity correlated false asymmetries which are generated by non-polarization effects. Therefore, the observed sign change in the horizontal component is a clear indication of an asymmetry modulation generated by helicity correlated position differences.

Until a better method of regressing false asymmetries generated by beam parameters is available, the average of the horizontal and vertical components  $P^H = 0.0 \pm 0.2\%$  and  $P^V = 1.0 \pm 0.2\%$  will not be used in the estimation of the BNSSA leakage. Clearly, these are underestimated values since the Wien angle error alone can produce a 3.0% residual transverse polarization in the beam. Based on this observation, for the time being, the 3.0% associated with a  $2^\circ$  error on the Wien angle will be used as the amount of residual vertical and horizontal transverse polarization present in the full  $Q_{\text{weak}}$  data set. i.e.  $P^H = P^V = 0.0 \pm 3.0\%$ .

When estimating the BNSSA leakage, the choice of using the leakage extracted

from the transverse data or the simulations depends on the desired magnitude of the final systematic uncertainty and how well it is represented. To demonstrate this, I will estimate the BNSSA leakage systematic uncertainty for both cases.

Table 7.4: Residual transverse polarization in Wien periods determined from the fits over five-parameter regressed Čerenkov detector asymmetries. See Appendix H.2 for the plots. The values are corrected for the additional spin flip coming from the Wien.

Wien	slugs	$P^V$ (%)		$P^H$ (%)	
		Mean	Error	Mean	Error
0 (right)	32 - 40	-3.8	0.9	4.2	0.9
1 (left)	42 - 58	1.4	0.8	1.5	0.8
2 (right)	59 - 80	2.1	0.7	2.4	0.7
3 (left)	81 - 98	-0.6	0.8	1.1	0.8
4 (right)	99 - 112	-2.3	0.8	4.6	0.8
5 (left)	117 - 136	2.0	0.7	-5.1	0.7
6 (right)	137 - 155	0.6	0.8	5.3	0.8
7 (left)	158 - 171	0.3	1.0	-3.4	1.0
8 (right)	172 - 225	1.5	0.4	-0.7	0.4
9 (left)	226 - 306	1.1	0.3	-0.5	0.3
10 (right)	307 - 321	-0.9	1.0	-0.7	1.0

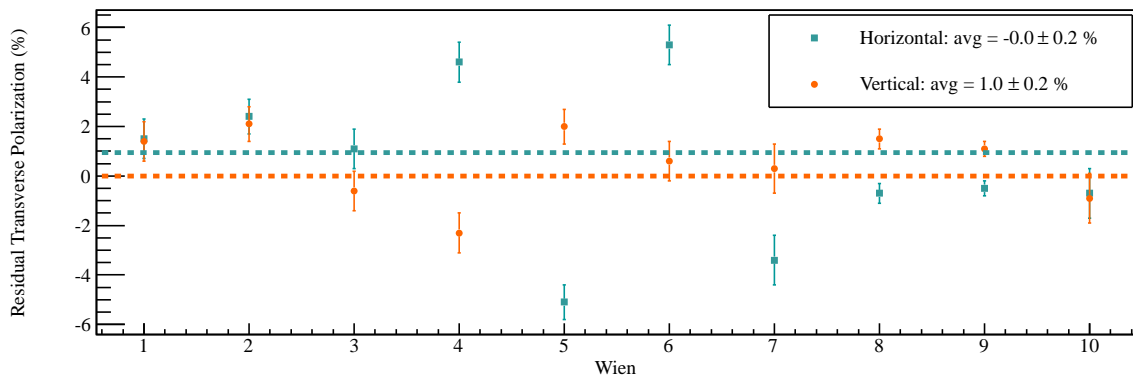


Figure 7.6: Variation of the residual transverse polarization in the beam over the  $Q_{\text{weak}}$  Run I and Run II determined from transverse polarization monitoring. Each data point represents the average over a Wien (2-3 weeks). The data points are corrected for the IHWP and Wien flips. See Table 7.4 for the values. Due to large position differences, the large changes in the horizontal transverse component between Wiens 4 to 7 were not thought to be coming from the transverse polarization and were not corrected by adjusting the Wien angle.

- Using BNSSA leakage from the measurements,

$$(dA^{Phys})_{\text{BNSSA leakage}}^{\text{Wiens 1-10}} |_{\text{Meas.}} = \pm 0.0009 \text{ ppm.}$$

- Using BNSSA leakage from the simulations,  $C^V = -0.0002 \pm 0.0005 \text{ ppm}$  and  $C^H = 0.0519 \pm 0.0005 \text{ ppm}$ ,

$$(dA^{Phys})_{\text{BNSSA leakage}}^{\text{Wiens 1-10}} |_{\text{Sim.}} = \pm 0.0016 \text{ ppm.}$$

From the above two estimates, one can see that using the measured BNSSA leakage results in a systematic uncertainty which is smaller than the one obtained from the simulated leakage. This is due to the fact that the simulated leakage from the horizontal transverse polarization is larger than the combined leakages from the vertical and horizontal transverse measurements. Therefore, using the BNSSA leakage from the measurements under predicts the actual leakage and thereby the associated uncertainty. Based on this observation, I propose the simulation based systematic uncertainty of  $\pm 0.0016 \text{ ppm}$  to be used for the final  $Q_{\text{weak}}$  parity violating asymmetry measurement to take into account the BNSSA leakage due to the residual transverse polarization in the electron beam.

## 8 Results and Conclusions

This dissertation presents the highlights of my PhD research work in the context of the  $Q_{\text{weak}}$  experiment. In this chapter, I will summarize the results and conclusions I have presented so far.

### 8.1 Contributions Towards the Measurement of the Weak Charge of the Proton

The  $Q_{\text{weak}}$  experiment is the start of a new generation of experiments which pushes the precision boundaries of parity violating asymmetry measurements. The success of  $Q_{\text{weak}}$  lies in a decade of meticulous planning and hard work of about 100 collaborators from all over the world. All the experience gained by this experiment will help the upcoming and future precision parity violating experiments at the Jefferson Lab such as the MOLLER experiment [46]. My contributions to the  $Q_{\text{weak}}$  experiment towards the measurement of the weak charge of the proton can be summarized under four categories; the data acquisition and analysis software, helicity correlated false asymmetries, transverse polarization monitoring, and the beam normal single spin asymmetry measurement and determination of the BNSSA leakage and the associated systematic.

#### *8.1.1 Data Acquisition and Analysis Related Work*

In Chapter 4, I summarized the data acquisition and analysis software. The experiment used two modes of specialized data acquisition systems for the integrating parity asymmetry measurement and the low current counting  $Q^2$  measurement. I was involved with the initial setup and testing of the integrating mode data acquisition system. During the experiment, I was a part of the four person group who was responsible for the maintenance of the data acquisition, analysis and storage 24/7. Aiming towards a 5 ppb statistical error, one of the concerns of the collaboration was the contribution from noise sources. Noise sources, such as the electronic noise in the signal chains, increase the standard deviation of the measured asymmetry distributions thereby increasing the statistical error of the measurement. Based on noise measurements performed under realistic conditions, I showed in Chapter 5 the

contribution from the electronic noise into the asymmetries is below 5 ppm. This is a negligible contribution compared to the 660 ppm standard deviation of a single detector asymmetry distribution.

All the data readout via the DAQ system was processed using a specialized analysis software specially developed for the use of  $Q_{\text{weak}}$ . The  $Q_{\text{weak}}$  analysis software uses the object oriented framework in C++ and has an event processing rate of 1 kHz. One of my main contributions to the software framework includes the implementation of the helicity signal readout and asymmetry formation routines. I also implemented the beam position monitor decoding and beam position reconstruction in the software which involved devising a method to project beam position, angle and energy at the target. In Chapter 3, I presented the results of this work which identified the combination of beam position monitors to provide a  $1 \mu\text{m}$  position difference resolution, a  $0.2 \mu\text{rad}$  angle difference resolution and a 2 ppm energy asymmetry resolution at beam currents above  $150 \mu\text{A}$  for beam parameter measurements at the target. The resolution of beam parameters becomes the limiting factor for properly removing false asymmetries generated by helicity correlated differences in the beam. Except for the angle, the position and energy resolutions are at a level acceptable for the experiment. The angle resolution however needs to be further improved at by at least a factor of 2 and work is already underway to make the necessary changes in the analysis.

### *8.1.2 Helicity Correlated False Asymmetries*

Helicity correlated false asymmetries are generated by either helicity correlated differences in the beam parameters or by the leakage of the helicity signal into electronics. In Chapter 5, I presented my work on the minimization of sources of helicity correlated beam parameters at the polarized source. The best  $Q_{\text{weak}}$  polarized source setups typically yielded helicity correlated position differences less than 50 nm, angle differences less than 1 nrad and energy asymmetries less than 0.01 ppm. Except for the position differences, all other parameters were within the specifications of the experiment. The large position differences were identified to be generated by the residual energy dispersion at the target.

In Chapter 5, I also presented the first parts per billion measurement of the helicity leakage on an experiment running at Jefferson Lab and demonstrated the effectiveness of using a delayed helicity. When in direct contact with the ADCs digitizing the detector signals, the helicity signal is seen to create a false asymmetry of about -80 ppb. This asymmetry goes to zero when using a delayed helicity signal in



the electronics. In relation to helicity leakage, the leakages from other helicity control signals (MPS, QRT) were also measured and are seen to create a pattern dependent cancelling false asymmetry of 50 ppb. Although this asymmetry is harmless for the  $Q_{\text{weak}}$  analysis, diagnostic studies on the data based on quartets should take into account its presence in the signals.

### ***8.1.3 Transverse Polarization Monitoring and BNSSA Leakage***

Using the Čerenkov detector system, I performed the first known transverse polarization monitoring in an experiment at Jefferson Lab. For situations where position differences are small and properly accounted for in the regression analysis, I have shown this method is capable of identifying the residual transverse polarization in the beam. In addition to aiding the  $Q_{\text{weak}}$  analysis, the transverse polarization monitoring has also led to the observation of the non-linearity of the Wien filters used at the Jefferson Lab injector. This will help to improve the use of the Wien filters to control the transverse polarization in the beam for future parity violating electron scattering experiments. Using the results from the beam normal single spin asymmetry measurement, in Chapter 7, I estimated the beam normal single spin asymmetry leakage into the parity violating asymmetry due to residual transverse polarization in the beam and the broken symmetry of the Čerenkov detector array. Using the  $2^\circ$  Wien angle error as the only cause of residual transverse polarization in the beam, I proposed a  $\pm 0.0016$  ppm to be used as the systematic uncertainty due to beam normal single spin asymmetry leakage on the full  $Q_{\text{weak}}$  data set.

## **8.2 The Determination of the Weak Charge of the Proton**

After a successful two-year running period, the  $Q_{\text{weak}}$  experiment concluded its data taking in May 2012. The ongoing analysis of the full data set is expected to be completed by the end of 2014. But the analysis of the commissioning data set (about 4% of the total data set) is complete and will be published in the near future as a proof of concept of the data analysis [167]. The complete analysis of the commissioning data is presented in the dissertation of R. Beminiwattha [41] and was not repeated in this dissertation. However, the results and a discussion will be presented here for completeness.

The analysis of the  $Q_{\text{weak}}$  commissioning data set yielded the smallest and most precise measurement of the parity violating elastic electron-proton asymmetry

of  $-0.279 \pm 0.035_{Stat} \pm 0.031_{Sys}$  ppm [167]. Using this result in a global fit of the parity violating electron scattering (PVES) asymmetries (see Figure 8.1), yields the weak charge of the proton [167]

$$Q_w^p(PVES) = 0.064 \pm 0.012.$$

This is a 19% measurement which is in a good agreement with the Standard Model prediction of  $Q_w^p(\text{SM}) = 0.0710 \pm 0.0007$ . Combined with the atomic parity violating (APV) measurement, this result provides new constraints on the neutral-current quark coupling constants as shown in Figure 8.2. The neutral-current couplings extracted from this global analysis  $C_{1u} = -0.1835 \pm 0.0054$  and  $C_{1d} = 0.3355 \pm 0.0050$  are in agreement with the Standard Model prediction at 68% C.L. In addition, the  $C_1$ 's extracted from this measurement are used to determine the weak charge of the neutron,  $Q_w^n = -2(C_{1u} + 2C_{1d}) = 0.975 \pm 0.010$ , which is also in agreement with the Standard Model value. The current precision of the  $Q_w^p$  updates the mass scale of the new parity violating physics to 1.1 TeV at 95% C.L. As it stands, this 19% measurement of the  $Q_w^p$  confirms the predictions of the Standard Model. The analysis of the full  $Q_{\text{weak}}$  data set which will yield a five times better precision measurement on the  $Q_w^p$  is under way and is anticipated to be completed by the end of 2014.

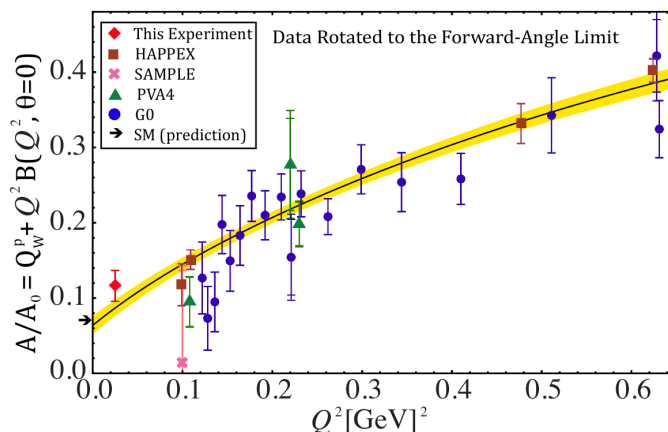


Figure 8.1: Extracting  $Q_w^p$  from the global fit (solid black line) of the reduced PVES asymmetries in the forward angle limit. The result from the  $Q_{\text{weak}}$  commissioning data is shown in red. The yellow band indicates the uncertainty in the fit.  $Q_w^p$  is the intercept of the fit and it is in a good agreement with the Standard Model prediction. Figure from Ref. [167].

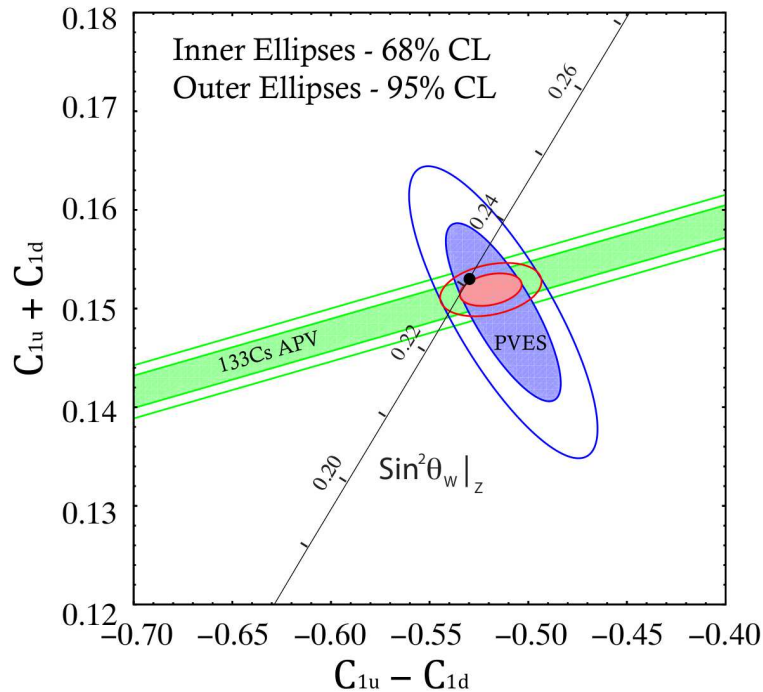


Figure 8.2: The constraints on the isovector ( $C_{1u} - C_{1d}$ ) and isoscalar ( $C_{1u} + C_{1d}$ ) neutral-weak quark couplings. The green band is from the atomic parity violation (APV) measurement from  $^{133}\text{Cs}$  [168] with updated nuclear corrections [169]. The purple ellipses are from a global analysis of the parity violating electron scattering (PVES) experiments including the 19%  $Q_{\text{weak}}$  result. The red ellipses results from the combined fit from APV and PVES. The black filled circle is the Standard Model prediction. Current experimental constraints are in a good agreement with the Standard Model prediction. Figure from Ref. [167].

### 8.3 The 3% Measurement of the Beam Normal Single Spin Asymmetry

With the precision improvements in parity violating electron scattering experiments (PVES), the beam normal single spin asymmetry (BNSSA) is seen to become one of the well determined observables of the two-photon exchange process. As an excellent example, the  $Q_{\text{weak}}$  collaboration has made a 3% relative measurement of the beam normal single spin asymmetry of

$$B_n = -5.350 \pm 0.067_{\text{Stat}} \pm 0.137_{\text{Sys}} \text{ ppm} \quad (8.1)$$

using a transversely polarized electrons of 1.155 GeV scattering elastically with a  $Q^2$  of  $0.025 \text{ (GeV/c)}^2$  from protons.

This is the most precise measurement of the beam normal single spin asymmetry available at the time (see Table 8.1). A measurement of this precision is an excellent test of theoretical calculations as shown in Table 8.2. Out of the three model calculations presented in Table 8.2, one calculation shows a good agreement with the measurement while the others are significantly off. For further comparison of these models, Figure 8.3 shows the modelled beam normal single spin asymmetry variation in the  $Q_{\text{weak}}$  acceptance. Even though the magnitudes are different, all three models show that the BNSSA is proportional to the scattering angle at these low-energy forward angle scattering kinematics. The differences in the magnitudes are generated by the types of intermediate states considered in the calculation of the imaginary part of the two-photon exchange.

As discussed in Subsection 2.2.6.1, the dominant contributor to the beam normal single spin asymmetry is the excited intermediate states in the two-photon exchange process. Compared to the contribution from the excited states, the contribution from the ground state is negligible (see Figure 8.4). In the Pasquini & Vanderhaeghen model, under the  $\pi N$  intermediate state assumption, the dominant contribution to BNSSA at  $Q_{\text{weak}}$  kinematics comes from the resonant excited states

Table 8.1: World data on the beam normal single spin asymmetry measurements including the unpublished  $Q_{\text{weak}}$  result from the analysis presented in this dissertation.

Experiment	Energy (GeV)	$\theta_{Lab}$ (deg)	Asymmetry (ppm)	$dB_n/B_n$ %
Backward Angle Scattering				
SAMPLE [79]	0.200	146.1	$-15.4 \pm 5.4$	35
A4 [170]	0.300	$140 < \theta_{lab} < 150$	$-87 \pm 6$	7
G0 Backward [81]	0.362	108	$-176.5 \pm 9.4$	5
G0 Backward [81]	0.687	108	$-21 \pm 24$	87
Forward Angle Scattering				
G0 Forward [171]	3.000	$52 < \theta_{lab} < 76.5$	$-4.06 \pm 0.99 \pm 0.63$	29
G0 Forward [171]	3.000	$52 < \theta_{lab} < 76.5$	$-4.82 \pm 1.87 \pm 0.98$	44
A4 [82]	0.569	$30 < \theta_{lab} < 40$	$-8.59 \pm 0.89 \pm 0.79$	14
A4 [82]	0.855	$30 < \theta_{lab} < 40$	$-8.52 \pm 2.31 \pm 0.87$	29
<b>QWEAK</b>	<b>1.155</b>	<b>7.9</b>	<b><math>-5.35 \pm 0.07 \pm 0.14</math></b>	<b>3</b>
HAPPEX [172]	3.026	6	$-6.80 \pm 1.54 \pm 0.24$	23
E158 [173]	43.000	0.24	$2.89 \pm 0.36 \pm 0.17$	14

Table 8.2: Theoretical predictions for the beam normal single spin asymmetry at the nominal scattering angle of  $7.9^\circ$  and the vertex energy of 1.155 GeV. These calculations were provided by Pasquini & Vanderhaeghen [72], Afanasev & Merenkov [73] and Gorchtein [75] (see Appendix I). The model predictions differ from the  $Q_{\text{weak}}$  result by 4% to 50%.

Model	Predicted BNSSA (ppm)	Deviation from the $Q_{\text{weak}}$ result
Pasquini & Vanderhaeghen [72]	-2.92	$\approx 50\%$
Afanasev & Merenkov [73]	-4.56	$\approx 15\%$
Gorchtein [75]	$-5.42 \pm 0.067$	$\approx 2\%$

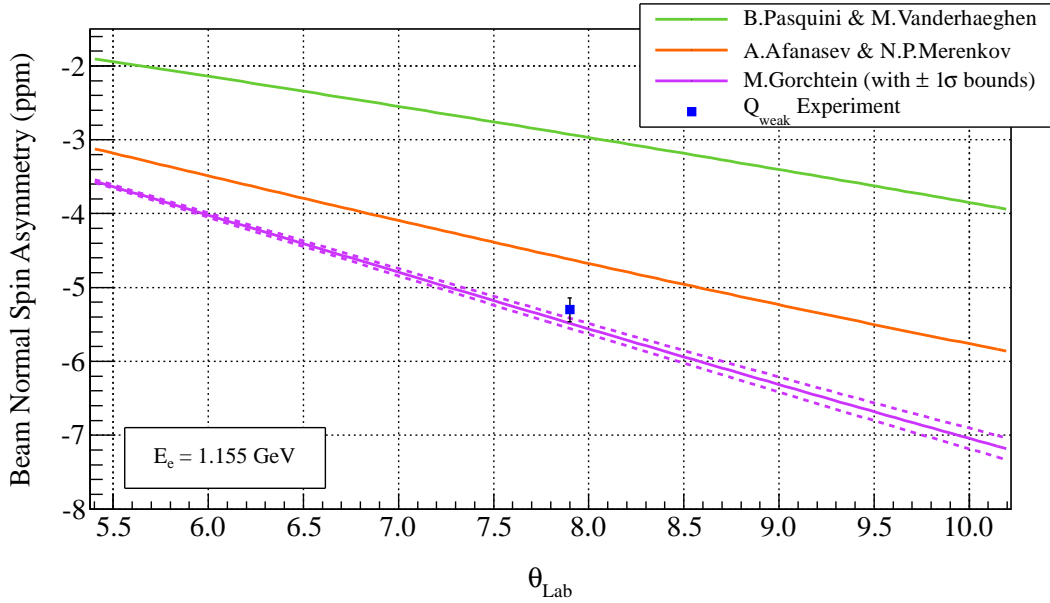


Figure 8.3: Scattering angle dependence of the beam normal single spin asymmetry model calculations in the  $Q_{\text{weak}}$  acceptance  $5.6^\circ$  to  $10^\circ$ . The  $Q_{\text{weak}}$  BNSSA result is quoted at the nominal scattering angle of  $7.9^\circ$ .

$\Delta(1232)$ ,  $D_{13}(1520)$  and  $F_{15}(1680)$  as shown in Figure 8.5. Since the area under the curve gives the total contribution from the excited state into  $B_n$ , when considering  $\pi N$  states, one can see the dominant contribution to the BNSSA at  $Q_{\text{weak}}$  kinematics comes from the  $\Delta(1232)$  resonance. Based on this observation, the factor of two difference between the Pasquini & Vanderhaeghen model and Afanasev & Merenkov and Gorchtein models is explained by the exclusion of the resonances of the proton, which decay into two-pions, in the calculation of the contribution from the excited

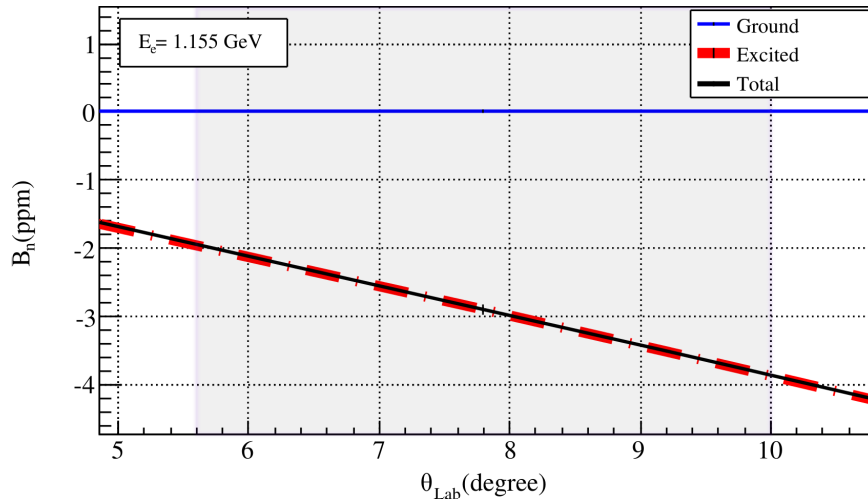


Figure 8.4: Contributions from the ground and excited intermediate states in the two-photon exchange process into the BNSSA. The shaded region shows the the  $Q_{\text{weak}}$  acceptance. The contribution from the ground state is negligible compared to that of the excited states. The calculations are based on the Pasquini & Vanderhaeghen model but the dominance of the excited states over the ground state is a model independent observation.

states. Specifically, the contributions from the  $D_{13}(1520)$  and  $F_{15}(1680)$  resonances, which decay into  $\pi\pi N$  with a  $\approx 50\%$  branching ratio [38].

The factor of two discrepancy between the data and the Pasquini & Vanderhaeghen model was first observed in the forward angle beam normal single spin asymmetry measurement performed by the G0 experiment (see the discussion in Subsection 2.2.6.1 and Figure 2.18). In fact, the G0 measurement done at  $20^\circ$  C.M. angle was  $2\sigma$  away (95% C.L.) from all three of these model calculations with Pasquini & Vanderhaeghen model under predicting the result and Afanasev & Merenkov and Gorchtein models over predicting the result. The  $Q_{\text{weak}}$  measurement confirms with a more than  $3\sigma$  deviation (100% C.L.) that the single pion excitations in the excited intermediate state of the two-photon exchange process under Pasquini & Vanderhaeghen model are not adequate for electron energies above the two-pion threshold of 1.216 GeV in COM. The Afanasev & Merenkov and Gorchtein models which use  $\pi\pi N$  excited intermediated states are in fairly good agreement with the  $Q_{\text{weak}}$  result. But the difference of about 1 ppm seen between these two model calculations comes from the different parametrization of the cross-section for photoproduction of pions off of protons and the Compton amplitude [175].

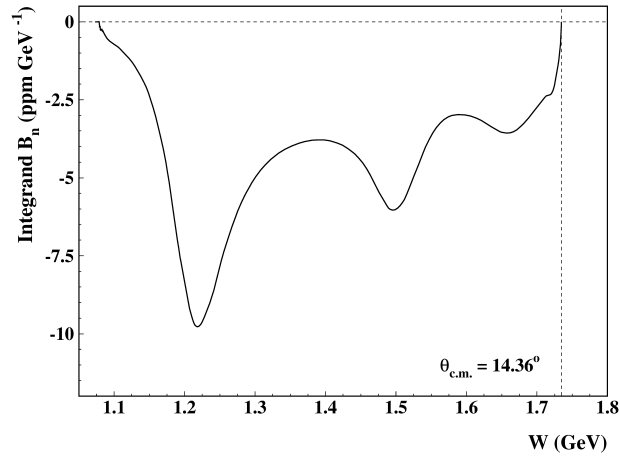


Figure 8.5: The contributions from the different intermediate states into the beam normal single spin asymmetry for  $e+p \rightarrow e+p$  at a beam energy of 1.155 GeV and a center of mass angle  $14.36^\circ$ . The vertical axis shows the size of the contribution by the different intermediate states in the two-photon exchange. The horizontal axis shows the mass range 1.077 GeV to 1.732 GeV, of all the intermediate states accessible for a beam energy of 1.155 GeV. This calculation is from the Pasquini & Vanderhaeghen model where the excited intermediate states are assumed to be  $\pi p$ . The curve shows the total contribution from  $\pi^0 p$  and  $\pi^+ n$  channels. In this case the curve displays three prominent structures corresponding to the resonances  $\Delta(1232)$ ,  $D_{13}(1520)$  and  $F_{15}(1680)$ . Calculation and figure from Ref. [174].

Together with the G0-backward angle beam normal spin asymmetry measurement, the  $Q_{\text{weak}}$  result confirms the importance of using multiple pions in the excited intermediate state of the two-photon exchange for beam energies above pion-threshold. In addition, our result shows the importance of parametrization of the experimental inputs, such as the photo-production cross-section, used for the estimation of the imaginary part of the two-photon exchange process. Moreover, the fine tuning of the experimental inputs in the models will help to remove the model dependent uncertainty in the BNSSA predictions.

So far, I have presented a discussion of the  $Q_{\text{weak}}$  elastic beam normal single spin asymmetry measurement. In addition to the elastic data from the proton,  $Q_{\text{weak}}$  has data on the beam normal single spin asymmetry measurements (see Table 8.3) from several other physics processes. Some of these measurements are the first of their kind and carry interesting physics. The analysis of these data is ongoing. Due to the small relative precisions of these measurements, when finalized, they can be

Table 8.3: Remainder of the  $Q_{\text{weak}}$  beam normal single spin asymmetry measurements and their relative statistical precisions.

Target	Relative precision
Elastic electron-proton scattering	
Aluminum	$\approx 4\%$
Carbon	$\approx 7\%$
Inelastic electron-proton scattering with a $\Delta$ in the final state	
Hydrogen	$\approx 3\%$
Aluminum	$\approx 5\%$
Carbon	$\approx 3\%$

expected to be good candidates to test model calculations of beam normal single spin asymmetry.

Going further,  $Q_{\text{weak}}$  beam normal single spin asymmetry measurements can be used to estimate the real part of the two-photon exchange with the use of dispersion relations. This will provide a valuable cross-check of both the dispersion relations and the models of the real part of the two-photon exchange process.



## Bibliography

- [1] L. W. Mo and Y.-S. Tsai, “Radiative Corrections to Elastic and Inelastic  $ep$  and  $\mu p$  Scattering,” *Rev.Mod.Phys.*, vol. 41, pp. 205–235, 1969.
- [2] G. Greenhut, “Two-photon Exchange in Electron-Proton Scattering,” *Phys.Rev.*, vol. 184, pp. 1860–1867, 1969.
- [3] P. A. Guichon and M. Vanderhaeghen, “How to Reconcile the Rosenbluth and the Polarization Transfer Method in the Measurement of the Proton Form-factors,” *Phys.Rev.Lett.*, vol. 91, p. 142303, 2003.
- [4] P. Blunden, W. Melnitchouk, and J. Tjon, “Two-Photon Exchange in Elastic Electron-Nucleon scattering,” *Phys.Rev.*, vol. C72, p. 034612, 2005.
- [5] M. Jones *et al.*, “ $G_{E_p}/G_{M_p}$  Ratio by Polarization Transfer in Polarized  $\vec{e}p \rightarrow e\vec{p}$ ,” *Phys.Rev.Lett.*, vol. 84, pp. 1398–1402, 2000.
- [6] D. S. Armstrong *et al.*, “The  $Q_{\text{weak}}$  Experiment: A Search for New Physics at the TeV Scale via a Measurement of the Proton’s Weak Charge,” 2012. arXiv:1202.1255.
- [7] M. K. Gaillard, P. D. Grannis, and F. J. Sciulli, “The Standard Model of Particle Physics,” *Rev.Mod.Phys.*, vol. 71, pp. S96–S111, 1999.
- [8] American Association for the Advancement of Science. <http://membercentral.aaas.org/>. Reference website for figure.
- [9] F. J. Hasert *et al.*, “Observation of Neutrino Like Interactions Without Muon Or Electron in the Gargamelle Neutrino Experiment,” *Phys.Lett.*, vol. B46, pp. 138–140, 1973.
- [10] F. J. Hasert *et al.*, “Search for Elastic Muon-Neutrino Electron Scattering,” *Phys.Lett.*, vol. B46, pp. 121–124, 1973.
- [11] F. J. Hasert *et al.*, “Observation of Neutrino Like Interactions without Muon or Electron in the Gargamelle Neutrino Experiment,” *Nucl.Phys.*, vol. B73, pp. 1–22, 1974.

- [12] CERN Document Server. <http://cds.cern.ch/record/39468>. Reference website for figure.
- [13] C. Y. Prescott *et al.*, “Parity Nonconservation in Inelastic Electron Scattering,” *Phys.Lett.*, vol. B77, pp. 347–352, 1978.
- [14] P. Soding, B. Wiik, G. Wolf, and S. Wu, “The First Evidence for Three Jet Events in  $e^+ e^-$  Collisions at PETRA: First Direct Observation of the Gluon,” 1996. DESY-96-193.
- [15] G. Arnison *et al.*, “Experimental Observation of Lepton Pairs of Invariant Mass Around  $95(GeV/c^2)$  at the CERN SPS Collider,” *Phys.Lett.*, vol. B126, pp. 398–410, 1983.
- [16] P. Bagnaia *et al.*, “Evidence for  $Z^0 \rightarrow e^+e^-$  at the CERN  $\bar{p} p$  Collider,” *Phys.Lett.*, vol. B129, pp. 130–140, 1983.
- [17] G. Arnison *et al.*, “Experimental Observation of Isolated Large Transverse Energy Electrons with Associated Missing Energy at  $\sqrt{s} = 540$  GeV,” *Phys.Lett.*, vol. B122, pp. 103–116, 1983.
- [18] M. Banner *et al.*, “Observation of Single Isolated Electrons of High Transverse Momentum in Events with Missing Transverse Energy at the CERN  $\bar{p} p$  Collider,” *Phys.Lett.*, vol. B122, pp. 476–485, 1983.
- [19] S. Chatrchyan *et al.*, “Observation of a new boson at a mass of 125 GeV with the CMS experiment at the LHC,” *Phys.Lett.*, vol. B716, pp. 30–61, 2012.
- [20] G. Aad *et al.*, “Observation of a new particle in the search for the Standard Model Higgs boson with the ATLAS detector at the LHC,” *Phys.Lett.*, vol. B716, pp. 1–29, 2012.
- [21] J. Erler and M. J. Ramsey-Musolf, “Low Energy Tests of the Weak Interaction,” *Prog.Part.Nucl.Phys.*, vol. 54, pp. 351–442, 2005.
- [22] J. M. Maldacena, “Gravity, Particle Physics and Their Unification,” *Int.J.Mod.Phys.*, vol. A15S1, pp. 840–852, 2000.
- [23] G. Bertone, D. Hooper, and J. Silk, “Particle Dark Matter: Evidence Candidates and Constraints,” *Phys.Rept.*, vol. 405, pp. 279–390, 2005.

- [24] V. M. Abazov *et al.*, “Evidence for an Anomalous Like-Sign Dimuon Charge Asymmetry,” *Phys.Rev.*, vol. D82, p. 032001, 2010.
- [25] C. E. Pagliarone, “Searching for physics beyond the standard model with high energy colliders,” *Journal of Physics: Conference Series*, vol. 287, no. 1, p. 012011, 2011.
- [26] M. Ramsey-Musolf, “Low-energy Parity Violation and New Physics,” *Phys.Rev.*, vol. C60, p. 015501, 1999.
- [27] M. Musolf and T. Donnelly, “The Interpretation of Parity Violating Electron Scattering Experiments,” *Nucl.Phys.*, vol. A546, pp. 509–587, 1992.
- [28] M. Musolf *et al.*, “Intermediate-energy Semileptonic Probes of the Hadronic Neutral Current,” *Phys.Rept.*, vol. 239, pp. 1–178, 1994.
- [29] S. Sakakibara, “The Use of the Minimal Subtraction Scheme in Electroweak Theories,” *Z.Phys.*, vol. C11, p. 43, 1981.
- [30] P. Bamert, C. Burgess, and I. Maksymyk, “New Physics and Recent High Precision Electroweak Measurements,” *Phys.Lett.*, vol. B356, pp. 282–290, 1995.
- [31] D. Y. Bardin, P. Christova, L. Kalinovskaya, and G. Passarino, “Atomic Parity Violation and Precision Physics,” *Eur.Phys.J.*, vol. C22, pp. 99–104, 2001.
- [32] S. Davidson, “Interpretations of the NuTeV  $\sin^2\theta_W$ ,” *J.Phys.*, vol. G29, pp. 2001–2004, 2003.
- [33] W. Bentz, I. Cloet, J. Londergan, and A. Thomas, “Reassessment of the NuTeV Determination of the Weak Mixing Angle,” *Phys.Lett.*, vol. B693, pp. 462–466, 2010.
- [34] P. Anthony *et al.*, “Precision Measurement of the Weak Mixing Angle in Moller Scattering,” *Phys.Rev.Lett.*, vol. 95, p. 081601, 2005.
- [35] V. Abazov *et al.*, “Measurement of the Forward-Backward Charge Asymmetry and Extraction of  $\sin^2\theta_W^{eff}$  in  $p\bar{p} \rightarrow Z/\gamma^* + X \rightarrow e^+e^- + X$  Events Produced at  $\sqrt{s} = 1.96$  TeV,” *Phys.Rev.Lett.*, vol. 101, p. 191801, 2008.

- [36] D. Acosta *et al.*, “Measurement of the Forward-Backward Charge Asymmetry of Electron Positron Pairs in  $p\bar{p}$  Collisions at  $\sqrt{s} = 1.96$  TeV,” *Phys.Rev.*, vol. D71, p. 052002, 2005.
- [37] H. Arason *et al.*, “Renormalization Group Study of the Standard Model and its Extensions,” *Phys.Rev.*, vol. D46, pp. 3945–3965, 1992.
- [38] J. Beringer *et al.*, “Review of Particle Physics (RPP),” *Phys.Rev.*, vol. D86, p. 010001, 2012.
- [39] J. Erler and M. J. Ramsey-Musolf, “The Weak Mixing Angle at Low Energies,” *Phys.Rev.*, vol. D72, p. 073003, 2005.
- [40] J. Erler, A. Kurylov, and M. J. Ramsey-Musolf, “The Weak Charge of the Proton and New Physics,” *Phys.Rev.*, vol. D68, p. 016006, 2003.
- [41] R. S. Beminiwattha, *A Measurement of the Weak Charge of the Proton Through Parity Violating Electron Scattering using the Qweak Apparatus A 21% Result*. PhD thesis, Ohio University, 2013.
- [42] A. Leike, “The Phenomenology of Extra Neutral Gauge Bosons,” *Phys.Rept.*, vol. 317, pp. 143–250, 1999.
- [43] A. Kurylov, M. Ramsey-Musolf, and S. Su, “Probing Supersymmetry with Parity Violating Electron Scattering,” *Phys.Rev.*, vol. D68, p. 035008, 2003.
- [44] J. C. Pati and A. Salam, “Lepton Number as the Fourth Color,” *Phys.Rev.*, vol. D10, pp. 275–289, 1974.
- [45] P. Anthony *et al.*, “Observation of Parity Nonconservation in Moller Scattering,” *Phys.Rev.Lett.*, vol. 92, p. 181602, 2004.
- [46] J. Mammei, “The MOLLER Experiment,” *Nuovo Cim.*, vol. C035N04, pp. 203–208, 2012.
- [47] R. D. Young, R. D. Carlini, A. W. Thomas, and J. Roche, “Testing the Standard Model by Precision Measurement of the Weak Charges of Quarks,” *Phys.Rev.Lett.*, vol. 99, p. 122003, 2007.
- [48] N. Mott, “High Energy Elastic Scattering of Electrons on Protons,” *Proc.R.Soc.Lond.A.*, vol. 135, pp. 429–458, 1932.

- [49] L. Maximon and J. Tjon, “Radiative Corrections to Electron Proton Scattering,” *Phys.Rev.*, vol. C62, p. 054320, 2000.
- [50] M. Gorchtein, P. A. Guichon, and M. Vanderhaeghen, “Beam Normal Spin Asymmetry in Elastic Lepton-Nucleon Scattering,” *Nucl.Phys.*, vol. A741, pp. 234–248, 2004.
- [51] P. Blunden, W. Melnitchouk, and J. Tjon, “Two Photon Exchange and Elastic Electron Proton Scattering,” *Phys.Rev.Lett.*, vol. 91, p. 142304, 2003.
- [52] J. Arrington, P. Blunden, and W. Melnitchouk, “Review of Two-Photon Exchange in Electron Scattering,” *Prog.Part.Nucl.Phys.*, vol. 66, pp. 782–833, 2011.
- [53] R. Arnold, C. E. Carlson, and F. Gross, “Polarization Transfer in Elastic electron Scattering from Nucleons and Deuterons,” *Phys.Rev.*, vol. C23, p. 363, 1981.
- [54] M. Rosenbluth, “High Energy Elastic Scattering of Electrons on Protons,” *Phys.Rev.*, vol. 79, pp. 615–619, 1950.
- [55] J. Arrington, W. Melnitchouk, and J. Tjon, “Global Analysis of Proton Elastic Form Factor Data With Two-Photon Exchange Corrections,” *Phys.Rev.*, vol. C76, p. 035205, 2007.
- [56] M. Meziane *et al.*, “Search For Effects Beyond The Born Approximation In Polarization Transfer Observables In  $\vec{e}p$  Elastic Scattering,” *Phys.Rev.Lett.*, vol. 106, p. 132501, 2011.
- [57] R. Madey *et al.*, “Measurements of  $G(E)n / G(M)n$  from the  $H-2(\vec{e}, e' \vec{n})$  reaction to  $Q^2 = 1.45 (GeV/c)^2$ ,” *Phys.Rev.Lett.*, vol. 91, p. 122002, 2003.
- [58] J. Tjon, P. Blunden, and W. Melnitchouk, “Detailed Analysis of Two-Boson Exchange in Parity Violating e-p Scattering,” *Phys.Rev.*, vol. C79, p. 055201, 2009.
- [59] A. Browman, F. Liu, and C. Schaerf, “Positron-Proton Scattering,” *Phys.Rev.*, vol. 139, pp. B1079–B1085, 1965.
- [60] R. Anderson *et al.*, “Scattering of Positrons and Electrons from Protons,” *Phys.Rev.Lett.*, vol. 17, pp. 407–409, 1966.

- [61] J. Mar *et al.*, “A Comparison of Electron-Proton And Positron-Proton Elastic Scattering At Four Momentum Transfer Up To  $5.0 \text{ (GeV/c)}^2$ ,” *Phys.Rev.Lett.*, vol. 21, pp. 482–484, 1968.
- [62] R. Anderson *et al.*, “Positron-Proton Elastic Scattering at 800 and 1200 MeV,” *Phys.Rev.*, vol. 166, pp. 1336–1342, 1968.
- [63] J. Arrington, “Evidence for Two Photon Exchange Contributions in Electron Proton and Positron Proton Elastic Scattering,” *Phys.Rev.*, vol. C69, p. 032201, 2004.
- [64] R. G. Milner, “The OLYMPUS Experiment,” *AIP Conf.Proc.*, vol. 1441, pp. 159–161, 2012.
- [65] J. Arrington *et al.*, “Beyond the Born Approximation: A Precise Comparison of  $e^+p$  and  $e^-p$  Elastic Scattering in CLAS.” [http://www.jlab.org/exp\\_prog/proposals/07/PR-07-005.pdf](http://www.jlab.org/exp_prog/proposals/07/PR-07-005.pdf). A Proposal Prepared for Jefferson Lab PAC31.
- [66] S. Stepanyan, “Beyond the Born approximation: Resolving the Proton Form Factor Puzzle With Positrons at CLAS.” Presented at the Baryons2013- International Conference on the Structure of Baryons, June 2013. <http://nuclear.gla.ac.uk/~baryons2013/Talks/>.
- [67] A. De Rujula, J. Kaplan, and E. De Rafael, “Elastic Scattering of Electrons from Polarized Protons and Inelastic Electron Scattering Experiments,” *Nucl.Phys.*, vol. B35, pp. 365–389, 1971.
- [68] Y. Chen, A. Afanasev, S. Brodsky, C. Carlson, and M. Vanderhaeghen, “Partonic Calculation of the Two Photon Exchange Contribution to Elastic Electron Proton Scattering at Large Momentum Transfer,” *Phys.Rev.Lett.*, vol. 93, p. 122301, 2004.
- [69] M. Gorchtein, “Beam Normal Spin Asymmetry in the Equivalent Photon Approximation,” 2005. hep-ph/0505022.
- [70] R. Tarrach, “Invariant Amplitudes for Virtual Compton Scattering Off Polarized Nucleons Free from Kinematical Singularities, Zeros and Constraints,” *Nuovo Cim.*, vol. A28, p. 409, 1975.

- [71] L. Diaconescu and M. Ramsey-Musolf, “The Vector Analyzing Power in Elastic Electron-Proton Scattering,” *Phys.Rev.*, vol. C70, p. 054003, 2004.
- [72] B. Pasquini and M. Vanderhaeghen, “Resonance Estimates for Single Spin Asymmetries in Elastic Electron-Nucleon Scattering,” *Phys.Rev.*, vol. C70, p. 045206, 2004.
- [73] A. V. Afanasev and N. Merenkov, “Collinear Photon Exchange in the Beam Normal Polarization Asymmetry of Elastic Electron-Proton Scattering,” *Phys.Lett.*, vol. B599, p. 48, 2004.
- [74] D. Borisjuk and A. Kobushkin, “Two-Photon Exchange at Low  $Q^2$ ,” *Phys. Rev.*, vol. C75, p. 038202, 2007.
- [75] M. Gorchtein, “Beam Normal Spin Asymmetry in the Quasi-RCS Approximation,” *Phys.Rev.*, vol. C73, p. 055201, 2006.
- [76] A. Airapetian *et al.*, “Search for a Two-Photon Exchange Contribution to Inclusive Deep-Inelastic Scattering,” *Phys.Lett.*, vol. B682, pp. 351–354, 2010.
- [77] J. M. Katich, *Measurement of the Target-Normal Single-Spin Asymmetry  $A(n,y)$  in the Deep Inelastic Region from the Reaction Helium-3 ( $e,e'$ )*. PhD thesis, The College of William and Mary, 2011.
- [78] A. Afanasev, I. Akushevich, and N. Merenkov, “Nucleon Compton Scattering with Two Space - Like Photons,” pp. 142–150, 2002. hep-ph/0208260.
- [79] S. Wells *et al.*, “Measurement of the Vector Analyzing Power in Elastic Electron Proton Scattering as a Probe of Double Photon Exchange Amplitudes,” *Phys.Rev.*, vol. C63, p. 064001, 2001.
- [80] D. Drechsel, O. Hanstein, S. Kamalov, and L. Tiator, “A Unitary Isobar Model for Pion Photoproduction and Electroproduction on the Proton up to 1-GeV,” *Nucl.Phys.*, vol. A645, pp. 145–174, 1999.
- [81] D. Androic *et al.*, “Transverse Beam Spin Asymmetries at Backward Angles in Elastic Electron-Proton and Quasi-elastic Electron-Deuteron Scattering,” *Phys.Rev.Lett.*, vol. 107, p. 022501, 2011.

- [82] F. Maas *et al.*, “Measurement of the Transverse Beam Spin Asymmetry in Elastic Electron Proton Scattering and the Inelastic Contribution to the Imaginary part of the Two-Photon Exchange Amplitude,” *Phys.Rev.Lett.*, vol. 94, p. 082001, 2005.
- [83] D. Armstrong *et al.*, “Strange Quark Contributions to Parity Violating Asymmetries in the Forward G0 Electron-Proton Scattering Experiment,” *Phys.Rev.Lett.*, vol. 95, p. 092001, 2005.
- [84] Q<sub>weak</sub> Collaboration, “The Q<sub>weak</sub> Experiment: A Search for New Physics at the TeV Scale via a Measurement of the Proton’s Weak Charge,” Qweak-doc-703-V5, 2007. <http://qweak.jlab.org/doc-public/DocumentDatabase>.
- [85] K. Aniol *et al.*, “Parity Violating Electron Scattering from He-4 and the Strange Electric Form-Factor of the Nucleon,” *Phys.Rev.Lett.*, vol. 96, p. 022003, 2006.
- [86] K. Myers, *The First Determination of the Proton’s Weak Charge Through Parity Violating Asymmetry Measurements in Elastic e + p and e + Al Scattering*. PhD thesis, The George Washington University, 2012.
- [87] C. W. Leemann, D. R. Douglas, and G. A. Krafft, “The Continuous Electron Beam Accelerator Facility: CEBAF at the Jefferson Laboratory,” *Annual Review of Nuclear and Particle Science*, vol. 51, no. 1, pp. 413–450, 2001.
- [88] J. M. Grames, *Measurement of a Weak Polarization Sensitivity to the Beam Orbit of the CEBAF Accelerator*. PhD thesis, University of Illinois at Urbana-Champaign, 2000.
- [89] P. A. Adderley, J. Clark, J. Grames, J. Hansknecht, K. Surles-Law, D. Machie, M. Poelker, M. L. Stutzman, and R. Suleiman, “Load-Locked DC High Voltage GaAs Photogun with an Inverted-Geometry Ceramic Insulator,” *Phys. Rev. ST Accel. Beams*, vol. 13, p. 010101, Jan 2010.
- [90] J. Grames, P. Adderley, J. Clark, J. Hansknecht, M. Poelker, M. Stutzman, R. Suleiman, K. Surles-Law, M. BastaniNejad, and J. McCarter, “CEBAF 200 kV Inverted Electron Gun,” *JLAB-ACC-11-1381; DOE/OR/23177-1609*, 2011 Mar 01.



- [91] J. Hansknecht and M. Poelker, “Synchronous Photoinjection Using a Frequency-Doubled Gain-Switched Fiber-Coupled Seed Laser and ErYb-doped Fiber Amplifier,” *Phys. Rev. ST Accel. Beams*, vol. 9, p. 063501, Jun 2006.
- [92] M. Poelker, “Qweak e-Source Issues.” Qweak-doc-1436-v1, 2011. <https://qweak.jlab.org/doc-private/DocumentDatabase>.
- [93] C. Hovater and M. Poelker, “Injection Modelocked Ti-Sapphire Laser with Discretely Variable Pulse Repetition Rates to 1.56 GHz,” *Nuclear Instruments and Methods in Physics Research Section A: Accelerators, Spectrometers, Detectors and Associated Equipment*, vol. 418, no. 2-3, pp. 280 – 284, 1998.
- [94] R. Flood, S. Higgins, and R. Suleiman, *Helicity Control Board Users Guide: Programming and Hardware*. Jefferson Science Associates, LLC, 2 ed., February 2010.
- [95] D. Ramsey, “False Asymmetry from Fixed-Frequency Noise in the Qweak DAQ,” Qweak-doc-906-v1, 2009. <https://qweak.jlab.org/doc-private/DocumentDatabase>.
- [96] M. Salomaa and H. Enge, “Velocity Selector for Heavy-Ion Separation,” *Nuclear Instruments and Methods*, vol. 145, no. 2, pp. 279 – 282, 1977.
- [97] J. Grames *et al.*, “Two Wien spin Flipper,” Proceedings of 2011 Particle Accelerator Conference, New York, NY, USA, 2011.
- [98] R. Suleiman, M. Poelker, and J. Grames, “Mott Measurements For Hall C.” Jefferson Lab Electronic Logbook entry 1567146, February 2011. <https://logbooks.jlab.org>.
- [99] T. J. Gay and F. B. Dunning, “Mott Electron Polarimetry,” *Review of Scientific Instruments*, vol. 63, no. 2, pp. 1635–1651, 1992.
- [100] M. Hauger *et al.*, “A High-Precision Polarimeter,” *Nucl. Instrum. Meth.*, vol. A462, pp. 382–392, 2001.
- [101] A. Narayan, “Precision Compton Polarimetry During the Qweak Experiment.” Qweak-doc-1732-v3, 2012. <https://qweak.jlab.org/doc-private/DocumentDatabase>.

- [102] T. Powers, “Improvement of the Noise Figure of the CEBAF Switched Electrode Electronics BPM System,” Prepared for 8th Beam Instrumentation Workshop (BIW 98), Stanford, CA, 4-7 May 1998.
- [103] T. Powers, L. Doolittle, R. Ursic, and J. Wagner, “Design, Commissioning and Operational Results of Wide Dynamic Range BPM Switched Electrode Electronics,” *AIP Conf. Proc.*, vol. 390, pp. 257–265, 1997.
- [104] R. Dickson and V. A. Lebedev, “Fast Digital Feedback System for Energy and Beam Position Stabilization,” pp. 646–648, 1999. Inspire-516625.
- [105] T. Powers, “Effects of Intensity and Position Modulation on Switched Electrode Electronics beam Position Monitor Systems at Jefferson Lab,” Prepared for 9th Beam Instrumentation Workshop (BIW 2000), Cambridge, Massachusetts, 8-11 May 2000.
- [106] A. S. Hofer *et al.*, “Performance of the CEBAF Arc Beam Position Monitors,” Prepared for 1993 IEEE Particle Accelerator Conference (PAC 93), Washington, DC, 17-20 May 1993.
- [107] T. Powers and B. Bevins. Accelerator Operations Division, Jefferson Lab, 2013. Private Communication.
- [108] Q<sub>weak</sub> Collaboration, “Q<sub>weak</sub> Experiment NIM Paper,” *To be published in Nuclear Instruments and Methods in Physics Research*.
- [109] K. Unser, “Beam Current Transformer with D.C. to 200 MHz Range,” *IEEE Trans. Nucl. Sci.*, vol. 16, pp. 934–938, 1969.
- [110] C. Yan, R. Carlini, and D. Neuffer, “Beam Energy Measurement Using the Hall C Beamline,” *Conf.Proc.*, vol. C930517, pp. 2136–2138, 1993.
- [111] C. Yan and R. Carlini, “Hall C Beam Line Instrumentation,” *AIP Conference Proceedings*, vol. 269, no. 1, pp. 571–582, 1992.
- [112] C. Yan *et al.*, “Superharp: A Wire Scanner With Absolute Position Readout for Beam Energy Measurement at CEBAF,” *Nucl.Instrum.Meth.*, vol. A365, pp. 261–267, 1995.
- [113] Nuruzzaman, “How Beam Energy Changes Will Be Identified in Qweak,” tech. rep., 2010. <https://qweak.jlab.org/doc-private/DocumentDatabase>.

- [114] C. Yan, N. Sinkine, and R. Wojcik, “Linear Beam Raster for Cryogenic Targets,” *Nucl.Instrum.Meth.*, vol. A539, pp. 1–15, 2005.
- [115] R. Carlini, “ $Q^2$  Defining Collimator System, Infrastructure and Misc..” Qweak Collaboration Meeting held on 18 Jul 2009, 2009. <https://qweak.jlab.org/doc-private/DocumentDatabase>.
- [116] P. Wang, *A Measurement Of The Protons Weak Charge Using An Integration ČerenkovDetector System*. PhD thesis, University of Manitoba, 2011.
- [117] P. Wang, “Simulated Elastic Flux Images On Main Bars.” Qweak Electronic Logbook entry 588, May 2012. <https://qweak.jlab.org/eelog/>.
- [118] J. Pan, *Towards a Precision Measurement of Parity Violating e-p Elastic Scattering at Low Momentum Transfer*. PhD thesis, The University of Manitoba, 2012.
- [119] D. Abbot *et al.*, “The CODA System and Its Performance in the First Online Experiments at CEBAF.” [ftp://ftp.jlab.org/pub/coda/docs/pdf/papers/RT95\\_CODA.pdf](ftp://ftp.jlab.org/pub/coda/docs/pdf/papers/RT95_CODA.pdf), 2004.
- [120] Wind River, “Wind River VxWorks.” <http://www.windriver.com/products/vxworks.html>.
- [121] Argonne National Laboratory, “Experimental Physics and Industrial Control System.” <http://www.aps.anl.gov/epics/index.php>.
- [122] W. Watson, D. Barker, M. Bickley, P. Gupta, and R. Johnson, “The CEBAF Accelerator Control System: Migrating from a TACL to an EPICS Based System,” *Nucl.Instrum.Meth.*, vol. A352, pp. 118–121, 1994.
- [123] IEEE, *IEEE Standard for a Versatile Backplane Bus: Vmebus (Ansi)*. IEEE.
- [124] E. Jastrzembki, D. Abbott, W. Heyes, R. MacLeod, C. Timmer, and E. Wolin, “The Jefferson Lab Trigger Supervisor System,” in *Real Time Conference, 1999. Santa Fe 1999. 11th IEEE NPSS*, pp. 538–542, 1999.
- [125] TRIUMF, “TRIUMF-Canada’s National Laboratory for Particle and Nuclear Physics.” <http://www.triumf.ca/>.

- [126] B. Roberts and H. Hui, *VME QWEAK 8 Channel 18-bit ADC*, 2006. <https://qweak.jlab.org/doc-private/DocumentDatabase>.
- [127] Struck Innovative Systeme, “SIS3801 32 Channel 32-bit 200 MHz Multi Channel Scaler/Counter.” <http://www.struck.de/sis3801.htm>.
- [128] Struck Innovative Systeme, “STR7200 32 Channel VME Scaler.” <http://www.usatlas.bnl.gov/~poblague/doc/hw/STR7200.pdf>.
- [129] ROOT Team, “ROOT-A Data Analysis Framework.” <http://root.cern.ch/drupal//>.
- [130] MySQL Team, “MySQL-The World’s Most Popular Open Source Database.” <http://www.mysql.com/>.
- [131] Qweak Analysis Group, “QwAnalysis: the Qweak Analysis Framework.” [http://qweak.jlab.org/QwAnalysis\\_Docs/html/](http://qweak.jlab.org/QwAnalysis_Docs/html/). HTML documentation directory for QwAnalysis.
- [132] R. Beminiwattha, “Qweak Event Cut Framework,” Qweak-doc-1682-v1, 2012. <https://qweak.jlab.org/doc-private/DocumentDatabase>.
- [133] P. Pébay, “Formulas for robust, One-Pass Parallel Computation of Covariances and Arbitrary-Order Statistical Moments,” *Sandia Report SAND2008-6212*, Sandia National Laboratories, 2008.
- [134] K. Paschke, “Controlling helicity-correlated beam asymmetries in a polarized electron source,” *Eur.Phys.J.*, vol. A32, pp. 549–553, 2007.
- [135] G. Cates, V. Hughes, R. Michaels, H. Schaefer, T. Gay, M. Lubell, R. Wilson, G. Dodson, K. Dow, S. Kowalski, K. Isakovich, K. Kumar, M. Schulze, P. Souder, and D. Kim, “The Bates Polarized Electron Source,” *Nuclear Instruments and Methods in Physics Research Section A: Accelerators, Spectrometers, Detectors and Associated Equipment*, vol. 278, no. 2, pp. 293 – 317, 1989.
- [136] R. Silwal, *Probing the Strangeness Content of the Proton and the Neutron Radius of  $^{208}\text{Pb}$  using Parity Violating Electron Scattering*. PhD thesis, University of Virginia, May 2012.
- [137] M. Dalton, “PC Ringing Increase.” Jefferson Lab Electronic Logbook entry 1560680. <https://logbooks.jlab.org>.

- [138] H. Wiedemann, *PARTICLE ACCELERATOR PHYSICS I: Basic principles and Linear Beam Dynamics*. Springer-Verlag, second ed., a938.
- [139] M. Kargiantoulakis, “Helicity Magnets Correction.” Qweak Electronic Logbook entry 215, December 2011. <https://qweak.jlab.org/eelog/>.
- [140] M. Kargiantoulakis, “Successful operation of the helicity magnets over a longer period.” Qweak Electronic Logbook entry 240, December 2011. <https://qweak.jlab.org/eelog/>.
- [141] Wiener, “Introduction to VME/VXI/VXS Standards.” [http://wiener-d.com/documents/uploads/WIENER\\_VME\\_Intro.pdf](http://wiener-d.com/documents/uploads/WIENER_VME_Intro.pdf).
- [142] J. Leacock, “Battery pattern dependence during inelastic running - possibly resolved..” Qweak Electronic Logbook entry 397, August 2011. <https://qweak.jlab.org/eelog/>.
- [143] D. Mack. Hall C Physics Division, Jefferson Lab, 2010. Private Communication.
- [144] O. Hashimoto *et al.*, “Hypernuclear spectroscopy at JLab Hall C,” *Nucl.Phys.*, vol. A835, pp. 121–128, 2010.
- [145] D. Ramsey and B. Roberts, “TRIUMF Qweak VME integrator Test Records,” Qweak-doc-849-v2, 2008. <https://qweak.jlab.org/doc-private/DocumentDatabase>.
- [146] J. Birchall, “Effect Of Averaging Over Azimuthal Angle.” Qweak Electronic Logbook entry 373, June 2011. <https://qweak.jlab.org/eelog/>.
- [147] D. J. Mack, “BCM Normalization Issues Part II: Calibrations and Linearity,” Qweak-doc-1369-v1, March 2011. <https://qweak.jlab.org/doc-private/DocumentDatabase>.
- [148] R. Beminiwattha, D. Gaskell, J. Magee, and P. Solvignon, “Møller Measurements and Beam Polarization for  $Q_{Weak}^p$  Wien-0,” tech. rep., 2012. <https://qweak.jlab.org/eelog/Moller/109>.
- [149] J. Magee. Collage of William & Mary, 2012. Private Communication.
- [150] D. Gaskell. Hall C Physics Division, Jefferson Lab, 2012. Private Communication.

- [151] E. Cooper and C. Horowitz, “The Vector Analyzing Power in Elastic Electron-Nucleus Scattering,” *Phys.Rev.*, vol. C72, p. 034602, 2005.
- [152] M. Gorchtein and C. J. Horowitz, “Analyzing power in elastic scattering of the electrons off a spin-0 target,” *Phys.Rev.*, vol. C77, p. 044606, 2008.
- [153] J. Magee, “The Preliminary Aluminum Window Dilution for Run 1,” Qweak-doc-1781-v2, February 2013. <https://qweak.jlab.org/doc-private/DocumentDatabase>.
- [154] H. Olsen and L. Maximon, “Photon and Electron Polarization in High-Energy Bremsstrahlung and Pair Production with Screening,” *Phys.Rev.*, vol. 114, pp. 887–904, 1959.
- [155] M. Pitt, “Radiative Corrections Focus Session Talk.” Qweak-doc-1795-v1, 2013. <https://qweak.jlab.org/doc-private/DocumentDatabase>.
- [156] A. Subedi, “Electromagnetic Radiative Corrections for Wein 0.” Qweak-doc-1799-v1, 2013. <https://qweak.jlab.org/doc-private/DocumentDatabase>.
- [157] M. Dalton, “Depolarization is Negligible (<0.11%) for Elastic Scattering.” Qweak Electronic Logbook entry 716. <https://qweak.jlab.org/elog/>.
- [158] V. Gray, “Beam Position And Angle Scans in GEANT4.” Qweak Electronic Logbook entry 873. <https://qweak.jlab.org/elog/>.
- [159] D. Armstrong, “ $Q^2$  Dependence On Beam Angle For Reconstructed Tracks.” Qweak Electronic Logbook entry 166. <https://qweak.jlab.org/elog/>.
- [160] P. Wang, “Simulated Octant-by-octant Event Rate, Scattering Angle and Momentum Transfer.” Qweak Electronic Logbook entry 589, May 2012. <https://qweak.jlab.org/elog/>.
- [161] C. K. Sinclair, “Beam Energy Combinations Which Provide Simultaneous Longitudinal Electron Polarization in Two Experimental Halls,” tech. rep. TJNAF-TN-97-021.
- [162] D. Gaskell, J. Magee, P. Solvignon, and R. Beminiwattha, “Moller: Super Spin Dance Summary.” Hall C Electronic Logbook entry 243012, December 2012. <https://hallcweb.jlab.org/hclog/>.

- [163] K. Paschke, “Beam Corrections-Qweak Collaboration Meeting,” 04-18-2013. <https://qweak.jlab.org/doc-private/DocumentDatabase>.
- [164] D. Gaskell, “Summary of Spin Dances in 2012.” Qweak Electronic Logbook entry 92, under Moller, March 2012. <https://qweak.jlab.org/elog/>.
- [165] D. Gaskell, “Fitting a Correction to the Wien Calibration.” Qweak Electronic Logbook entry 93, under Moller, March 2012. <https://qweak.jlab.org/elog/>.
- [166] B. P. Waidyawansa, “Preliminary Beam Normal Single Spin Asymmetry Result for Hydrogen Elastic Scattering.,” June 2012. <https://qweak.jlab.org/doc-private/DocumentDatabase>.
- [167] D. Androic *et al.*, “First Determination of the Weak Charge of the Proton,” 2013. arXiv:1307.5275.
- [168] C. Wood *et al.*, “Measurement of Parity Nonconservation and an Anapole moment in Cesium,” *Science*, vol. 275, pp. 1759–1763, 1997.
- [169] V. Dzuba, J. Berengut, V. Flambaum, and B. Roberts, “Revisiting parity non-conservation in cesium,” *Phys.Rev.Lett.*, vol. 109, p. 203003, 2012.
- [170] L. Capozza, “Transverse Single Spin Asymmetry at the A4 Experiment: Preliminary Backward-Scattering Results,” *Eur.Phys.J.*, vol. A32, pp. 497–499, 2007.
- [171] D. S. Armstrong *et al.*, “Transverse Beam Spin Asymmetries in Forward-Angle Elastic Electron-Proton Scattering,” *Phys.Rev.Lett.*, vol. 99, p. 092301, 2007.
- [172] S. Abrahamyan *et al.*, “New Measurements of the Transverse Beam Asymmetry for Elastic Electron Scattering from Selected Nuclei,” *Phys.Rev.Lett.*, vol. 109, p. 192501, 2012.
- [173] P. LaViolette, Y. Kolomensky, K. Kumar, and Z. Marshall, “E158 Transverse Asymmetries,” tech. rep. [http://hallaweb.jlab.org/12GeV/Moller/review/downloads/technote\\_jun09.pdf](http://hallaweb.jlab.org/12GeV/Moller/review/downloads/technote_jun09.pdf).
- [174] B. Pasquini. Dipartimento di Fisica Nucleare e Teorica, Universita di Pavia, Italy, 2012. Private Communication.

- [175] A. Afanasev. George Washington University, 2012. Private Communication.
- [176] W.R.Leo, *Techniques for Nuclear and Particle Physics Experiments: a How-To Approach*. Springer-Verlag, second ed., 1987,1994.
- [177] E. Stangland, R. Flood, and H. Dong, “G0 Helicity Digital Controls,” tech. rep. <http://g0web.jlab.org/doc-public/ShowDocument?docid=236>.
- [178] R. Suleiman and R. Flood, “Measured the Rise Time of the Helicity Magnets.” Jefferson Lab Electronic Logbook entry 1636588. <https://logbooks.jlab.org>.



## A Beam Position Monitoring Misc

### A.1 List of BPMs Used by $Q_{\text{weak}}$ and Their Configurations

Tables A.1 and A.2 shows the BPMs used by  $Q_{\text{weak}}$  and their configuration information used for position construction. See Appendix A.8 for the reference drawings of the beamlines.

- **X/Y offset**

The difference in the ideal position and the surveyed position of a BPM in X/Y axis while Z offset the location of the BPM in the beamline (along Z axis) from the beginning of the beamline to the center of the device or the origin of the device coordinate system.

- **SENSitivity (BSEN)**

The factor to convert from ADC counts to position in millimetres.

- $\alpha_{X/Y}$

Ratio of the gain of the positive and negative wire pairs, XP, XM and YP, YM.

- **X/Y\_gains**

Non-linearity corrective factors used for beam projection at the target as discussed in Section 3.4.1.6.

Table A.1: List of BPMs in the injector beamline used by  $Q_{\text{weak}}$ .

BPM	X offset (mm)	Y offset (mm)	Z offset (mm)	BSEN/ $\kappa$ (mm <sup>-1</sup> )	$\alpha_x$	$\alpha_y$	X_gain	Y_gain	rotation (degrees)
QWK_1I02	0.0	0.0	0.0	0.7283	1.08093	0.981316	1	1	0
QWK_1I04	0.0	0.0	0.0	0.7283	0.943577	0.997052	1	1	0
QWK_1I06	0.0	0.0	0.0	0.7283	1.03493	1.02038	1	1	0
QWK_0I01	0.0	0.0	0.0	0.7340	1.053700	1.032170	1	1	0
QWK_0I01A	0.0	0.0	0.0	0.7340	1.006630	0.923753	1	1	0
QWK_0I02	0.0	0.0	0.0	0.7283	1.001370	0.888284	1	1	0
QWK_0I02A	0.0	0.0	0.0	0.7283	1.013430	1.053080	1	1	0
QWK_0I05	0.0	0.0	0.0	0.7283	1.33584	0.981869	1	1	0
QWK_0I07	0.0	0.0	0.0	0.7283	0.988324	1.080590	1	1	0
QWK_0I07	0.0	0.0	0.0	0.7283	0.988324	1.080590	1	1	0
QWK_0L01	0.0	0.0	0.0	1.0	0.992225	0.96240	1	1	45
QWK_0L02	0.0	0.0	0.0	1.0	0.995954	1.00242	1	1	45
QWK_0L03	0.0	0.0	0.0	1.0	0.922674	0.938655	1	1	45
QWK_0L04	0.0	0.0	0.0	1.0	1.009710	0.951593	1	1	45
QWK_0L05	0.0	0.0	0.0	1.0	1.08104	1.08872	1	1	45
QWK_0L06	0.0	0.0	0.0	1.0	1.00268	1.08067	1	1	45
QWK_0L07	0.0	0.0	0.0	1.0	1.05915	0.981831	1	1	45
QWK_0L08	0.0	0.0	0.0	1.0	0.947238	1.03771	1	1	45
QWK_0L09	0.0	0.0	0.0	1.0	0.993246	1.00114	1	1	45
QWK_0L10	0.0	0.0	0.0	1.0	0.982111	1.00883	1	1	45
QWK_0R03	0.0	0.0	0.0	1.0	0.961462	0.98283	1	1	45
QWK_0R04	0.0	0.0	0.0	1.0	1.0651	1.07899	1	1	45
QWK_0R05	0.0	0.0	0.0	1.0	0.949823	0.995016	1	1	45
QWK_0R06	0.0	0.0	0.0	1.0	0.988932	1.00676	1	1	45

Table A.2: List of BPMs in the Hall C beamline used by  $Q_{\text{weak}}$ .

BPM	X offset (mm)	Y offset (mm)	Z offset (mm)	BSEN/ $\kappa$ (mm <sup>-1</sup> )	$\alpha_x$	$\alpha_y$	X_gain	Y_gain	rotation (degrees)
QWK_BPM3C07	0.127	-1.160	49025.3	18.81	1.033450	0.901159	1	1	45
QWK_BPM3C07A	-0.030	-0.795	53031.9	18.81	1.032580	0.969186	1	1	45
QWK_BPM3C08	0.166	-0.366	55125.3	18.81	1.127040	1.008810	1	1	45
QWK_BPM3C11	0.387	0.397	70725.3	18.81	0.984608	1.102810	1	1	45
QWK_BPM3C12	0.736	-0.202	75926.1	18.81	0.982274	0.950626	1	1	45
QWK_BPM3C14	0.526	0.099	86325.3	18.81	0.955249	0.972192	1	1	45
QWK_BPM3C16	-0.662	0.020	96726.1	18.81	0.980290	0.988578	1	1	45
QWK_BPM3C17	0.223	-0.356	99815.6	18.81	0.947455	0.877913	1	1	45
QWK_BPM3C18	0.200	0.684	101611.0	18.81	0.741194	1.041640	1	1	45
QWK_BPM3C19	0.003	0.015	102922.0	18.81	1.026000	1.011010	1	1	45
QWK_BPM3P02A	-1.0	-0.7	109212.0	13.70	0.982250	0.986716	1	1	0
QWK_BPM3P02B	0.2	-0.1	110602.0	13.70	1.000000	1.000000	1	1	29
QWK_BPM3P03A	0.6	-0.7	113292.0	25.67	0.909295	1.006700	1	1	45
QWK_BPM3C20	0.2	0.1	116858.0	18.81	0.904796	0.995870	1	1	45
QWK_BPM3C21	0.2	-0.2	118216.0	18.81	1.113200	0.945974	1	1	45
QWK_BPM3H02	0.2	0.7	127153.0	18.81	0.973625	1.052130	1	1	45
QWK_BPM3H04	-0.6	-0.4	129632.0	18.81	1.082250	1.032040	1	1	45
QWK_BPM3H07A	0.6823	0.0892	138406.0	18.81	0.960181	1.071930	0.9844	1.0020	45
QWK_BPM3H07B	0.5896	-0.1550	139363.0	18.81	1.022240	1.015710	0.8410	0.8710	45
QWK_BPM3H07C	0.6	0.0	140319.0	18.81	1.013110	0.985986	1	1	45
QWK_BPM3H08	-0.3718	-1.3940	143576.0	18.81	1.039360	1.055470	0.9844	0.8347	45
QWK_BPM3H09	0.865	-1.0160	144803.0	18.81	1.025930	0.993640	0.9762	0.8710	45
QWK_BPM3H09B	-0.6	0.3	147351.0	18.81	0.948778	1.264910	1	1	45

## A.2 Error on Position Estimates Due to an Error on $\alpha$ Gains of the BPMs

SEE BPMs (see Section 3.4.1.1) use a single RF module to handle positive and negative X and Y wire signals. Ideally, this implies that the  $\alpha$  gains should be unity where

$$\alpha_x = \frac{XP}{XM} \quad \text{and} \quad \alpha_y = \frac{YP}{YM} \quad (\text{pedestal corrected}). \quad (\text{A.1})$$

But due to geometrical imperfections, the alpha gains are not unity. The error on position estimation due to imperfect alpha can be derived as follows. Consider the reconstructed beam position in X

$$X_0 = k \times \frac{XP - \alpha XM}{XP + \alpha XM},$$

with k being the position conversion factor. If we assume  $\alpha \rightarrow \alpha(1+\beta)$  where  $\beta \ll 1$ ,

$$X_M = k \times \left( \frac{XP - \alpha XP - \alpha\beta XM}{XP + \alpha XM + \alpha\beta XM} \right),$$

but  $\beta \ll 1 \rightarrow (XP + \alpha XM + \alpha\beta XM) \rightarrow (XP + \alpha XM)$  therefore,

$$\begin{aligned} X_M &= k \times \left( \frac{XP - \alpha XP - \alpha\beta XM}{XP + \alpha XM} \right) \\ &= k \times \left( \frac{XP - \alpha XM}{XP + \alpha XM} \right) - k \times \alpha\beta \left( \frac{XM}{XP + \alpha XM} \right) \\ &= X_0 - k \times \alpha\beta \left( \frac{XM}{XP + \alpha XM} \right). \end{aligned}$$

Dividing both numerator and denominator by  $\alpha XM$

$$\begin{aligned} X_M &= X_0 - k \times \frac{\beta}{\frac{XP}{\alpha XM} + 1}, \\ \text{using } \frac{XM}{XP} &= \alpha, \\ X_M &= X_0 - k \times \frac{\beta}{2} \end{aligned}$$

As an example, when  $\alpha$  is 1.1  $\rightarrow \beta = 0.1$  and  $k = 18.81$ ,

$$X_M = X_o - 18.81 \times \frac{0.1}{2}$$

$$X_M = X_o - 0.941.$$

### A.3 BPM Resolutions

Table A.3 is relevant to the analysis presented in Subsection 3.4.1.3.

Table A.3: Dependence of the measured X and Y resolution of BPM 3H07B on the beam current. The corresponding resolution curve is shown in Figure 3.15

Run	current $\mu A$	$\sigma_{\delta X}$ ( $\mu m$ )	$\sigma_{\delta Y}$ ( $\mu m$ )	$R_X$ ( $\mu m$ )	$R_Y$ ( $\mu m$ )
11695	27	4.180 $\pm$ 0.010	4.213 $\pm$ 0.010	2.639 $\pm$ 0.006	2.660 $\pm$ 0.006
17755	45	2.624 $\pm$ 0.008	2.686 $\pm$ 0.008	1.657 $\pm$ 0.005	1.696 $\pm$ 0.005
17395	53	2.151 $\pm$ 0.006	2.202 $\pm$ 0.006	1.358 $\pm$ 0.004	1.390 $\pm$ 0.004
15185	60	2.152 $\pm$ 0.006	2.248 $\pm$ 0.006	1.359 $\pm$ 0.004	1.419 $\pm$ 0.004
16150	75	1.851 $\pm$ 0.005	1.946 $\pm$ 0.006	1.169 $\pm$ 0.003	1.229 $\pm$ 0.004
17795	90	1.713 $\pm$ 0.005	1.809 $\pm$ 0.005	1.082 $\pm$ 0.003	1.142 $\pm$ 0.003
17720	100	1.683 $\pm$ 0.005	1.763 $\pm$ 0.005	1.063 $\pm$ 0.003	1.113 $\pm$ 0.003
9645	110	1.654 $\pm$ 0.004	1.774 $\pm$ 0.004	1.044 $\pm$ 0.003	1.120 $\pm$ 0.003
11835	130	1.517 $\pm$ 0.004	1.612 $\pm$ 0.004	0.958 $\pm$ 0.003	1.018 $\pm$ 0.003
10810	150	1.496 $\pm$ 0.004	1.678 $\pm$ 0.004	0.945 $\pm$ 0.003	1.060 $\pm$ 0.003
10225	155	1.486 $\pm$ 0.004	1.671 $\pm$ 0.004	0.938 $\pm$ 0.003	1.055 $\pm$ 0.003
16095	180	1.424 $\pm$ 0.004	1.514 $\pm$ 0.004	0.899 $\pm$ 0.003	0.956 $\pm$ 0.003

### A.4 Stability of the BPM Pedestals

During the two year running period of  $Q_{weak}$ , a total of two BPM calibrations were performed to determine the BPM pedestals (see Table A.4). The stability of the pedestals between the two calibrations is clearly visible in Figure A.1.

Table A.4: BPM calibration runs taken during  $Q_{\text{weak}}$ .

Run	Current range ( $\mu\text{A}$ )
11956 (Run I)	118 - 176
13847 (Run II)	120 - 189

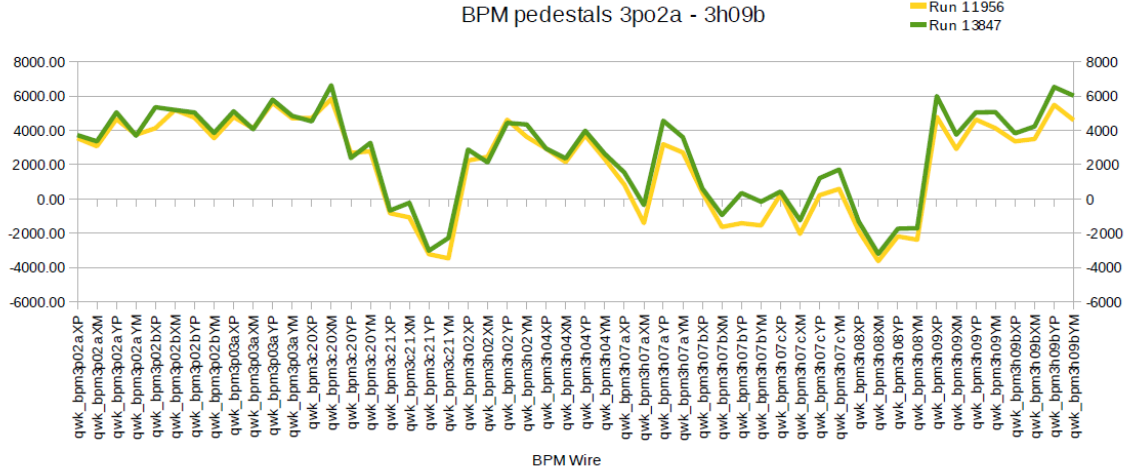


Figure A.1: Comparison of BPM pedestals between Run I and Run II. Run I pedestals are obtained from the calibration run 11596 and Run II are from the calibration run 13847. Horizontal axis shows the names of the BPM wires and the vertical axis gives the pedestal in ADC counts.

### A.5 Linear Least Square Fit Algorithm used to Project Beam Position and Angle at the $Q_{\text{weak}}$ Target

Given a set of BPM readings  $X_i$  and their locations along beamline  $Z_i$ , the linear least squares method [176] calculates the slope  $\mathbf{a}$  and offset  $\mathbf{b}$  of a linear fit of the form  $\mathbf{X} = \mathbf{Z}\mathbf{a} + \mathbf{b}$  as

$$a = \frac{EB - CA}{DB - A^2}, \quad b = \frac{DC - EB}{DB - A^2}, \quad (\text{A.2})$$

with

$$\sigma(a)^2 = \frac{B}{BD - A^2}, \quad \sigma(b)^2 = \frac{D}{BD - A^2}, \quad \text{cov}(a, b) = \frac{-A}{BD - A^2}. \quad (\text{A.3})$$

Here

$$\begin{aligned} A &= \sum \frac{Z_i}{\sigma_i^2} & B &= \sum \frac{1}{\sigma_i^2} & C &= \sum \frac{X_i}{\sigma_i^2} \\ D &= \sum \frac{Z_i^2}{\sigma_i^2} & E &= \sum \frac{Z_i X_i}{\sigma_i^2} & F &= \sum \frac{X_i^2}{\sigma_i^2} \end{aligned}$$

### A.6 Error Associated With Beam Projection on the $Q_{\text{weak}}$ Target

According to W.R. Leo [176], the error on the slope and offset of the linear least-squares fit (parameters  $a$  and  $b$ ) introduced in Section 3.4.1.5 is

$$\sigma_a^2 = \frac{B}{BD - A^2}, \quad \sigma_b^2 = \frac{D}{BD - A^2}, \quad (\text{A.4})$$

and

$$\text{cov}(a, b) = \frac{-A}{BD - A^2}. \quad (\text{A.5})$$

The error on the projection to  $Z=Z_{tgt}$ ,  $X_{tgt} = aZ_{tgt} + b$ , can be written as

$$\sigma_{X_{tgt}}^2 = Z_{tgt}^2 \sigma_a^2 + \sigma_b^2 + 2Z_{tgt} \text{cov}(a, b). \quad (\text{A.6})$$

Using A.4 and A.5,

$$\sigma_{X_{tgt}}^2 = Z_{tgt}^2 \left( \frac{B}{BD - A^2} \right) + \left( \frac{D}{BD - A^2} \right) + 2Z_{tgt} \left( \frac{-A}{BD - A^2} \right). \quad (\text{A.7})$$

With the substitution of the BPM resolution  $R = \sigma_i = 1.0 \mu\text{m}$  (for beam currents greater than  $120 \mu\text{A}$ ),

$$\begin{aligned} A &= \sum \frac{Z_i}{R^2}, & B &= \frac{N}{R}, & C &= \sum \frac{X_i}{R^2}, \\ D &= \sum \frac{Z_i^2}{R^2}, & E &= \sum \frac{Z_i X_i}{R^2}, & F &= \sum \frac{X_i^2}{R^2}, \end{aligned}$$

with  $N$  being the number of BPMs in the fit. Substituting to  $\sigma_{X_{tgt}}$ ,

$$\sigma_{X_{tgt}}^2 = \frac{Z_{tgt}^2 \frac{N}{R^2} + \sum \frac{Z_i^2}{R^2} - 2Z_{tgt} \sum \frac{Z_i}{R^2}}{\frac{N}{R^2} \sum \frac{Z_i^2}{R^2} - \sum \frac{Z_i}{R^2}}, = \left( \frac{Z_{tgt}^2 + \text{avg}(Z_i^2) - 2Z_{tgt} \text{avg}(Z_i)}{[\text{avg}(Z_i^2) - \text{avg}(Z_i)^2]} \right) \frac{R^2}{N}.$$

$$\sigma_{X_{tgt}} = \sqrt{\frac{[Z_{tgt}^2 + \text{avg}(Z_i^2) - 2Z_{tgt}\text{avg}(Z_i)]}{\text{avg}(Z_i^2) - \text{avg}(Z_i)^2}} \left( \frac{R}{\sqrt{N}} \right). \quad (\text{A.8})$$

Using  $R = 1.0 \mu\text{m}$ , the error on projected beam position is

$$\sigma_{X_{tgt}} = \sigma_{X_{tgt}} = \sqrt{\frac{Z_{tgt}^2 + \text{avg}(Z_i^2) - 2Z_{tgt}\text{avg}(Z_i)}{\text{avg}(Z_i^2) - \text{avg}(Z_i)^2}} \frac{1.0\mu\text{m}}{\sqrt{N}}. \quad (\text{A.9})$$

The values of  $Z_i$  and  $Z_{tgt}$  can be found in Appendix A.1. Similarly, for the angle, using  $\sigma_a^2$ ,

$$\sigma_a^2 = \sigma_{X_\theta}^2 = \frac{B}{(BD - A^2)} = \frac{\frac{N}{R^2}}{\frac{N}{R^2} \sum Z_i^2 - \frac{\sum Z_i^2}{R^2}}. \quad (\text{A.10})$$

The error on the angle calculation is

$$\sigma_a = \sqrt{\frac{\frac{N}{R^2}}{N \sum Z_i^2 - (\sum Z_i)^2}}. \quad (\text{A.11})$$

### A.7 Extracting the Differential Non-linearity Factor of the BPMs

The following technique was used to extract the  $X_{non-linear}$  and  $Y_{non-linear}$  multiplicative factors for the BPMs used to project to the target in Subsection 3.4.1.6.

1. Select a run with stable beam. In this case, I used 11705 which was run taken with a beam current of  $163\mu\text{A}$ .
2. Use orbit lock BPMs 3H07C and 3H09B to project to the rest of the BPMs in the combinations given in Table 3.4. For these two BPMs, set  $X_{non-linear}$  and  $Y_{non-linear}$  to 1.0 and the  $X_{offset}$  and  $Y_{offset}$  to 0.
3. Draw correlations between the projected and the measured beam positions in X and Y (see Figure A.2). Fit with a linear fit and extract slopes and offsets. The slopes will be used as  $X_{non-linear}$  and  $Y_{non-linear}$  and the offsets as  $X_{offset}$  and  $Y_{offset}$ .
4. Re-analyze run 11705 with the new factors.
5. Check correlations to make sure they are  $\approx 1$ .



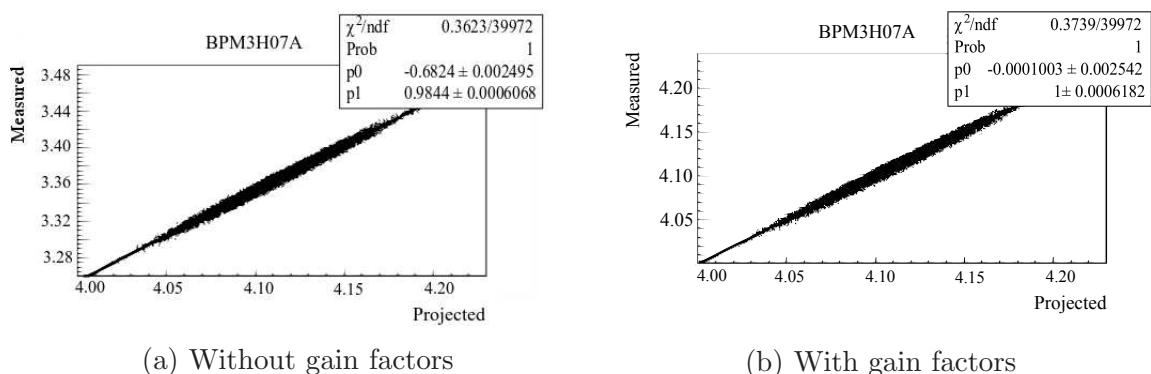


Figure A.2: (a) Correlation between projected and measured X beam position at BPM3H07A in run 11705. In this the correlation is 0.9844 (b) Correlations after applying the slope from figure (a) as a gain factor. The correlation in this case is 1.

Table A.2 lists the values obtained using the above method. Figure A.3 shows the results of random checks done with the new multiplicative factors on runs with different beam currents. The correlations between BPMs have improved to  $\leq 1\%$  from the previous 5-15%.

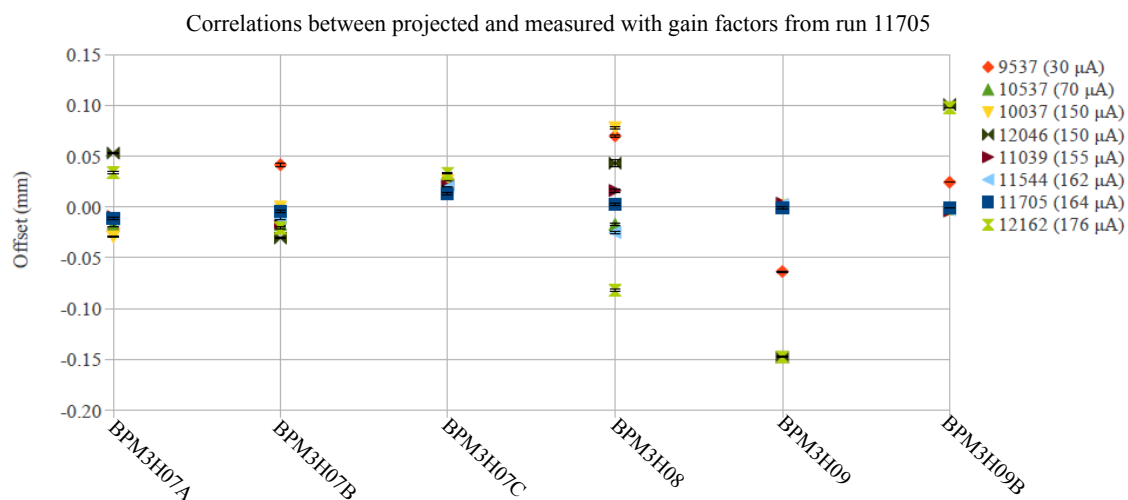
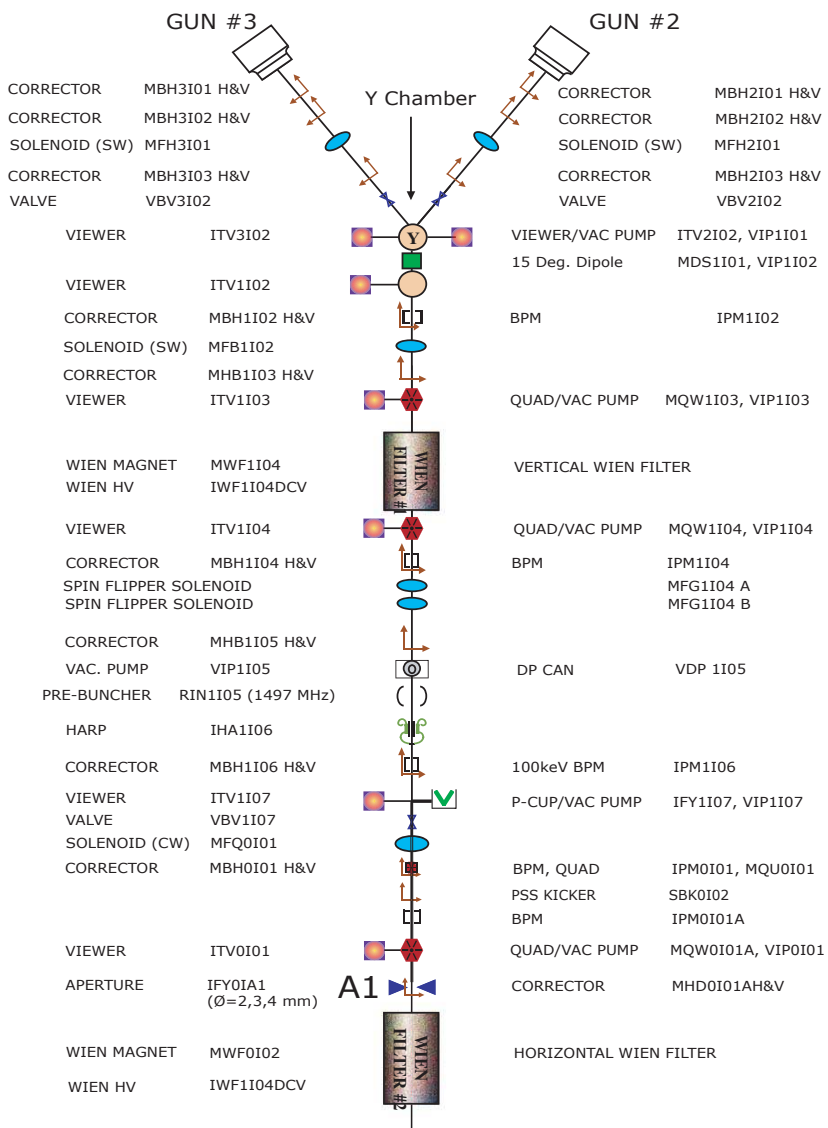
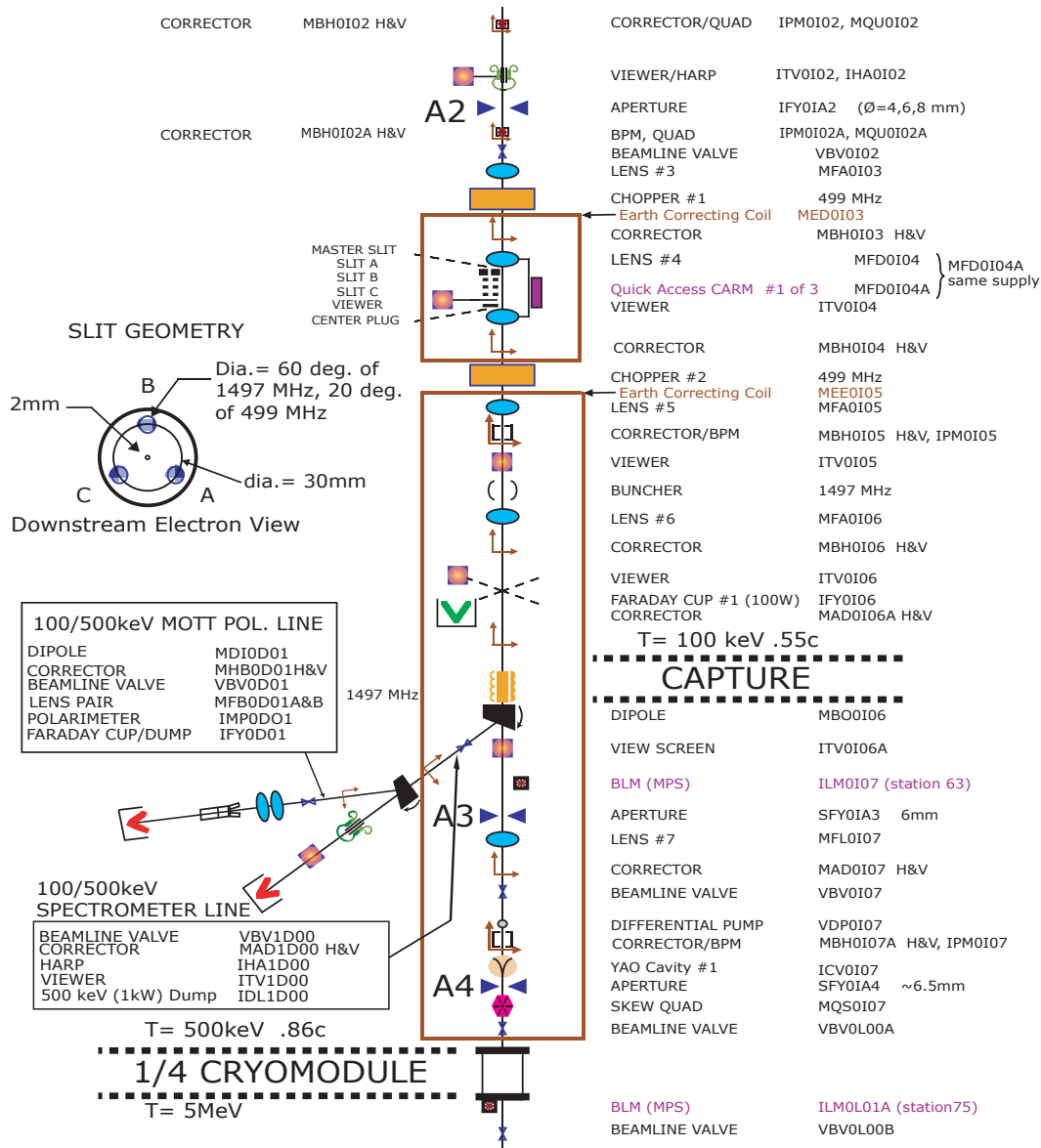


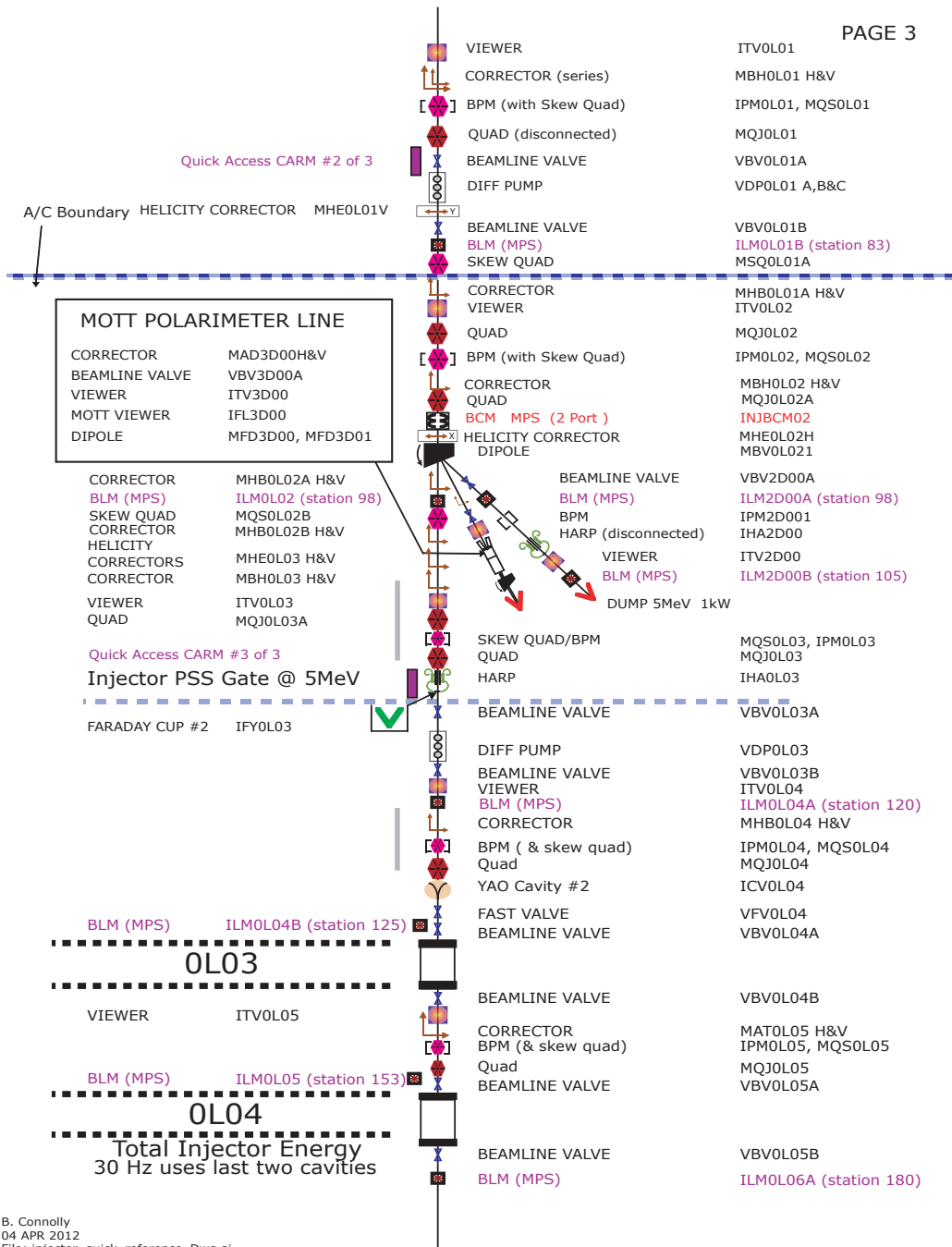
Figure A.3: Improvements in the differential non-linearity of the BPMs over a range of beam currents.

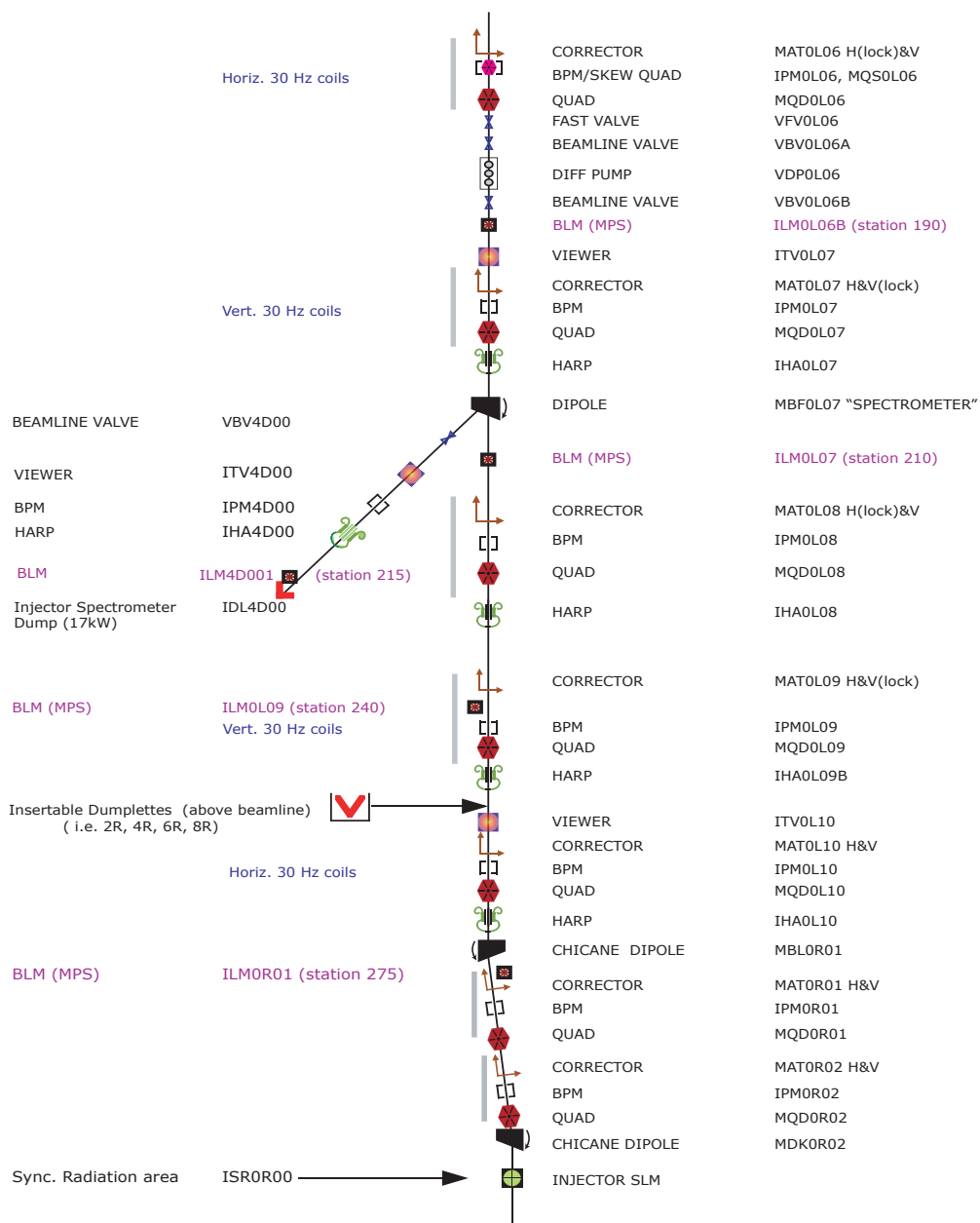
### A.8 Locations of the BPMs in the Injector and Hall C Beamlines

## INJECTOR QUICK REFERENCE DRAWING PAGE 1

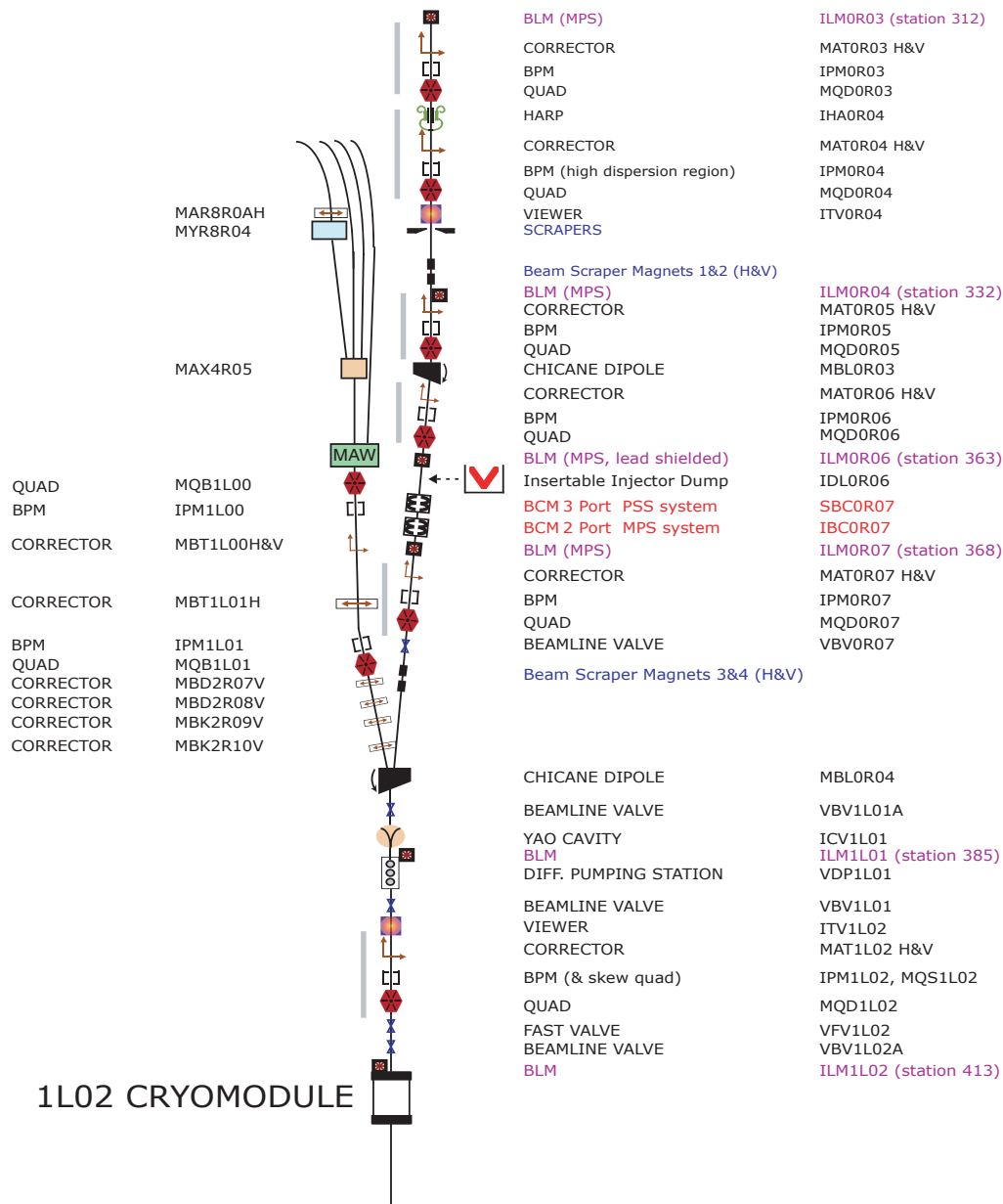








B. Connolly  
 04 APR 2012  
 File: injector\_quick\_reference\_Dwg.ai



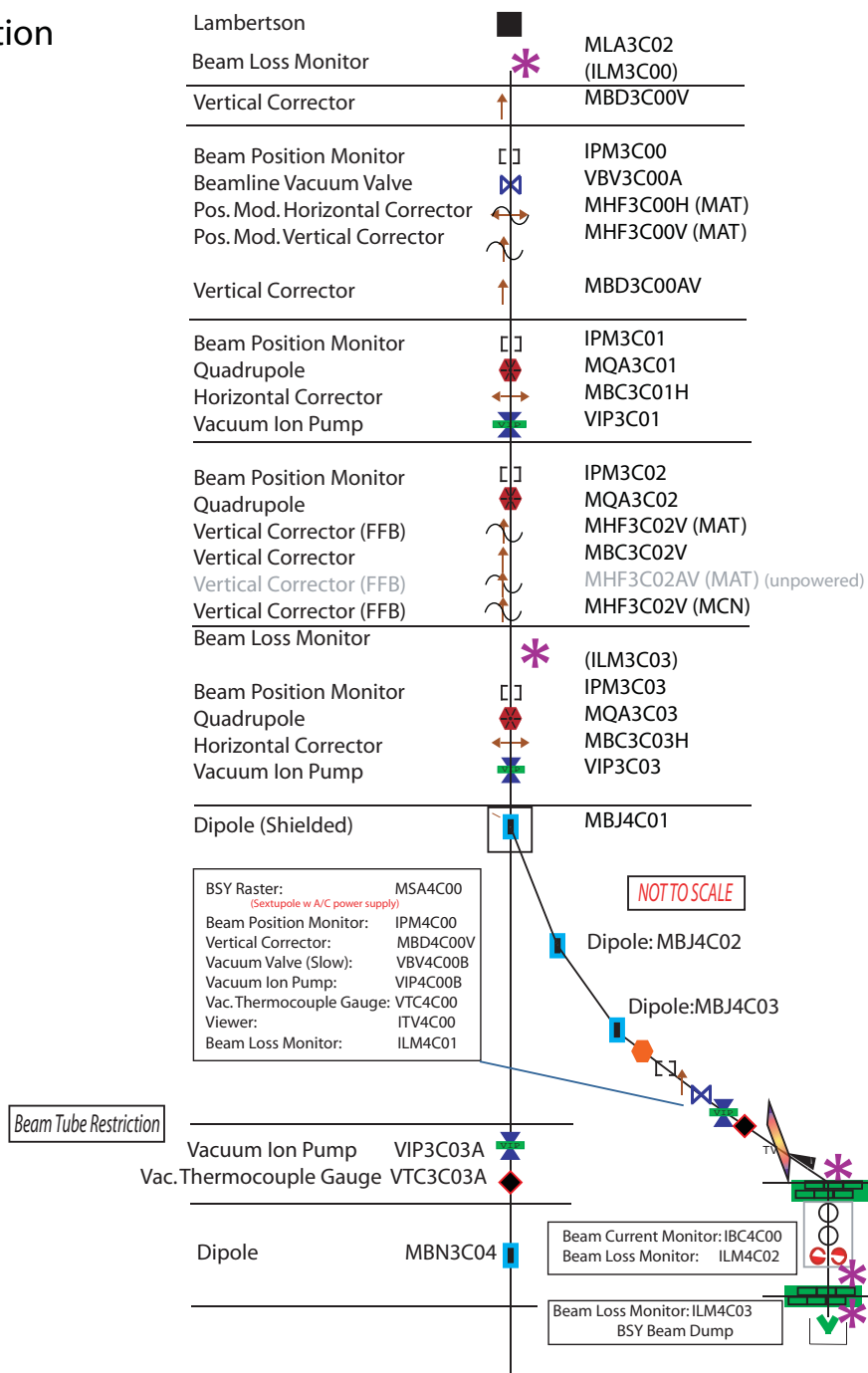
- MAR8R0AH
- MYR8R04
- MAX4R05
- MAW
- QUAD MQB1L00
- BPM IPM1L00
- CORRECTOR MBT1L00H&V
- CORRECTOR MBT1L01H
- BPM IPM1L01
- QUAD MQB1L01
- CORRECTOR MBD2R07V
- CORRECTOR MBD2R08V
- CORRECTOR MBK2R09V
- CORRECTOR MBK2R10V

- BLM (MPS)
- CORRECTOR
- BPM
- QUAD
- HARP
- CORRECTOR
- BPM (high dispersion region)
- QUAD
- VIEWER
- SCRAPERS
- Beam Scraper Magnets 1&2 (H&V)
- BLM (MPS)
- CORRECTOR
- BPM
- QUAD
- CHICANE DIPOLE
- CORRECTOR
- BPM
- QUAD
- BLM (MPS, lead shielded)
- Insertable Injector Dump
- BCM 3 Port PSS system
- BCM 2 Port MPS system
- BLM (MPS)
- CORRECTOR
- BPM
- QUAD
- BEAMLINE VALVE
- Beam Scraper Magnets 3&4 (H&V)
- CHICANE DIPOLE
- BEAMLINE VALVE
- YAO CAVITY
- BLM
- DIFF. PUMPING STATION
- BEAMLINE VALVE
- VIEWER
- CORRECTOR
- BPM (& skew quad)
- QUAD
- FAST VALVE
- BEAMLINE VALVE
- BLM
- ILM0R03 (station 312)
- MATOR03 H&V
- IPM0R03
- MQD0R03
- IHA0R04
- MATOR04 H&V
- IPM0R04
- MQD0R04
- ITV0R04
- ILM0R04 (station 332)
- MATOR05 H&V
- IPM0R05
- MQD0R05
- MBL0R03
- MATOR06 H&V
- IPM0R06
- MQD0R06
- ILM0R06 (station 363)
- IDL0R06
- SBC0R07
- IBC0R07
- ILM0R07 (station 368)
- MATOR07 H&V
- IPM0R07
- MQD0R07
- VBV0R07
- MBL0R04
- VBV1L01A
- ICV1L01
- ILM1L01 (station 385)
- VDP1L01
- VBV1L01
- ITV1L02
- MAT1L02 H&V
- IPM1L02, MQS1L02
- MQD1L02
- VFV1L02
- VBV1L02A
- ILM1L02 (station 413)

1L02 CRYOMODULE

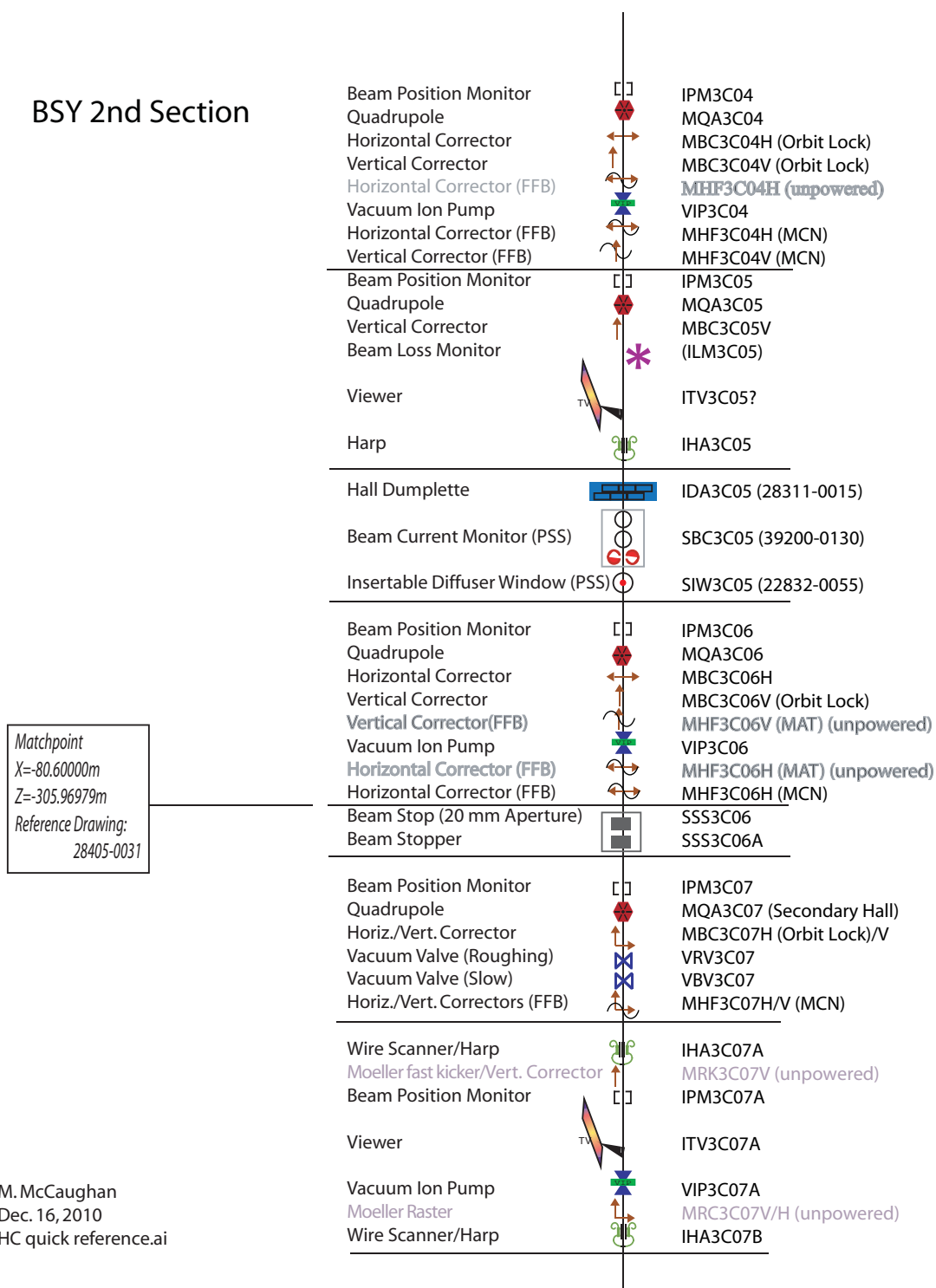
# EXPERIMENTAL HALL C BEAMLINE

## BSY 1st Section



M. McCaughan  
 Dec. 16, 2010  
 HC quick reference.ai

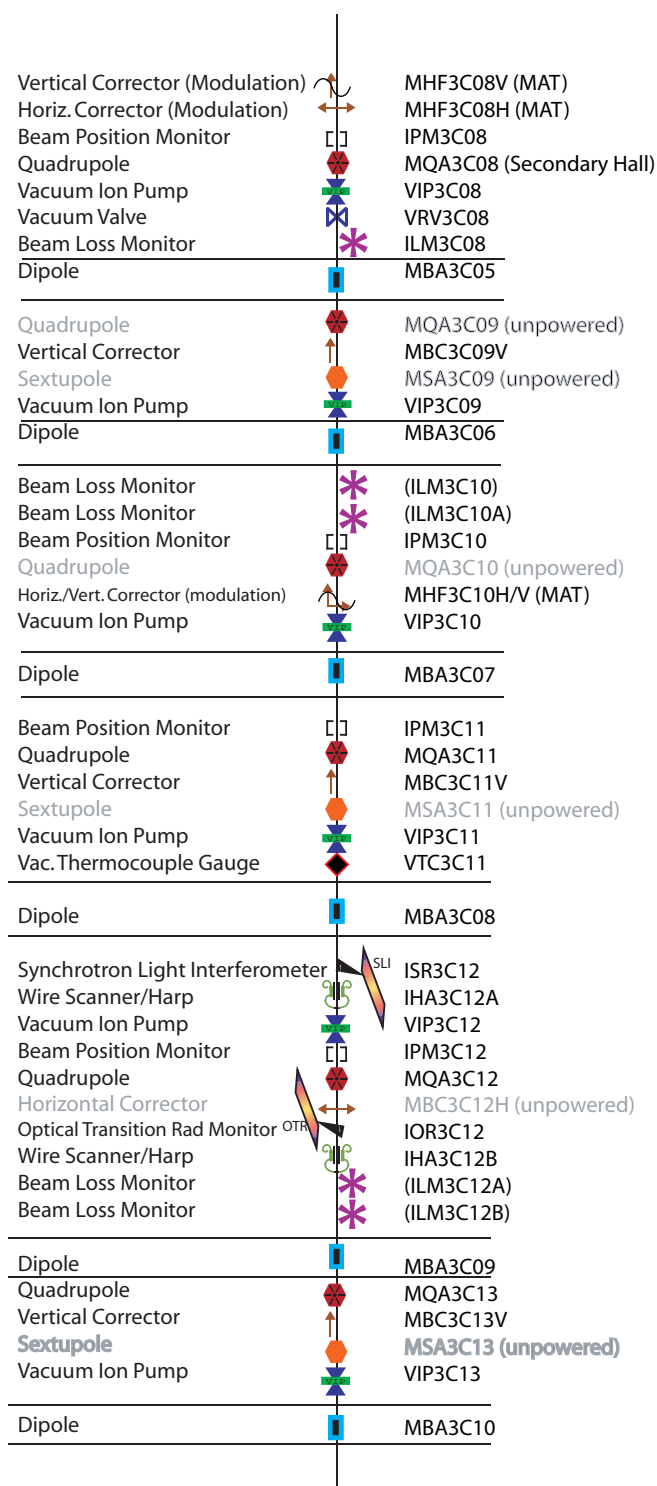
### BSY 2nd Section

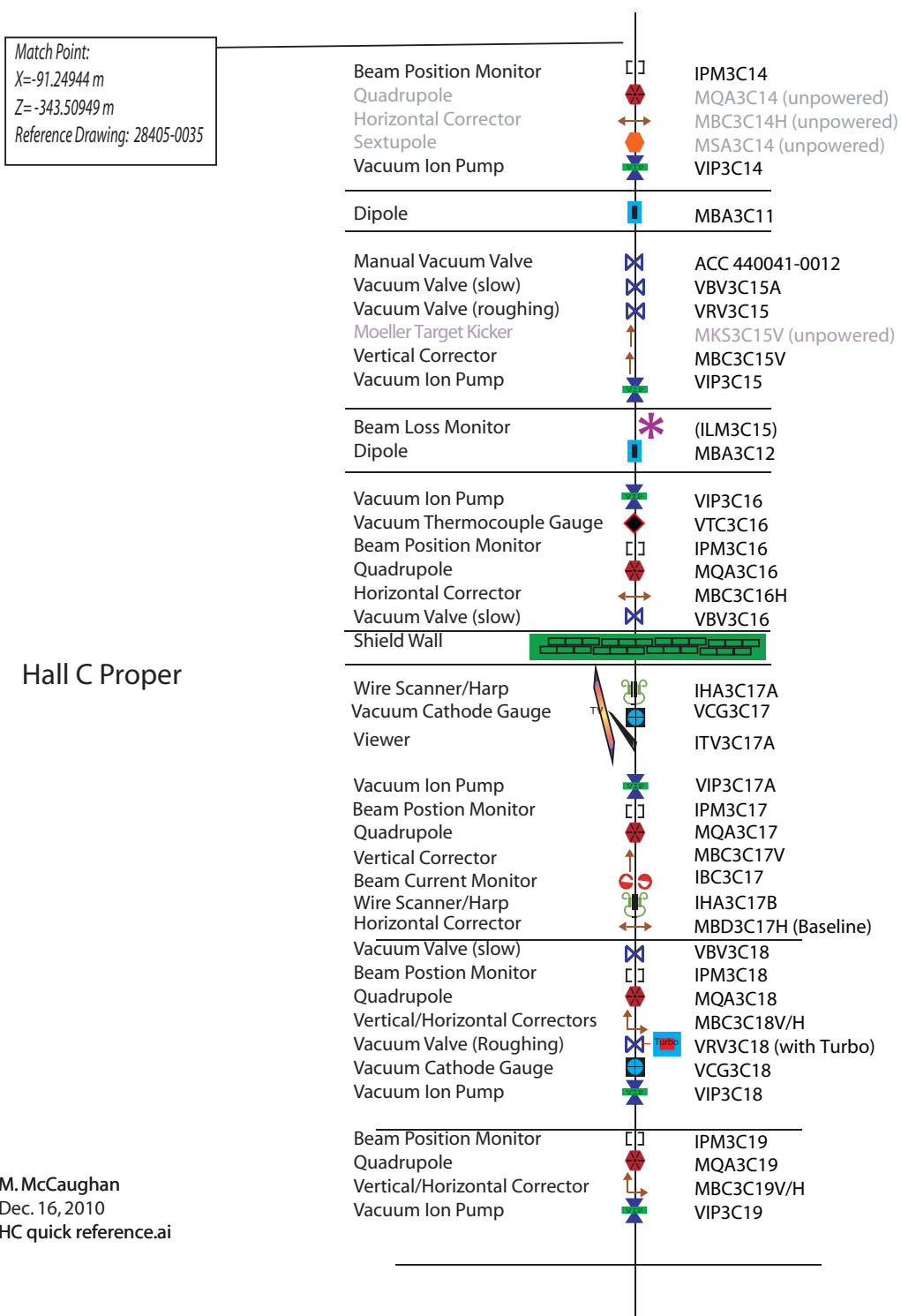


M. McCaughan  
 Dec. 16, 2010  
 HC quick reference.ai

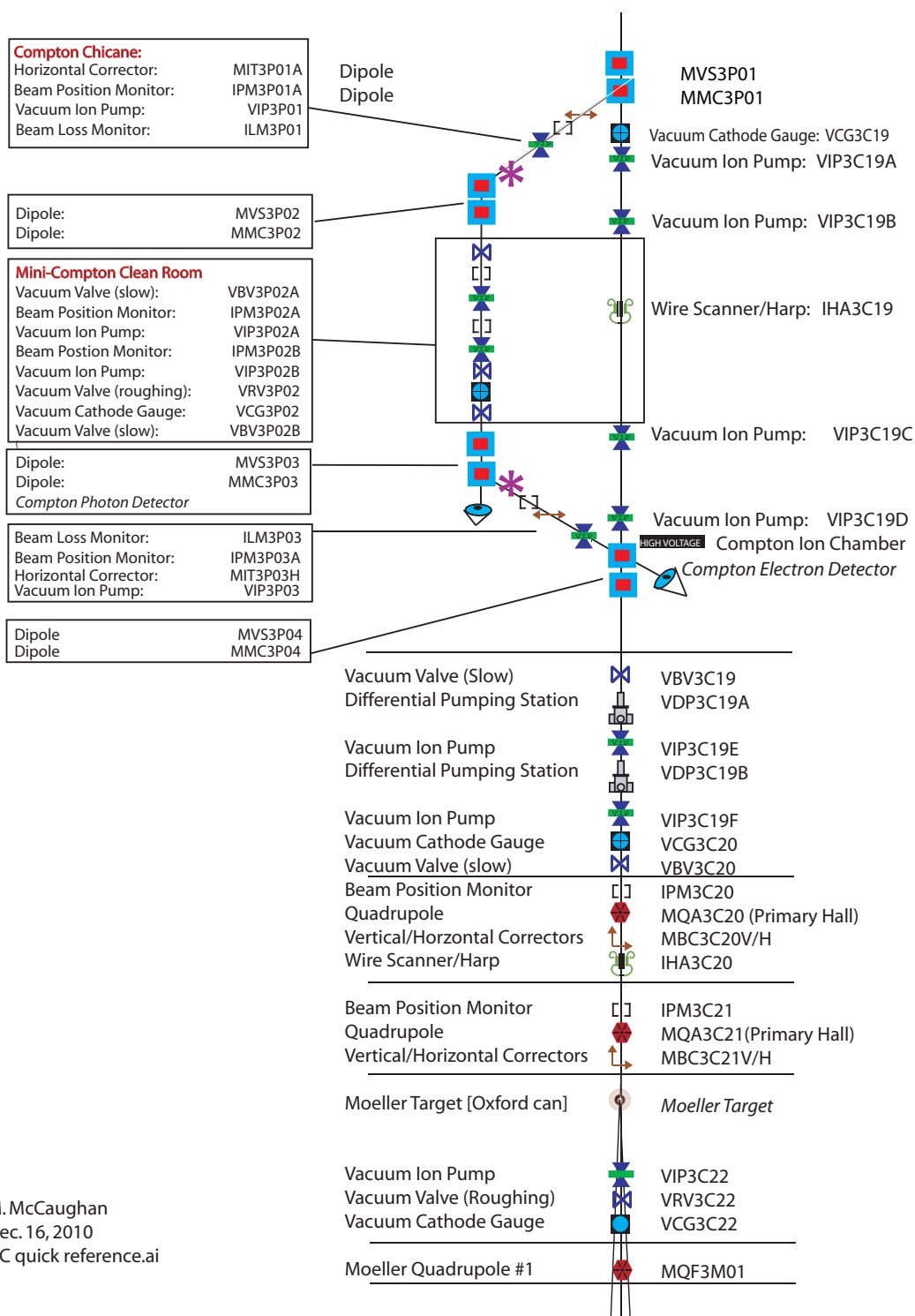


## Line 'C'- to Hall Entrance

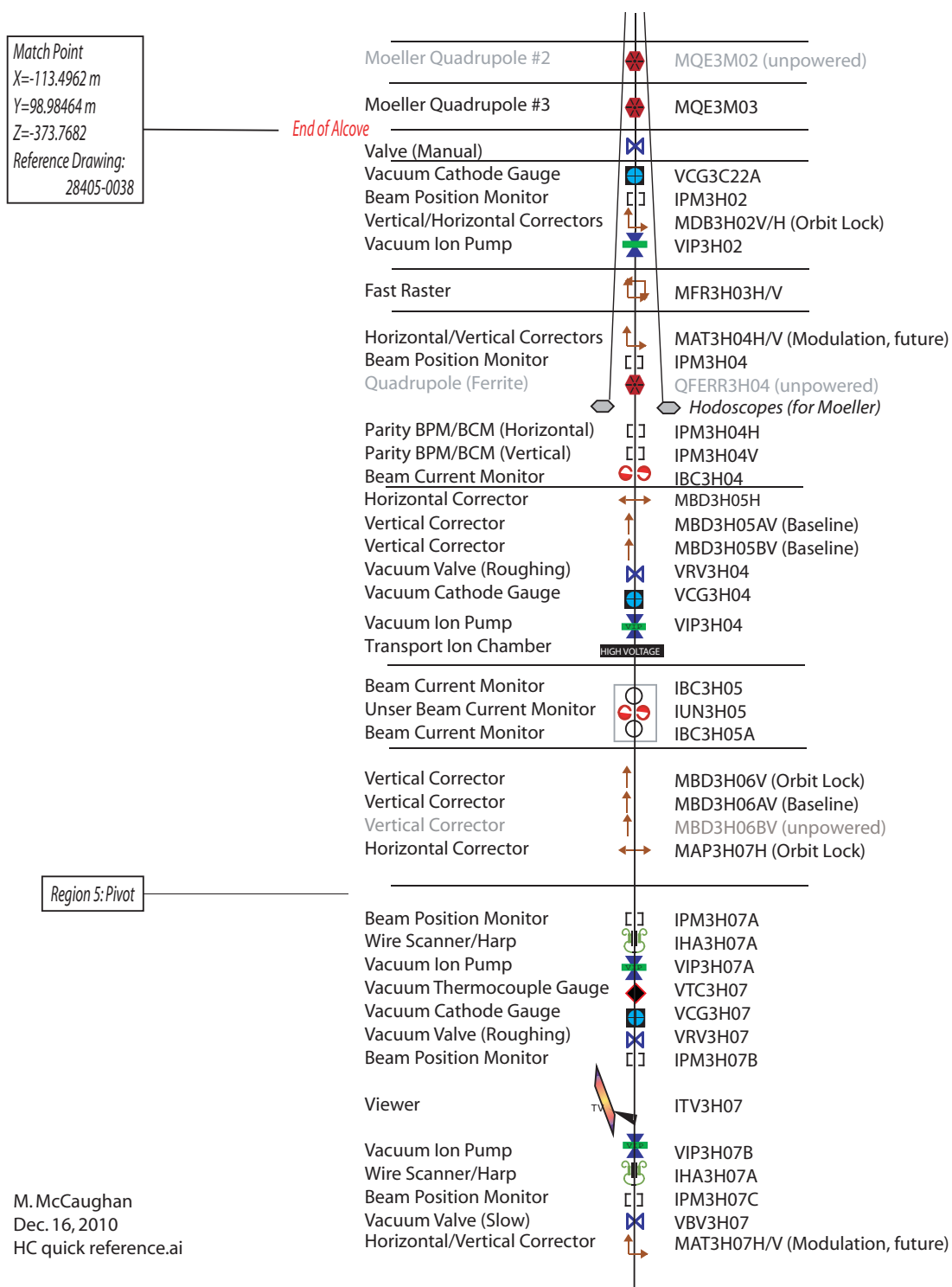


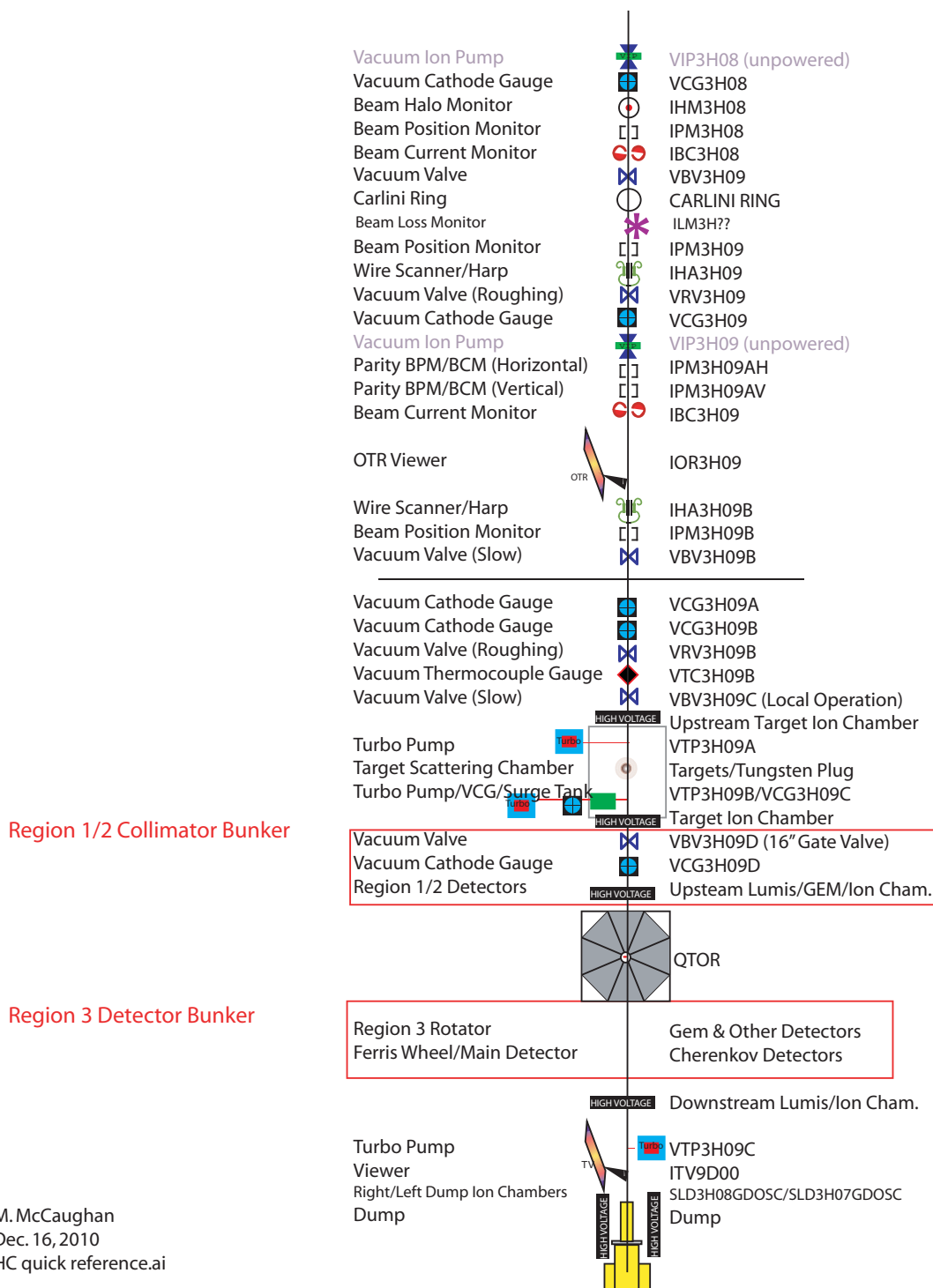


M. McCaughan  
 Dec. 16, 2010  
 HC quick reference.ai




M. McCaughan  
 Dec. 16, 2010  
 HC quick reference.ai





M. McCaughan  
 Dec. 16, 2010  
 HC quick reference.ai

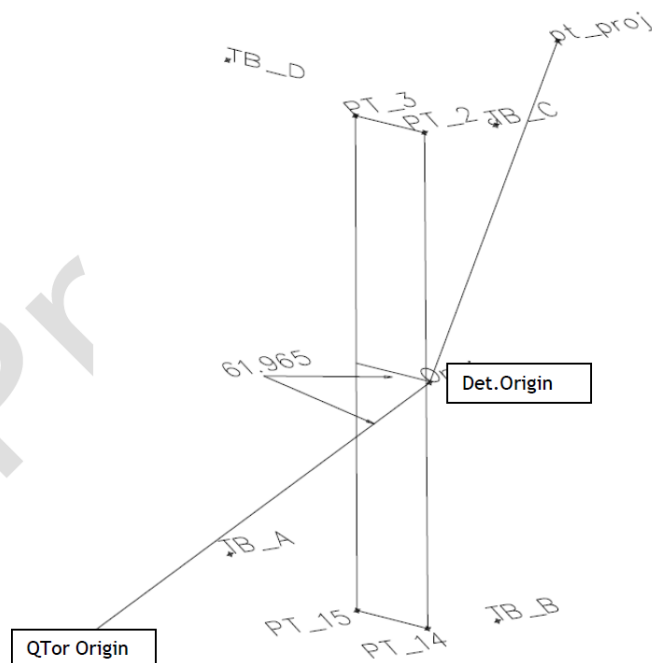
## B Čerenkov Detector Post-Experiment Survey

 <b>Jefferson Lab Alignment Group</b> <b>Data Transmittal</b>		
<b>TO:</b> D.Mack, D. Gaskell, D.Wood, M. Dalton		<b>DATE:</b> 25 Oct 2012
<b>FROM:</b> Kelly Tremblay	<b>Checked:</b>	<b># :</b> C1482
<b>DETAILS:</b>		data: step2b\hallc\qweak\120530a
<p>The Quartz Bar Detectors in Hall C were surveyed post run on June 30<sup>th</sup>, 2012. The table shown on the following page contains the as-found coordinates in both the Qtor magnet system and the local Quartz Bar system as defined in Dave Mack's alignment system (see sketch on final page). Additionally the movements in the local system are shown.</p> <p>The first group of coordinates are the as-found locations of the bars in the Qtor coordinate system, with the origin at the center of the Qtor magnet. The axis are: Z+ following the beam, X+ transverse in the horizontal direction and Y+ vertically up. Units are meters.</p> <p>The second group of coordinates describes the as-found locations in the local system for each individual detector. Z+ is in the beam direction with origin at the downstream edge of the bar (570.625 cm downstream of Qtor center, 341 cm radially from beam centerline), X is radially outward from the beamline, and Y follows the downstream top edge of the bar at the appropriate angle.</p> <p>The column labeled "Ri Component", is the amount that the bars need to be radial displaced in the local quartz X direction. The Ri amount is based upon the amount of Z movement from the ideal Z location and based upon the formula <math>Ri = \tan(22.24^\circ) * (Zi - 570.625\text{cm}) + 341\text{cm}</math>. The formula corrects the radial (local X coordinate) position of the bars to catch the beam envelope, as described by D. Mack. Units are centimeters.</p> <p>The final group of coordinates labeled "Movements", are the calculated amounts the detectors need to move in the local system. The X radial column is the amount the detectors would have to move out after applying the correction amount in the Ri column. A + value indicates the detector needs to move away from the beam centerline. The Y column indicates how much the detector needs to move along the local Y axis. A +Y value would mean the detector moves in positively along the Y axis. A + Z value indicates the detector needs to move downstream from the ideal local value (570.625cm from Qtor center). Units are centimeters.</p> <p>On the third page, the position of Detector #9 relative to the Qtor coordinate system is shown. There is no ideal location for this 9<sup>th</sup> detector. The data has a table of coordinates, and rotation values associated with this detector.</p>		

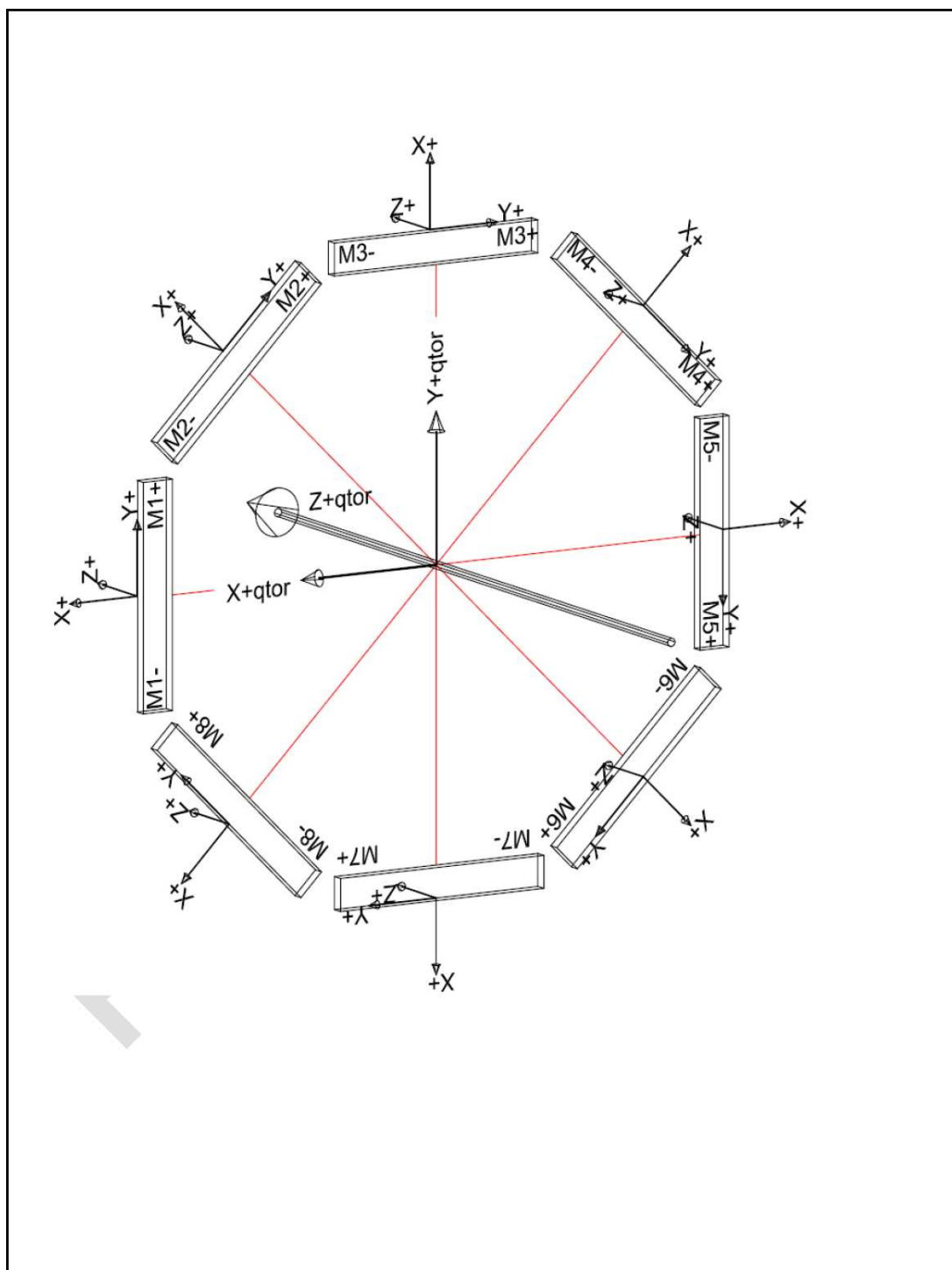
Detector Side	Qtor Coord System			Phi angle (deg)	Local Quartz Bar Coords			Ri component	Movements (cm)		
	Z (M)	X (M)	Y (M)		Local X (cm)	Local Y (cm)	Local Z (cm)		X Radial (cm)	Y (cm)	Z (cm)
MD1+	5.7757	3.4380	1.2532	0.00	343.80	125.32	577.57	343.84	0.04	0.41	6.94
MD1-	5.7725	3.4364	-1.2614		343.64	-126.14	577.25	343.71	0.07	0.41	6.63
MD2+	5.7796	1.5414	3.3185	45	343.65	125.66	577.96	344.00	0.35	0.07	7.34
MD2-	5.7687	3.3171	1.5381		343.31	-125.80	576.87	343.55	0.24	0.07	6.25
MD3+	5.7734	-1.2575	3.4331	90	343.31	125.75	577.34	343.74	0.44	-0.02	6.71
MD3-	5.7808	1.2571	3.4362		343.62	-125.71	578.08	344.05	0.43	-0.02	7.46
MD4+	5.7846	-3.3266	1.5376	135	343.95	126.50	578.46	344.20	0.25	-0.77	7.84
MD4-	5.7770	-1.5454	3.3125		343.50	-124.95	577.70	343.89	0.39	-0.78	7.07
MD5+	5.7817	-3.4395	-1.2609	180	343.95	126.09	578.17	344.09	0.14	-0.36	7.55
MD5-	5.7831	-3.4418	1.2537		344.18	-125.37	578.31	344.14	-0.04	-0.36	7.69
MD6+	5.7843	-1.5345	-3.3341	225	344.26	127.25	578.43	344.19	-0.07	-1.52	7.80
MD6-	5.7880	-3.3150	-1.5585		344.61	-124.21	578.80	344.34	-0.27	-1.52	8.18
MD7+	5.7877	1.2597	-3.4455	270	344.55	125.97	578.77	344.33	-0.22	-0.24	8.14
MD7-	5.7826	-1.2549	-3.4434		344.34	-125.49	578.26	344.12	-0.22	-0.24	7.64
MD8+	5.7769	3.3105	-1.5540	315	343.97	124.20	577.69	343.89	-0.08	1.53	7.07
MD8-	5.7777	1.5344	-3.3341		344.25	-127.26	577.77	343.92	-0.33	1.53	7.14

The 9<sup>th</sup> detector is shown below with coordinates based on the Qtor coordinate system referenced above. The units are meters, with angular units in decimal degrees. The horizontal angle formed between the line from the Qtor origin to the detector origin point that is made with the detector plane is  $61.9645^\circ$ . The face of the detector is yawed  $-1.0546$  from the X axis and pitched  $0.2074$ . The Det.Origin is the origin point of the detector and the pt\_proj is a point projected perpendicular downstream from the Det.Origin.

Detector 9			
Plane Corner Points			
PT_2	7.3765	-3.7730	-0.2229
PT_3	7.3750	-3.6900	-0.2241
PT_14	7.3803	-3.7756	-1.2293
PT_15	7.3786	-3.6907	-1.2286
detector Points			
Det.Origin	7.3786	-3.7784	-0.7286
pt_proj	7.8785	-3.7688	-0.7268
Survey Targets			
TB_A	7.4104	-3.5270	-1.2321
TB_B	7.4159	-3.8483	-1.2300
TB_C	7.4122	-3.8474	-0.2236
TB_D	7.4059	-3.5255	-0.2282







## C PMT Weight Estimates for the Transverse Running

As discussed in Section 4.2.1, there are couple of ways to determine the asymmetry of a single Čerenkov detector: yield based or asymmetry based. In the yield based method, where the yields of the positive ( $Y_{pos}$ ) and negative ( $Y_{neg}$ ) PMTs are used as

$$Y_{barsum} = \frac{W_{pos}Y_{pos} + W_{neg}Y_{neg}}{W_{pos} + W_{neg}}, \quad (C.1)$$

to determine the yield of the detector,  $Y_{barsum}$ , it is important that the weights  $W_{pos/neg}$  are determined appropriately to remove the differences in the PMT gains. A wrong weight will result in a wrong yield for the barsum and hence a shift in the asymmetry determined therein. The weights were typically generated once every 8 hours by taking the average yield of the PMT distributions as

$$W = \frac{1}{\langle Y \rangle}. \quad (C.2)$$

### C.1 Stability of Improper Weights

The stability of the weights used over a running period can be observed by looking at the relative difference between the weighted positive and negative PMT yields given by

$$\% \text{ Difference w.r.t average yield} = 100 \times 2 \left( \frac{Y_{pos}W_{pos} - Y_{neg}W_{neg}}{Y_{pos}W_{pos} + Y_{neg}W_{neg}} \right). \quad (C.3)$$

This should be less than a 1% for properly weighted PMT yields in a given detector. Figure C.1 shows the % difference of the weighted yields in both Transverse\_Run I and Transverse\_Run II periods.

The difference between the weighted yields during the LH2-cell target data collection period are within  $\pm 2\%$  for all the detectors. In comparison, the aluminum running period which used the same weights as the LH2-cell period, shows large differences between the weighted yields in a detector. In some cases these differences are as large as 10%. The change from the LH2-cell to aluminum running in the middle is clearly noticeable indicating the change in the yields when going from 150  $\mu\text{A}$  to 24  $\mu\text{A}$ . Clearly, new weights were needed for the aluminum target running period in

Transverse\_Run I. In comparison, the weights in the LH2-cell target running period were stable for all detectors and were below 2%.

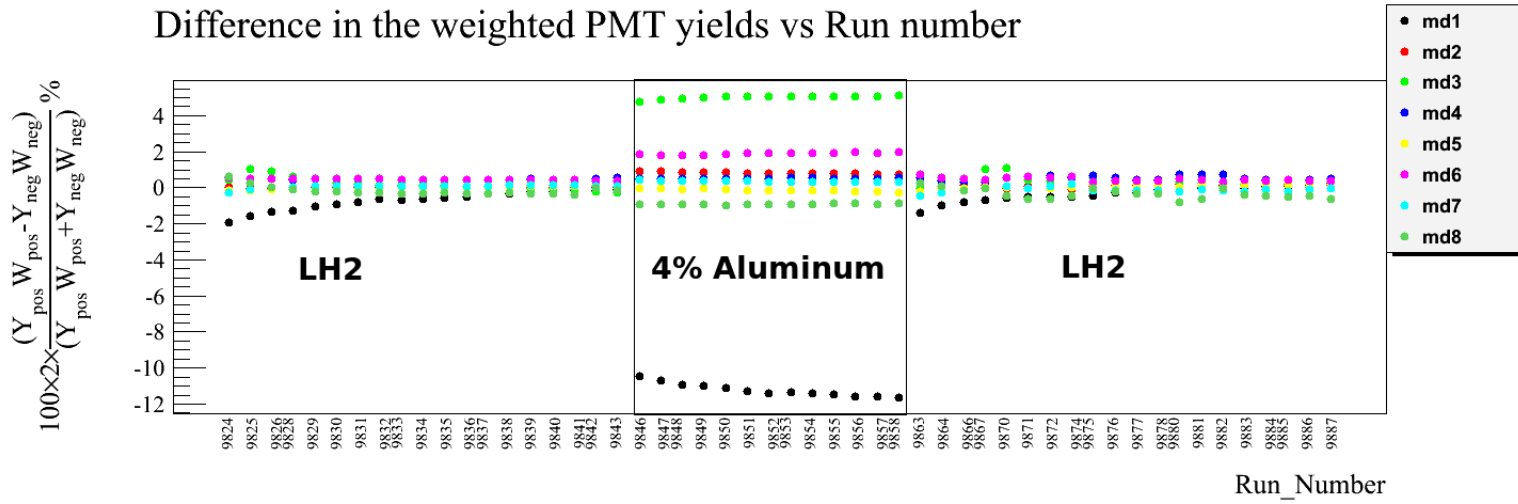
Moving onto Transverse\_Run II, the changes between the different running periods using different targets and QTOR settings ( $N \rightarrow \Delta$  compared to elastic) vary between 5% to 15 %. This was an indication that each of the different run periods needed new weights. Similar to Transverse\_Run I, a single set of weights were used for the full running period and these old weights were extracted at the beginning of the running period. In both figures one can see the largest difference in the weighted yields are occurring in the detector 1. This is due to the loose glue joint in the middle of the bar which allows the two PMTs to behave independently of each other unlike the rest of the detectors with the proper glue joints.

## C.2 Weights Used in Pass5 Transverse Analysis

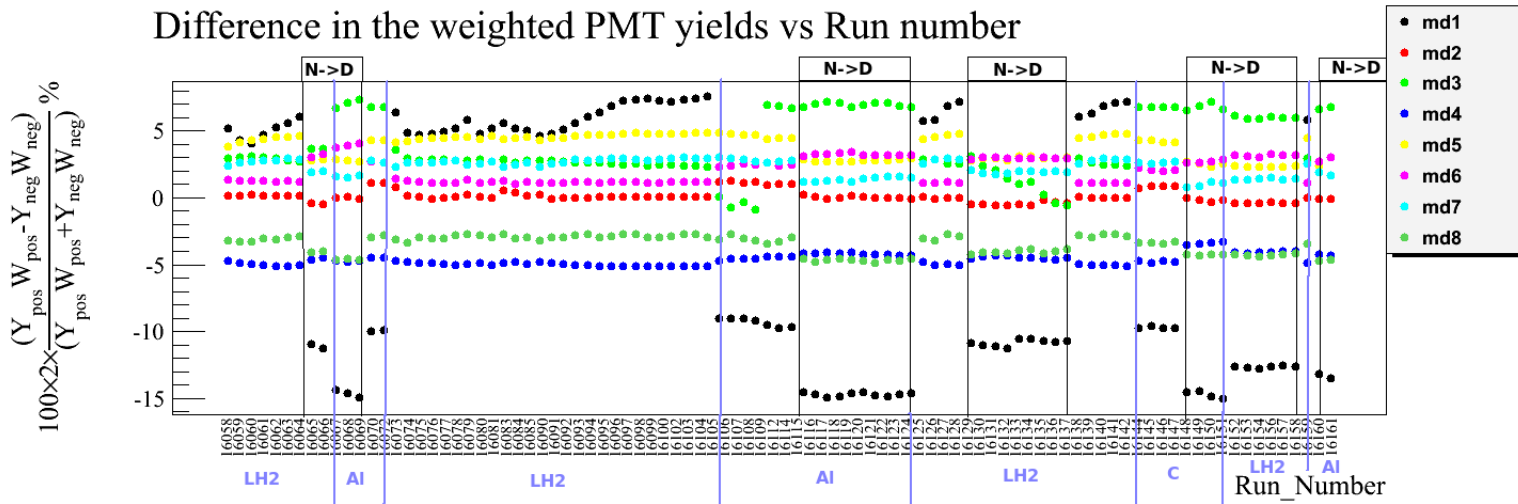
New weights (see Table C.2) were calculated after separating the transverse running periods into regions which were clearly noticeable in Figure C.1. The new weights brought down the % differences between the weighted PMT yields from 15% to  $< 1.5\%$  for all cases (see Figure C.2). These new weights are used for the transverse analysis from pass5 replay onwards.

Table C.1: Run ranges corresponding to the weights given in Table C.2. Also given are the runs used to calculate the weights for the particular run range.

Symbol	Weights calculated from run	Weights applied on run range
a	9846	9845-9858
b	16057	16055-16159
c	16096	16096-16105
d	16070	16070-16072 and 16112-16114
e	16106	16106-16111
f	16145	16144-16147
g	16065	16065-16066
h	16132	16129-16132
i	16135	16133-16137
j	16152	16152-16158
k	16067	16067-16069,16115-16124
l	16160	16160-16161
m	16148	16148-16151



(a) Transverse\_Run I



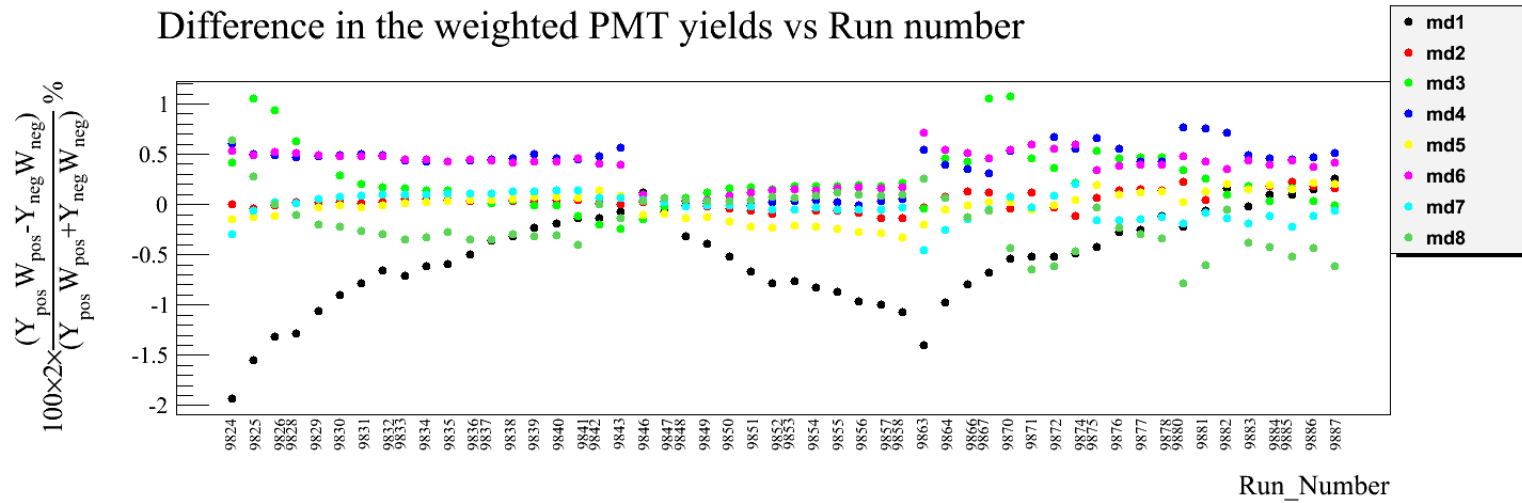
(b) Transverse\_Run II

Figure C.1: % Difference between weighted positive and negative PMT yields in a detector at the run level before updating the weights in the pass5 replay. See text for explanation.

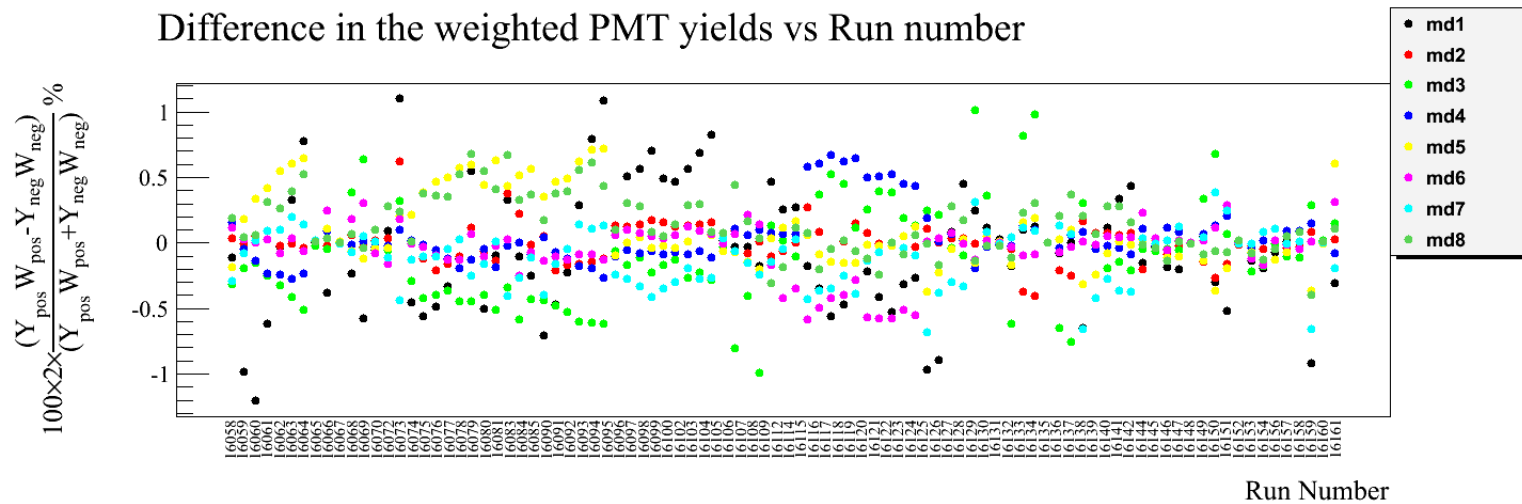
Table C.2: New PMT weights used for the transverse running period from pass5 replay onwards. The symbols  $a-m$  represent the run ranges these weights were used on as shown in Table C.1. 9 NEG was saturating during some of the inelastic running period and therefore was removed from the full analysis.

PMT	Run I	Run II											
	Elastic					Inelastic							
	Al27	LH2	LH2	Al27	Al27	C12	LH2	LH2	LH2	LH2	Al27	Al27	C12
	a	b	c	d	e	f	g	h	i	j	k	l	m
1NEG	67.96	31.18	31.91	71.31	72.63	96.87	330.53	331.45	266.15	477.68	563.11	476.91	1205.93
1POS	73.91	25.81	25.99	68.75	69.31	93.00	321.53	322.97	258.29	472.54	567.02	474.55	1216.42
2NEG	106.44	36.06	36.53	98.60	100.49	132.88	445.53	444.79	355.58	644.87	791.22	665.13	1681.83
2POS	64.10	22.47	22.79	60.89	62.00	82.22	279.28	279.14	222.27	404.04	494.04	415.50	1050.15
3NEG	65.47	23.05	23.39	63.05	64.17	84.76	287.57	286.43	228.44	415.04	508.67	428.05	1081.45
3POS	117.97	41.75	42.50	109.86	119.59	147.71	516.73	523.10	424.97	728.01	887.07	746.67	1888.87
4NEG	110.72	39.33	39.75	106.13	107.80	142.66	483.90	484.08	386.26	704.68	854.39	723.40	1818.89
4 POS	71.69	27.38	27.79	73.74	75.05	99.50	336.57	335.84	268.60	487.68	595.17	501.22	1251.25
5NEG	75.28	28.80	29.29	77.86	79.41	104.92	356.84	356.53	284.30	517.91	632.23	530.54	1343.76
5POS	61.74	22.04	22.21	59.29	60.15	79.90	275.79	275.19	219.45	401.91	488.48	411.74	1039.57
6NEG	71.39	26.11	26.43	69.56	70.76	93.95	325.23	324.61	259.70	474.09	577.29	487.62	1219.92
6POS	82.16	30.67	31.11	80.62	82.36	109.62	375.76	375.21	300.10	546.77	662.45	565.32	1415.71
7 NEG	85.03	31.67	32.07	84.08	85.57	113.89	397.93	396.61	316.82	576.27	691.08	582.95	1473.61
7POS	72.51	26.45	26.64	69.97	71.05	95.00	333.96	333.44	266.07	486.40	582.10	489.55	1250.64
8NEG	69.54	25.32	25.60	67.44	68.64	91.72	314.09	313.45	249.52	456.65	552.07	464.54	1183.15
8POS	62.10	23.88	24.08	63.47	64.68	86.65	298.76	298.32	237.63	435.26	528.07	444.88	1127.14
9NEG	471.99	40.00	40.56	110.21	114.45	159.70	-	-	2.64	20.08	-	7.47	32.28
9POS	1179.07	129.41	131.29	374.36	383.01	521.65	43.97	43.95	11.28	81.72	87.78	31.03	141.58

Even though the analysis presented in this dissertation used the average PMT asymmetry to determine the asymmetry of a single detector, there are other parts of the  $Q_{\text{weak}}$  analysis which require the use of yield based asymmetry estimation. The beam modulation based beam parameter sensitivity estimations is such a case. Therefore, this analysis ensures that the PMT weights are not a systematic in analysis based on yield weighted detector asymmetries.



(a) Transverse\_Run I



(b) Transverse\_Run II

Figure C.2: % Difference between weighted positive and negative PMT yields in a detector at the run level with updated weights in pass5. See text for explanation.

## D Data Acquisition and Analysis Software Misc

### D.1 List of Integrating DAQ signals

Table D.1 contains the list of parity signals which were digitized by the  $Q_{\text{weak}}$  integrating-mode DAQ.

Table D.1: List of signals integrated via the integrating DAQ.

ROC	Module	Signal
0	VQWK ADC	Raster X, Y, Sum of X and Y Scanner X, Y Scanner Power Phase Monitor Inverted T_stable
	FLEXIO	MPS, HEL, QRT
	SCALER	BCM1, BCM2, BCM5, BCM6 Unser Hall A BCM 31MGHz Clock and 4 MGHz clock Halo Monitors 3-10
1	VQWK ADC	BPM3C07 XP, XM, YP, YM BPM3C07a XP, XM, YP, YM BPM3C08 XP, XM, YP, YM BPM3C011 XP, XM, YP, YM BPM3C012 XP, XM, YP, YM BPM3C014 XP, XM, YP, YM BPM3C016 XP, XM, YP, YM BPM3C018 XP, XM, YP, YM BPM3C019 XP, XM, YP, YM BPM3P02A XP, XM, YP, YM BPM3P02B XP, XM, YP, YM BPM3P03A XP, XM, YP, YM



Table D.1: Continued ..

ROC	Module	Signal
		BPM3C20 XP, XM,YP, YM BPM3C21 XP, XM,YP, YM BPM3H02 XP, XM,YP, YM BPM3H04 XP, XM,YP, YM BPM3H07A XP, XM,YP, YM BPM3H07B XP, XM,YP, YM BPM3H07C XP, XM,YP, YM BPM3H08 XP, XM,YP, YM BPM3H09 XP, XM,YP, YM BPM3H09B XP, XM,YP, YM BCM1, BCM2, BCM5, BCM6, BCM7 and BCM8
2	VQWK ADC	PMT+ of MD1 to MD9 PMT- of MD1 to MD9 Background detectors (PMTLTG, PMTLED, PM- TONL) Spares (ISource, Preamp, CageSr) US LUMI1, 3, 5, 7 PMT+ US LUMI1, 3, 5, 7 PMT- PMT+ of DS LUMI 1 to 8 PMT- of DS LUMI 1 to 8 Beammod (FGX1, FGX2, FGY1, FGY2, FGE, Ramp, HWTrig)
		BPM1I02 XP,XM, YP, YM BPM1I04 XP, XM,YP, YM BPM1I06 XP, XM,YP, YM BPM0I01 XP, XM,YP, YM BPM0I01A XP, XM,YP, YM BPM0I02 XP, XM,YP, YM BPM0I02A XP, XM,YP, YM BPM0I05 XP, XM,YP, YM

Table D.1: Continued ..

ROC	Module	Signal
		BPM0I07 XP, XM,YP, YM
		BPM0L02 XP, XM,YP, YM
		BPM0L03 XP, XM,YP, YM
		BPM0L04 XP, XM,YP, YM
		BPM0L05 XP, XM,YP, YM
		BPM0L06 XP, XM,YP, YM
		BPM0L07 XP, XM,YP, YM
		BPM0L08 XP, XM,YP, YM
		BPM0L09 XP, XM,YP, YM
		BPM0L10 XP, XM,YP, YM
		BPM0R03 XP, XM,YP, YM
		BPM0R04 XP, XM,YP, YM
		BPM0R05 XP, XM,YP, YM
		BPM0R06 XP, XM,YP, YM
		BCM0L02
		Battern6 and 7
		Phase Monitor

## D.2 Integrating-Mode Data Rate and Data Size

The integrating-mode DAQ read 35 modules (see Table 4.1). Table D.2 shows the output rates of these modules.

Table D.2: Integrating-mode readout module output rates.

Module	Channels	words per channel		Total bits
		32-bit	16-bit	
VQWK ADC (33 modules)	8	5	1	1408
Scaler (2 modules)	32	1	-	1024

Taking the total number of bits per channel given in Table D.2 one can estimate the integrating-mode data rate to be,

$$(1408 \times 33 + 2 \times 1024) \times 960s^{-1} \approx 5.6 \text{ MBs}^{-1}.$$

At this rate, the total amount of data collected within the 2 year running period is  $\approx 120$  TB.

### D.3 VME QWEAK 8 Channel 18 bit ADC module

The VME QWEAK module was custom built by TRIUMF to handle the high event rates of the  $Q_{\text{weak}}$  experiment. Each module has eight ADC channels which were synchronised and triggered by the MPS signal sent by the helicity board. Table D.3 shows a summary of the features of VQWK ADC [126].

Table D.3: Some important features of the VQWK ADCs

Property	
Sampling rate	500 kSPS (kilo samples per second)
Input voltage range	$\pm 10$ V
Input offset/pedestal	-28.61 mV
Least Square Bit/Resolution	$10\text{V}/2^{17} = 76.29 \mu\text{V}$

#### D.3.1 Configuration used for 960 Hz Running

To achieve the desired conversion rates, the VQWK ADCs needed to be configured according to the following formula

$$T_{\text{Stable}} = T_{\text{Sample}} \times (\text{SAMPLE\_PER\_BLOCK} \times 4 + \text{GATE\_DELAY}) + 2.5\mu\text{s} + 1\mu\text{s}, \quad (\text{D.1})$$

where  $T_{\text{Sample}} = 2\mu\text{s}$  is the time taken for a single sample at 500kSPS rate, SAMPLE\_PER\_BLOCK is the number of analog to digital conversions within a sub\_block, GATE\_DELAY in samples is the delay between the leading edge of the ADC gate. An additional  $2.5 \mu\text{s}$  delay is required for module synchronization. During the running of  $Q_{\text{weak}}$  it was noted by Paul King that the first sub-block was shorter than the other

3. This was supposedly a result of shifts in the voltage levels of the ADC with the arrival of the gate. This issue was fixed by setting a  $1 \mu s$  delay to allow the ADC voltage levels to settle. For a 960 Hz event rate ( $T_{Stable} = 70 \mu s$ ), the VQWK ADC were configured by setting following values to the above parameters.

$$\text{SAMPLE\_PER\_BLOCK} = 464 \text{ samples } (928 \mu s)$$

$$\text{GATE\_DELAY} = 20 \text{ samples } (40 \mu s)$$

This results in a total ADC delay of  $43.5 \mu s$  and an active integrating period of  $928 \mu s$ .

#### D.4 Helicity Pattern Generator

The 30-bit helicity generator is a 30-bit long linear feedback shift generator which determines the polarity of the first event in a helicity pattern pseudo-randomly. The pseudo-random generator used by the helicity board was initially built as a 24-bit generator according to the requirements of the G0 experiment [177]. The bit size was increased from 24 to 30 bit to achieve a longer repetition time without effecting the pseudo-random sequence. The repetition rate can be calculated using

$$T_{Repeat} = \frac{\text{Length of the pseudo-random sequence}}{f_{Pattern}}, \quad (\text{D.2})$$

where  $f_{Pattern}$  is the frequency of the helicity pattern. For  $Q_{weak}$ 's 240 Hz pattern rate (corresponding to the 960 Hz event rate), the repeatability of the 30-bit pseudo-random pattern was about 52 days. With the 24-bit generator, it would have been about 19 hrs. QwAnalysis was implemented with the capability of analyzing data taken with both the 24-bit and 30-bit pseudo-random generators. Using the number of patterns delayed and the delayed-helicity of the first event of a pattern, the analyzer was able to predict the actual/true helicity of the first event using the following algorithms. The helicity prediction is required only for the first event in the pattern since knowing the helicity of the first event by default means the next three events will have helicities of either  $++-$  or  $--+$ .

##### D.4.1 Algorithm for the 24-bit Pseudo-Random Generator

This algorithm is based on G0 Helicity algorithm [177]. It was implemented in the QwAnalysis parity analyzer.

```

//Bit 1 of shift register 000000000000000000000001
const UInt_t IB1 = 1;
//Bit 3 of shift register 000000000000000000000100
const UInt_t IB3 = 4;
//Bit 4 of shift register 000000000000000000001000
const UInt_t IB4 = 8;
//Bit 24 of shift register 100000000000000000000000
const UInt_t IB24 = 8388608;
//Sum of the four feedback bits is 100000000000000000001101
const UInt_t MASK = IB1+IB3+IB4+IB24;

//The generated pattern
UInt_t result;

if(ranseed<=0){
    QwError << "ranseed must be greater than zero!" << QwLog::endl;
    result = 0;
}

// if bit 24 of ranseed = 1, then output 1
if(ranseed & IB24) {
    ranseed = ((ranseed^MASK) << 1|IB1);
    result = 1;
}
else {
    ranseed <<= 1;
    result = 0;
}
return(result);

```

#### *D.4.2 Algorithm for the 30-bit Pseudo-Random Generator*

Modified algorithm for the 30-bit generator [94].

```

UInt_t bit7    = (ranseed & 0x00000040) != 0;
UInt_t bit28   = (ranseed & 0x08000000) != 0;
UInt_t bit29   = (ranseed & 0x10000000) != 0;
UInt_t bit30   = (ranseed & 0x20000000) != 0;

UInt_t result = (bit30 ^ bit29 ^ bit28 ^ bit7) & 0x1;

if(ranseed<=0) {
    QwError << "ranseed must be greater than zero!" << QwLog::endl;

```

```

    result = 0;
}
ranseed = ( (ranseed << 1) | result ) & 0x3FFFFFFF;

return(result);

```

## D.5 Sign of the Physics Asymmetry

Due to Wien flips, IHWP reversals and spin precession changes associated with energy changes in the accelerator (pass changes), it is important to know the proper sign of the measured asymmetries when combining data taken with these configurations. The positive helicity state is identified in the  $Q_{\text{weak}}$  DAQ as the the helicity state with the spin parallel to the direction of motion. However, the natural spin direction of the electrons out of the photocathode (IHWP is OUT) and into the vertical Wien filter is actually spin anti-parallel to the direction of motion. For vertical transverse running, only the vertical Wien filter is used. Therefore, in a natural (IHWP OUT) positive helicity state a plus rotation from the vertical Wien in the YZ plane would leave the spin pointing down words. Since the net spin precession in the vertical plane is zero, the spin entering the Hall C for positive helicity with IHWP OUT will also be pointing down wards. If we consider scattering into the octant 1 for this case, the normal to the scattering plane in octant 1 will be pointing upwards with the helicity pointing down wards. Physically, this resembles a negative helicity state. Therefore, vertical transverse with IHWP OUT needs to be sign corrected to extract the proper sign of the physics asymmetry.

## E Helicity Magnets First Performance Check at 960 Hz

Previous Hall C experiments like the G0 experiment have successfully used the helicity magnets for position feedback. But, since the magnets were not tested to operate at high helicity reversal rates such as 960 Hz,  $Q_{\text{weak}}$  refrained from using these initially. The G0 experiment used the helicity magnets at 30 Hz and they were also tested at 250 Hz helicity reversal rate. On March 20th 2011, during beam studies, under Riad Suleimans instructions, Mark Dalton and I carried out the first functionality test of these helicity magnets at the helicity reversal rate of 960 Hz. Following is a summary of that work and our findings.

### E.1 Helicity Magnet Locations

Helicity magnets are dipole magnets that can be used to move the beam in the horizontal (H) and vertical (V) directions in a helicity correlated manner. There are four helicity magnets installed in the CEBAF injector beamline (see the list below).

- MHEL0L01V is located between IPM0L01 and IPM0L02
- MHEL0L02H is located between IPM0L02 and IPM0L03
- MHEL0L03V is located between IPM0L03 and IPM0L04
- MHEL0L03H is located between IPM0L03 and IPM0L04

### E.2 Test Procedure

The beam was kicked using individual helicity magnets, one at a time, and the resulting position differences were measured along the injector and the hall C beamlines using the BPMs. The magnitude of the beam kicks were set by a Digital to Analog Converter. The beam kicks were applied at both positive (even) and negative (odd) helicity states and data were collected for 960Hz and 120 Hz helicity reversal rates. The lower 120 Hz rate was used to check the helicity magnet calibrations. Table E.1 shows the list of runs taken during these studies.

Table E.1: List of runs taken during helicity magnet tests. The beam current was  $155 \mu\text{A}$  and the beam was terminated at the inline dump.

Run	Comment	Even DAC	Odd DAC
2247	Using helicity magnet MHE0L01V @ 960 Hz	0, 500, -500	0, -500, 500
2249	Using helicity magnet MHE0L02H @ 960 Hz	0, 500, -500	0, -500, 500
2250	Using helicity magnet MHE0L03V @ 960 Hz	0, 500, -500	0, -500, 500
2251	Using helicity magnet MHE0L03H @ 960 Hz	0, 500, -500	0, -500, 500
2252	Using helicity magnet MHE0L01V @ 120 Hz	0, 500, -500	0, -500, 500
2253	Using helicity magnet MHE0L02H @ 120 Hz	0, 500, -500	0, -500, 500
2254	Using helicity magnet MHE0L03V @ 120 Hz	0, 500, -500	0, -500, 500
2255	Using helicity magnet MHE0L03H @ 120 Hz	0, 500, -500	0, -500, 500

### E.3 Induced Position Differences

Observing the position differences induced by each helicity magnet, it was noted that a DAC count of 500 can induce position differences as large as  $50 \mu\text{m}$  (see Figures E.2 and E.1). The magnets seem to be working at 960 Hz. But the results were not an indication of whether the magnetic field was actually changing at the beginning of each helicity window. This was determined by looking at the position differences inside the four sub-blocks of an event provided by the ADCs.

#### *E.3.1 Helicity Magnet Response Within Sub-blocks*

If the helicity magnets change their magnetic fields at a rate of 960 Hz, then the position differences vs DAC counts slopes inside each sub-block should match with that of the `hw_sum` of an event. If it does not, then the magnets are not working at the 960Hz. For an effective position feedback system for  $Q_{\text{weak}}$  the magnets needed to have a response rate of 960 Hz. Figure E.3 and E.5 shows the induced position differences inside the sub-blocks vs DAC counts at 960Hz and 120 Hz for a vertical and a horizontal magnet. It is clear from the figures that both magnets are capable of changing their fields at the 120 Hz rate but not at the 960Hz rate. The sub-block slopes at 960 Hz do not match the slopes of the `hw_sum` of the event.

#### *E.3.2 Configuring for 960 Hz Operations*

The fact that the magnets are operational at 120 Hz indicates that they need to be configured to work at 960 Hz. This required time adjustments in the magnet



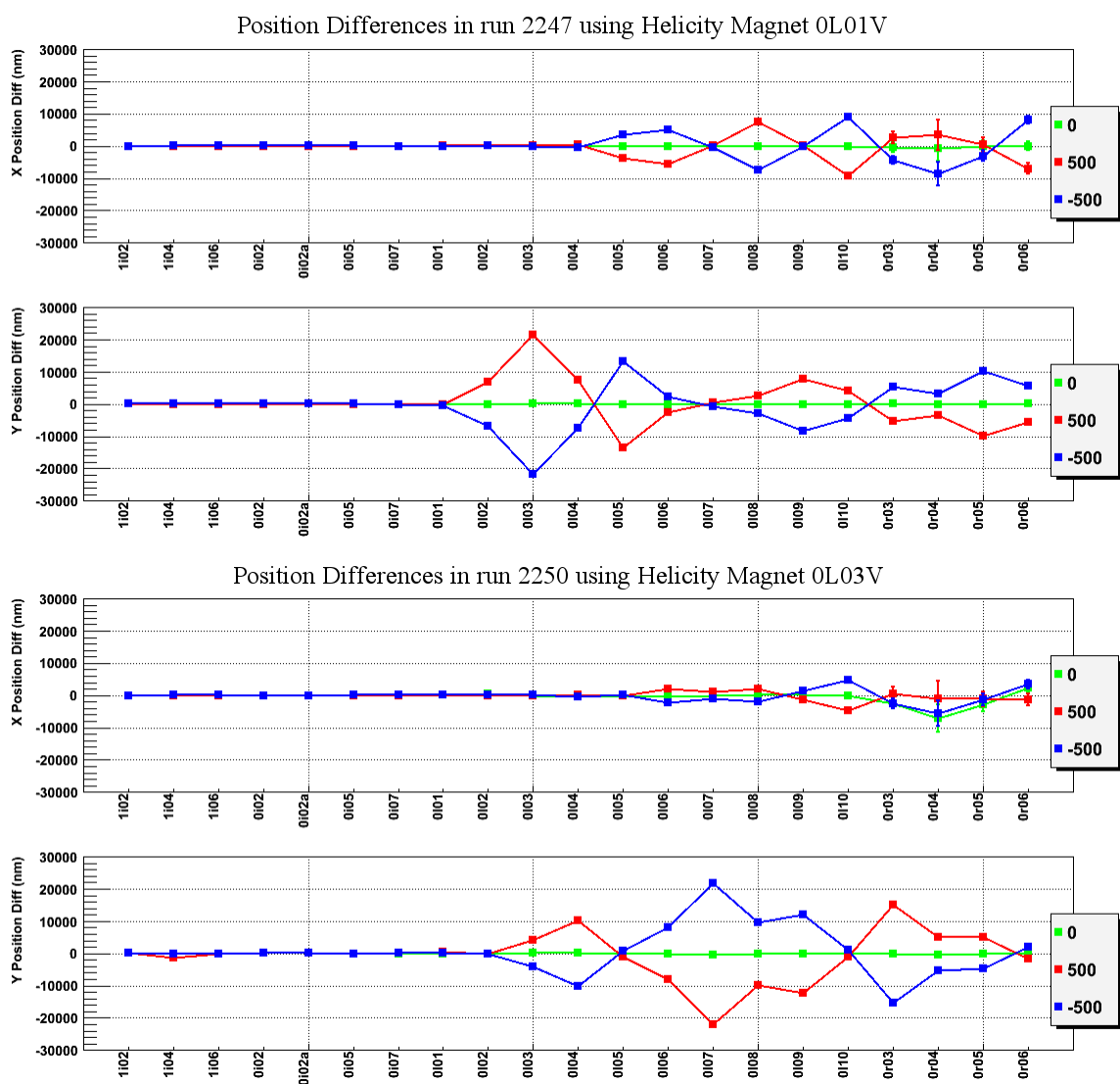


Figure E.1: Position differences induced by the vertical helicity magnets when the beam is kicked using 0L01V (top) and when the beam is kicked using 0L03V (bottom). As expected, one can see a large position differences in Y starting at the location of the magnet (0L01V/0L03V) and propagate along the beam line. In both cases we can also see a small correlation between X and Y.

voltage supply circuits. The magnet response time includes the rise time, a default delay of  $17 \mu\text{s}$  and a loop delay<sup>1</sup>. The rise time was measured to be  $2.5 \mu\text{s}$  (see Figure E.4). During the tests, the loop delay was set to 70 ( $210 \mu\text{s}$ ). So the total delay in the magnet response was about  $227 \mu\text{s}$ . Since the  $t_{\text{settle}}$  time is  $70 \mu\text{s}$  (at 960

<sup>1</sup>Processing time allowance. 1 loop delay is roughly  $3 \mu\text{s}$  [178].

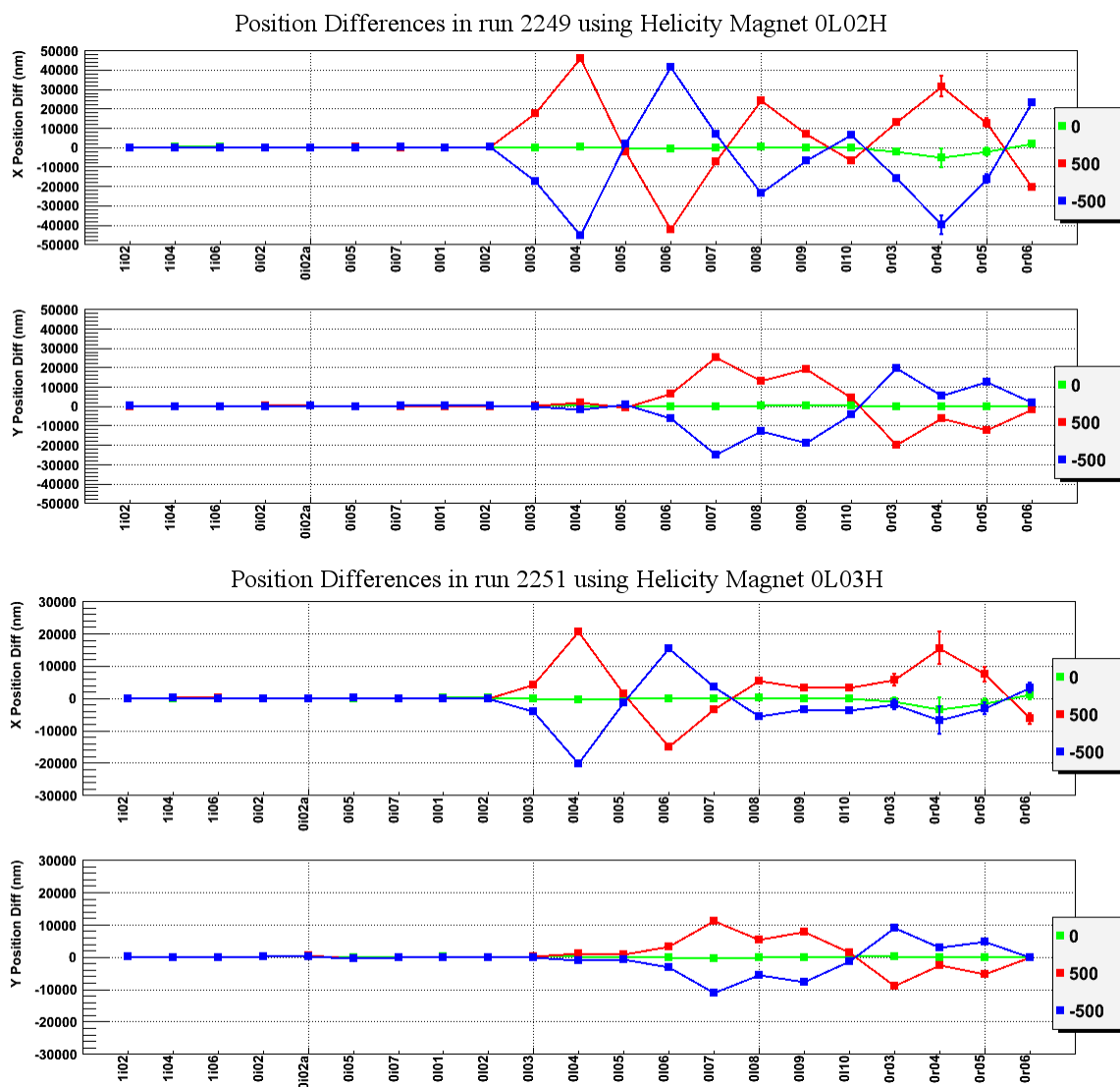


Figure E.2: Position differences induced by the horizontal helicity magnets 0L02H and 0L03H when the beam is kicked with 0L02H (top) and when the beam is kicked with 0L03H (bottom). As expected, we can see a large position differences in X starting at the location of the magnet (0L02H/0L03H) and propagate along the beam line and again in both cases we can see a small correlation between X and Y.

Hz), the magnet response was delayed by  $157 \mu\text{s}$  and it was occurring in the middle of sub-block0. To properly match the magnet response to the 960Hz rate, the loop delay needed to be set to 10 ( $30 \mu\text{s}$ ). This constrained the delay in magnet response to less than the length of  $t_{\text{settle}}$  of  $70 \mu\text{s}$  enabling their use for position feedback in  $Q_{\text{weak}}$ .

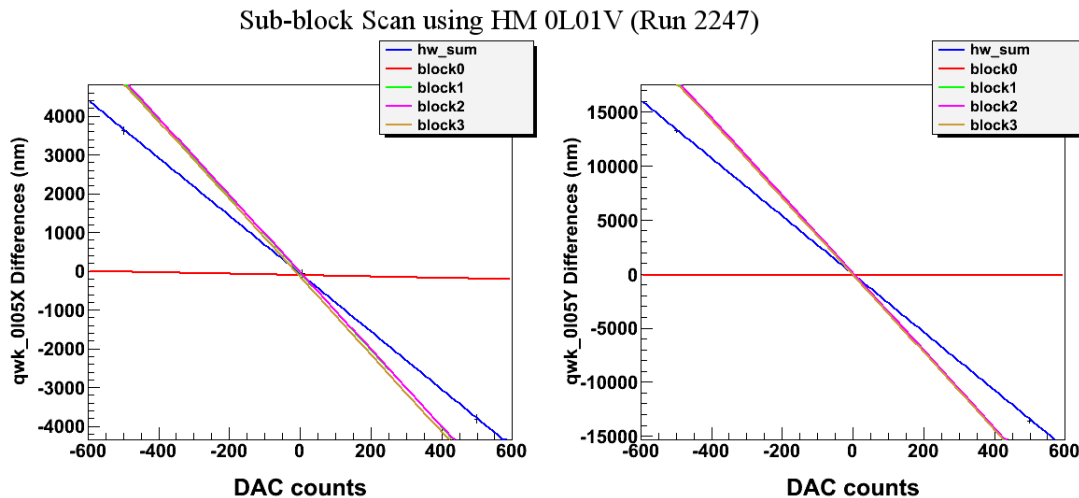


Figure E.3: Induced position differences inside sub-blocks and the hw\_sum for 0L01V helicity magnet at 960 Hz (top row) and at 120 Hz (bottom row). At 960 Hz the slopes of sub-blocks does not match slope of hw\_sum. This indicates that the response of the magnet is not exactly matched to 960 Hz rate. But at 120 Hz one can see matching slopes for sub-blocks and hw\_sum indicating the magnet is capable of switching the field at 120 Hz rate.

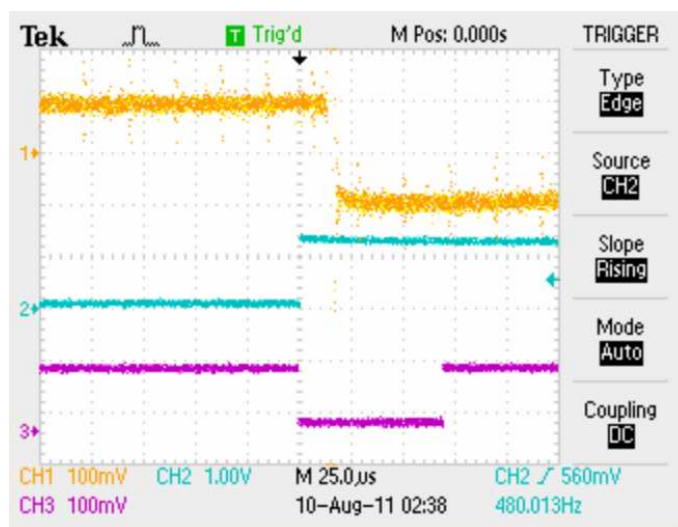


Figure E.4: Oscilloscope capture of the voltage applied to helicity magnet 0L01V (channel 1), helicity signal (channel 2) and  $t_{\text{settle}}$  (channel 3) [178]. The loop delay = 0, even DAC = 4000 and odd DAC = -4000. The magnet rise time is about  $2.5\mu\text{s}$ . Even with a 0 loop delay there is a  $17\mu\text{s}$  delay that seems to be coming from the electronics.

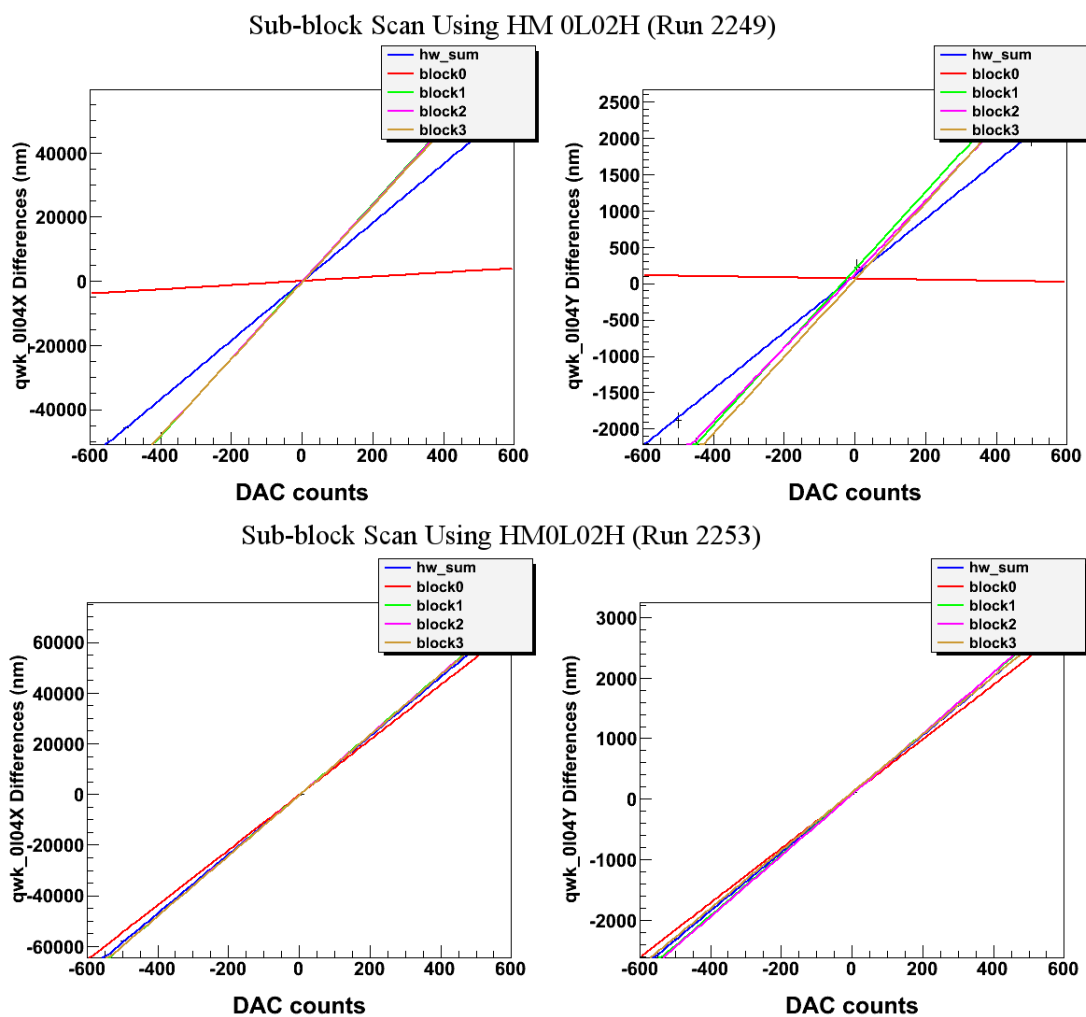


Figure E.5: Induced position differences inside sub-blocks and the hw\_sum for 0L02H helicity magnet at 960 Hz (top row) and at 120 Hz (bottom row). At 960 Hz the slopes of sub-blocks does not match slope of hw\_sum. This indicates that the response of the magnet is not exactly matched to 960 Hz rate. But at 120 Hz one can see matching slopes for sub-blocks and hw\_sum indicating the magnet is capable of switching the field at 120 Hz rate.

## F Noise Studies Misc

### F.1 The List of Hall C Patch Panel Channels Used for $Q_{\text{weak}}$ Signals and Their Channel Noise Content

After the completion of the noise tests discussed in Subsection 5.3.1, a series of separate tests was carried out to identify low noise channels in the Hall C patch panel that can be used for the Čerenkov detectors. Fifty channels were tested using an analysis identical to what was presented in subsection 5.3.1. The results of this analysis are summarized in Table F.1 with the  $Q_{\text{weak}}$  detector signals which were later used in that particular channel. Based on the standard deviation of the asymmetry distributions, 45 channels out of the 50 were identified as suitable to be used for the main detector signal chains. Channels 512, 517, 522, 527, and 542 were removed from the list due to the large amount of noise present in them.

Table F.1: Noise levels on the Hall C patch panel channels used by  $Q_{\text{weak}}$ .

Channel	Asymmetry RMS (ppm)	Assigned $Q_{\text{weak}}$ Signal
503	1.9	Lumis
504	2.1	Lumis
505	2.1	Lumis
506	1.8	Lumis
507	3.1	Lumis
508	1.9	Lumis
509	2.0	Lumis
510	1.9	Lumis
511	1.8	Lumis
512	19.9	—
513	2.1	Lumis
514	2.0	Lumis
515	2.0	Lumis
516	1.8	Lumis
517	883.1	—

Table F.1: Continued ..

Channel	Asymmetry RMS (ppm)	Assigned $Q_{\text{weak}}$ Signal
518	1.9	Lumis
519	2.1	Lumis
520	2.1	Lumis
521	1.9	Lumis
522	1826.64	—
523	2.0	Lumis
524	2.1	Lumis
525	2.1	Lumis
526	1.9	Lumis
527	1400.35	—
528	2.2	Lumis
529	2.2	PMT1 Negative
530	2.1	PMT2 Negative
531	1.9	PMT3 Negative
532	2.7	PMT4 Negative
533	1.9	PMT5 Negative
534	2.2	PMT6 Negative
535	2.1	PMT7 Negative
536	1.9	PMT8 Negative
537	3.1	Background detectors
538	2.2	Background detectors
539	2.1	Background detectors
540	2.1	Background detectors
541	1.9	Background detectors
542	17.3	—
543	2.0	Background detectors
544	2.3	Background detectors
545	2.0	PMT1 Positive
546	1.9	PMT2 Positive

Table F.1: Continued ..

Channel	Asymmetry RMS (ppm)	Assigned $Q_{\text{weak}}$ Signal
547	3.0	PMT3 Positive
548	2.0	PMT4 Positive
549	2.2	PMT5 Positive
550	1.9	PMT6 Positive
551	1.8	PMT7 Positive
552	4.6	PMT8 Positive

## F.2 Full Results from the Čerenkov Detector Electronics Chain Noise Measurements

This section contains the full set of measurements taken during the electronic noise measurements on the main detector electronics chain using the setup in figure 5.14 in subsection 5.3.1 and their results.

### F.2.1 Startup Configuration

Noise measured from the setup as it was first built (with bad cables and connections) quantified as,

$$\text{Noise} = \text{Average Signal} \times \text{Asymmetry RMS} \quad (\text{F.1})$$

#### F.2.1.1 With beam in the hall

Run number 992, 993 and 995.

Table F.2: Results from run 995. The beam in the hall was about  $2 \mu\text{A}$ .

Channel	Average Signal (V)	Asymmetry RMS (ppm)	Noise ( $\mu\text{V}$ )	Noise per root Hertz ( $\mu\text{V}/\sqrt{\text{Hz}}$ )
0 (Topward)	5.5	10.3	57.1	5.0
1 (Texico)	5.5	2.9	15.7	1.4
2 (Voltage)	8.4	4.5	38.3	3.4

**F.2.1.2 Without beam in the hall**

Run number 996 and 1003

Table F.3: Results from run 996.

Channel	Average Signal (V)	Asymmetry RMS (ppm)	Noise ( $\mu V$ )	Noise per root Hertz ( $\mu V/\sqrt{Hz}$ )
0 (Topward)	5.5	9.8	53.8	4.7
1 (Texico)	5.5	3.1	16.8	1.5
2 (Voltage)	8.4	4.7	39.1	3.4

**F.2.2 Configuration with the Power Supplies Switched Between the Preamplifiers**

Switched the powers supplies at the preamplifier inputs.

Table F.4: Results from run 1000. No beam.

Channel	Average Signal (V)	Asymmetry RMS (ppm)	Noise ( $\mu V$ )	Noise per root Hertz ( $\mu V/\sqrt{Hz}$ )
0 (Texico)	5.5	6.4	34.6	3.0
1 (Topward)	5.5	3.8	20.9	1.8
2 (Voltage)	8.1	4.1	33.4	2.9

Switching the power supplies showed the large noise seen in channel 0 drop down to about 6 ppm from the 10 ppm seen in the previous section. However, this run was taken a week later after run 996 and 995. So it could have been due to a change in the environment in the hall (decrease in the use of machinery used for the commissioning of  $Q_{\text{weak}}$  etc). Run 1003 taken with the voltage source connected to channel 0 further proves this observation. The contribution from the power supplies to the noise are therefore negligible (i.e. well below 1 ppm).



Table F.5: Results from run 1003. No beam. The noise in channel 0 is now small.

Channel	Average Signal (V)	Asymmetry RMS (ppm)	Noise ( $\mu V$ )	Noise per root Hertz ( $\mu V/\sqrt{Hz}$ )
0 (Voltage)	7.9	5.1	40.3	3.5
1 (Topward)	5.5	3.7	20.3	1.8
2 (Texico)	5.5	8.9	48.7	4.3

### *F.2.3 Configuration with the Preamplifiers Switched Between Chain 1 and Chain 2*

Run 1030 was taking after switching the preamplifiers between electronics chain 1 and chain 2 (see Figure 5.14).

Table F.6: Results from run 1030. No beam. Preamp 1 is in chain 2 with the Texico power supply. Chain 1 now has the preamp 2.

Channel	Average Signal (V)	Asymmetry RMS (ppm)	Noise ( $\mu V$ )	Noise per root Hertz ( $\mu V/\sqrt{Hz}$ )
0 (Preamp 2)	5.4	7.2	39.4	3.4
1 (Preamp 1)	5.5	3.6	19.8	1.7
2 (Voltage)	7.9	3.2	25.4	2.2

The noise levels in Table F.6 are comparable to what is shown in Table F.4. The fact that the noise per root Hertz observed in the three channels are relatively constant implies the dominant source of noise should be in the coaxial cables. With about  $1\mu V/\sqrt{Hz}$  noise from the ADC channels, the noise content in the cables must be in the order of 1-2  $1\mu V/\sqrt{Hz}$ .

## G Transverse Data Analysis Misc

### G.1 IHWP Reversal and Slug Numbers

Table G.1 shows the amount of data collected in each IHWP reversal state. Table G.2 shows the slug numbers assigned for each of the different slugs.

Table G.1: Durations of the IHWP reversals in the transverse data set.

Target	Pol.	QTOR (A)	Current ( $\mu$ A)	(1IN,2OUT) (hrs)	(1OUT,2OUT) (hrs)	Total (hrs)
LH2-cell	Horizontal	8901	180	10	9.25	$\approx 20$
LH2-cell	"	6700	180	2	2	4
LH2-cell	"	7300	180	0.5	2	2.5
LH2-cell	"	6000	180	1.5	1.5	3
4% DS Al	"	8901	60	2	2	4
4% DS Al	"	6700	60	2	2	4
4% DS Al	"	7300	60	1.5	1.5	3
1.6% DS C	"	8901	70	1.5	1.5	3
1.6% DS C	"	6700	70	1.5	1.5	3

Table G.2: Slug numbers assigned for the transverse data set.

Target	Slug Numbers	
	T_Run I (hrs)	T_Run II (hrs)
LH2-cell (elastic)	100001 - 100006	100007 - 100009 200001 - 200010
DS4Al (elastic)	101001 - 101002	101003 - 101004 201001 - 201002
C12 (elastic)	–	203001 - 203002
LH2-cell (inelastic)	–	600001 - 600002 700001 - 700002
DS4Al (inelastic)	–	601001 - 601002 701001 - 701002
C12 (inelastic)	–	703001 - 703002

## G.2 Beam Parameters

Additional Figures relevant to the discussion in Subsection 6.4.1.

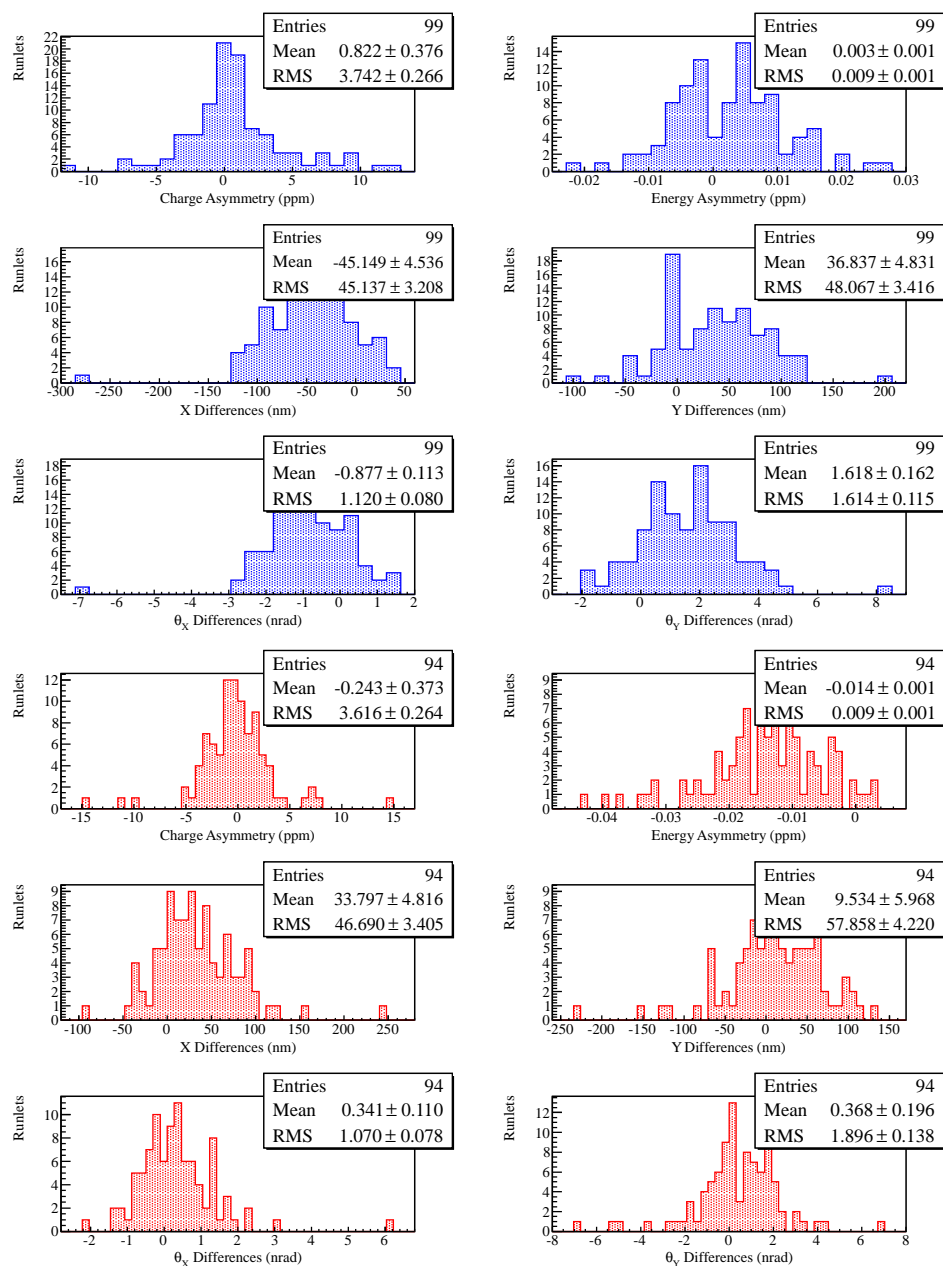


Figure G.1: Runlet distributions of the beam parameters measured during horizontal transverse running in Transverse\_Run I. IHWP IN (OUT) data are shown in blue (red).

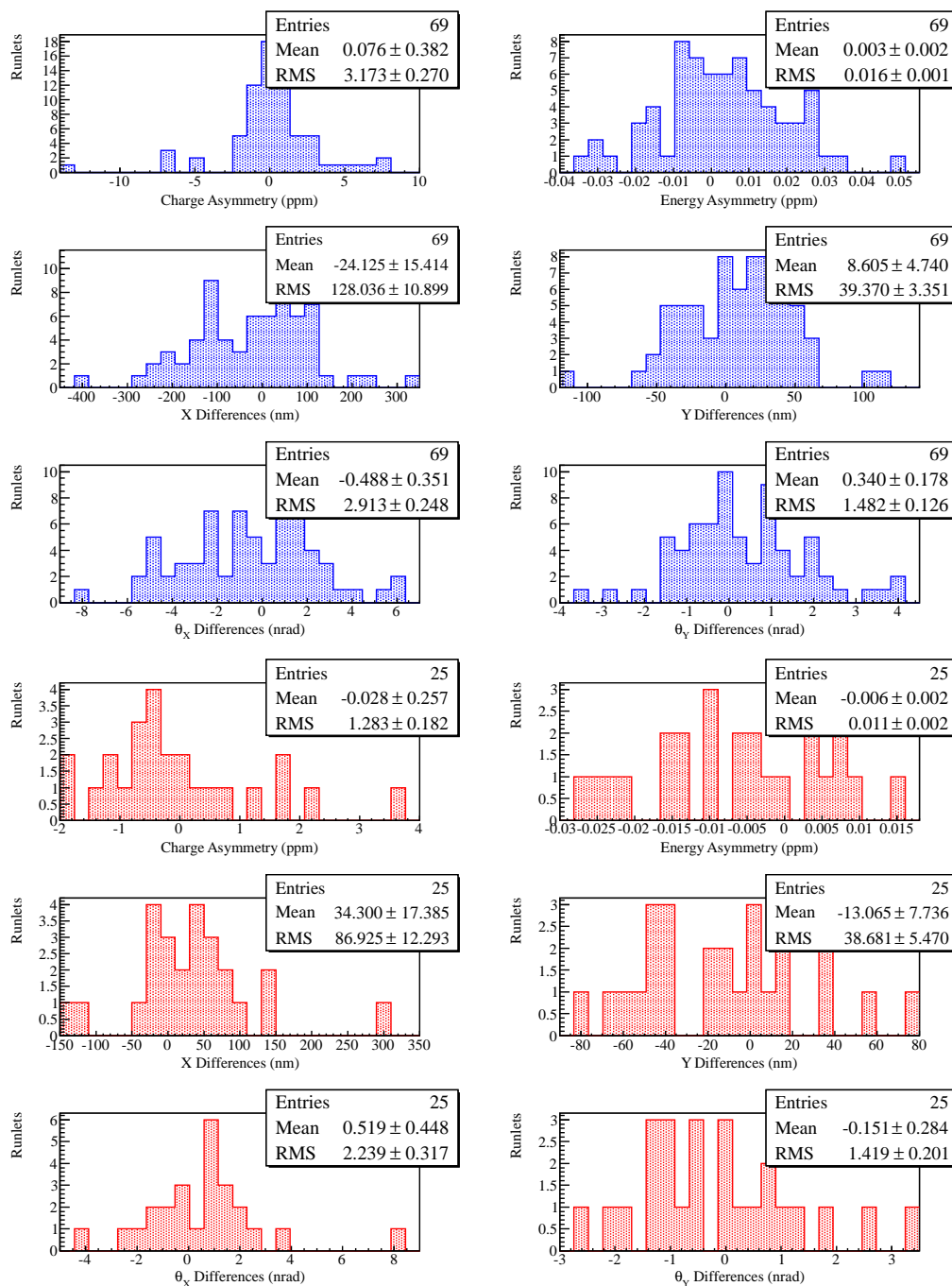


Figure G.2: Runlet distributions of the beam parameters measured during vertical transverse running in Transverse\_Run II. Each runlet contains the average measurement over a 5 min long time interval. IHPW IN (OUT) data are shown in blue (red).

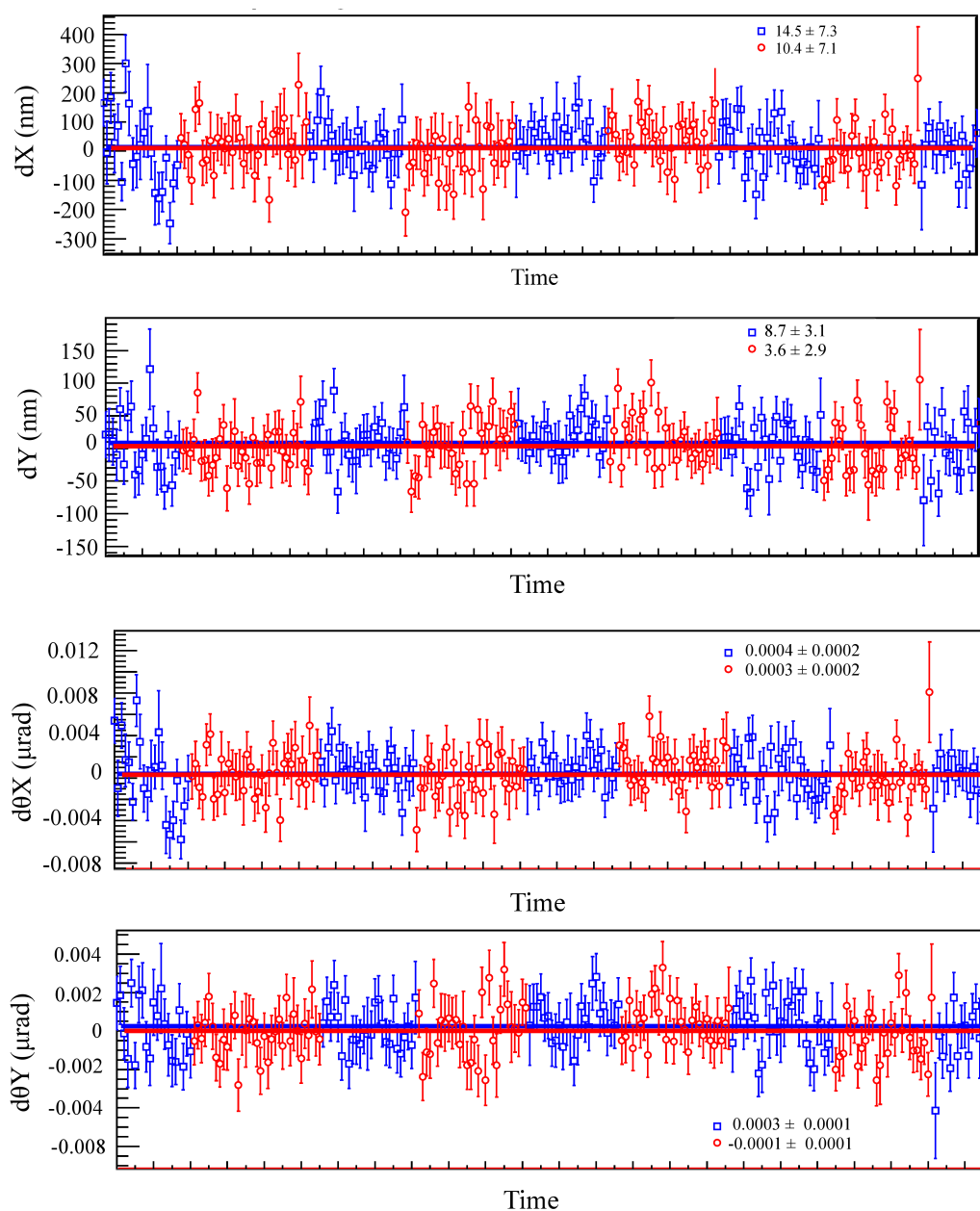


Figure G.3: Typical helicity correlated position and angle differences measured at the  $Q_{\text{weak}}$  target during transverse running. Each data point represents the average over a 5 min time period (a runlet). Red (blue) shows data with IHWP OUT (IN) periods each about 2 hours long. The printed values are from the constant fits over the two IHWP settings. This data set is from the LH2-cell target with horizontal transverse polarization in Run II.

### G.3 Detector Sensitivity to Beam Parameters

The detector sensitivities measured in the horizontal LH2-cell transverse data set are shown in Table G.3. Figures G.5 and G.4 show the detector sensitivity plots from the rest of the transverse data sets after what was shown in Subsection 6.4.2.

Table G.3: Detector sensitivities to the beam parameters from the horizontal LH2-cell transverse data set. The errors are statistical.

MD	$\frac{\partial A}{\partial X}$ ppm/ $\mu\text{m}$	$\frac{\partial A}{\partial Y}$ ppm/ $\mu\text{m}$	$\frac{\partial A}{\partial \theta_X}$ ppm/ $\mu\text{rad}$	$\frac{\partial A}{\partial \theta_Y}$ ppm/ $\mu\text{rad}$	$\frac{\partial A}{\partial A_E}$ ppm/ppm
1	$-8.47 \pm 0.03$	$-0.02 \pm 0.03$	$92.78 \pm 0.94$	$-2.35 \pm 0.78$	$-7.26 \pm 0.09$
2	$-5.98 \pm 0.03$	$2.02 \pm 0.03$	$62.63 \pm 0.94$	$-23.09 \pm 0.78$	$-4.65 \pm 0.09$
3	$2.04 \pm 0.03$	$2.71 \pm 0.03$	$-18.00 \pm 0.90$	$-29.04 \pm 0.74$	$-4.20 \pm 0.09$
4	$7.18 \pm 0.03$	$1.45 \pm 0.03$	$-67.57 \pm 0.91$	$-11.85 \pm 0.75$	$-5.03 \pm 0.09$
5	$8.71 \pm 0.03$	$0.11 \pm 0.03$	$-80.48 \pm 0.91$	$0.74 \pm 0.75$	$-4.78 \pm 0.09$
6	$4.76 \pm 0.03$	$-1.36 \pm 0.03$	$-37.63 \pm 0.89$	$14.38 \pm 0.74$	$-6.09 \pm 0.08$
7	$-1.17 \pm 0.03$	$-2.47 \pm 0.03$	$23.50 \pm 0.89$	$27.09 \pm 0.73$	$-6.21 \pm 0.08$
8	$-7.43 \pm 0.03$	$-1.92 \pm 0.03$	$85.45 \pm 0.88$	$19.74 \pm 0.73$	$-6.48 \pm 0.08$

### G.4 Beam Asymmetry Correction

Supplement tables from the discussion in Subsection 6.4.3. Beam asymmetry corrections (see Table G.6) are estimated by taking the average beam parameters (see Table G.4) and detector sensitivities (see Table G.5) and multiplying them.

Table G.4: Average HCBA measured in slug 200005.

Beam Parameter	Value
dX (nm)	$36.99 \pm 15.57$
dY (nm)	$19.09 \pm 6.48$
d $\theta_X$ (nrad)	$0.89 \pm 0.41$
d $\theta_Y$ (nrad)	$0.61 \pm 0.25$
A <sub>E</sub> (ppb)	$-3.40 \pm 1.69$

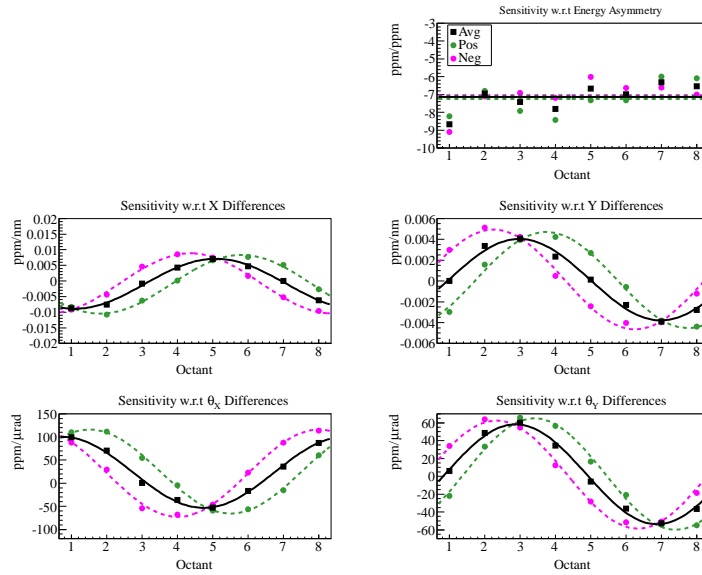


Figure G.4: Detector sensitivities in vertical transverse running period in Transverse\_Run I.

Table G.5: Average detector sensitivities measured in slug 200005.

MD	Sensitivity				
	dX (ppm/nm)	dY (ppm/nm)	d $\theta_X$ (ppm/ $\mu$ rad)	d $\theta_Y$ (ppm/ $\mu$ rad)	$A_E$ (ppm/ppm)
1	-0.009	0.000	94.592	-6.213	-8.175
2	-0.006	0.002	67.446	-19.359	-5.134
3	0.002	0.003	-19.467	-26.755	-3.705
4	0.007	0.002	-74.262	-13.178	-4.246
5	0.009	0.000	-78.468	0.638	-4.678
6	0.005	-0.001	-35.907	10.391	-5.998
7	-0.001	-0.002	20.789	26.305	-6.520
8	-0.008	-0.002	91.547	16.827	-7.231

Using the measured HCBA and the detector sensitivities, the individual beam asymmetry corrections can be calculated as

$$\text{Beam asymmetry correction} = \text{HCBA} \times \text{Sensitivity} \quad (\text{G.1})$$

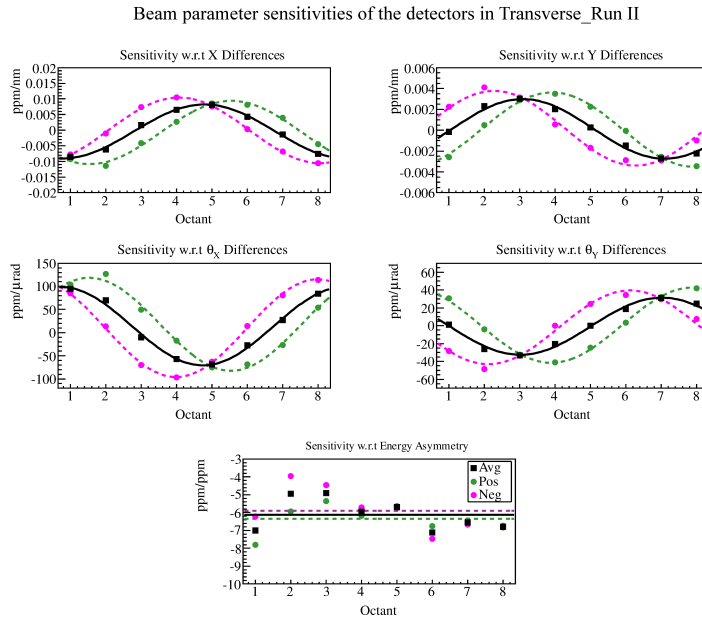


Figure G.5: Detector sensitivities in vertical transverse running period in Transverse\_Run II.

Table G.6: Beam asymmetry corrections applied on raw asymmetries in slug 200005 using HCBA in table G.4 and sensitivities in table G.5. Correction = HCBA  $\times$  sensitivity.

MD	Correction (ppm)					Total
	dX	dY	$d\theta_X$	$d\theta_Y$	$A_E$	
1	-0.32	0.00	0.08	0.00	0.03	-0.21
2	-0.23	0.04	0.06	-0.01	0.02	-0.13
3	0.08	0.05	-0.02	-0.02	0.01	0.11
4	0.27	0.03	-0.07	-0.01	0.01	0.24
5	0.32	0.00	-0.07	0.00	0.02	0.27
6	0.18	-0.02	-0.03	0.01	0.02	0.15
7	-0.04	-0.05	0.02	0.02	0.02	-0.03
8	-0.28	-0.03	0.08	0.01	0.02	-0.20



## G.5 Aluminum Background Analysis

Additional Figures from the analysis in Subsection 6.6.2.1.

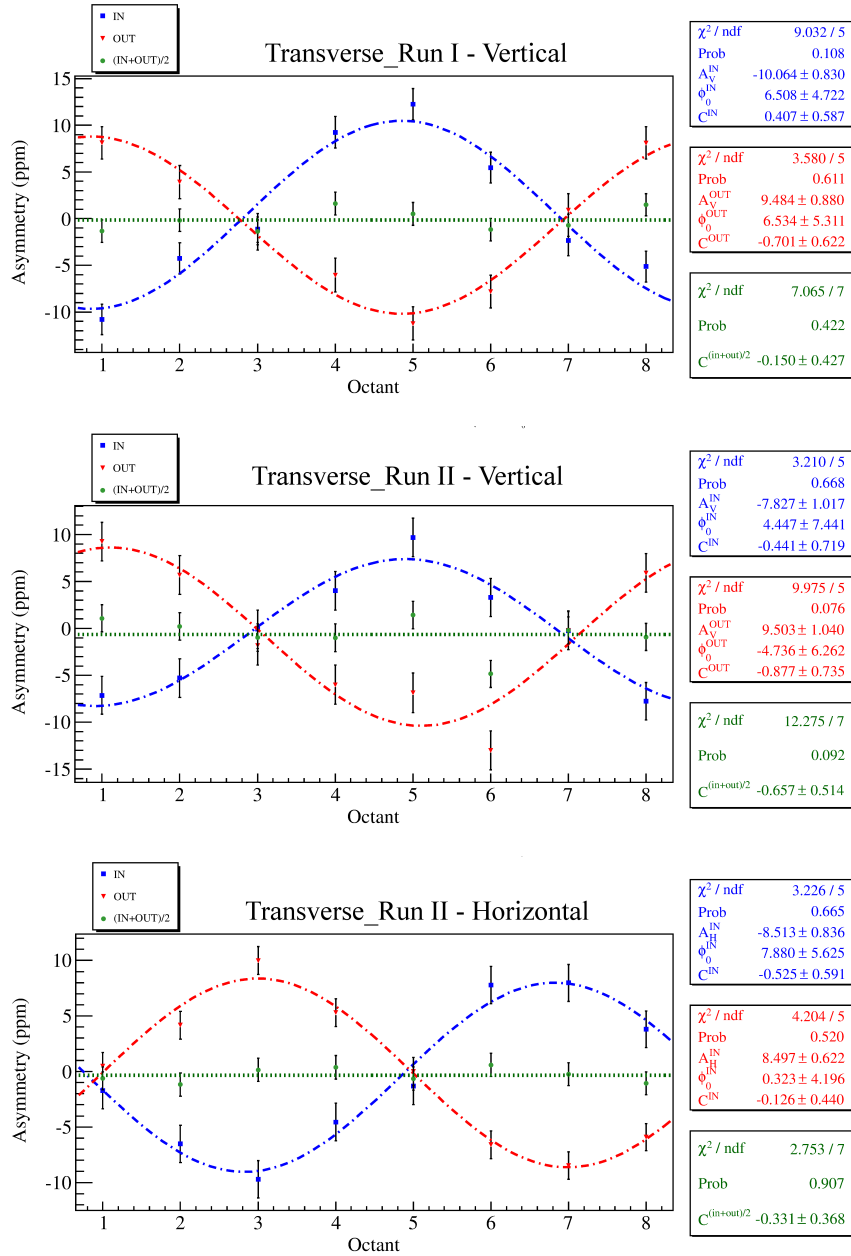
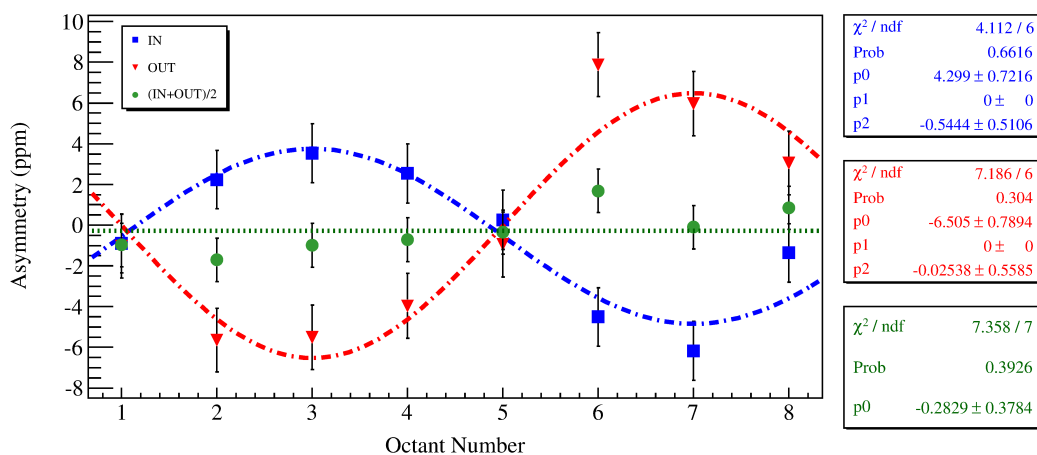


Figure G.6:  $(\text{IN}+\text{OUT})/2$  of the five-parameter regressed asymmetries from the full DS4Al data set. The azimuthal modulating asymmetry flips sign with the insertion of the IHWP as expected. The  $(\text{IN}+\text{OUT})/2$  given by the  $C^{(\text{In}+\text{Out})/2}$  are compatible with zero.

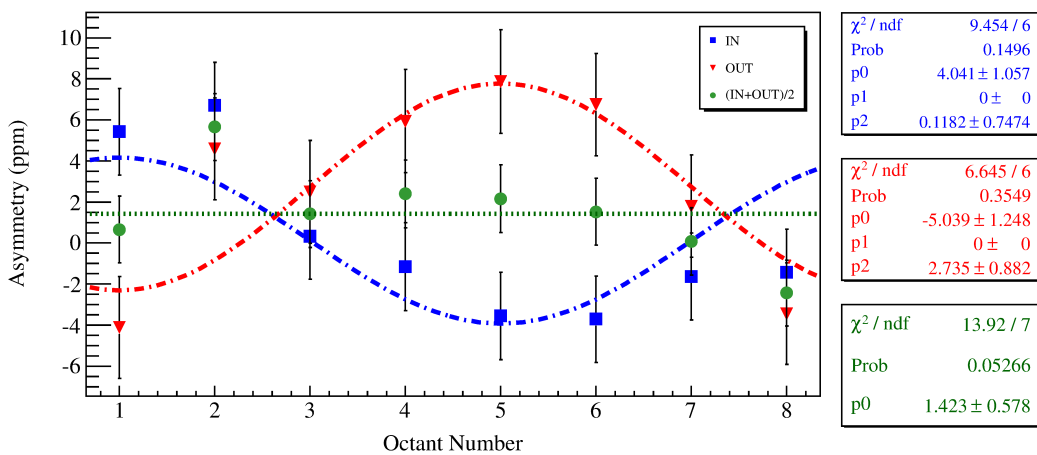
## G.6 Inelastic Background Analysis

Supplementary figures and analysis relevant to determining the inelastic background correction in Subsection 6.6.2.2.

### G.6.1 Inelastic LH2-cell Asymmetry



(a) Horizontal.

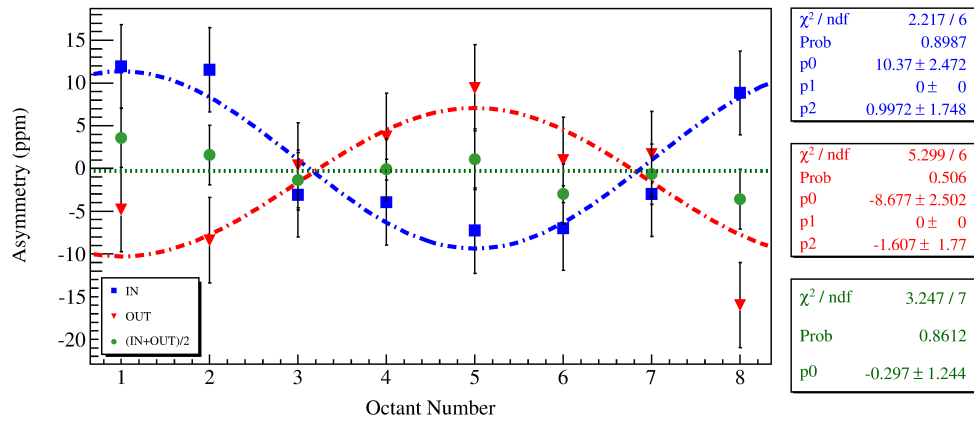


(b) Vertical.

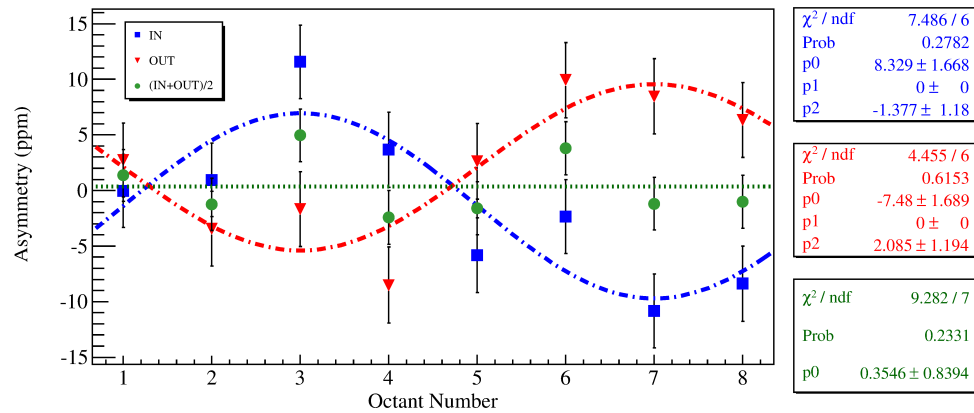
Figure G.7:  $(IN+OUT)/2$  of the inelastic LH2-cell asymmetry. The constants  $C^{(In+Out)/2}$  are consistent with zero.

### G.6.2 Inelastic Aluminum Asymmetry

Figures and tables relevant to the inelastic asymmetry extraction from the DS4Al target from the discussion in Subsection 6.6.2.2. The IHWP cancellation are shown in Figure G.8 and the fits over the AVG(IN-OUT) asymmetries are shown in Figure G.9. Results from both figures are summarized in Table G.7.



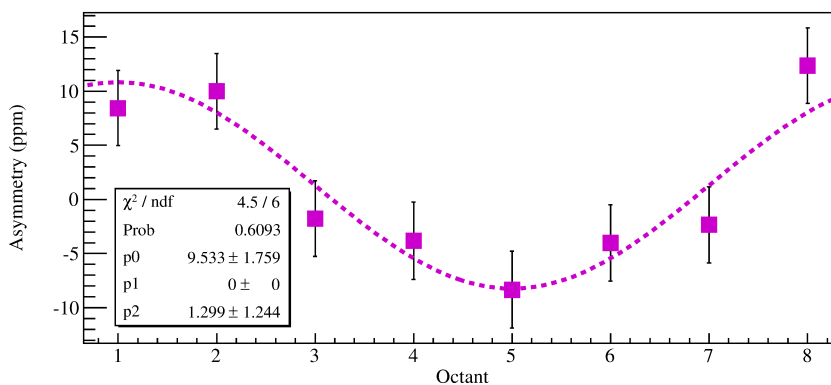
(a) Vertical



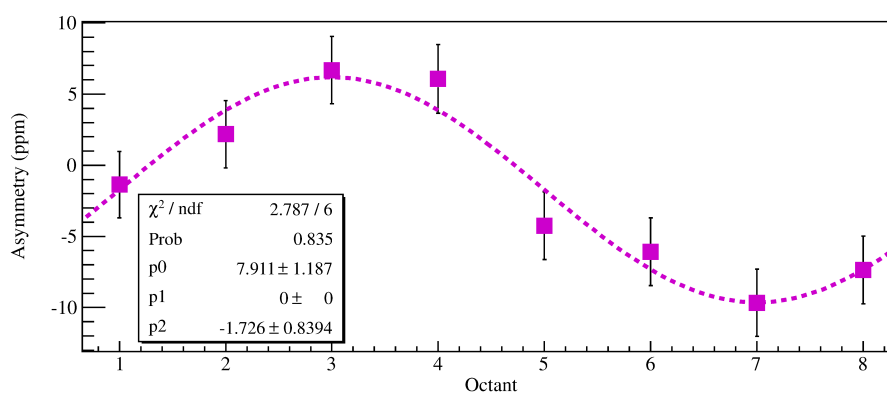
(b) Horizontal

Figure G.8: IHWP cancellation of the inelastic asymmetry from aluminum target. The constant fit  $C^{(In+Out)/2}$  over both data sets are consistent with zero.

The average physics asymmetry from Table G.7 needs to be corrected for the 0.9938 acceptance averaging of the detectors and an additional systematic uncertainty of  $0.04A_{Al}^{Phys}$  needs to be assigned for the system non-linearity. With the acceptance



(a) Vertical



(b) Horizontal

Figure G.9: Inelastic asymmetry extracted from the aluminum target. The asymmetry has a opposite sign to the elastic asymmetry.

Table G.7: Inelastic asymmetry extracted from the DS4Al target. The values are from the fits shown in Figures G.8 and Figure G.9. Both data sets have  $(\text{IN}+\text{OUT})/2$  consistent with zero. Due to similar kinematics, the physics asymmetry for the full data set is the average of the physics asymmetries from the two data sets.

Polarization	$(\text{IN}+\text{OUT})/2$ (ppm)	AVG(IN,-OUT) (ppm)
Vertical	$0.847 \pm 1.758$	$9.533 \pm 1.759$
Horizontal	$0.425 \pm 1.187$	$7.911 \pm 1.187$
Error weighted average		$8.419 \pm 0.984$

correction and the additional systematics, the inelastic physics asymmetry from the DS4Al target is

$$A_{Al}^{Phys} = 8.472 \pm 0.984_{Stat} \pm 0.338_{Sys} \text{ ppm} \quad (\text{G.2})$$

The DS4Al asymmetry is then corrected for the 20% difference between the upstream and downstream target windows (see Subsection 6.6.2.1) resulting in an inelastic aluminum physics asymmetry of  $8.024 \pm 1.011$  ppm. With the correction for the beam polarization in Transverse\_Run II  $P = 0.8778 \pm 0.0099$ , the effective inelastic aluminum asymmetry is

$$A_{Al}^{ie} = \frac{A_{Al}^{Phys}}{P} = \frac{8.478}{0.8778} = 9.141 \pm 1.156 \text{ ppm} \quad (\text{G.3})$$

where the associated error was estimated from Equation G.9.

### G.7 $Q^2$ Dependence of the Measured Asymmetry

Following the discussion in Subsection 6.6.3.1, Table G.8 shows the simulated light-weighted  $Q^2$  from Ref. [160] and the associated changes induced in the measured beam normal single spin asymmetry according to

$$\frac{dB_n}{B_n} = \frac{d(Q^2)}{2Q^2}. \quad (\text{G.4})$$

### G.8 Regression Scheme Dependence Study

Tables G.9 and G.10 contains the values plotted in Figure 6.11 on Subsection 6.5.2.

Table G.8: Relative changes expected in the measured beam normal single spin asymmetry due to changes in the light weighted  $Q^2$  in the detectors. Octants 2 and 4 are removed from the analysis due to having unrealistic simulated  $Q^2$  caused by the presence of the horizontal drift chambers. The average momentum of  $0.0251 \text{ (GeV/c)}^2$  (excluding octants 2 and 4) was used to estimate the momentum deviations in each of the Čerenkov detectors and Equation G.4. On average, the beam normal single spin asymmetry in each octant changes by a 0.09% from the asymmetry expected for the average  $Q^2$ .

Octant	$Q^2$	dB/B
1	$0.025147 \pm 0.000072$	0.0005
3	$0.025222 \pm 0.000071$	0.0020
5	$0.025100 \pm 0.000071$	-0.0004
6	$0.025093 \pm 0.000073$	-0.0006
7	$0.025074 \pm 0.000072$	-0.0009
8	$0.025091 \pm 0.000072$	-0.0006
Average	0.025121	

Table G.9: Regression corrections applied on the regressed LH2-cell asymmetries from Transverse\_Run I vertical transverse running period.

MD	Off-on	Off-on_5+1	off-on_set3	off-on_set7	off-on_set8
md1	0.27	0.18	0.18	0.28	0.22
md2	0.25	0.28	0.28	0.25	0.20
md3	0.05	0.04	0.04	0.04	0.01
md4	-0.15	-0.19	-0.19	-0.21	-0.21
md5	-0.29	-0.29	-0.29	-0.36	-0.30
md6	-0.26	-0.27	-0.27	-0.26	-0.27
md7	-0.15	-0.16	-0.16	-0.13	-0.14
md8	0.07	0.08	0.08	0.06	0.06

Table G.10: Regression corrections applied on the regressed LH2-cell asymmetries from Transverse\_Run II horizontal transverse running period.

MD	Off-on	Off-on_5+1	off-on_set3	off-on_set7	off-on_set8
md1	-0.017	-0.016	-0.016	-0.014	-0.011
md2	0.049	0.018	0.018	0.032	0.037
md3	-0.022	0.024	0.024	0.001	-0.019
md4	-0.006	-0.007	-0.007	0.026	0.009
md5	0.009	0.010	0.010	0.008	0.009
md6	-0.015	0.003	0.003	0.001	0.004
md7	0.035	0.035	0.035	0.012	0.035
md8	0.013	-0.001	-0.001	-0.005	-0.018

## G.9 Error Analysis

### *G.9.1 General Error Analysis of a Physics Asymmetry Corrected with Two Backgrounds and Polarization*

$$A = R \left[ \frac{\left( \frac{A^{Phy}}{P} \right) - A_{B1}f_{B1} - A_{B2}f_{B2}}{1 - f_{B1} - f_{B2}} \right]. \quad (G.5)$$

Error propagation on Equation G.5 yields

$$\begin{aligned}
 dA^2 = & \left( \frac{\partial A}{\partial A^{Phy}} \right)^2 (dA^{Phy})^2 + \left( \frac{\partial A}{\partial P} \right)^2 (dP)^2 + \left( \frac{\partial A}{\partial R} \right)^2 (dR)^2 \\
 & + \left( \frac{\partial A}{\partial A_{B1}} \right)^2 (dA_{B1})^2 + \left( \frac{\partial A}{\partial A_{B2}} \right)^2 (dA_{B2})^2 \\
 & + \left( \frac{\partial A}{\partial f_{B1}} \right)^2 (df_{B1})^2 + \left( \frac{\partial A}{\partial f_{B2}} \right)^2 (df_{B2})^2,
 \end{aligned} \tag{G.6}$$

with

$$\begin{aligned}
 \frac{\partial A}{\partial A^{Phy}} &= \frac{R}{P(1 - f_{B1} - f_{B2})}, \\
 \frac{\partial A}{\partial P} &= \frac{-RA^{Phy}}{P^2(1 - f_{B1} - f_{B2})}, \\
 \frac{\partial A}{\partial R} &= \frac{A}{R}, \\
 \frac{\partial A}{\partial A_{B1}} &= \frac{-Rf_{B1}}{(1 - f_{B1} - f_{B2})}, \\
 \frac{\partial A}{\partial A_{B2}} &= \frac{-Rf_{B2}}{(1 - f_{B1} - f_{B2})}, \\
 \frac{\partial A}{\partial f_{B1}} &= \frac{R(f_{B2} - 1)A_{B1}}{(1 - f_{B1} - f_{B2})^2}, \\
 \frac{\partial A}{\partial f_{B2}} &= \frac{R(f_{B1} - 1)A_{B2}}{(1 - f_{B1} - f_{B2})^2}.
 \end{aligned} \tag{G.7}$$

### G.9.2 Aluminum Background

The total error on  $A_{DS4Al}^{Phys}$  is estimated using a 50% uncertainty on the acceptance correction and 0.04 non-linearity as:

$$\text{Weighted aluminum asymmetry} = -8.929 \pm 0.340 \text{ ppm}$$

$$\text{Error on the acceptance correction} = (-8.929 + 8.985) \times 0.5 = \pm 0.028 \text{ ppm}$$

$$\text{Error on non-linearity} = -8.929 \times 0.04 = \pm 0.358 \text{ ppm}$$

$$\text{Total Error } dA_{DS4Al}^{Phys} = \sqrt{0.34^2 + 0.028^2 + 0.357^2} = \pm 0.494 \text{ ppm}$$



The error on the correction applied for the acceptance difference in the upstream and downstream target windows is estimated as:

$$\text{Error on the acceptance difference correction} = \pm 0.237 \text{ ppm}$$

$$\text{Statistical error} = dA_{DS4Al}^{Phys} * (1 + \sqrt{0.8})/2 = \pm 0.468 \text{ ppm}$$

$$dA_{Al}^{Phys} = \sqrt{0.468^2 + 0.237^2} = \pm 0.525 \text{ ppm}$$

The error on the polarization corrected aluminum asymmetry is then

$$A_{Al}^e = \frac{A_{Al}^{Phys}}{P_{Beam}}, \quad (\text{G.8})$$

$$d(A_{Al}^e)^2 = \left( \frac{1}{P_{Beam}} d(A_{Al}^{Phys}) \right)^2 + \left( \frac{A_{Al}^e}{P_{Beam}} dP_{Beam} \right)^2, \quad (\text{G.9})$$

$$P_{Beam} = 0.8804 \pm 0.0087,$$

$$d(A_{Al}^{Phys}) = \pm 0.525 \text{ ppm},$$

$$A_{Al}^e = -9.667 \text{ ppm},$$

$$\implies dA_{Al}^e = \pm 0.603 \text{ ppm}.$$

## H BNSSA Leakage Analysis Misc

### H.1 Correlations Between Azimuthal Dependence of the Regressed Asymmetries and Helicity Correlated Beam Asymmetries

In the presence of large helicity correlated position differences, fitting over regressed Čerenkov detector asymmetries does not necessarily provide information about the amount of residual transverse polarization in the beam. This is a known issue in the regression which is currently being investigated. But here I will summarize its effect on the estimation of residual transverse polarization in the beam.

This analysis uses five-parameter and charge regressed<sup>1</sup> asymmetries from Wien 1 to 5. Consecutive IHWP IN and OUT slugs were used to calculate the physics asymmetry and the fit in Equation 6.1 was used to extract the vertical, horizontal transverse components and the leakage term C. The correlation between the values extracted as vertical and horizontal transverse polarization on the helicity correlated beam position, angle differences and energy asymmetry<sup>2</sup> are then drawn to check for residual correlations as shown in Figures H.1, H.2, H.3, H.4 H.5 and H.6.

From Figures H.1, H.2, H.3, H.4, H.5 and H.5 one can see that the correlation between the HCBA and the residual transverse polarization extracted from azimuthal fits are not always zero except for the charge asymmetry. There certainly is a correlation between large position, angle and energy differences and the extracted residual transverse polarization. Since some properties in the beam, like double peaking in the position difference distributions can cause large position differences which are hard to remove using regression, they can be mistaken for residual transverse polarization. This poses a problem for using Čerenkov detectors to extract residual transverse polarization in the beam in the presence of large position and angle differences.

---

<sup>1</sup>The charge regression was chosen in this case to remove the charge non-linearity in the detectors.

<sup>2</sup>The beam differences and asymmetries in each slug pair was corrected for the IHWP reversal.

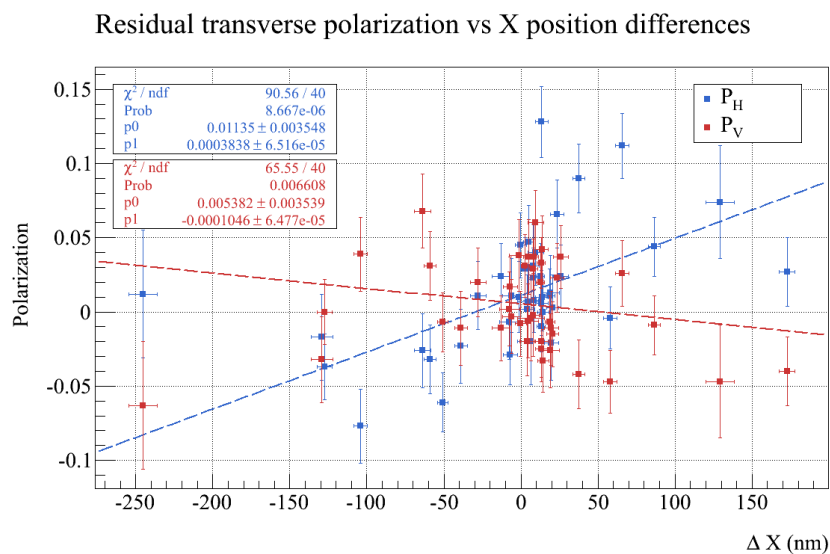


Figure H.1: Correlations between horizontal (X) position differences and the residual transverse polarization in Wien 1-5. Each data point represents a data from a slug pair. The correlations with the horizontal component is non-zero. This indicates that the azimuthal modulation is caused by left over false asymmetries from position differences.

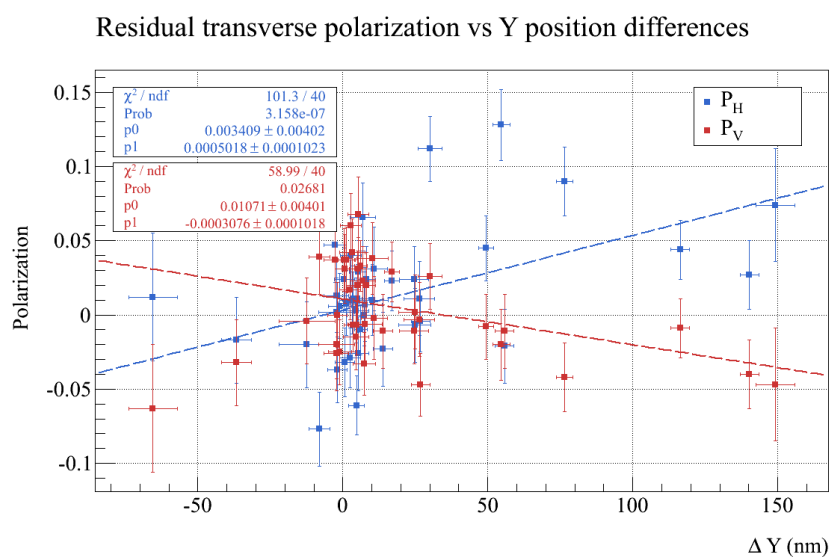


Figure H.2: Correlations between vertical (Y) position differences and the residual transverse polarization in Wien 1-5. Each data point represents data from a slug pair. In this case, the correlations with both horizontal and vertical residual transverse polarization are non-zero.

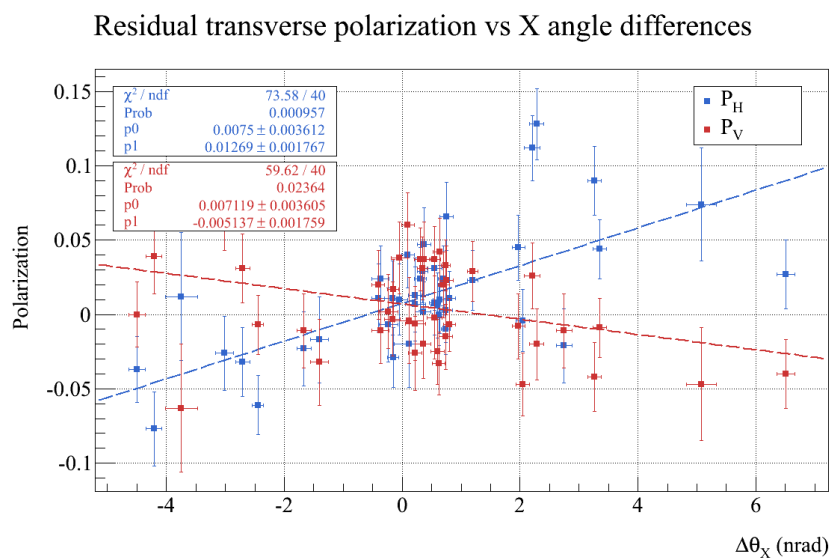


Figure H.3: Correlations between horizontal angle differences and the residual transverse polarization in Wien 1-5. Each data point represents a slug pair. The correlations with both horizontal and vertical transverse polarization are non-zero.

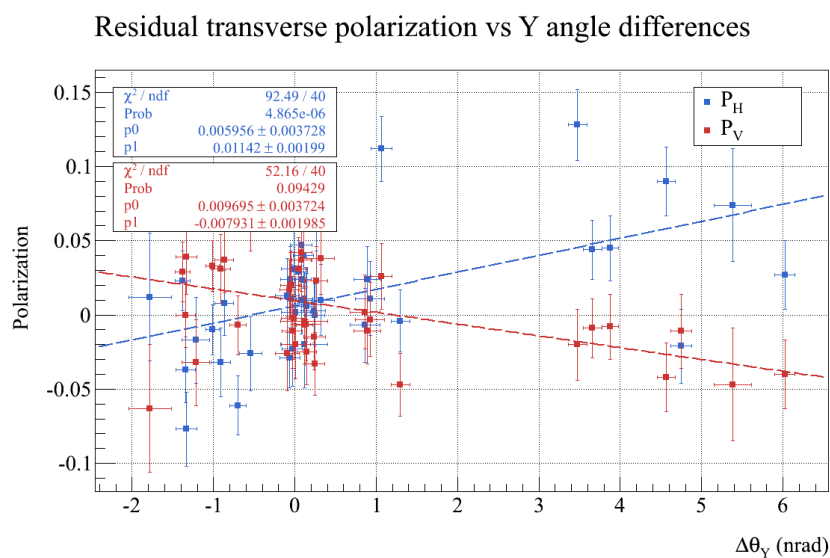


Figure H.4: Correlations between vertical angle differences and the residual transverse polarization in Wien 1-5. Each data point represents a slug pair. The correlations with both horizontal and vertical residual transverse polarization are non-zero.

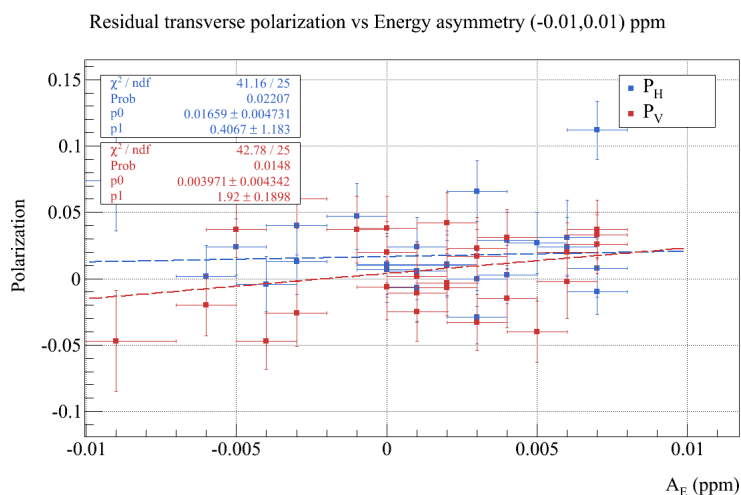


Figure H.5: Correlations between energy asymmetry and the residual transverse polarization in Wien 1-5. Each data point represents a slug pair. The correlations with the horizontal residual transverse components are non-zero. Since energy differences are governed by X position differences, this is an effect of X differences rather than actual beam energy.

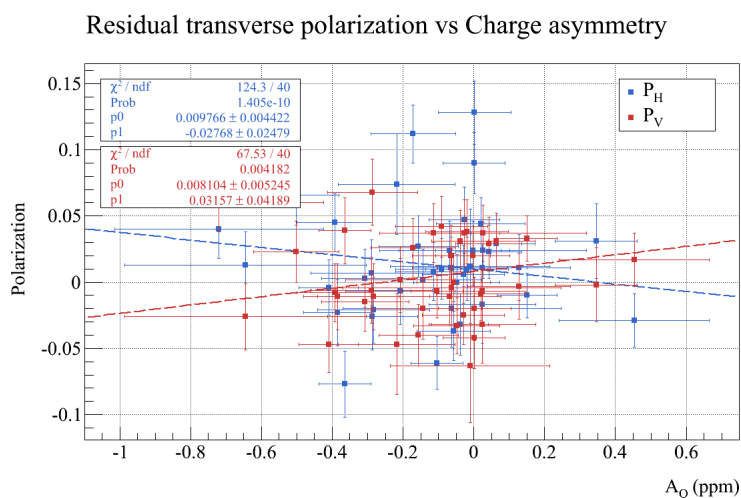
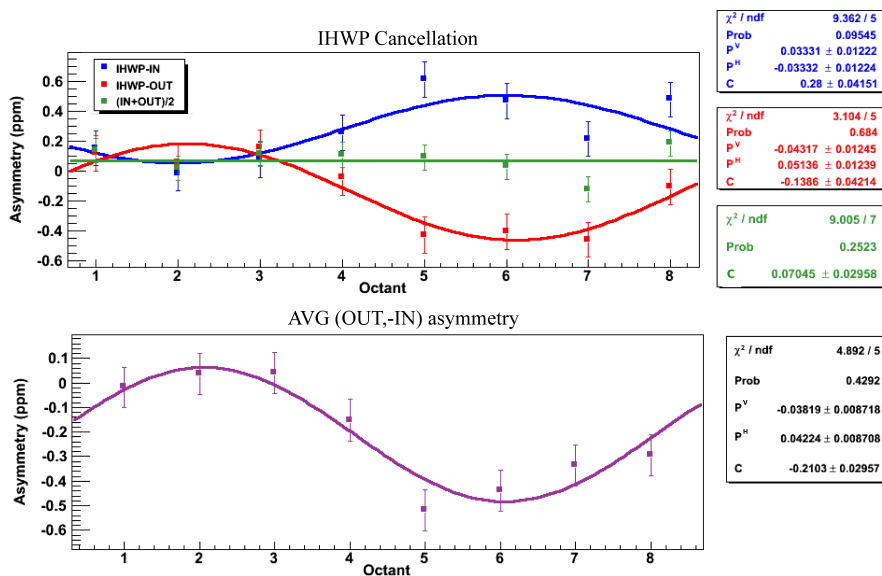


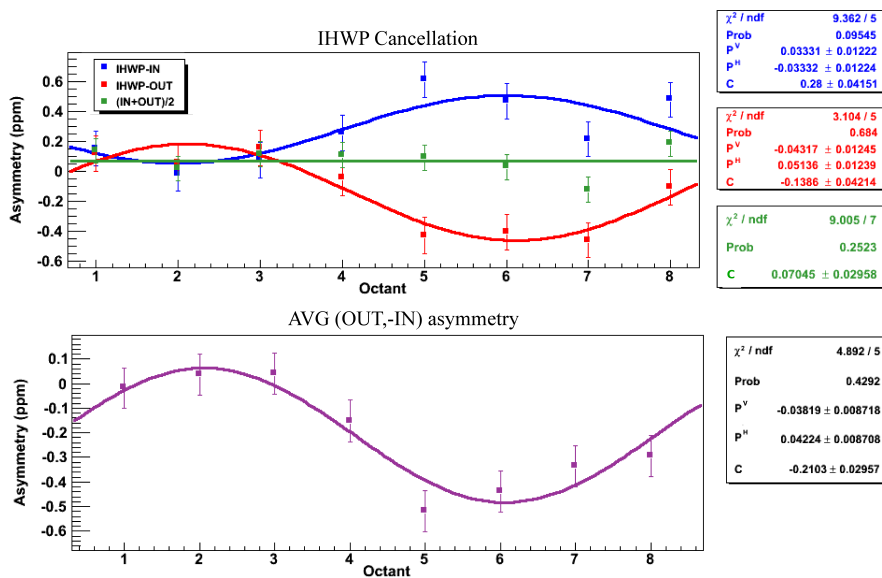
Figure H.6: Correlations between charge asymmetry and the residual transverse polarization in Wien 1-5. Each data point represents a slug pair. The correlations are zero at least within the precision of the fit. The azimuthal fits therefore does not depend on the charge asymmetry.

## H.2 Residual Transverse Polarization in the Wiens

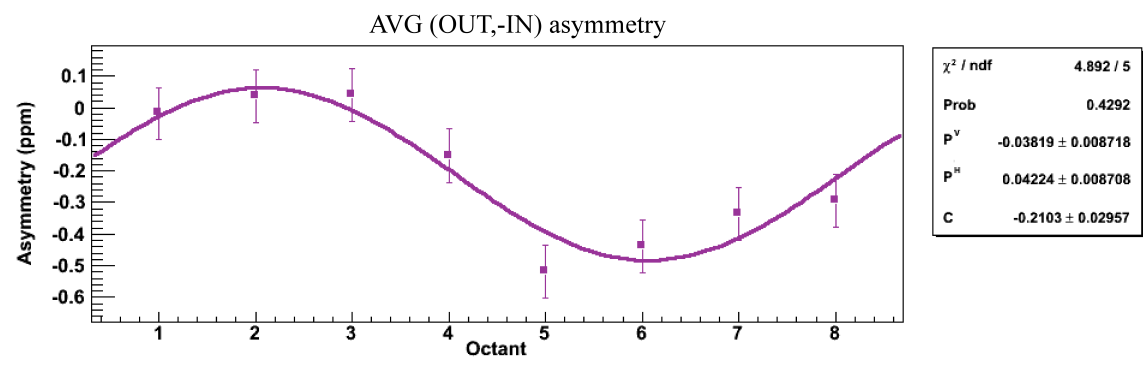
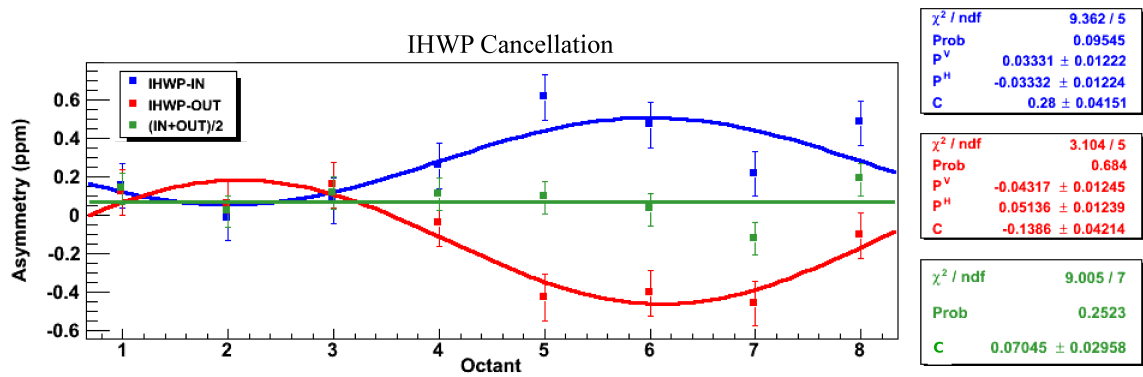
Additional figures for the discussion in Subsection 7.2.1. See [https://hallcweb.jlab.org/qweak/transverse\\_monitor/](https://hallcweb.jlab.org/qweak/transverse_monitor/) for the online transverse monitoring web page of  $Q_{\text{weak}}$  for more details.



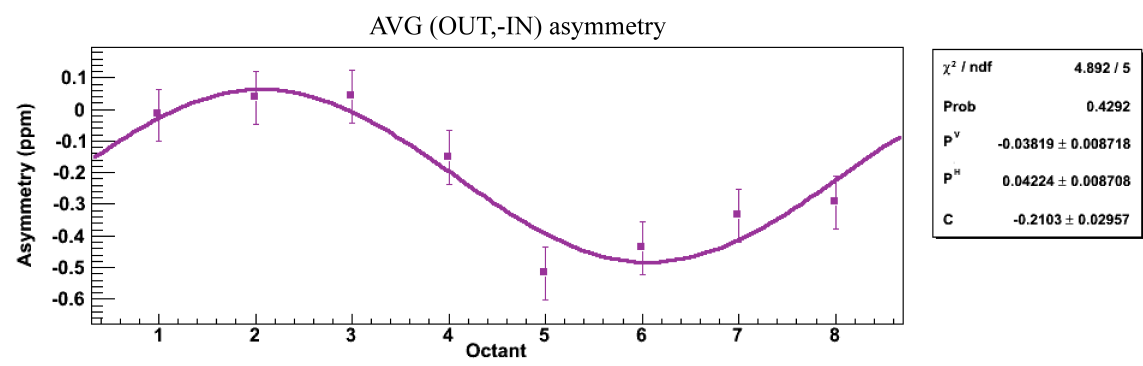
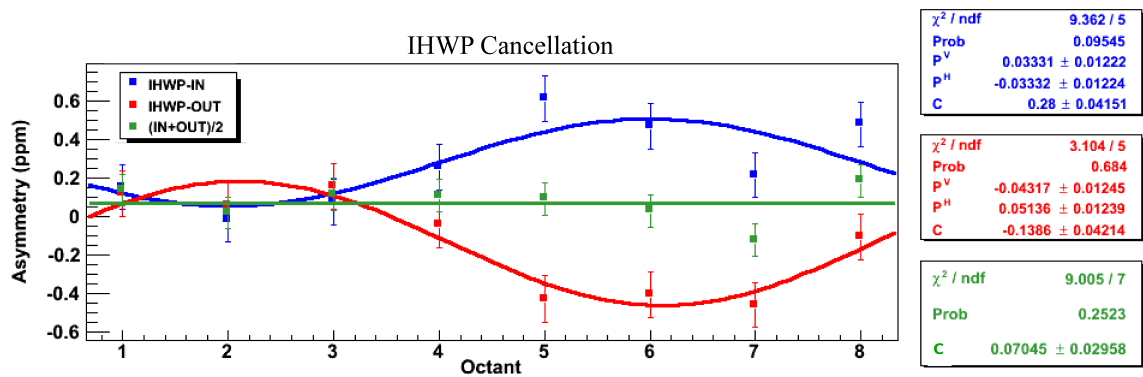
(a) Wien 1



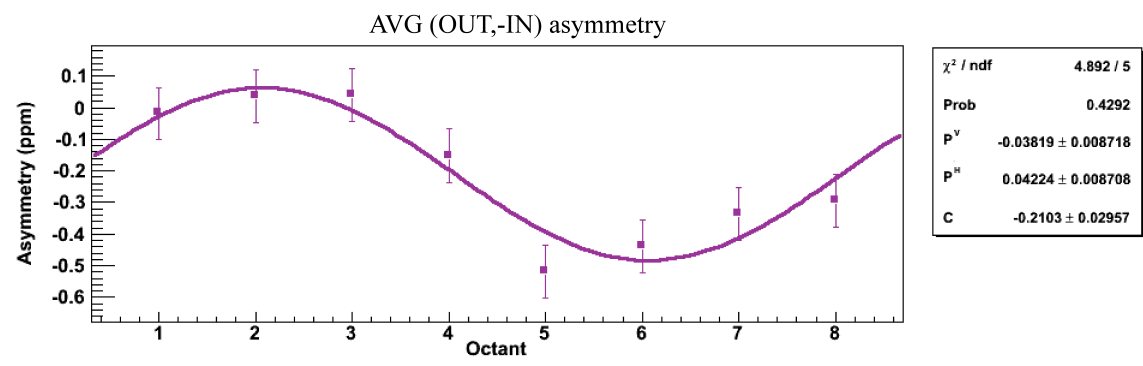
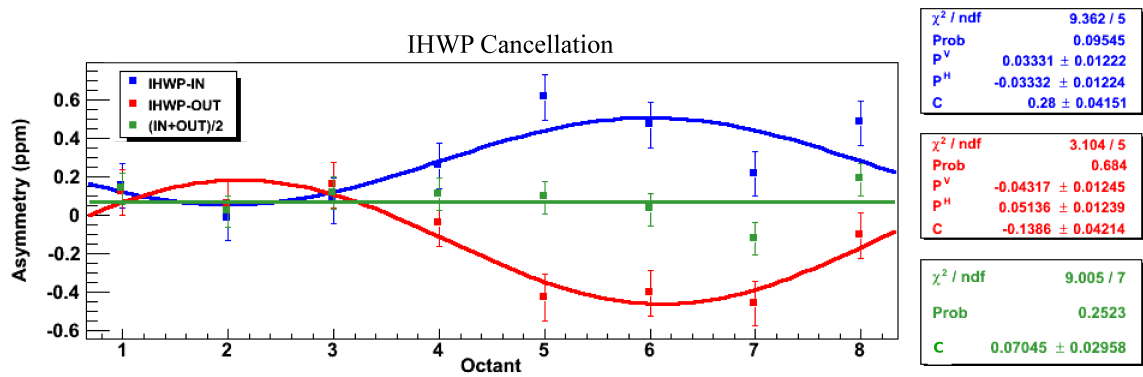
(b) Wien 2



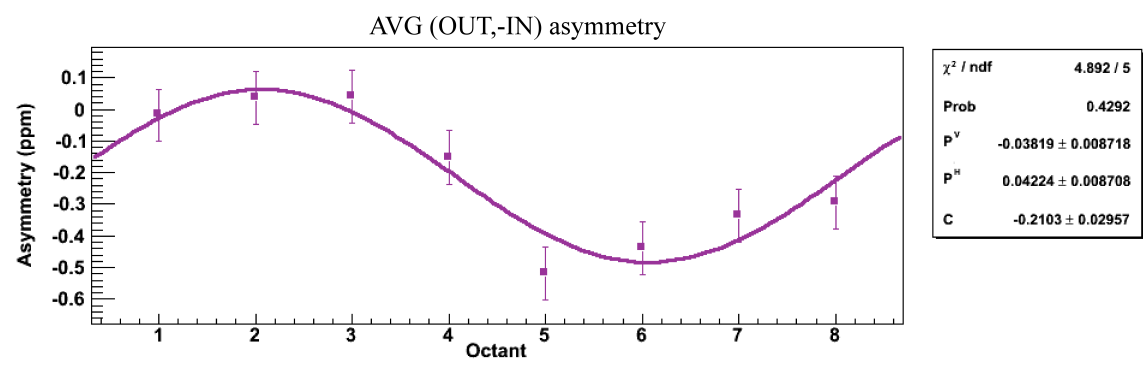
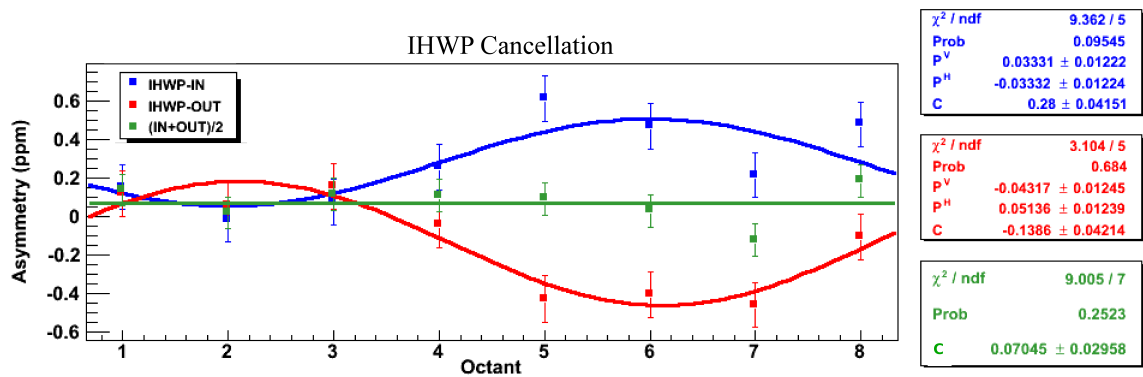
(c) Wien 3



(d) Wien 4

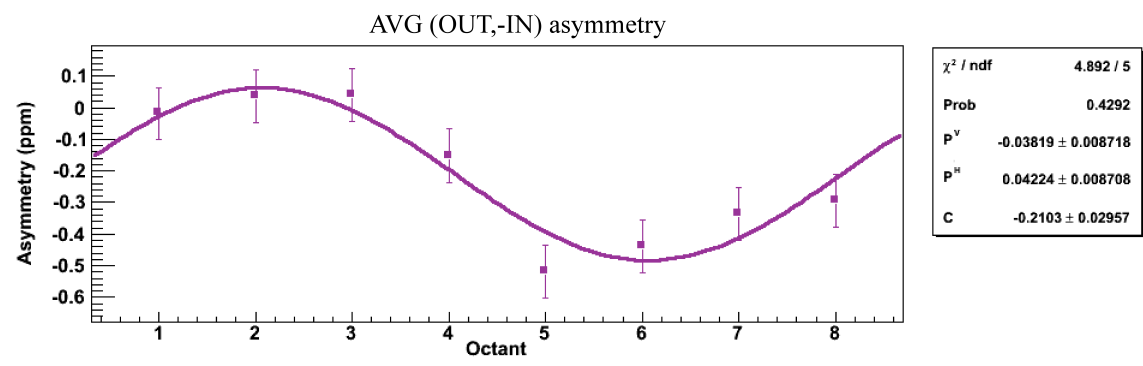
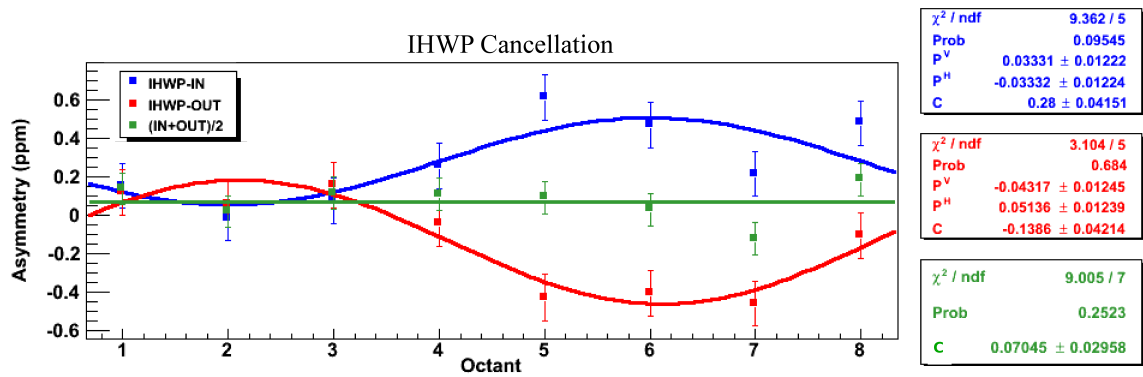


(e) Wien 5

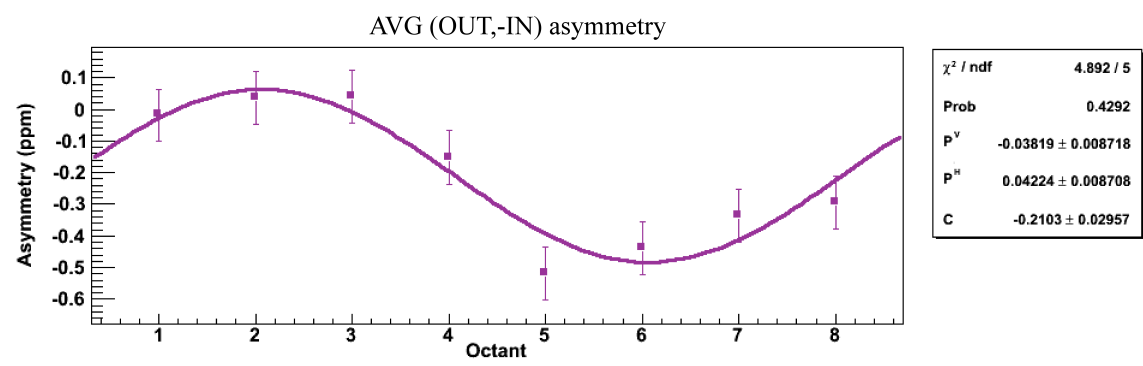
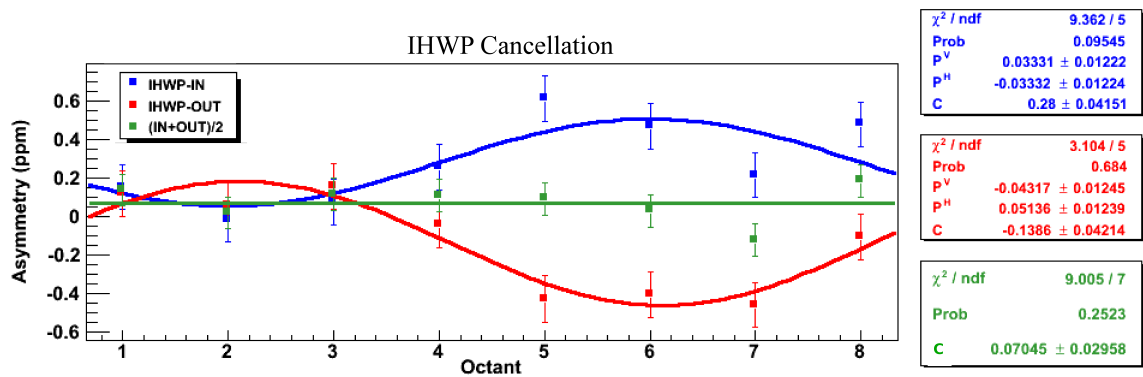


(f) Wien 6

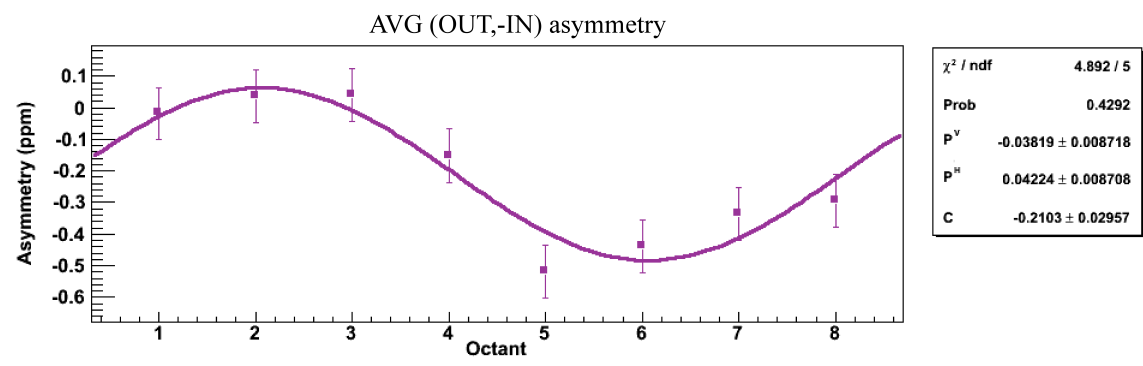
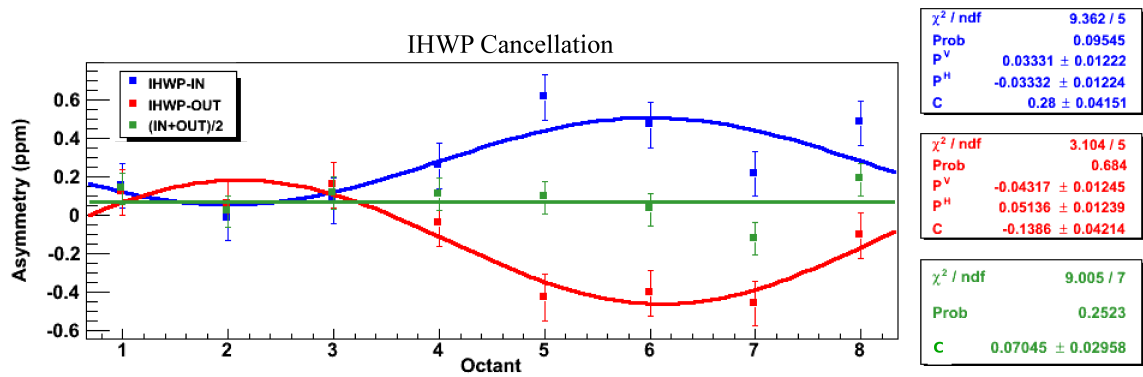




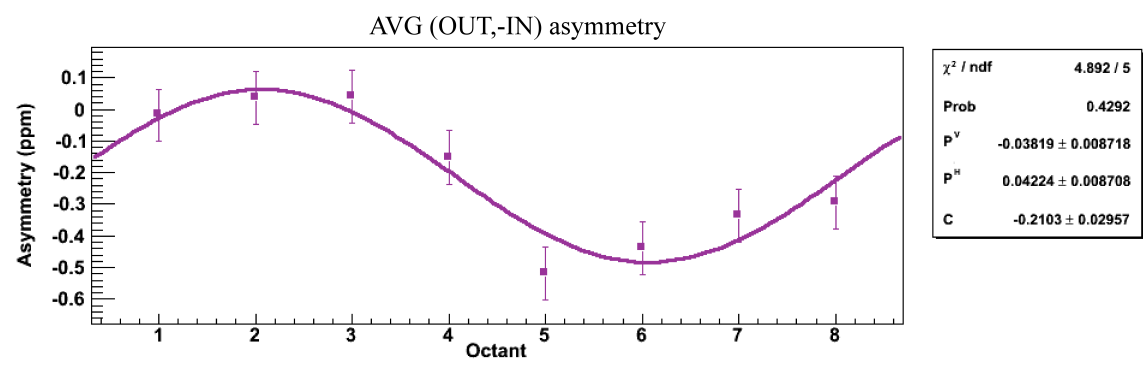
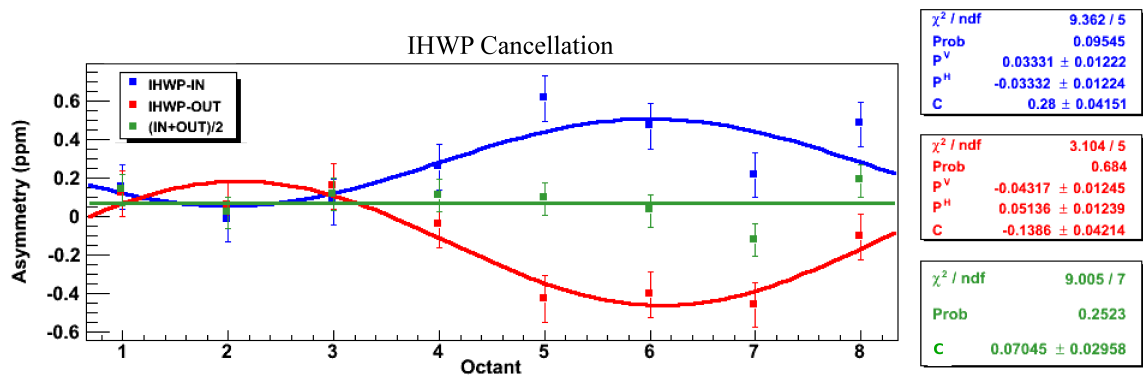
(g) Wien 7



(h) Wien 8



(i) Wien 9



(j) Wien 10

## I Theory Calculations

These are the theory calculations for beam normal single spin asymmetry in electrons scattering with a vertex energy of 1.155 GeV from protons, provided by B.Pasquini, A.Afanasev and M.Gorchtein via private communication.

Table I.1: Theory calculation from A.Afanasev

$\theta_{Lab}$ (deg)	$B_n$ (ppm)	$\theta_{Lab}$ (deg)	$B_n$ (ppm)	$\theta_{Lab}$ (deg)	$B_n$ (ppm)
0.0	0.0	8.0	-4.70921283	15.25	-7.79440879
1.0	-0.380898897	8.25	-4.85456601	15.5	-7.85305408
1.25	-0.511606624	8.5	-4.99781052	15.75	-7.90837945
1.5	-0.648619409	8.75	-5.13876457	16.0	-7.9603234
1.75	-0.790696953	9.0	-5.27753906	16.25	-8.00901115
2.0	-0.936919563	9.25	-5.41359202	16.5	-8.05445836
2.25	-1.08658125	9.5	-5.5472692	16.75	-8.09703098
2.5	-1.23911425	9.75	-5.67829977	17.0	-8.13611326
2.75	-1.39399725	10.0	-5.8066821	17.25	-8.17130574
3.0	-1.55086051	10.25	-5.93244705	17.5	-8.20391157
3.25	-1.70932467	10.5	-6.05523405	17.75	-8.23332382
3.5	-1.86905711	10.75	-6.17522806	18.0	-8.25965626
3.75	-2.02979102	11.0	-6.29211872	18.25	-8.28291359
4.0	-2.19119064	11.25	-6.40614699	18.5	-8.30318623
4.25	-2.35307836	11.5	-6.51709976	18.75	-8.3204153
4.5	-2.51524391	11.75	-6.62505463	19.0	-8.33487053
4.75	-2.6774391	12.0	-6.72985992	19.25	-8.34631972
5.0	-2.83941867	12.25	-6.83139883	19.5	-8.35463823
5.25	-3.00107859	12.5	-6.92968823	19.75	-8.36071253
5.5	-3.1621693	12.75	-7.02478843	20.0	-8.36386038
5.75	-3.3225242	13.	-7.11672635		
6.0	-3.48202486	13.25	-7.20528515		
6.25	-3.64051988	13.5	-7.29060272		
6.5	-3.79778806	13.75	-7.3726854		
6.75	-3.95376828	14.0	-7.45128058		
7.0	-4.10823396	14.25	-7.52656826		
7.25	-4.26121084	14.5	-7.59860618		
7.5	-4.41239989	14.75	-7.66721371		
7.75	-4.56181777	15.0	-7.73247767		

Table I.2: Theory calculation from M.Gorchtein

$\theta_{Lab}$ (deg)	$Q^2(\text{GeV}/c)^2$	$B_n$ (ppm)	$+dB_n$ (ppm)	$-dB_n$ (ppm)
2.000000e-01	1.569650e-05	-3.524259e-02	-3.524231e-02	-3.524287e-02
4.000000e-01	6.278442e-05	-1.115812e-01	-1.115777e-01	-1.115847e-01
6.000000e-01	1.412590e-04	-2.034828e-01	-2.034685e-01	-2.034972e-01
8.000000e-01	2.511124e-04	-3.055178e-01	-3.054795e-01	-3.055562e-01
1.000000e+00	3.923335e-04	-4.151033e-01	-4.150219e-01	-4.151847e-01
1.200000e+00	5.649082e-04	-5.307136e-01	-5.305638e-01	-5.308636e-01
1.400000e+00	7.688190e-04	-6.513369e-01	-6.510866e-01	-6.515873e-01
1.600000e+00	1.004046e-03	-7.762499e-01	-7.758603e-01	-7.766397e-01
1.800000e+00	1.270564e-03	-9.049087e-01	-9.043340e-01	-9.054837e-01
2.000000e+00	1.568348e-03	-1.036887e+00	-1.036075e+00	-1.037701e+00
2.200000e+00	1.897367e-03	-1.171843e+00	-1.170732e+00	-1.172955e+00
2.400000e+00	2.257589e-03	-1.309492e+00	-1.308015e+00	-1.310971e+00
2.600000e+00	2.648977e-03	-1.449596e+00	-1.447678e+00	-1.451518e+00
2.800000e+00	3.071492e-03	-1.591951e+00	-1.589508e+00	-1.594397e+00
3.000000e+00	3.525091e-03	-1.736377e+00	-1.733320e+00	-1.739440e+00
3.200000e+00	4.009730e-03	-1.882720e+00	-1.878949e+00	-1.886498e+00
3.400000e+00	4.525360e-03	-2.030839e+00	-2.026249e+00	-2.035439e+00
3.600000e+00	5.071929e-03	-2.180609e+00	-2.175086e+00	-2.186146e+00
3.800000e+00	5.649382e-03	-2.331917e+00	-2.325340e+00	-2.338513e+00
4.000000e+00	6.257663e-03	-2.484660e+00	-2.476898e+00	-2.492446e+00
4.200000e+00	6.896711e-03	-2.638741e+00	-2.629657e+00	-2.647856e+00
4.400000e+00	7.566461e-03	-2.794072e+00	-2.783521e+00	-2.804663e+00
4.600000e+00	8.266847e-03	-2.950571e+00	-2.938401e+00	-2.962793e+00
4.800000e+00	8.997800e-03	-3.108162e+00	-3.094210e+00	-3.122176e+00
5.000000e+00	9.759247e-03	-3.266770e+00	-3.250868e+00	-3.282750e+00
5.200000e+00	1.055111e-02	-3.426328e+00	-3.408300e+00	-3.444451e+00
5.400000e+00	1.137332e-02	-3.586770e+00	-3.566431e+00	-3.607225e+00
5.600000e+00	1.222578e-02	-3.748034e+00	-3.725192e+00	-3.771015e+00
5.800000e+00	1.310842e-02	-3.910059e+00	-3.884516e+00	-3.935771e+00
6.000000e+00	1.402115e-02	-4.072790e+00	-4.044337e+00	-4.101443e+00
6.200000e+00	1.496387e-02	-4.236171e+00	-4.204594e+00	-4.267984e+00
6.400000e+00	1.593650e-02	-4.400148e+00	-4.365226e+00	-4.435349e+00

Table I.2: Continued ..

$\theta_{Lab}$ (deg)	$Q^2(\text{GeV}/c)^2$	$B_n$ (ppm)	$+dB_n$ (ppm)	$-dB_n$ (ppm)
6.600000e+00	1.693894e-02	-4.564669e+00	-4.526172e+00	-4.603494e+00
6.800000e+00	1.797109e-02	-4.729686e+00	-4.687377e+00	-4.772376e+00
7.000000e+00	1.903285e-02	-4.895147e+00	-4.848784e+00	-4.941954e+00
7.200000e+00	2.012412e-02	-5.061007e+00	-5.010338e+00	-5.112188e+00
7.400000e+00	2.124479e-02	-5.227219e+00	-5.171987e+00	-5.283040e+00
7.600000e+00	2.239475e-02	-5.393736e+00	-5.333677e+00	-5.454471e+00
7.800000e+00	2.357389e-02	-5.560514e+00	-5.495357e+00	-5.626443e+00
8.000000e+00	2.478209e-02	-5.727509e+00	-5.656978e+00	-5.798921e+00
8.200000e+00	2.601924e-02	-5.894679e+00	-5.818488e+00	-5.971868e+00
8.400000e+00	2.728522e-02	-6.061980e+00	-5.979841e+00	-6.145248e+00
8.600000e+00	2.857990e-02	-6.229371e+00	-6.140987e+00	-6.319028e+00
8.800000e+00	2.990317e-02	-6.396810e+00	-6.301879e+00	-6.493171e+00
9.000000e+00	3.125489e-02	-6.564257e+00	-6.462472e+00	-6.667645e+00
9.200000e+00	3.263494e-02	-6.731671e+00	-6.622719e+00	-6.842416e+00
9.400000e+00	3.404318e-02	-6.899013e+00	-6.782574e+00	-7.017450e+00
9.600000e+00	3.547948e-02	-7.066242e+00	-6.941994e+00	-7.192714e+00
9.800000e+00	3.694370e-02	-7.233321e+00	-7.100935e+00	-7.368176e+00
1.000000e+01	3.843571e-02	-7.400210e+00	-7.259352e+00	-7.543802e+00
1.020000e+01	3.995536e-02	-7.566871e+00	-7.417203e+00	-7.719560e+00
1.040000e+01	4.150250e-02	-7.733267e+00	-7.574445e+00	-7.895418e+00
1.060000e+01	4.307700e-02	-7.899359e+00	-7.731038e+00	-8.071345e+00
1.080000e+01	4.467870e-02	-8.065110e+00	-7.886939e+00	-8.247307e+00
1.100000e+01	4.630746e-02	-8.230485e+00	-8.042107e+00	-8.423274e+00
1.120000e+01	4.796312e-02	-8.395445e+00	-8.196504e+00	-8.599214e+00
1.140000e+01	4.964552e-02	-8.559954e+00	-8.350088e+00	-8.775095e+00
1.160000e+01	5.135452e-02	-8.723978e+00	-8.502821e+00	-8.950886e+00
1.180000e+01	5.308995e-02	-8.887479e+00	-8.654665e+00	-9.126556e+00
1.200000e+01	5.485165e-02	-9.050424e+00	-8.805581e+00	-9.302074e+00
1.220000e+01	5.663947e-02	-9.212776e+00	-8.955532e+00	-9.477409e+00
1.240000e+01	5.845323e-02	-9.374501e+00	-9.104481e+00	-9.652529e+00
1.260000e+01	6.029276e-02	-9.535565e+00	-9.252392e+00	-9.827404e+00
1.280000e+01	6.215791e-02	-9.695933e+00	-9.399228e+00	-1.000200e+01

Table I.2: Continued ..

$\theta_{Lab}$ (deg)	$Q^2(\text{GeV}/c)^2$	$B_n$ (ppm)	$+dB_n$ (ppm)	$-dB_n$ (ppm)
1.300000e+01	6.404850e-02	-9.855573e+00	-9.544956e+00	-1.017630e+01
1.320000e+01	6.596436e-02	-1.001445e+01	-9.689539e+00	-1.035026e+01
1.340000e+01	6.790532e-02	-1.017253e+01	-9.832945e+00	-1.052385e+01
1.360000e+01	6.987119e-02	-1.032979e+01	-9.975140e+00	-1.069704e+01
1.380000e+01	7.186181e-02	-1.048618e+01	-1.011609e+01	-1.086981e+01
1.400000e+01	7.387700e-02	-1.064168e+01	-1.025577e+01	-1.104212e+01

Table I.3: Theory calculation from B.Pasquini

$\theta_{Lab}$ (deg)	$B_n$ (ppm)
0.0	0.0
2.0	-0.5725273
7.8	-2.915045
14.0	-5.754369



**OHIO**  
UNIVERSITY

Thesis and Dissertation Services